KU LEUVEN

ARENBERG DOCTORAL SCHOOL
Faculty of Science

High resolution collinear resonance ionization spectroscopy of neutron-rich ^{76,77,78}Cu isotopes

Ruben de Groote

Supervisor:
Prof. dr. G. Neyens

Dissertation presented in partial
fulfillment of the requirements for the
degree of Doctor of Science (PhD):
Physics

September 2017

High resolution collinear resonance ionization spectroscopy of neutron-rich ^{76,77,78}Cu isotopes

Ruben DE GROOTE

Examination committee:
Prof. dr. M. Huyse, chair
Prof. dr. G. Neyens, supervisor
Prof. dr. P. Van Duppen
Prof. dr. P. Lievens
Prof. dr. T. E. Cocolios
Prof. dr. K. Wendt
(J.G.U. Mainz)
Prof. dr. I. Moore
(U. of Jyväskylä)

Dissertation presented in partial fulfillment of the requirements for the degree of Doctor of Science (PhD): Physics

September 2017

Uitgegeven in eigen beheer, Ruben de Groote, Celestijnenlaan 200D box 2418, B-3001 Leuven (Belgium)

Acknowledgements

The challenges of experimental nuclear physics would be quite hard to face alone, and this thesis would have been impossible without the help of many wonderful people.

Gerda, thank you for giving me difficult problems to solve, and for providing the freedom to solve those problems in my own (usually chaotic) way. I don't think I could've found a better supervisor even if I wanted to.

Kieran, thank you for our many in-depth discussions and lengthy Skype conversations. They made me understand the technical aspects of laser spectroscopy as well as the challenges of academia.

I would also like to thank members of my jury (in no particular order): Mark, Piet, Peter, Thomas, Klaus and Iain. I had the pleasure of interacting with all of you on many occasions, and consistently found your critical questions and helpful suggestions to be incredibly valuable.

To my friends in the CRIS group: thank you for making work at ISOLDE infinitely more feasible fun. You made CRIS into the kick-ass experiment that it is today. To all the wonderful people at IKS: thanks for the many fun chats-at-the-coffee-machine, parties, and for not trying to steal my office chair *too* often. Special mention of course the amazing team of technicians and administrative staff: your work makes the life of everyone else much, much easier.

Ik wil natuurlijk mijn fantastische ouders en mijn al even geweldige broer bedanken voor hun steun, zelfs toen ik vreemd genoeg besloot om fysica te gaan studeren. Zonder jullie was ik er nooit aan begonnen, en was ik er al helemaal niet in geslaagd.

Finally, Agi, Köszönöm neked, hogy az elmùlt èv, èletem egyik legjobbja volt. Tegyük az elkövetkező èveket mèg jobbà.

Ruben

Abstract

In this work, nuclear magnetic dipole moments, electric quadrupole moments, nuclear spins and changes in the mean-squared charge radii of radioactive copper isotopes are presented. Reaching up to ^{78}Cu ($Z = 29$, $N = 49$), produced at rates of only 10 particles per second, these measurements represent the most exotic laser spectroscopic investigations near the doubly-magic and very exotic ^{78}Ni ($Z = 28$,$N = 50$) to date. This thesis outlines the technical developments and investigations of laser-atom interactions that were performed during this thesis. These developments were crucial for establishing a high-resolution, high sensitivity collinear resonance ionization spectroscopy experiment at ISOLDE, CERN. This thesis furthermore provides a detailed description of the analysis tools that were implemented and applied to extract the nuclear observables from the experimental data. The results were compared to several large-scale shell model calculations, and provide deep insight into the structure of ^{78}Ni and the region around it.

The importance of excitations across both spin-orbit shell gaps at $Z = 28$ and $N = 50$ could be investigated through comparison with theory. The structure of the odd-odd neutron-rich copper isotopes in particular proved vitally important. All data was found in agreement with the hypothesis of a doubly-magic ^{78}Ni nucleus, yet small amounts of core excitations are required to reproduce the observed nuclear moments. Furthermore, the nuclear spins of ^{76,77}Cu could be unambiguously assigned, which will provide important input for β-decay studies in the region. Finally, the odd-even staggering of the radii was found to rapidly quench as $N = 50$ is approached. Theoretical understanding of this phenomenon will present a challenge for future theoretical investigations of the charge radii of exotic nuclei.

Beknopte samenvatting

Deze thesis bespreekt de magnetische dipoolmomenten, elektrische quadrupoolmomenten, kernspin en veranderingen in de gemiddelde kwadratische ladingsstraal van radioactieve koperisotopen. Deze isotopen zijn de meest exotische isotopen in de buurt van de dubbel-magische ^{78}Ni kern ($Z = 28$,$N = 50$) die tot nu toe met laser spectroscopie bestudeerd zijn. De metingen geven dan ook gedetailleerde informatie over de structuur van ^{78}Ni. Deze thesis geeft een overzicht van de technische ontwikkelingen die gedurende de voorbije vier jaar werden verwezenlijkt, en beschrijft verder ook een theoretische studie van de interactie van lasers met atomen. Deze combinatie van technische en theoretische studies was cruciaal in het verwezenlijken van een collineair resonantie-ionizatiespectroscopie experiment in ISOLDE, CERN, dat toelaat de hyperfijnstructuur van exotische atomen op te meten met een hoge resolutie en efficientie. Deze thesis brengt verder verslag uit over de analysetechnieken die ontwikkeld werden om de resultaten te verwerken. De eigenschappen van de kernen die op die manier werden bepaald, worden verder vergeleken met theoretische shillenmodelberekeningen. Deze vergelijking resulteert in een dieper inzicht in de structuur van ^{78}Ni.

Het belang van excitaties over de spin-baan schilkloven bij $Z = 28$ en $N = 50$ kon worden onderzocht. De structuur van de oneven-oneven neutronrijke koperisotopen was hierbij cruciaal. De data ondersteunt de hypothese dat ^{78}Ni een dubbelmagische kern is. Verder konden de kernspins van ^{76,77}Cu voor het eerst worden vastgelegd. Dit zal een belangrijke bijdrage leveren aan vervalstudies in de regio. Verder treedt er een plotse afname op in de oneven-even-effecten in de ladingsstralen van de exotische koperisotopen. Dit fenomeen is op dit moment nog niet volledig begrepen, en zal een uitdaging vormen voor toekomstig theoretisch onderzoek.

Contents

List of Figures

List of Tables

Chapter 1

Introduction

The start of nuclear physics research is closely tied to the pioneering work of Rutherford, who found that atoms consist of a small, positively charged nucleus with orbiting negatively charged electrons. Since then, our understanding of the atomic nucleus has enormously improved. Early work, primarily done with stable or long-lived isotopes, presented a rich picture of the nucleus. The nuclear shell model, which proved very successful in describing many nuclear properties, established itself as one of the pillars of nuclear theory.

With the advent of radioactive beam facilities, and the flurry of new experiments that spawned as a result, our understanding of nuclear physics was challenged. Magic numbers, once thought immutable, were proven dynamic [1]. The appearance and disappearance of magic numbers has since found an explanation. The crucial realization is that an increased number of neutrons results in increasing changes of the properties of the protons, in a way that becomes most pronounced for nuclei with a large ratio of neutrons to protons [2, 3]. This can lead to large changes in the structure of exotic nuclei.

A clear illustration of this shell evolution phenomenon is found in the isotopic chain of copper from ^{69}Cu onwards, where a sudden strong lowering of the $5/2^-$ level was observed more than a decade ago [4]. Otsuka et al. explained soon afterwards [2, 3] that as the neutron $g_{9/2}$ orbit is filled, the single-particle energy of the proton orbits shift, resulting in a lowering of the $\pi f_{5/2}$ with respect to the $\pi p_{3/2}$ orbit, as shown in Figure 1.1. This is reflected in the increasing importance of the $\pi f_{5/2}$ orbit in the nuclear wavefunctions of $^{69-74}$Cu [5–7]. The odd-even copper isotopes ^{75,77}Cu have a spin 5/2 [6, 8], confirming unambiguously the inversion of the $\pi p_{3/2}$ and the $\pi f_{5/2}$ orbits. A consequence of the shell evolution in this region of the nuclear chart is the potential reduction in the size of the proton shell gap at $Z = 28$ [9]. This reduction in the shell gap could lead to a destabilization of the ^{78}Ni core, a system that should in principle be doubly magic. Recent theoretical calculations confirm this doubly magic status, despite the reduction in the size of the proton shell gap [10, 11].

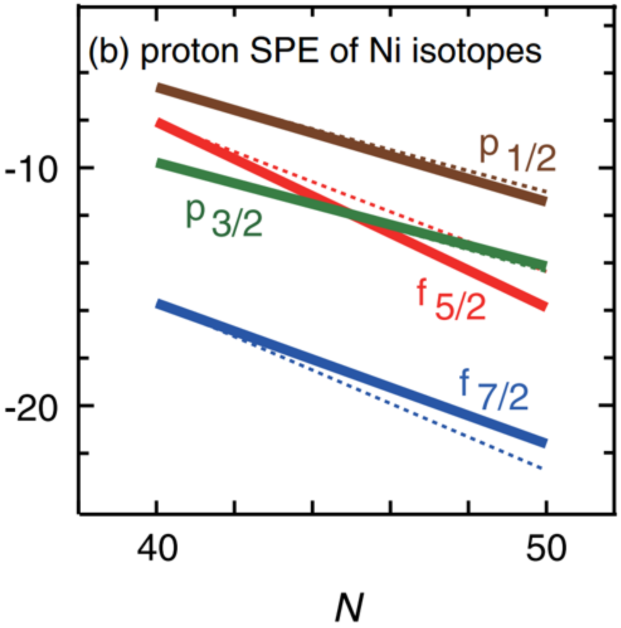

Figure 1.1: Proton single particle energies for the nickel isotopes. Picture taken from [3].

With the previous paragraphs in mind, the following question can be stated: is ^{78}Ni a good, doubly magic nucleus? The answer to this question requires experimental input, and can only be formulated once a full spectrum of experimental observables is determined. The contribution of this thesis lies in the measurement of electromagnetic moments, spins and changes in the mean-squared charge radius of very neutron-rich isotopes of copper, namely $^{76-78}$Cu. With only one proton outside of a nickel core, the moments of these isotopes are very sensitive tests of nuclear shell model theories. For instance, the isotope ^{78}Cu can be described as a ^{78}Ni core with a single valence proton and neutron hole. The simple structure of this nucleus makes it a very pure probe of the underlying ^{78}Ni core.

The structure of this thesis is as follows. First, in chapter 2, an overview of basic concepts of nuclear physics, atomic physics and laser spectroscopy is given.

Then, in chapter 3, the technique that was used for the experiments presented, focusing on the improvements that were implemented during this PhD work. These developments were crucial in achieving the sensitivity and resolution required to study the most exotic copper isotopes. In the following chapter, chapter 4, the choice of laser ionization scheme is discussed. The methods used to analyze the data are outlined in chapter 5. The results of this analysis are then presented in chapter 6. Finally, in the concluding chapter 7, this thesis is summarized, and an outlook towards possibilities for future work is presented.

The following peer-reviewed publications are inserted at various points in the thesis. For readability, these articles do not match in the final two-column format specified by the journal, but are rather presented in a single-column format.

I. Use of a continuous wave laser and pockels cell for sensitive high-resolution collinear resonance ionization spectroscopy,
RP de Groote, I Budinčević, J Billowes, ML Bissell, TE Cocolios, GJ Farooq-Smith, VN Fedosseev, KT Flanagan, S Franchoo, RF Garcia Ruiz, H Heylen, R Li, KM Lynch, BA Marsh, G Neyens, RE Rossel, S Rothe, HH Stroke, KDA Wendt, SG Wilkins, X Yang,
Physical Review Letters, 115(13), 132501, 2015.

II. High-resolution laser spectroscopy with the Collinear Resonance Ionisation Spectroscopy (CRIS) experiment at CERN-ISOLDE.
TE Cocolios, **RP de Groote**, J Billowes, ML Bissell, I Budinčević, T Day Goodacre, GJ Farooq-Smith, VN Fedosseev, KT Flanagan, S Franchoo, RF Garcia Ruiz, W Gins, H Heylen, T Kron, R Li, KM Lynch, BA Marsh, G Neyens, RE Rossel, S Rothe, AJ Smith, HH Stroke, KDA Wendt, SG Wilkins, X Yang,
Nuclear Instruments and Methods in Physics Research Section B: Beam Interactions with Materials and Atoms, 376, 284-287, 2016

III. Efficient, high-resolution resonance laser ionization spectroscopy using weak transitions to long-lived excited states
RP de Groote, M Verlinde, V Sonnenschein, KT Flanagan, I Moore, and G Neyens,
Physical Review A, 95 (3), 032502, 2017.

IV. Double-resonance-ionization mapping of the hyperfine structure of the stable Cu isotopes using pulsed narrowband Ti: sapphire lasers.
RP de Groote, T Kron, A Hakimi, G Neyens, K Wendt,
Physical Review A, 92(2), 022506, 2015

V. Dipole and quadrupole moments of $^{73-78}$Cu as a test of the robustness of the $Z = 28$ shell closure near ^{78}Ni

RP de Groote, J Billowes, CL Binnersley, ML Bissell, TE Cocolios, T Day Goodacre, GJ Farooq-Smith, DV Fedorov, KT Flanagan, S Franchoo, RF Garcia Ruiz, A Koszorús, K M Lynch, G Neyens, F Nowacki, T Otsuka, S Rothe, HH Stroke, Y Tsunoda, AR Vernon, KDA Wendt, SG Wilkins, ZY Xu, and XF Yang,
Submitted to Physical Review C

The work in this thesis has contributed to many other experiments. An overview of the articles that resulted from those experiments is given below.

1. Combined high-resolution laser spectroscopy and nuclear decay spectroscopy for the study of the low-lying states in Fr 206, At 202, and Bi 198.
   KM Lynch, TE Cocolios, J Billowes, ML Bissell, I Budinčević, T Day Goodacre, **RP de Groote**, GJ Farooq-Smith, VN Fedosseev, KT Flanagan, S Franchoo, RF Garcia Ruiz, H Heylen, R Li, BA Marsh, G Neyens, RE Rossel, S Rothe, HH Stroke, KDA Wendt, SG Wilkins, X Yang,
   Physical Review C, 93(1), 014319, 2016.

2. Laser and decay spectroscopy of the short-lived isotope Fr 214 in the vicinity of the N= 126 shell closure.
   GJ Farooq-Smith, TE Cocolios, J Billowes, ML Bissell, I Budinčević, T Day Goodacre, **RP de Groote**, VN Fedosseev, KT Flanagan, S Franchoo, RF Garcia Ruiz, H Heylen, R Li, KM Lynch, BA Marsh, G Neyens, RE Rossel, S Rothe, HH Stroke, KDA Wendt, SG Wilkins, XF Yang,
   Physical Review C, 94(5), 054305, 2016.

3. Achieving sensitive, high-resolution laser spectroscopy at CRIS.
   RP de Groote, KM Lynch, SG Wilkins, and the CRIS collaboration,
   Hyperfine Interactions, 238(1), 5, 2017.

4. Analysis of counting data: development of the SATLAS Python package,
   W Gins, **RP de Groote**, ML Bissell, C Granados Buitrago, R Ferrer, KM Lynch, G Neyens and S Sels,
   Accepted for publication in Computational Physics Communications.

5. The quadrupole moment of ^{203}Fr: onset of static deformation at $N = 116$,
   SG Wilkins, KM Lynch, J Billowes, CL Binnersley MLBissell TE Cocolios, T Day Goodacre, **RP de Groote**, GJ Farooq-Smith, VN Fedosseev, KT lanagan S Franchoo, RF Garcia Ruiz, H Heylen, A Koszorús, BA Marsh, G Neyens, S Rothe, HH Stroke, AR Vernon, KDA Wendt, and XF Yang,
   Submitted to Physical Review C.

6. Probing the ${}_{31}$Ga ground-state properties near the $Z = 28$ region with high-resolution laser spectroscopy,
   GJ Farooq-Smith, AR Vernon, J Billowes, CL Binnersley, ML Bissell, TE Cocolios, T Day Goodacre, **RP de Groote**, KT Flanagan, S Franchoo, RF Garcia Ruiz, W Gins, KM Lynch, BA Marsh, G Neyens, S Rothe, HH Stroke, SG Wilkins, and XF Yang,
   Sumbitted to Physical Review C.

Chapter 2

Concepts from nuclear and atomic physics

Laser spectroscopy methods use the atomic structure of an isotope to access information on the structure of the atomic nucleus. This chapter will provide a brief overview of some of the basic ideas in nuclear and atomic physics that are of relevance for this thesis.

2.1 Nuclear structure

The atomic nucleus is a complex quantum system consisting of many protons and neutrons that all interact with one another. Despite the inherent complications of solving such a many-body problem, and the limited understanding of the inter-nucleon forces in the nuclear medium, great strides have been made in the description of nuclear properties. A cornerstone of nuclear theory is the shell model, which will be introduced first.

2.1.1 The nuclear shell model

An important insight into nuclear structure came with the observation of regular patterns in many experimental observables, which lead to the development of the concept of magic numbers [12, 13]. These magic numbers are particular numbers of protons or neutrons that lead to enhanced stability. This can be ascertained experimentally: magic nuclei have e.g. a more tightly bound valence proton or neutron, or high 2^+ excited state energies. Near stability, there is considerable experimental evidence for magicity at nucleon numbers 2, 8, 20, 28, 50, 82 and 126. This led to the development of the nuclear shell model [14]. This model provides a quantum-mechanical description of nuclear structure in which protons and neutrons can only occupy specific shells, which are separated by an energy gap. Describing the properties of a particular nucleus is then achieved by gradually filling up the proton and neutron shells according to the rules imposed by quantum mechanics. Particular numbers of protons or neutrons will lead to complete filling of a shell. If the energy gap above that shell is sufficiently large, and the nuclear correlations are not too large, the corresponding nucleus will possess magic experimental properties.

To see how the nuclear shell model is constructed, and to understand how current state-of-the-art shell models work, some theoretical concepts need to be introduced. The nuclear many body problem can be succinctly written down as follows:

$$H\left|\Psi\right\rangle = (T+V)\left|\Psi\right\rangle = E\left|\Psi\right\rangle. \tag{2.1}$$

In this definition, T is the kinetic energy operator, and V is the potential energy of the many interacting nucleons. This potential energy is determined by the inter-nucleon interactions, and determining the form of V has proven a significant challenge. To simplify things, the potential V can be limited to only include two-body interactions:

$$V = \sum_{i<j} v_{ij} + \sum_{i<j<k} v_{ijk} + \dots \tag{2.2}$$

$$\approx \sum_{i<j} v_{ij}. \tag{2.3}$$

It is now understood that e.g. the three-body terms do play a role, and that they should in principle not be neglected (see e.g. [15]).

Even after restricting the calculations to only include two-body interactions, solving (2.1) is still a difficult problem. Progress can be made by introducing the mean-field potential U and rewriting the Hamiltonian as follows

$$H = T + \sum_i U_i + V - \sum_i U_i \tag{2.4}$$

$$= \quad H_0 \qquad + \quad H_{\text{res}}. \tag{2.5}$$

While in effect nothing changed here (a term was added and then later subtracted again), this way of writing down the Hamiltonian enables it to be interpreted in a different way. Note that H_0 describes a system of nucleons that move independently of each other, in an average potential generated by all other nucleons. The residual Hamiltonian H_{res} can then be considered a perturbation that is added to H_0.

The independent-particle shell model

In the independent particle shell model, one sets $H = H_0$. One then needs to choose an appropriate form for the potential U. A starting point is the harmonic oscillator potential

$$U(r) = \frac{1}{2} m\omega^2 r^2. \tag{2.6}$$

Using the harmonic oscillator potential leads to magic numbers at nucleon numbers 2, 8, 20, 40, 70, ... While this seems to work for light systems, the magic numbers of e.g. 28 and 50 are not reproduced. One modification which leads to the reproduction of the experimentally observed magic numbers is to take this harmonic oscillator potential, and to add a spin-orbit term and a term proportional to the square of the orbital angular momentum l [12, 13]:

$$U(r) = \frac{1}{2} m\omega^2 r^2 + C\, \boldsymbol{l} \cdot \boldsymbol{s} + D\, l^2. \tag{2.7}$$

Figure 2.1 shows the single particle energies (SPE) calculated with the harmonic oscillator potential of equation (2.6), and adds the two additional terms in equation (2.7) one by one to show their effect. The shell gaps at 28 and 50 are both a consequence of the spin orbit term. Note for example how the $g_{9/2}$ level becomes more bound (reduces in energy) due to the spin-orbit term.

The independent-particle shell model can explain many features of the nuclear landscape, and provides an intuitive framework to help with the interpretation of many experimental results. However, the inclusion of two-body interactions is a crucial step towards a better description of the details of nuclear structure.

The interacting shell model

In the interacting shell model, H_{res} is no longer neglected but rather included in the calculations. Since H_{res} contains the nucleon-nucleon interactions, all orbits close to the Fermi surface should be included in these calculations. Ideally, as many orbitals as possible are included in the calculations, but in practice this quickly leads to insurmountable computational cost. For this reason the nucleus

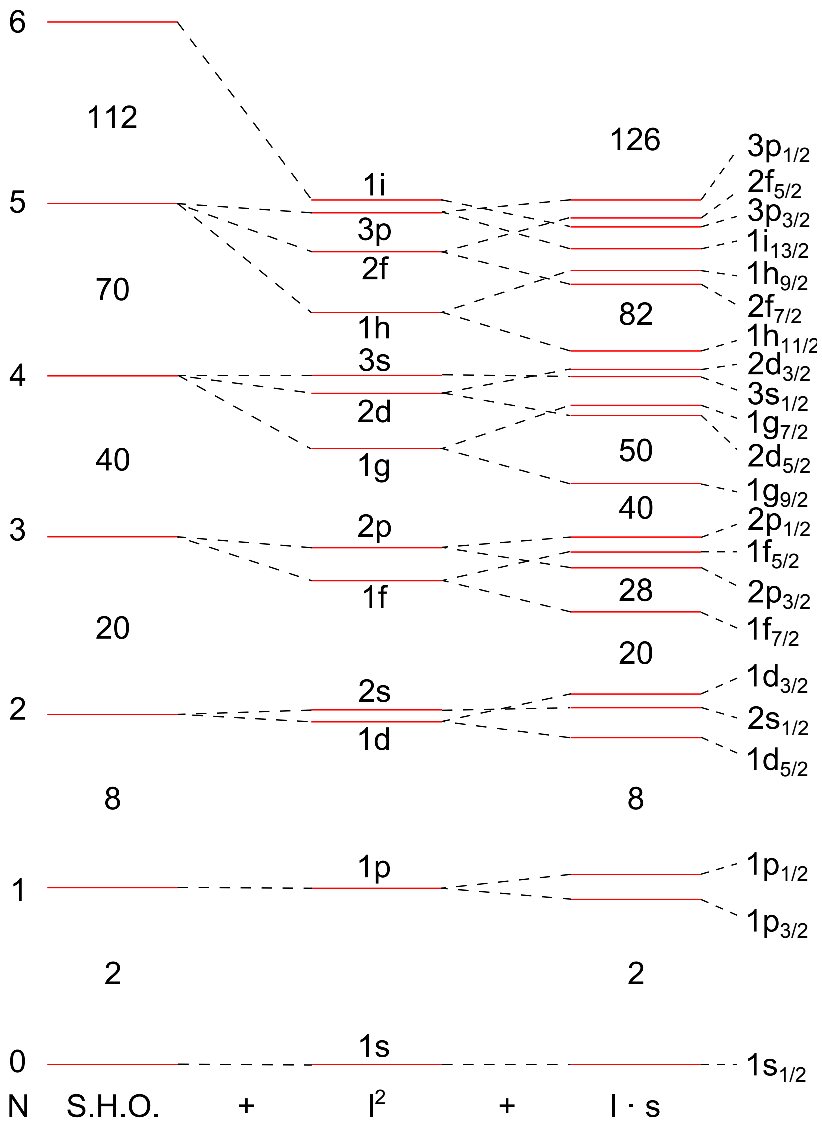

Figure 2.1: Single particle energies calculated with a harmonic oscillator potential, with an additional l^2 term, and then with an additional spin-orbit term. Figure adapted from [16].

is rather considered as an inert core with additional valence particles that are free to move around in a restricted valence space outside of this core.

That this simplification of the nuclear many-body system is in fact an over-simplification is also reflected in calculated quadrupole moments. In order to match experimental data in a particular region of the nuclear chart, effective proton and neutron charges need to be introduced. In order to compensate for the missing core excitations and the corresponding deformation, the charge of the proton and neutron needs to be increased. For example, in the nickel region, the JUN45 interaction uses effective proton- and neutron charges $e_p = 1.5, e_n = 1.1$ [17]. Ideally, as the core space gets smaller, these effective charges should converge to the free-nucleon charges of $e_p = 1, e_n = 0$.

Typically, the core space consists of filled shells for both protons and neutrons. A logical choice for the valence space is then the collection of orbitals in between two shell gaps, since the energy gap inhibits both core excitations and excitations from orbitals in the valence space to higher orbits. For example, the model space that is used with the JUN45 interaction consists of a ^{56}Ni core and the valence space consists of the $2p_{3/2}, 1f_{5/2}2p_{1/2}1g_{9/2}$ orbits. However, as will be shown in this thesis, care needs to be taken when choosing a model and valence space. For instance, accurate prediction of g-factors and quadrupole moments of exotic copper isotopes is not possible using a ^{56}Ni core. To reproduce the observed nuclear moments requires requires including the $\pi\nu f_{7/2}$ orbital as well as orbits above $N = 50$ into the valence space, as will be illustrated in this thesis.

The inter-nucleon interaction has to be adapted for each choice of model and valence space, resulting in an effective interaction. When $n_{j'}$ nucleons are added to orbital j', the monopole component of H_{res} will shift the single particle energy ϵ_j of a nucleon in orbital j by [2]

$$\Delta\epsilon_j = \frac{\sum_J (2J+1) \langle jj'J| V |jj'J\rangle}{\sum_J 2J+1} n_{j'} \tag{2.8}$$

The sum of the SPE and this monopole shift is referred to as the Effective Single Particle Energy (ESPE). Since $\Delta\epsilon_j$ grows with increasing occupation of $n_{j'}$, it can lead to sizable changes in the ESPE and can drive shell evolution [18]. In particular, the tensor component of this monopole drift gives rise to an attractive interaction between orbits with opposite relative orientation of the orbital angular momentum j and the spin angular momentum s, and a repulsion otherwise. This mechanism is what gives rise to e.g. the spin inversion in the neutron-rich copper isotopes [6]: as neutrons are added to $\nu g_{9/2}$, the ESPE of the proton orbits shift, leading to a lowering of $\pi f_{5/2}$ ESPE compared to the $\pi p_{3/2}$.

Large-scale shell model calculations

This thesis will compare experimental results to calculations performed with the JUN45, A3DA-m and PFSDG-U interactions. These are effective interactions, which derive values of the two-body matrix elements by fitting them to experimental data. Figure 2.2 shows a diagram of the model spaces that were used for the calculations in this thesis.

The JUN45 interaction [17] provides the starting point for this work, and is the baseline that more advanced calculations will be compared to. The model space consists of a ^{56}Ni core with a valence space that spans the $f_{7/2}$, $p_{3/2}$, $f_{5/2}$, $p_{1/2}$ and $g_{9/2}$ orbits for both protons and neutrons.

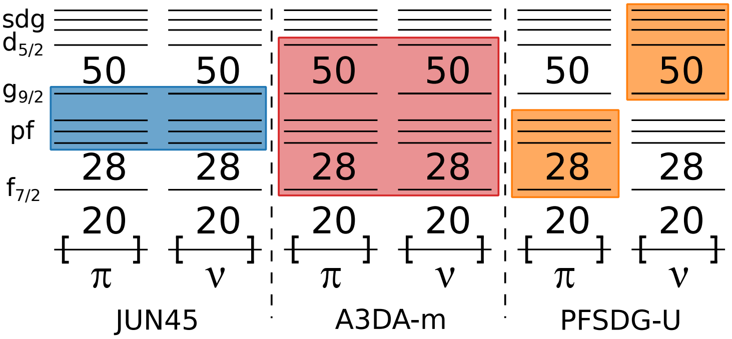

Figure 2.2: Diagram of the model spaces used with the JUN45 interaction, the A3DA-m interaction, and the PFSDG-U interaction.

The model space that is used with the A3DA-m interaction [19, 20] consists of a ^{40}Ca core with a valence space that spans the full *pf*-shell, the $g_{9/2}$ and $d_{5/2}$ orbits. This makes it well suited to investigate the role of excitations across both the $Z = 28$ and $N = 50$ shell gaps. The two-body matrix elements are obtained by combining several existing interactions (including JUN45), and by making some additional phenomenological modifications [19].

The PFSDG-U interaction has a valence space that consists of the *pf* shell for the protons and the *sdg* shell for neutrons [10]. It has been applied previously to study shape coexistence near ^{78}Ni, and has demonstrated good agreement with many experimental observations in the region of ^{78}Ni. It is therefore particularly appropriate to study the very neutron-rich copper isotopes.

2.1.2 Nuclear ground-state properties

Understanding the structure of atomic nuclei requires sensitive probes into its inner workings. Laser spectroscopy techniques such as the one used in this thesis can determine several properties of the nuclear ground state and of isomeric states (if their lifetime permits), which will be discussed next.

Nuclear spin

The nucleons inside the nucleus occupy orbitals that are characterized by an orbital angular momentum l_i and a spin angular momentum s_i, which couple to a total angular momentum j_i. For nuclei near closed shells, the total nuclear spin I is then the result of the coupling of all the spins j_i. Luckily, the pairing force favours coupling nucleon pairs to a total spin 0, which means that for these systems only the angular momenta of the valence particles need to be considered. The nuclear spin of odd-A isotopes therefore provides an important first indication on the configuration of the valence particle(s).

For many systems with both an odd number of protons and neutrons, the nuclear ground-state spin can in principle assume any value allowed by the angular momentum coupling rules. An approximate rule, called Paar's rule [21], can often be used to estimate which particular spin value will have the lowest energy.

Deviations from these general principles provide evidence for collective effects that are not considered in this single-particle picture.

Nuclear mean-squared charge radius

Using the nuclear density distribution, one can define the radial moments of the nuclear matter distribution [22, 23]:

$$\left\langle r^N \right\rangle = \frac{1}{Ze} \int r^N \rho(r, \theta, \phi)\, \mathrm{d}V \tag{2.9}$$

Laser spectroscopy techniques only have access to the second moment of the charge distribution, called the mean-squared charge radius:

$$\left\langle r_{\mathrm{ch}}^2 \right\rangle = \frac{1}{Ze} \int r^2 \rho_{\mathrm{ch}}(r, \theta, \phi)\, \mathrm{d}V, \tag{2.10}$$

which we will from here on out simply denote with $\left\langle r^2 \right\rangle$. This quantity provides a well-defined parameter that can be used to compare the size of nuclei. An overview of charge radii values can be found in [24]. Laser spectroscopy techniques cannot extract the values $\left\langle r^2\right\rangle$, but rather allow extraction of the difference in $\left\langle r^2\right\rangle$, between two isotopes A and A', denoted with $\delta\left\langle r^2\right\rangle^{AA'}$.

The mean-squared charge radius $\left\langle r^2\right\rangle$ of an axially symmetric deformed nucleus with quadrupole deformation parameter β can be parameterized relative to $\left\langle r^2_{\mathrm{sph}}\right\rangle$, the mean-squared charged radius of a spherical nucleus with the same volume:

$$\left\langle r^2\right\rangle = \left\langle r^2_{\mathrm{sph}}\right\rangle\left(1+\frac{5}{4\pi}\left\langle\beta^2\right\rangle\right). \tag{2.11}$$

So, an increase in deformation leads to an increase in the mean-squared charge radius. Since the radius of nuclei behaves roughly according to the liquid drop-model, $\left\langle r^2_{\mathrm{sph}}\right\rangle$ is often equated to the liquid-drop mean-squared charge radius $\left\langle r^2_{\mathrm{LD}}\right\rangle$:

$$\left\langle r^2_{\mathrm{LD}}\right\rangle = \frac{3}{5}R_0^2A^{2/3}, \tag{2.12}$$

where $R_0 \approx 1.2\,\mathrm{fm}$.

In addition to the liquid-drop behaviour and the link to nuclear deformation, a sudden change in the slope of the charge radius for an isotopic chain has been correlated to the crossing of a magic number. This effect is clearly visible throughout the nuclear chart [24].

Another feature of charge radii that is prevalent across the nuclear chart is called the odd-even staggering (OES). This term refers to the observation that, usually, the radius of an isotope with an odd number of neutrons is smaller than the average radius of its even-N neighbours. Some exceptions have been identified; this inversion of OES has for instance been linked to reflection-asymmetric nuclear shapes (see [25] and references therein) or deformation induced by the valence neutron [26]. Several mechanisms for OES have been discussed in literature, which will be further investigated in section 6.3.4. However, a complete understanding of the microscopic origins of the effect remains challenging.

The magnetic dipole moment

A vast amount of experimental data suggests that nuclei with $I \neq 0$ have a magnetic dipole moment $\mu = gI\mu_N$ [27], where g is called the g-factor and $\mu_N = \frac{e\hbar}{2m_\pi} = 5.050783699(31)\cdot 10^{-27}\mathrm{J/T}$ the nuclear magneton. The magnetization of the nucleus can be attributed to orbiting (charged) protons inside the nucleus, and the intrinsic spin of the nucleons. The magnetic dipole operator $\boldsymbol{\mu}$ is therefore given by [27]

$$\boldsymbol{\mu} = \left(\sum_{i=0}^{Z} g_L^{\pi} \boldsymbol{L}_i + \sum_{i=0}^{Z} g_S^{\pi} \boldsymbol{S}_i + \sum_{j=0}^{N} g_L^{\nu} \boldsymbol{L}_j + \sum_{j=0}^{N} g_S^{\nu} \boldsymbol{S}_j \right) \mu_N. \tag{2.13}$$

The factors g_L and g_S are the orbital and spin gyromagnetic factors. They are different for protons and neutrons: $g_L^{\pi} = 1, g_L^{\nu} = 0$, since neutrons have no net charge, and $g_S^{\pi} = +5.585694702(17), g_S^{\nu} = -3.82608545(90)$, which are determined using the magnetic moment of the free proton and neutron. The magnetic moment is defined as the expectation value of the z-component of the magnetic dipole operator for the nuclear substate which has the maximal spin projection $m = I$:

$$\mu = \langle I, m = I | \, \boldsymbol{\mu}_z \, | I, m = I \rangle \tag{2.14}$$

$$= \left(\frac{I}{I+1} \right)^{1/2} \langle I \| \, \boldsymbol{\mu} \, \| I \rangle \tag{2.15}$$

When going from the first to the second line, the Wigner-Eckhart theorem was used. This shows that a state with $I = 0$ has no observable magnetic dipole moment. This also means that pairs of nucleons that couple to $|[j_1, j_1], J = 0\rangle$ do not contribute to the magnetic dipole moment of the nucleus - only the unpaired valence nucleons do.

The magnetic dipole moment operator is a tensor of rank one. Interestingly, for any such tensor, one can show that [16]

$$\mu(j^n \nu I)/I = \mu(j)/j. \tag{2.16}$$

In other words, when n nucleons are placed in an orbital with angular momentum j (with ν of those nucleons unpaired), the g-factor of that final state $|j^n \nu I\rangle$ is identical to the g-factor of a single nucleon in that orbit. This has powerful implications, since it makes g-factors (or, if the nuclear spin is known, magnetic moments) ideal probes to verify in which orbital valence nucleons are placed, irrespective of the total spin. A sudden change in the g-factor in an isotopic chain is therefore a clear sign of structural change in the nuclear wavefunction.

Furthermore, using the machinery of tensor algebra, one can also derive an addition theorem which can be used to compute the g-factor of a composite system $|[j_1, j_2], J \neq 0\rangle$, consisting of two nucleons with angular momenta j_1 and j_2 and g-factors g_1 and g_2 [28]:

$$g = \frac{1}{2}(g_1 + g_2) + \frac{1}{2}(g_1 - g_2) \frac{j_1(j_1+1) - j_2(j_2+1)}{J(J+1)} \tag{2.17}$$

This addition theorem can for instance be used to investigate the configuration of odd-odd nuclei, by taking empirical g-factors of neighbouring odd-even and even-odd isotopes with known configurations, and inserting them into (2.17).

The addition theorem (2.17) can also be used to calculate the g-factor for a single nucleon with orbital angular momentum l, spin s and total angular momentum j:

$$g = \frac{1}{2}\left(g_l + g_s\right) + \frac{1}{2}\left(g_l - g_s\right)\frac{l(l+1) - 3/4}{j(j+1)} \tag{2.18}$$

These g-factors are referred to as the Schmidt values [29]. Experimentally, large deviations from this simple expression are observed (see e.g. [30, 31] for some of the pioneering work). There are two reasons for this [27]. Firstly, there are additional contributions to the total magnetic moment of a nucleus, due to e.g. meson exchange currents and core polarization effects. The magnetic moment operator is therefore no longer of the simple form (2.13). Rather than using a more complicated form of the magnetic dipole moment operator, an effective operator is introduced, which gives rise to effective moments. Typically $g_{s,\mathrm{eff}}$ is found to be between $\approx 0.7 g_s$ and $0.9 g_s$, $g^{\pi}_{l,\mathrm{eff}} \approx 1.1$ and $g^{\nu}_{l,\mathrm{eff}} \approx -0.1$. Secondly, the wavefunction of real nuclei is usually not a pure single-particle wavefunction, and the g-factor therefore contains contributions from several different configurations.

Comparison of experimental g-factors to simple calculations using (2.18) and (2.17) for odd-odd systems, with effective values of $g_{l,s}$ provides a very powerful tool to establish nuclear configurations in a way that does not depend on the intricacies of e.g. more advanced shell model calculations. Furthermore, deviations from these effective g-factors are often interpreted as a sign of mixing in the nuclear configuration. Magnetic moments are particularly sensitive to mixing of spin-orbit partners [32]. These orbits have the same orbital angular momentum, but opposite spin angular momentum. Labeling the state with $j = l + 1/2$ as $|{\uparrow}\rangle$ and the state with $j = l - 1/2$ as $|{\downarrow}\rangle$, the magnetic moment of $|\Psi\rangle = c_1 |{\downarrow}\rangle + (1 - c_1) |{\downarrow}\rangle$ is equal to

$$\mu_\Psi = c_1^2 \mu_\uparrow + (1 - c_1)^2 \mu_\downarrow + 2c_1(1 - c_1) \langle{\uparrow}|\, \boldsymbol{\mu}\, |{\downarrow}\rangle \tag{2.19}$$

Since the angular momentum of $|{\downarrow}\rangle$ and $|{\uparrow}\rangle$ differ by one unit of angular momentum, and the magnetic dipole moment operator is a rank one tensor, the third term in this expression is nonzero. It can therefore significantly impact the magnetic moment of the mixed state $|\Psi\rangle$.

The electric quadrupole moment

Since the nucleus contains charged protons, non-spherical nuclei also posses a non-zero electrical quadrupole moment, which can be described using the electrical quadrupole moment tensor $\boldsymbol{Q}$. The components of this tensor are

$$\boldsymbol{Q}_{ij} = e\sum_{l=0}^{Z}(3r_{il}r_{jl} - r_l^2), \tag{2.20}$$

or, using spherical tensors:

$$\boldsymbol{Q}_m = e\sqrt{\frac{4\pi}{5}}\sum_l r_l^2 Y_m^2(\theta_l, \phi_l). \tag{2.21}$$

The quadrupole moment is defined as the expectation value of $\boldsymbol{Q}_z$ in a nuclear state with $m = I$:

$$Q = \langle I, m = I|\, \boldsymbol{Q}_z \,|I, m = I\rangle \tag{2.22}$$

$$= \left(\frac{16\pi}{5}\frac{I(2I-1)}{(I+1)(2I+3)}\right)^{1/2} \langle I \| \sum_{i=0}^{Z} r_i^2 Y_0^2(\theta_i, \phi_i) \, \| I\rangle, \tag{2.23}$$

where once again the Wigner-Eckhart theorem was used. This expression shows that, for $I \leq 1/2$, the value of the quadrupole moment evaluates to zero, even if the charge distribution is nonspherical.

Since closed-shell systems tend to couple to a total spin of $I = 0$, the quadrupole moment of a system with a single proton outside a closed shell is completely determined by the single particle quadrupole moment of that proton [27]

$$Q_{s.p.} = -e\frac{2j-1}{2j+2}\left\langle r^2 \right\rangle_{s.p.}, \tag{2.24}$$

where $\left\langle r^2 \right\rangle_{s.p.}$ is the mean-squared charge radius associated with the wave function of the single proton. This is rather unfortunate, since unlike single particle magnetic moments, calculating $Q_{s.p.}$ requires assumptions on the wave function of the single proton.

The quadrupole moment of a closed shell system with an odd number n of valence protons (assuming a seniority $\nu = 1$ configuration) can also be calculated in a straightforward way using [27]

$$Q = Q_{s.p.}\frac{2j+1-2n}{2j-1}. \tag{2.25}$$

The quadrupole therefore varies linearly with the occupation of the proton orbit, and is zero when the shell is half-full (or, equivalently, half-empty). This single particle picture can of course break down; if nuclei get collectively deformed, deviations from this linear trend will be observed. For instance, as neutrons are added to the nucleus, they can polarize the core, which in turn will influence the protons. So, even though the neutrons do not directly contribute to the quadrupole moment, they can induce an increase in the quadrupole moment.

2.2 Atomic physics

Atomic structure is the result of the interaction of the electron-electron interaction and the electron-nucleus interaction. To account for the observed atomic energy levels, the interaction of all the electrons with the nucleus and with each other have to be described fully. If the Coulomb interaction, relativistic corrections to the Schrödinger equation, the spin-orbit coupling, Darwin term and Lamb shift are included in this treatment, the fine structure of the atom is obtained. Further corrections due to the finite size and the electromagnetic moments of the nucleus lead to the hyperfine structure. By measuring the splitting of the atomic energy levels due to the hyperfine interaction, information can be extracted about the nucleus in a nuclear-model independent way.

2.2.1 Hyperfine structure

The interaction of the nuclear multipole moments with the fields generated by the electrons results in a splitting of the fine structure levels into the hyperfine levels. Labeling of these hyperfine levels is most conveniently done using their angular momenta. For a nucleus with nuclear spin $\boldsymbol{I}$ and an atomic fine structure level with spin $\boldsymbol{J}$ a total angular momentum $\boldsymbol{F} = \boldsymbol{I} + \boldsymbol{J}$ is defined. Possible values of F range from $|I - J|$ to $|I + J|$. In absence of hyperfine interactions, all F states are degenerate; $E_{IJF} = \langle I, J, F|H|I, J, F\rangle$ is the same for all values of F. By performing a multipole expansion of the Hamiltonian of the nucleus-electron interaction, the individual contributions of the nuclear moments to the final hyperfine structure energies can be investigated. Only the following terms have non-zero contribution to the hyperfine energies:

$$H = H_{E0} + H_{M1} + H_{E2} + H_{M3} + \dots, \tag{2.26}$$

where H_{M1} is the magnetic dipole contribution, H_{E2} the electrical quadrupole component contribution, and so on.

Magnetic dipole and electric quadrupole splitting

The magnetic dipole interaction is an interaction between the magnetic dipole moment of the nucleus $\boldsymbol{\mu}$ and the magnetic field generated by the electrons. For an extended nucleus, the Hamiltonian can be written schematically as

$$H_{M1} = -\int \boldsymbol{B}\,\mathrm{d}\boldsymbol{\mu}, \tag{2.27}$$

where the integration is taken over the nuclear volume. If the magnetic field is constant over the nuclear volume, a simple Hamiltonian is obtained:

$$H_{M1} = -\boldsymbol{\mu} \cdot \boldsymbol{B_0}, \tag{2.28}$$

which can be rewritten as

$$H_{M1} = -\frac{\mu B_0}{\hbar^2 IJ}\boldsymbol{I} \cdot \boldsymbol{J}, \tag{2.29}$$

which allows for straightforward evaluation of the change in energy of a hyperfine sublevel:

$$\Delta E_{M1}(F) = -\frac{1}{2} \cdot \frac{\mu B_0}{IJ} \cdot (F(F+1) - I(I+1) - J(J+1)) \tag{2.30}$$

$$= -\frac{1}{2} \cdot A \cdot K, \tag{2.31}$$

where the hyperfine A-parameter was defined as $\mu B_0/IJ$. The energy splitting of an atomic fine structure level factorizes into a part that contains both the magnetic dipole moment and atomic magnetic field, and a factor that is sensitive to the mutual alignment of these two vector quantities.

The electric quadrupole interaction is an interaction between the electric quadrupole moment of the nucleus and the electric field gradient generated by the electrons. The change of the energy eigenvalues due to H_{E2} can be shown to evaluate to

$$\Delta E_{E2}(F) = eQV_{zz} \cdot \frac{3\,(K(K+1) - 4I(I+1)J(J+1))}{8I(2I-1)J(2J-1)}, \tag{2.32}$$

$$= B\frac{3\,(K(K+1) - 4I(I+1)J(J+1))}{8I(2I-1)J(2J-1)}, \tag{2.33}$$

where the hyperfine B-parameter was defined as eQV_{zz}, with $V_{zz} = \frac{\partial^2 V}{\partial z \partial z}$ and Q the quadrupole moment. Note how this energy splitting can again be neatly split into a factor containing the nuclear moment and atomic field gradient, and a factor due the mutual alignment of the quadrupole moment and field gradient tensors.

Higher order multipole contributions

As indicated by the multipole expansion (2.26), higher order electromagnetic moments should also result in changes in the hyperfine structure. With each order in the expansion, the complexity of the Hamiltonian and corresponding energy eigenvalues increases, and the size of these effects decreases. In almost all cases, truncating the multipole expansion after the electric quadrupole term is sufficient. With laser spectroscopy, only very few magnetic octupole moment measurements have been performed (for example, see [33]).

2.2.2 Isotope and isomeric shift

When comparing the energies of the fine structure levels of two isotopes, there are two additional effects of note [23].

Firstly, since two isotopes differ in their number of neutrons, and therefore their mass, there will be a difference in the reduced mass of the nucleus-electron system. This influences the forces that act on the electron cloud, which leads to a change of the energies of fine structure levels. The energy of two fine structure levels is then shifted by an amount $h\delta\nu_{MS}^{AA'}$, where

$$\delta\nu_{MS}^{AA'} = M\frac{m_{A'} - m_A}{m_{A'}m_A} \tag{2.34}$$

and h Planck's constant. The frequency shift $\delta\nu_{MS}^{AA'}$ is referred to as the mass shift. Secondly, two isotopes of the same element (or isomers of the same isotope) can have a different charge radius, which also impacts the energy of fine structure transitions. This field shift can be attributed to the change in the electrostatic potential felt by the electrons due to the change in the nuclear charge distribution:

$$\delta\nu_{FS}^{AA'} = F\left(\delta\langle r^2\rangle^{AA'} + \frac{C_2}{C_1}\delta\langle r^4\rangle^{AA'} + \ldots\right), \tag{2.35}$$

where the C_i are expansion parameters to be determined by theory. Often one can truncate the expansion of the nuclear charge distribution and simply state $\delta\nu_{FS}^{AA'} = F\delta\langle r^2\rangle^{AA'}$.

The size of the mass and field shift is transition-dependent, and the sum of this mass and field shifts is called the isotope shift $\delta\nu^{AA'}$. Similarly, nuclear isomeric systems can have slightly different radii, which gives rise to an isomer shift.

2.3 Laser Spectroscopy: atomic physics as a probe of nuclear structure

Laser spectroscopy experiments rely on the atomic structure described in section 2.2 to extract the observables defined in 2.1.2, with the goal of learning more about the underlying nuclear structure.

In a laser spectroscopy experiment, the hyperfine structure of an atom is probed by irradiating it with laser light. The atom can be excited by absorbing a laser photon only if two conditions are met.

1. The energy of the photon $h\nu$ should match the difference between the energy of a hyperfine component of one fine structure level and the energy of a hyperfine component of another fine structure level. Combining all the contributions described earlier in this text, the energy shift of a hyperfine level with respect to its unperturbed energy is

   $$\Delta E_{JF} \approx \frac{1}{2} \cdot A \cdot K + B \frac{3\left(K(K+1) - 4I(I+1)J(J+1)\right)}{8I(2I-1)J(2J-1)}. \tag{2.36}$$

   Taking the mass- and field shift effects into account as well, the energy of the laser photons should then equal

   $$h\nu = h\nu_0 + h\delta\nu_{MS}^{AA'} + h\delta\nu_{FS}^{AA'} - \Delta E_{J_1,F_1} + \Delta E_{J_2,F_2}, \tag{2.37}$$

   where $h\nu_0$ is the energy of the fine structure transition of the reference isotope.

2. The transition between these two (hyperfine) states has to be allowed. Since a photon carries one unit of angular momentum, this means for instance that $\Delta F = 0, \pm 1$ for dipole transitions, and that a transition from $F = 0$ to $F = 0$ is forbidden [1].

The frequencies of the laser light that lead to excitation of the atom therefore provide information on the hyperfine A- and B-parameters and the isotope shift. Resonance laser ionization methods rely on irradiating the resonantly excited atoms or ions with one or more additional lasers which further excite the atom, until it finally ionizes. By recording the number of ions that are created as a function of the frequency of the first laser step, the resonance

---

[1] The polarization of the laser also matters if one is interested as well in what happens to the magnetic substates of the F-states, as is the case in e.g. optical pumping experiments. Since these magnetic substates can be considered degenerate in typical laser spectroscopy conditions, they are not directly relevant in the context of this thesis.

frequencies determined by (2.37) can be measured. In order to investigate the most exotic radioactive isotopes, a laser ionization scheme that is both efficient and sensitive to the nuclear observables needs to be developed. Chapter 4 will describe in some more detail the different constraints that had to be taken into account when choosing the appropriate laser ionization scheme for the study of radioactive copper.

2.3.1 Extracting nuclear observables from laser spectroscopy

By measuring the laser frequencies that meet requirement (2.37), hyperfine parameters and isotope shifts can be determined. These observables, in turn, can then be used to calculate the nuclear electromagnetic moments and charge radii. An overview of how the nuclear observables can be obtained from the atomic parameters will be given next.

Extracting the nuclear spin

The number of hyperfine states for a given fine structure level depends on the nuclear spin. Recall that the size of the total angular momentum $\boldsymbol{F}$ can take values between $|I+J|$ and $|I-J|$. This means that, if $I \geq J$, there always are $2J+1$ possible values of F. If on the other hand $I < J$, there will be less. The number of peaks in a hyperfine structure spectrum can therefore be used to determine the nuclear spin if $I < J$.

If an independent g-factor measurement exists, for instance obtained with β-NMR, the nuclear spin can be extracted from a laser spectroscopy measurement by simply taking the ratio of the experimental magnetic moment and the g-factor. By definition, this ratio equals the nuclear spin.

If the hyperfine anomaly can be neglected (see the discussion on the extraction of nuclear moments below), the ratio of the A parameters of the atomic ground- and excited state is constant. Indeed, from the definition of the A-parameter, it follows that

$$\frac{A_l}{A_u} = \frac{\mu B_{0,l}}{I J_l} / \frac{\mu B_{0,u}}{I J_u} \tag{2.38}$$

$$= \frac{B_{0,l}}{B_{0,u}} \frac{J_u}{J_l}. \tag{2.39}$$

Only if a hyperfine structure spectrum is analyzed using the correct I will the correct ratio of A be extracted. The precision with which the A parameters can be measured represents the limiting factor of this approach. Note furthermore that this test is less sensitive for higher values of I.

Another method that does not rely on any assumptions on the nuclear structure of the nucleus is to analyze the ratio of the heights of the components of a hyperfine spectrum obtained through laser spectroscopy (more details on laser spectroscopy are given in section 2.3). This idea has been successfully applied in conventional collinear laser spectroscopy [34], but requires careful investigation of e.g. saturation and optical pumping effects.

Finally, one can compare the extracted nuclear observables to either empirical rules or full shell-model calculations. For instance, analyzing the data with the wrong spin assignment could result in unphysical values of Q, or lead to a g-factor that deviates considerably from intuitive models. This class of spin determination methods is much more subjective and sometimes model-dependent, which is why the previous methods are preferred.

Extracting changes in nuclear charge radii

Extraction of charge radii from isotope shifts requires knowing the value of the field and mass shift parameters F and M [35]. Since there are only two isotopes of copper for which the absolute mean-squared charge radius is known, these values require theoretical input from electronic structure calculations. An extensive discussion of recent theoretical calculations of M and F, and a comparison with existing data from electron scattering and muonic X-ray data, is given in [36].

If values of M and F exist for one transition, a King plot method [35, 37] can be used to estimate what the values of M and F are for another transition, provided at least two isotope pairs have been studied using both transitions. The King plot method relies on the observation that for both transitions

$$\delta\langle r^2\rangle^{AA'} = \frac{1}{F}\left(\delta\nu^{AA'} - M\frac{m_{A'} - m_A}{m_{A'}m_A}\right). \tag{2.40}$$

Therefore

$$\frac{1}{F_1}\left(\delta\nu_1^{AA'} - M_1\frac{m_{A'} - m_A}{m_{A'}m_A}\right) = \frac{1}{F_2}\left(\delta\nu_2^{AA'} - M_2\frac{m_{A'} - m_A}{m_{A'}m_A}\right), \tag{2.41}$$

which can be rewritten by defining the reduced mass as

$$\mu_{AA'} = \left(\frac{m_{A'} - m_A}{m_{A'}m_A}\right)^{-1} \tag{2.42}$$

and isolating the isotope shift of one of the transitions:

$$\mu_{AA'}\delta\nu_1^{AA'} = \frac{F_1}{F_2}\cdot\mu_{AA'}\delta\nu_2^{AA'} - \frac{F_1}{F_2}M_2 + M_1. \tag{2.43}$$

This shows the linear relationship of the modified isotope shifts $\mu_{AA'}\delta\nu^{AA'}$, which has a slope $\frac{F_1}{F_2}$ and intercept $-\frac{F_1}{F_2}M_2 + M_1$. This reduces the task of determining values of M and F to the ubiquitous (and sometimes surprisingly challenging [38]) problem of fitting a straight line to data, in this case pairs of modified isotope shifts.

Extracting the nuclear dipole and quadrupole moment

The definition of the hyperfine A-parameter highlights that the value of B_0 needs to be determined first before magnetic moments can be extracted from hyperfine structure measurements. This is the case if there is an independent measurement of μ that does not rely on the atomic hyperfine structure. In this case, the ratio of the A parameter of the newly measured isotope and the reference isotope provides a way to determine μ:

$$\mu_2 = \frac{I_2}{I_1}\frac{A_2}{A_1}\mu_1 \tag{2.44}$$

Note that the definition of A assumed that the ratio of the A parameters of different fine structure levels is constant for the whole isotopic chain. However, this is only approximately true. The presence of an extended nuclear magnetization, which was neglegted when going from (2.27) to (2.28), can lead to small changes in this ratio as neutrons are added or removed from the nucleus. This is called the Bohr-Weisskopf effect [39]. The Bohr-Weisskopf also affects the ratio of hyperfine A parameters for different isotopes [40]:

$$\frac{A_1}{A_2} = \frac{\mu_1}{\mu_2}\cdot\frac{I_2}{I_1}\cdot(1+\Delta)\,. \tag{2.45}$$

This Δ-term is referred to as the hyperfine anomaly. Furthermore, the extended nuclear charge distribution leads to slight modifications of the electron wavefunctions, which is called the Breit-Rosenthal-Crawford-Schawlow-correction [41, 42]. This correction typically leads to even smaller effects than the hyperfine anomaly [43].

In order to extract Q from a measurement of the atomic hyperfine structure, the quantity V_{zz} needs to be evaluated first. A common method is to compare newly measured values of B to nuclei where an independent measurement of Q

exists, e.g. by calculating the ratio of B parameters:

$$Q_{s2} = Q_{s1}\frac{B_2}{B_1}. \tag{2.46}$$

Chapter 3

The CRIS experiment

Extraction of moments and radii for radioactive species requires experimental techniques that are sufficiently efficient and that also have sufficient resolution to resolve the hyperfine structure. This need for higher efficiencies and better resolving powers has lead to the development of many laser spectroscopy methods at radioactive beam facilities around the world [44]. The technique used for this work is the Collinear Resonance Ionization Spectroscopy (CRIS) technique [45, 46]. A dedicated beamline has been installed at the ISOLDE facility in CERN (for more details, see [47–55]).

Two aspects of this technique make it ideally suited to study exotic ion beams:

1. **Sensitivity:** The CRIS technique can be used to study exotic ion beams with low production rates, even when there is a large isobaric contaminant fraction. This is achieved through efficient and selective laser ionization and efficient ion detection schemes (using e.g. a Micro-Channel Plate (MCP) or other particle detectors). Since collisional ionization of the beam contaminants contributes to the background, this ionization channel has to be suppressed. This is achieved by maintaining the interaction region under ultra-high vacuum (UHV) conditions.
2. **Resolution:** By probing thermal beams that have been accelerated to 30-60 keV in a collinear geometry, Doppler broadening of the lineshapes is reduced to a few MHz. This gives the method the resolution required to study the hyperfine structure of nearly all elements in the periodic table.

The measurements presented in this work on exotic isotopes of copper illustrate these two aspects. For instance, ^{78}Cu, produced at an estimated rate of 20 pps, could be studied with a linewidth of ≈ 70 MHz, similar to the resolution achieved before for less exotic copper isotopes with optically detected collinear laser spectroscopy [5, 6, 56]. These results will be presented in chapter 6.

In this chapter, a general description of the CRIS technique and details on some of the developments made during this thesis will be presented on the basis of two publications.

I. High-resolution laser spectroscopy with the Collinear Resonance Ionisation Spectroscopy (CRIS) experiment at CERN-ISOLDE.
TE Cocolios, **RP de Groote**, J Billowes, ML Bissell, I Budinčević, T Day Goodacre, GJ Farooq-Smith, VN Fedosseev, KT Flanagan, S Franchoo, RF Garcia Ruiz, W Gins, H Heylen, T Kron, R Li, KM Lynch, BA Marsh, G Neyens, RE Rossel, S Rothe, AJ Smith, HH Stroke, KDA Wendt, SG Wilkins, X Yang,
Nuclear Instruments and Methods in Physics Research Section B: Beam Interactions with Materials and Atoms, 376, 284-287, 2016

II. Use of a continuous wave laser and Pockels cell for sensitive high-resolution collinear resonance ionization spectroscopy,
RP de Groote I Budinčević, J Billowes, ML Bissell, TE Cocolios, GJ Farooq-Smith, VN Fedosseev, KT Flanagan, S Franchoo, RF Garcia Ruiz, H Heylen, R Li, KM Lynch, BA Marsh, G Neyens, RE Rossel, S Rothe, HH Stroke, KDA Wendt, SG Wilkins, X Yang,
Physical Review Letters, 115(13), 132501, 2015.

A general overview of the CRIS experimental technique is presented in **article I**, reprinted below. Since doppler broadening is suppressed in collinear laser spectroscopy on accelerated ISOL beams [57], the experimental linewidth is dominated by only two other contributions: the bandwidth of the laser system, and a combination of natural and power broadening of the atomic levels. The first factor can be addressed by choosing a laser system with a sufficiently small bandwidth. In **article II**, more details are given on the development of a narrowband laser system that produces light pulses with a tunable length. It uses a continuous wave laser in combination with an optical chopping setup. More details on the influence of power broadening and other laser-related effects will be discussed in chapter 4.

Another development made during this thesis was the design and coding of a new python-based data acquisition system. The acquisition scheme has some implications for how data should be extracted and processed, which is discussed in appendix A.

Finally, the study of very light systems requires good long-term stabilization and characterization of the spectral properties of the lasers. A third aspect that is under development at the time of writing this thesis is therefore

3. **Stability:** Through the use of a high-precision wavemeter, a reference laser locked to an atomic transition and a Fabry-Pérot Interferometer, it should be possible to determine the drift of the frequency of the scanning laser accurately. This procedure then allows for accurate isotope shift measurements, even if data is only collected over long periods of time.

Once this third development is completed, the combination of these three aspects will make CRIS a versatile, efficient and precise technique for determining nuclear moments, spins and radii in a nuclear-model independent way for the majority of atomic systems.

3.1 Article I: High-resolution laser spectroscopy with the Collinear Resonance Ionisation Spectroscopy (CRIS) experiment at CERN-ISOLDE

High-resolution laser spectroscopy with the Collinear Resonance Ionization Spectroscopy (CRIS) experiment at CERN-ISOLDE

T.E. Cocolios,[1] R.P. de Groote,[2] J. Billowes,[1] M.L. Bissell,[2,1] I. Budinčević,[2]
T. Day Goodacre,[1,3] G.J. Farooq-Smith,[1] V.N. Fedosseev,[3] K.T. Flanagan,[1]
S. Franchoo,[4] R.F. Garcia Ruiz,[2] W. Gins,[2] H. Heylen,[2] T. Kron,[5] R. Li,[4]
K.M. Lynch,[2,6] B.A. Marsh,[3] G. Neyens,[2] R.E. Rossel,[3,5] S. Rothe,[3]
A.J. Smith,[1] H.H. Stroke,[7] K.D.A. Wendt,[5] S.G. Wilkins,[1] and X. Yang[2]

[1]*School of Physics and Astronomy, University of Manchester,*
*Manchester M13 9PL, United Kingdom**
[2]*KU Leuven, Instituut voor Kern- en Stralingsfysica, B-3001 Leuven, Belgium*†
[3]*EN Department, CERN, CH-1211 Geneva-23, Switzerland*
[4]*Institut de Physique Nucléaire d'Orsay, F-91406 Orsay, France*
[5]*Institut für Physik, Johannes Gutenberg Universität, D-55099 Mainz, Germany*
[6]*ISOLDE, PH Department, CERN, CH-1211 Geneva-23, Switzerland*
[7]*New York University, New York, N.Y. 10003, United States of America*

Abstract

The Collinear Resonance Ionization Spectroscopy (CRIS) experiment at CERN has achieved high-resolution resonance ionization laser spectroscopy with a full width at half maximum linewidth of 20(1) MHz for ^{219,221}Fr, and has measured isotopes as short lived as 5 ms with ^{214}Fr. This development allows for greater precision in the study of hyperfine structures and isotope shifts, as well as a higher selectivity of single-isotope, even single-isomer, beams. These achievements are linked with the development of a new laser laboratory and new data-acquisition systems.

INTRODUCTION

The Collinear Resonance Ionization Spectroscopy (CRIS) experiment at CERN-ISOLDE is a laser spectroscopy experiment combining the high-resolution of the accelerated-beam collinear geometry with the high detection efficiency of the resonance ionization process [1].

In its first application in 1991 [2], the CRIS technique used pulsed laser beams to obtain high power densities, but suffered from the duty cycle losses associated with a poor overlap between the continuous ion beam and the pulsed laser light. This limitation was recently addressed with the development of bunched-beam laser spectroscopy [3–5] and allowed the first study of the francium isotopes at the CRIS experiment [6–8]. The resolution of the spectra in this study was limited by the laser system, which had a full width at half maximum (FWHM) of 1.5 GHz [1, 9]. The 2014 campaign has benefited from a high-resolution continuous wave (cw) laser system and a higher repetition rate in the final, ionization-step, pulsed laser. These two developments have enabled high-resolution laser spectroscopy at CRIS, as well as the study of very short-lived isotopes. A new laser laboratory and new data-acquisition systems are currently being implemented to fully exploit the capabilities of the CRIS experiment.

THE CRIS EXPERIMENTAL SETUP

The CRIS beam line

The CRIS beam line (see Fig. 1) receives radioactive ion beams from the CERN-ISOLDE facility [10] at $30 - 60\,\mathrm{keV}$ via the high-resolution separator and linear Paul trap cooler and buncher ISCOOL [11], delivering a pulsed ion beam with $1 - 6\,\mu\mathrm{s}$ bunch width, and up to 200 Hz repetition rate.

The ion bunch is neutralised through a charge exchange cell filled with potassium vapour, operated in order to reach 50% neutralisation efficiency with francium beams. The non-neutralised fraction is deflected while the atom bunch is allowed to drift to the interaction region where it is overlapped collinearly with the laser beams. Good vacuum conditions (nominally $5 \times 10^{-9}\,\mathrm{mbar}$) in the interaction region are necessary to minimize collisional re-ionisation with rest-gas molecules, which is the main source of background. A series of differential pumping apertures are used between the charge exchange cell and the interaction

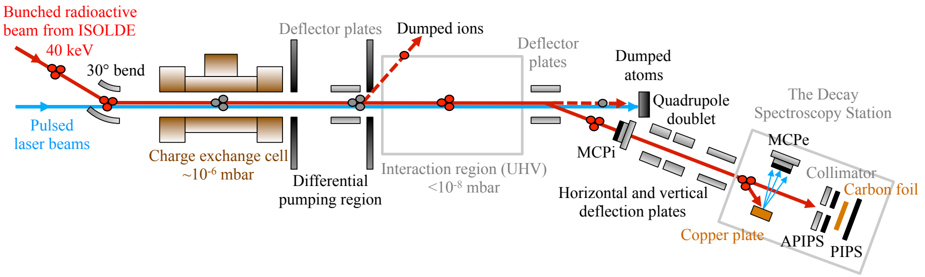

FIG. 1. Schematic layout of the CRIS beam line from the ion beam injection (left) to the detection setups (right), as updated from Ref. [7]. The ion MCP (MCPi) can be removed from the beam path to bring the ions to the DSS. An electric potential can then be applied to the horizontal deflection plates to switch between the copper plate dynode for the electron MCP (MCPe) or the carbon foil.

region, in order to maintain a pressure below 10^{-8} mbar in the interaction region. The re-ionised bunch is then deflected towards the CRIS detection setup.

The CRIS detection setup

The CRIS detection setup is made of three elements. A multi-channel plate (MCP) detector can be used to directly count impinging ions (MCPi - currently under commissioning). A second MCP detector can be used to measure secondary electrons emitted from a copper plate on which the ion bunch impacts (MCPe). Finally, a decay spectroscopy station (DSS) can be used to study the radioactive decay of the isotope of interest [12].

The MCPe detection system has been used in the study of the hyperfine structure of the francium isotopes. A small bias voltage (< 1 kV) is applied between the copper plate and the front of the MCP to guide the secondary electrons towards the detector. This configuration also ensures that the MCP does not suffer from any implantation damage and that it does not get contaminated by the radioactive ions.

The DSS consists of a rotating wheel housing eight thin carbon foils ($20\,\mu$g/cm^2 on average) [13], a copper plate for stable beam tuning, and two 50 Bq ^{241}Am α sources. The beam-axis position is surrounded by two silicon detectors, one of which has a 4 mm hole to let the ion beam through, with a total solid angle of 65% of 4π [14]. An off-axis position is

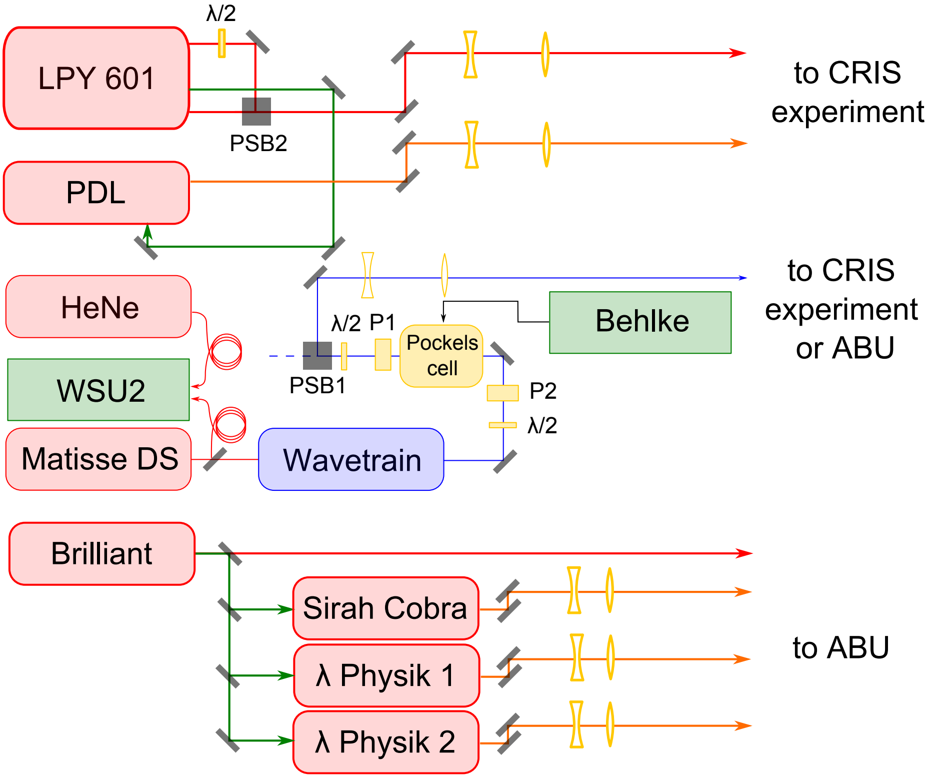

FIG. 2. Schematic layout of the CRIS laser laboratory for high-resolution laser spectroscopy. The cw laser light is chopped by a Pockels cell biased with a high-voltage switch and a polarization-dependent beam splitter to provide high-resolution light synchronised with the 200 Hz Nd:YAG laser and the ion beam delivery. A Brilliant pump laser can be used to pump three PDL lasers that can be used for tests in the ABU.

also equipped with two silicon detectors, with nearly 80% solid angle coverage.

The CRIS laser laboratory

The newly constructed CRIS laser laboratory (see Fig. 2) houses a Matisse DS cw dye laser, pumped by a 10 W Millenia prime Nd:YAG laser. The light from this laser can be frequency-doubled with an external Sirah Wavetrain 2 doubling cavity. The frequency of the cw light can be monitored using a confocal etalon and an iodine absorption cell, and is continually measured using a Highfinesse WSU2 wavemeter. The polarization of the light is manipulated via a Pockels cell controled by a fast Behlke high-voltage switch, and then passed through a polarization-dependent beam splitter to chop the cw beam into light pulses down to 50 ns width. The laser laboratory also contains a 10 Hz Quantel Brilliant Nd:YAG laser. The light from this laser can be doubled, tripled or quadrupled. The doubled light can be used to pump a Sirah Cobra pulsed dye laser or two Lambda Physik pulsed dye lasers (under commissioning). Light from these lasers can be sent into an atomic beam unit (ABU) used for ionization scheme development. The cw laser light can also be sent to the ISOLDE hall, where it can be coupled into the CRIS experiment. The laser table in the ISOLDE hall also features a Litron LPY-601 dual pulsed Nd:YAG laser, providing 1064 nm and 532 nm at either 100 Hz or 200 Hz. This laser light can be used for the ionization step as well as to pump a pulsed dye laser.

For the most recent francium campaign, a Matisse TS (on loan from the COLLAPS collaboration during the construction of the new laser laboratory) was frequency doubled and chopped using the Pockels cell. The Litron LPY-601 delivered 1064 nm for the ionization step.

The CRIS data acquisition systems

The CRIS experiment has two data acquisition systems: one for the control and monitoring of the laser systems and counting of MCP events, and one for the DSS.

The first system, called CRISTAL (CRIS laser Tuning, Acquisition and Logging) aggregates data from and sends instructions to several computers via TCP/IP. In this way, data from two wavemeters (a WSU2 and a WSU6) and two National Instruments USB-6211 cards (monitoring e.g. photodiodes and counting MCP events) can be combined into a final dataset, which can be visualized during the acquisition. CRISTAL simultaneously updates a LabVIEW Shared Variable which is used by the Matisse Commander software to scan the laser frequency. The CRISTAL software can also update LabVIEW Shared Variables to control and monitor the RILIS narrowband Ti:Sa pulsed laser system [15]. In addition, the software keeps an automatic logbook, which is supplemented by the users to provide an accurate description of the progress of the experiment. All the source code for CRISTAL is open source and written in Python [16].

The second system is an 8-channel digital CAEN V1724 acquisition module equipped with on-board digital pulse processing algorithms developed in partnership with the Daresbury Laboratory. The data acquisition software is based on MIDAS (Multi Instance Data Acquisition System) [17] and records the data event by event, from which correlations in time or between detectors can be reconstructed offline.

RECENT ACHIEVEMENTS OF THE CRIS EXPERIMENT

In 2014, an experimental campaign on the francium isotopes was performed using the ionization scheme shown in Fig. 3. Key achievements of this campaign include high-resolution laser spectroscopy of ^{206}Fr and ^{219}Fr [18, 19] and laser spectroscopy of the shortest-lived isotope studied online by laser spectroscopy, ^{214}Fr ($T_{1/2} = 5.0(2)$ ms [20]) [21].

High-resolution laser spectroscopy of ^{219}Fr

Using the cw chopped laser light a resolution of 20(1) MHz FWHM has been reached in the study of the hyperfine structure of the francium isotopes [19]. A comparison between the pulsed-laser-based data [1, 6–8] and the high-resolution data is shown in Fig. 4. This high resolution allows extraction of quadrupole moments and spins from the hyperfine structure, and provides for a greater selectivity in the production of pure ground-state or isomeric beams.

Laser spectroscopy of short-lived isotopes: ^{214}Fr

The new Litron LPY-601 laser system has increased the CRIS duty cycle from 30 Hz in 2012 to 200 Hz in the 2014 campaign. This corresponds to a cooling and bunching period of 5 ms, from which decay losses from short-lived isotopes can be minimized. Using the RILIS laser in the low-resolution CRIS mode, the hyperfine structure of the ground state of ^{214}Fr ($T_{1/2} = 5.0(2)$ ms [20]) was successfully scanned and was identified at the DSS. This represents the laser spectroscopy study of the shortest-lived isotope produced online at a radioactive ion beam facility.

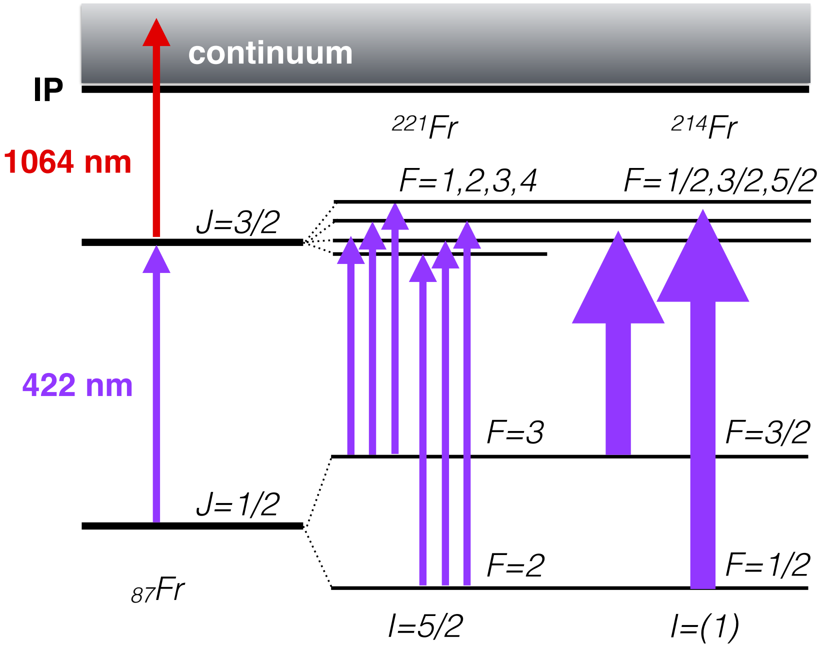

FIG. 3. Resonance ionization scheme for francium. A resonant step at 422 nm is followed by a non-resonant step at 1064 nm through the ionization potential (IP) into the ionization continuum. The hyperfine structure for ^{221}Fr and ^{214}Fr are shown (not to scale). The arrows represent the observed peaks in the spectrum: 6 separated peaks in the high-resolution study of ^{221}Fr; 2 peaks, corresponding to unresolved multiplets, for the low-resolution study of ^{214}Fr.

CONCLUSIONS

Through continuous developments of the CRIS experiment, high-efficiency, high-resolution laser spectroscopy has been achieved on the francium isotopes. The use of a Pockels cell with a cw laser has allowed the high-resolution study of ^{219}Fr to extract quadrupole moments, and the high-repetition rate of the new final-step laser, the study of the short-lived ^{214}Fr isotope ($T_{1/2} = 5.0(2)$ ms). New data acquisition systems have also allowed the integration of all the features of the CRIS beam line into complete data streams for laser spectroscopy and decay spectroscopy. These developments will enable the study of new cases in the

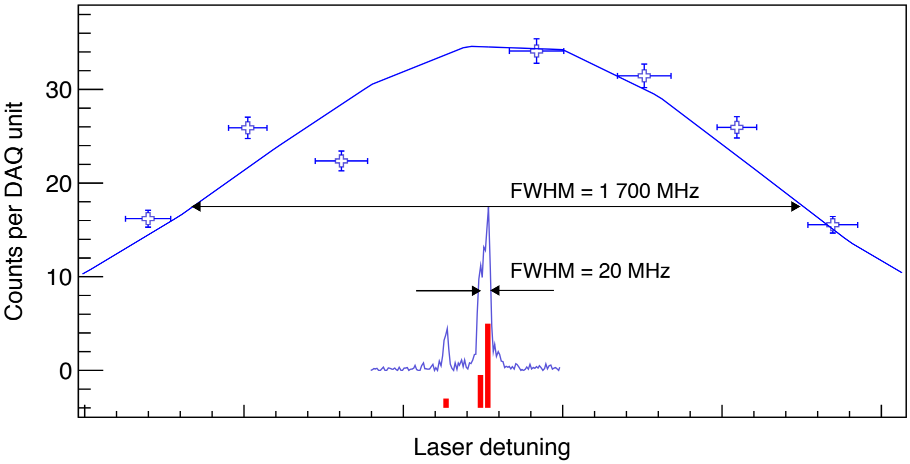

FIG. 4. Left component of the hyperfine structure of ^{221}Fr from the 2014 campaign using the low-resolution (RILIS laser) and high-resolution (chopped cw) modes. The red bars show the hyperfine components and their theoretical relative intensities.

upcoming campaigns.

We acknowledge the support of the ISOLDE collaboration and technical teams, and the GSI target laboratory for producing the carbon foils. This work was funded by the Science and Technology Facilities Council Consolidated Grant ST/F012071/1, Continuation Grant ST/J000159/1 and Ernest Rutherford Grant ST/L002868/1, The Royal Society of London, the IUAP-Belgian State Belgian Science Policy (BRIX network P7/12), FWO-Vlaanderen (Belgium) and GOA 10/010 and 15/010 from KU Leuven, ERC Consolidator Grant 648381, and the EU's Seventh Framework through ENSAR (506065). T. E. C. was supported by the STFC Ernest Rutherford Fellowship ST/J004189/1. K. T. F. was supported by STFC Advanced Fellowship Scheme Grant ST/G006415/1. K. M. L. was supported by the FWO Pegasus Marie Curie Fellowship under Grant 267216. We acknowledge the financial aid from the Ed Schneiderman Fund at New York University.

---

* Thomas.Elias.Cocolios@cern.ch

[†] Ruben.deGroote@fys.kuleuven.be

[1] T. E. Cocolios *et al.*, Nucl. Instrum. Meth. B **317**, 565 (2013).

[2] C. Schultz *et al.*, J. Phys. B **24**, 4831 (1991).

[3] P. Campbell *et al.*, Phys. Rev. Lett. **89**, 082501 (2002).

[4] P. Campbell *et al.*, Eur. Phys. J. A **15**, 45 (2002).

[5] E. Mané *et al.*, Eur. Phys. J. A **42**, 503 (2009).

[6] K. T. Flanagan *et al.*, Phys. Rev. Lett. **111**, 212501 (2013).

[7] K. M. Lynch *et al.*, Phys. Rev. X **4**, 011055 (2014).

[8] I. Budinčević *et al.*, Phys. Rev. C **90**, 014317 (2014).

[9] S. Rothe *et al.*, Nucl. Instrum. Meth. B **317**, 561 (2013).

[10] M. Garcia Borge, Nucl. Instrum. Meth. B **these proceedings** (2015).

[11] H. Frånberg *et al.*, Nucl. Instrum. Meth. B **266**, 4502 (2008).

[12] M. M. Rajabali *et al.*, Nucl. Instrum. Meth. A **707**, 35 (2013).

[13] B. Lommel, W. Hartmann, B. Kindler, J. Klemm, and J. Steiner, Nucl. Instrum. Meth. A **480**, 199 (2002).

[14] K. M. Lynch, T. E. Cocolios, N. Althubiti, G. J. Farooq-Smith, and A. J. Smith, Nucl. Instrum. Meth. A , in preparation (2015).

[15] R. E. Rossel *et al.*, Nucl. Instrum. Meth. B **317**, 557 (2013).

[16] R. P. de Groote and W. Gins, "CRISTAL: A network-based data acquisition for CRIS,".

[17] V. Pucknell and S. Letts, Http://npg.dl.ac.uk/MIDAS/.

[18] K. M. Lynch *et al.*, Phys. Rev. C , in preparation (2015).

[19] R. P. de Groote *et al.*, Phys. Rev. Lett. , in preparation (2015).

[20] S.-C. Wu, Nucl. Data Sheets **110**, 681 (2009).

[21] G. J. Farooq-Smith *et al.*, Phys. Rev. C , in preparation (2015).

3.2 Article II: Use of a continuous wave laser and Pockels cell for sensitive high-resolution collinear resonance ionization spectroscopy

Use of a Continuous Wave Laser and Pockells Cell for Sensitive High-Resolution Collinear Resonance Ionization Spectroscopy

R. P. de Groote,[1,*] I. Budinčević,[1] J. Billowes,[2] M. L. Bissell,[1,2] T. E. Cocolios,[2] G.J. Farooq-Smith,[2] V. N. Fedosseev,[3] K. T. Flanagan,[2] S. Franchoo,[4] R. F. Garcia Ruiz,[1] H. Heylen,[1] R. Li,[4] K. M. Lynch,[1,2,5] B. A. Marsh,[3] G. Neyens,[1] R. E. Rossel,[3,6] S. Rothe,[3] H. H. Stroke,[7] K. D. A. Wendt,[6] S.G. Wilkins,[2] and X. Yang[1]

[1]*KU Leuven, Instituut voor Kern- en Stralingsfysica, B-3001 Leuven, Belgium*

[2]*School of Physics and Astronomy,*
The University of Manchester, Manchester M13 9PL, UK

[3]*Engineering Department, CERN, CH-1211 Geneva 23, Switzerland*

[4]*Institut de Physique Nucléaire d'Orsay, F-91406 Orsay, France*

[5]*Physics Department, CERN, CH-1211 Geneva 23, Switzerland*

[6]*Institut für Physik, Johannes Gutenberg-Universität, D-55128 Mainz, Germany*

[7]*Department of Physics, New York University, New York, New York 10003, USA*

Abstract

New technical developments have led to a two orders of magnitude improvement of the resolution of the collinear resonance ionization spectroscopy (CRIS) experiment at ISOLDE, CERN, without sacrificing the high efficiency of the CRIS technique. Experimental linewidths of 20(1) MHz were obtained on radioactive beams of francium, allowing for the first time to determine the electric quadrupole moment of the short lived ($t_{1/2} = 22.0(5)$ ms) ^{219}Fr $Q_s = -1.21(2)$ eb, which would not have been possible without the advantages offered by the new method. This method relies on a continuous-wave laser and an external Pockels cell to produce narrowband light pulses, required to reach the high resolution in two-step resonance ionization. Exotic nuclei produced at rates of a few hundred ions/s can now be studied with high-resolution, allowing detailed studies of the anchor points for nuclear theories.

Laser spectroscopy of radioactive ion beams provides key nuclear observables to understand the evolution of the quantum many-body problem at the extremes of isospin by providing model-independent measurements of essential quantum observables. These observables are required to refine the current theories of the atomic nucleus and to further our understanding of the nuclear forces (see e.g. [1–3]). Alternatively, laser spectroscopy on exotic isotopes also provides input for precision tests of many-body QED [4] or to investigate hyperfine anomalies [5].

As the nucleon drip-lines are approached, nuclei often have short half-lives and are produced in minute quantities, which imposes strong efficiency requirements on laser spectroscopy techniques. At the same time, the spectral resolution of these experiments needs to be sufficiently high to allow extraction of all of the observables of interest. Over the past decades, many techniques have been developed with the aim of meeting both requirements, see for example [6] for a recent review.

One of these techniques is collinear laser spectroscopy, applied in a number of experiments around the world [7–11]. In this technique an accelerated ion or atom beam of a particular isotope is collinearly overlapped with a continuous wave (cw) laser beam, inducing resonant excitation of the hyperfine levels of the studied isotope. In most of these experiments the hyperfine structure is observed by measuring the fluorescence photons emitted by the de-excitations from the resonantly excited hyperfine levels. The use of accelerated ion beams in a collinear geometry enables typical collinear laser spectroscopy experiments to achieve resonance peak linewidths of the order of 40-70 MHz [7, 12, 13], which are sufficient to resolve the hyperfine structure in most elements. In combination with a bunched ion beam produced with a linear Paul trap, the technique is nowadays routinely performed on radioactive species with production rates down to several 1000 particles per second [7, 8]. A second very successful laser spectroscopic technique to study exotic isotopes is in-source laser spectroscopy [14]. It is based on the efficient resonant excitation of the hyperfine levels using a narrowband pulsed laser and the subsequent (resonant or non-resonant) laser ionization of these radioisotopes in the ion source. Ion detection is very efficient due to the high quantum efficiency of the particle detector and complete solid angle coverage. This allows very exotic nuclei with production rates down to a few particles per second to be accessed [15]. Resonance ionization spectroscopy (RIS) of radioactive beams is usually only performed with pulsed lasers, since only pulsed lasers can provide the high laser power densities required for efficient ionization in an ion source. Because the resonance ionization takes place in a hot cavity, Doppler broadening limits the experimental linewidths to typically 4-5 GHz [15, 16]. A modification of the in-source approach relies on resonance ionization of atoms in a gas cell [17]. A combination of Doppler and pressure broadening results in linewidths of a few GHz. The in-gas cell laser spectroscopy method has recently been improved by doing the RIS in a supersonic gas jet rather than in the gas cell, which allows for a reduction of the total linewidth to several hundred MHz [18].

The collinear resonance ionization spectroscopy (CRIS) technique was proposed as a way to combine the efficiency of RIS with the Doppler-free conditions of a collinear experiment [19]. The method relies on collinearly overlapping an atom beam with a laser beam, thus avoiding Doppler and pressure broadening, and uses the detection of the laser-ionized atoms rather than the fluorescence photons, enhancing the sensitivity and selectivity. The first demonstration of the technique in the nineties served as a promising proof-of-principle, reaching a total efficiency of 10^{-5}, background rate of 10^{-8} and a linewidth of 50 MHz [20]. Results obtained at the dedicated CRIS beam line at ISOLDE, CERN in 2012 demonstrated an improved total experimental efficiency reaching 1 %, using a combination of bunched beams and pulsed lasers [21]. This efficiency extended laser spectroscopy measurements to radioactive species with production yields down to 100 particles per second. The spectral linewidth of 1.5 GHz was completely determined by the pulsed titanium-sapphire laser system that was used [22].

Pulsed laser light with a linewidth of the order of 50 MHz has been produced by pulse dye amplification (PDA) of a cw laser beam [20]. With this method, the final linewidth of the pulsed light is limited by the width of the Fourier transform of the laser pulse and further increased by frequency chirp caused by nano-second scale changes in the refractive index of the medium. For solid-state Ti:Sa lasers, this chirp can be corrected to reduce the linewidth to 6 MHz [23–26]. Another way of producing spectrally narrow laser pulses is by using injection seeding [27]. An important advantage of both methods is the high output powers such systems can achieve, although both come with the disadvantage of a rather challenging experimental setup. A different approach to the production of narrowband laser pulses uses an Electro-Optical Modulator (EOM) to modulate the amplitude of a cw laser beam rather than amplifying it [9, 28]. The extinction ratio, defined as the laser power during the pulse divided by the laser power during the off-time can be as good as 1:180 [28].

Since there is no amplification of the cw beam, the peak fluence of the laser pulses is low, but the final spectral linewidth is purely determined by the transform of the modulation and is not influenced by frequency chirp effects. An additional advantage is the smaller experimental footprint, since no pump laser or stabilization electronics are required. The radio-frequency modulation can induce sidebands in the atomic spectra which have to be accounted for.

In this Letter, we present the development of a laser ionization method based on a Pockels cell and a cw laser system to overcome some of the disadvantages of the methods described above. Using this system, the spectral resolution of the CRIS experiment was improved by nearly two orders of magnitude, without inducing optical pumping to dark states or reducing the experimental efficiency. The spectral linewidth of the laser pulses is purely Fourier-limited. The ability to tune the pulse length to the decay time of the atomic excited state under investigation is a key advantage compared to PDA or injection seeding, where the pulse length is fixed. The system was running at a repetition rate of 100 or 200 Hz to match the Nd:YAG laser, which means the induced sidebands will appear at 100 or 200 Hz. These sidebands are therefore too close to influence the atomic spectra. Furthermore, for a sufficiently long-lived excited state, the ionization laser can be delayed until after the excitation pulse, which has two important implications. Firstly, the excitation laser can probe the atomic system without the perturbation of the strong ionizing laser field, removing potential lineshape distortions. Secondly, power broadening due to both the excitation and the ionization laser is removed completely, even for high laser powers [29–31]. By exciting to a long-lived state, the resolution of the experiment is also enhanced significantly due to the smaller natural linewidth. This advantage is more difficult to exploit for techniques that use fluorescence detection, since the use of weak tranistions will considerably reduce signal rates.

The advantages described in the previous paragraph in combination with the efficiency of the CRIS technique will give access to nuclei with lower production rates and shorter half-lives across the nuclear chart. The improved performance of the CRIS technique is illustrated here with the measurement of the electric quadrupole moments of ^{219}Fr. This isotope is situated near the region of reflection-asymmetry [32–35]. Previous laser spectroscopy experiments performed on francium beams [36–39] did not have the required combination of resolution and sensitivity to extract the electric quadrupole moment of ^{219}Fr

($t_{1/2} = 22.0(5)$ ms [40]), produced with rates around $10^3 - 10^4$ particles per second. From the measured spins and magnetic moments of ^{219,221}Fr [36, 38] it was concluded that the unpaired valence proton in these nuclei occupies the $h_{9/2}$ orbital, while the charge radii of the francium isotopes follow the trend of the neighboring radium isotopes, indirectly showing that ^{219}Fr is located at the border of a region of octupole collectivity [38]. Direct measurements of octupole moments of radioactive beams with laser spectroscopy require a resolution below 10 MHz and are at present not possible, but indirect information can be derived from the quadrupole collectivity.

The ^{219,221}Fr beams are produced at the ISOLDE facility at CERN through a spallation reaction in a thick UC$_x$ target induced by 1.4 GeV protons. The francium atoms are surface ionized in a hot capillary tube, accelerated to 40 keV, mass separated and then cooled and bunched in a gas-filled linear Paul trap [41]. The ion beam is then transported into the CRIS experiment [42], where it is neutralized through collisions with a potassium vapor. After passing through a differential pumping section, the neutral fraction of the beam is temporally and spatially overlapped with the laser beams in a UHV interaction region. The time synchronization is controlled using a Quantum Composers QC9258 digital delay generator. Once in the interaction region, the isotopes are resonantly excited through the $7s\ ^2S_{1/2} - 8p\ ^2P_{3/2}$ transition at 422.7 nm using chopped cw light. The lifetime of the excited state is $\tau = 83.5 \pm 1.5$ ns [43] and very well suited for delayed RIS. The resonantly excited atoms are non-resonantly ionized using 1064 nm laser light, using different delay times between the excitation and ionization laser pulses. These ions are deflected onto a copper plate, and the secondary electrons are detected using a microchannel plate (MCP). The signals produced by the MCP are then amplified, discriminated and processed by a National Instruments USB-6211 DAQ card. This USB card is triggered by the Quantum composer every 100 ms, in synchronization with the laser system and ion beam delivery.

The laser system used for the high-resolution resonance laser ionization is presented in Fig. 1. The laser light for the resonant step was provided by a Matisse TS cw titanium-sapphire laser, which was frequency scanned using the Matisse Commander software. A small pick-off of the 2.7 W fundamental laser beam was sent into a HighFinesse WSU2 wavemeter, which was regularly calibrated to an external temperature stabilized HeNe laser. The fundamental laser beam of the Matisse was frequency doubled to 422.7 nm using a Wavetrain external cavity frequency doubler. The laser beam then passed through a half-

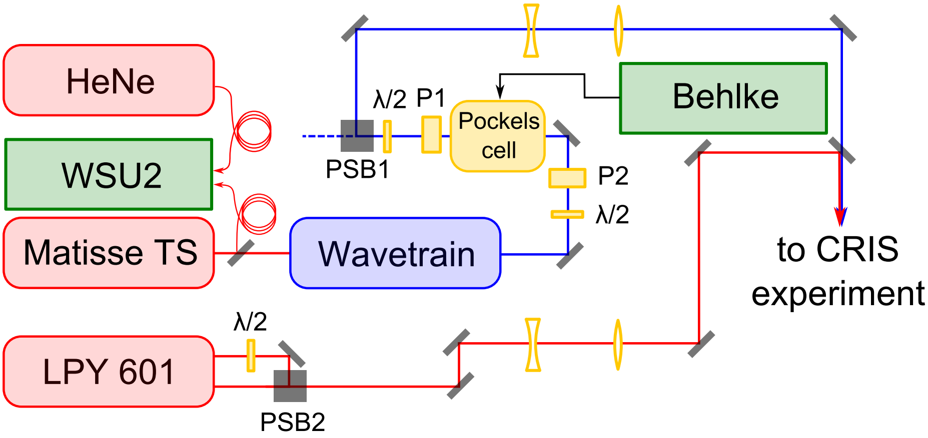

FIG. 1. [Color online] A schematic overview of the laser setup. The laser light for the excitation step is produced by a Matisse TS titanium-sapphire continuous wave laser which is frequency doubled by a Wavetrain doubler and sent through a light chopping setup (see text for more details). The 1064 nm light for the non-resonant ionization step is produced by a Litron LPY 601 50-100 PIV Nd:YAG laser operating at either 100 or 200 Hz. Light of both lasers is focused and spatially overlapped before being sent to the CRIS experiment.

wave plate, Glan-Taylor polarizer (P1) and Pockels cell, and then through another half-wave plate and a second Glan-Taylor polarizer (P2). A polarizing beam splitter cube (PSB1) positioned further along the beam path only reflected light with one particular polarization, which was then further transported into the CRIS beam line. The polarization axis of the light was rotated by $\pi/2$ by the Pockels cell for an applied voltage of 2.4 kV. Through the use of a Behlke FSWP91-01 fast square wave pulser, the voltage applied to the Pockels cell could be rapidly switched from 0 to 2.4 kV. The combination of the rapid switching of the laser light polarization and the polarization-sensitive beam splitter cube therefore allowed for creating short pulses of laser light. Optimized transmission efficiencies of 65% and extinction ratios of 1:2000 were achieved. The measured rise and fall times of the light pulses were 10 ns. The power of the 422.7 nm light was 25 mW just before the entry window to the CRIS beamline. The laser efficiency obtained with this laser system was comparable to the low-resolution laser system that was used for the previous CRIS experiment [21]. This was determined by comparing back-to-back measurements using the high-resolution laser system and the previous system on ^{206}Fr. Fig. 2 shows the saturation curve for the excitation step. The red curve is the best fitting saturation function, defined as

$$I(P) = A \cdot \frac{P/P_0}{1 + P/P_0}, \tag{1}$$

which yields a saturation power of $P_0 = 9 \pm 4\,\mathrm{mW}$. Light from the two Nd:YAG cavities in the Litron LPY 601 50-100 PIV laser system was overlapped using a half wave plate and a polarizing beam splitting cube (PSB2), yielding 2×4 W of laser light just before the CRIS entry window. The synchronization of the two cavities can be tuned to change the repetition rate of the Litron laser system to either 100 or 200 Hz.

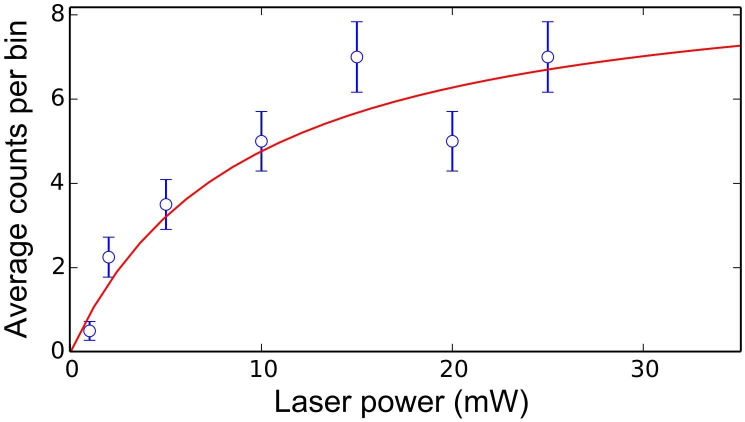

FIG. 2. [Color online] Saturation curve for the excitation laser step, obtained by fixing the laser frequency at the resonance frequency of the strongest peak in the left multiplet of ^{221}Fr. The ionization laser fired at the end of the excitation pulse, with a power of 8 W. From the best fitting saturation function (shown in red), a saturation power of $P_0 = 9 \pm 4\,\mathrm{mW}$ is extracted.

By performing systematic measurements of the hyperfine structure of ^{221}Fr, optimal pulse lengths of 100 ns and ionization laser delay of 100 ns with respect to the rise time of the excitation pulse were determined. With these settings the blue histogram in Fig. 3 is obtained. If the ionization step is delayed less then 100 ns, and therefore arrives temporally overlapped with the excitation pulse, the grey spectrum in Fig. 3 is obtained. The peaks

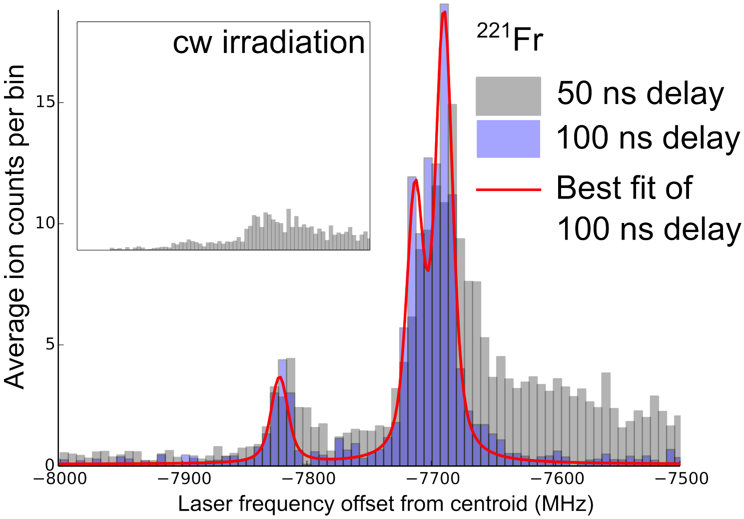

FIG. 3. [Color online] Inset: Resonance ionization spectrum with continuous wave laser light in the first step. The scale and range on x- and y-axis are the same as the main plot. Main: RIS of the lowest frequency multiplet of ^{221}Fr using chopped cw light with a pulse length of 100 ns for two delay times of the ionization step.

broaden and shift to the high-frequency side, and an additional structure also appears on the high-frequency side of the resonance peaks. When a constant 2.4 kV voltage is applied (and the atoms are therefore continuously irradiated), the spectrum in the inset of Fig. 3 is obtained. The event rate is much lower due to optical pumping effects, and the peaks are significantly broadened and shifted to higher frequencies. Fig. 3 also shows the best fitting function for the optimal settings (in red), consisting of the sum of Voigt profiles centered on the resonance positions. A total linewidth of 20(1) MHz is obtained. The total linewidth is dominated by the remaining Doppler spread of the atom beam and the spectral broadening of the excitation pulse due to the chopping, estimated at approximately 10 MHz by taking the Fourier transform of the time profile of the laser pulse.

An example of a resonance ionization spectrum of ^{219}Fr is shown in Fig. 4. The linewidth of 20(1) MHz is sufficient to resolve all six expected resonance peaks, which are fitted as described in e.g. [38]. The weighted mean of the fitted hyperfine parameters are summarized

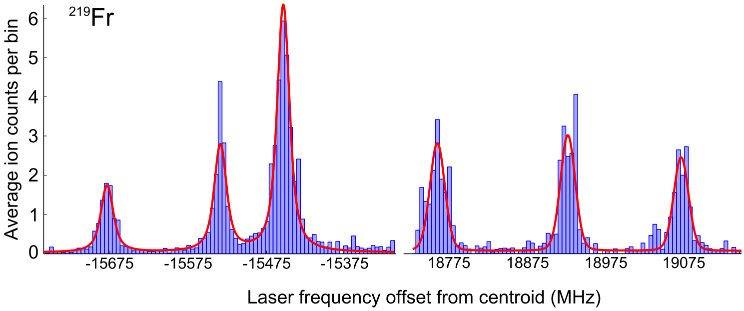

FIG. 4. [Color online] Example of an experimental hyperfine spectrum of ^{219}Fr and the best fitting function (red line) consisting of a sum of Voigt profiles centered on the resonance positions.

TABLE I. Summary of the extracted hyperfine structure constants for the $7s^2S_{1/2}$ atomic ground state and $8p^2P_{3/2}$ excited state of ^{219,221}Fr (values in MHz). The extracted magnetic dipole moment and electric quadrupole moment are also given. Literature values were obtained from [36–38].

	A($7s^2S_{1/2}$)	A($8p^2P_{3/2}$)	B($8p^2P_{3/2}$)	$\mu(\mu_N)$	Q_s(eb)
$219_{\text{lit.}}$	+6820(30)	–	–	+ 3.11(4)	–
$219_{\text{exp.}}$	+6851(1)	+24.7(5)	-104(1)	+ 3.13(4)	-1.21(2)
$221_{\text{lit.}}$	+6210(1)	+22.4(1)	-85.7(8)	+ 1.57(2)	-1.00(1)
$221_{\text{exp.}}$	+6209(1)	+22.3(5)	-87(2)	+ 1.57(2)	-1.02(3)

in Table I. From these parameters, the nuclear magnetic dipole moment μ and electric quadrupole moment Q_s were determined relative to the values for ^{221}Fr in [36, 37]. The newly measured value of $Q_s = -1.21(2)$ eb ($\beta_2 = 0.094$) for ^{219}Fr is plotted along with the Q_s values of other francium isotopes from literature [9, 36] in Fig. 5. The Q_s values illustrate the different structures in these odd-A francium isotopes: for $A < 215$ the quadrupole moment is nearly zero, as expected in the shell model for isotopes with a half-filled $h_{9/2}$ proton orbit [44]. The small deviation from zero is a signature of configuration mixing and an increasing contribution from core polarization towards the neutron-deficient region. The large absolute values for the quadrupole moments of $^{219-225}$Fr are a signature for deformation in their ground states. The sudden change from strongly negative to strongly positive spectroscopic quadrupole moments is understood in the Nilsson model as due to the changing influence of

Coriolis mixing on these prolate deformed structures. Coriolis mixing is strongest in $K = 1/2$ bands and tends to decouple the odd-particle spin from the deformation axis [45, 46]. The $9/2^-$ ground state in ^{219}Fr is known to be a member of the $K = 1/2^-$ band [47]. Thus the odd-proton spin is decoupled from the nuclear deformation axis (see (b) in Fig. 5), yielding a negative quadrupole moment ($K < I$). In the heavier francium isotopes, the deformation gradually increases and the nuclear spin gets gradually more coupled to the deformation axis. The $5/2^-$ ground state in ^{221}Fr was interpreted also as a member of the $K = 1/2^-$ band, but with a much smaller decoupling parameter a. In ^{223,225}Fr the $3/2^-$ ground state is a member of the $K = 3/2^-$ band and thus strongly coupled to the deformation axis ($K = I$), resulting in a positive quadrupole moment.

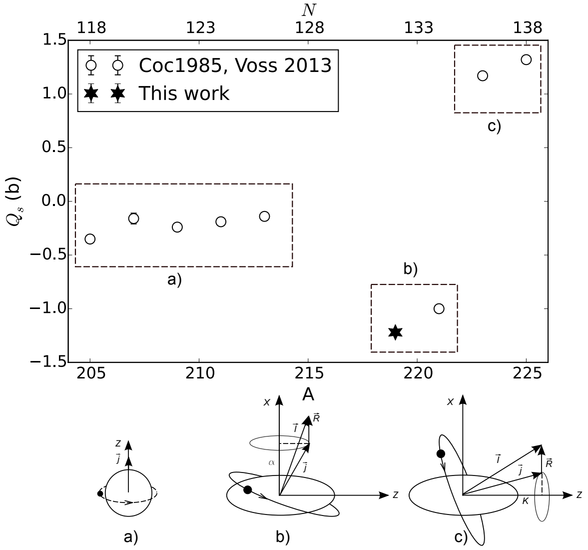

FIG. 5. Spectroscopic quadrupole moment values of ^{219}Fr measured in this work, along with literature values for the neighboring odd francium isotopes. The Z axis in the three schemes is the axis of deformation. $\vec{j}$ is the single particle angular momentum of the valence proton, $\vec{I}$ the total nuclear spin, and $\vec{R}$ the rotational angular momentum of the nucleus. K is the projection of j on Z and α is the projection on the X axis.

In summary, we have presented a novel high resolution, highly efficient collinear resonance ionization spectroscopy technique. By probing a weak atomic transition in francium, a linewidth of 20(1) MHz was achieved, which represents an improvement of the experimental resolution by nearly two orders of magnitude compared to our previous measurements [21]. The advantages of the new method in terms of resolution, efficiency and systematic lineshape effects were illustrated by performing laser spectroscopy on beams of radioactive francium, using the 422.7 nm transition to the excited $8p^2P_{3/2}$ state. The performance of the technique allowed measurement of the electric quadrupole moment of ^{219}Fr ($t_{1/2} = 22.0(5)$ ms) for the first time.

We acknowledge the support of the ISOLDE collaboration and technical teams. We are grateful to the COLLAPS collaboration for the use of their CW Ti:Sa laser system and wavetrain doubling unit. This work was supported by the BriX Research Program No. P7/12 and FWO-Vlaanderen (Belgium) and GOA 10/010 from KU Leuven, the Science and Technology Facilities Council consolidated grant ST/F012071/1 and continuation grant ST/J000159/1, and the EU Seventh Framework through ENSAR(506065). K. T. F. was supported by STFC Advanced Fellowship Scheme Grant No. ST/G006415/1 and ERC Consolidator Grant no. 648381. We acknowledge the financial aid from the Ed Schneiderman Fund at New York University.

---

* ruben.degroote@fys.kuleuven.be

[1] S. R. Beane, E. Chang, S. Cohen, W. Detmold, H. W. Lin, K. Orginos, A. Parreño, M. J. Savage, and B. C. Tiburzi ((NPLQCD Collaboration)), Phys. Rev. Lett. **113**, 252001 (2014).

[2] A. Ekström, G. R. Jansen, K. A. Wendt, G. Hagen, T. Papenbrock, B. D. Carlsson, C. Forssén, M. Hjorth-Jensen, P. Navrátil, and W. Nazarewicz, Phys. Rev. C **91**, 051301 (2015).

[3] Z.-T. Lu, P. Mueller, G. W. F. Drake, W. Nörtershäuser, S. C. Pieper, and Z.-C. Yan, Rev. Mod. Phys. **85**, 1383 (2013).

[4] W. Nörtershäuser, C. Geppert, A. Krieger, K. Pachucki, M. Puchalski, K. Blaum, M. L. Bissell, N. Frömmgen, M. Hammen, M. Kowalska, J. Krämer, K. Kreim, R. Neugart, G. Neyens, R. Sánchez, and D. T. Yordanov, Phys. Rev. Lett. **115**, 033002 (2015).

[5] J. Zhang, M. Tandecki, R. Collister, S. Aubin, J. A. Behr, E. Gomez, G. Gwinner, L. A. Orozco, M. R. Pearson, and G. D. Sprouse (FrPNC collaboration), Phys. Rev. Lett. **115**,

042501 (2015).

[6] K. Blaum, J. Dilling, and W. Nörtershäuser, Phys. Scripta **T152**, 014017 (2013).

[7] J. Papuga, M. L. Bissell, K. Kreim, C. Barbieri, K. Blaum, M. De Rydt, T. Duguet, R. F. Garcia Ruiz, H. Heylen, M. Kowalska, R. Neugart, G. Neyens, W. Nörtershäuser, M. M. Rajabali, R. Sánchez, N. Smirnova, V. Somà, and D. T. Yordanov, Phys. Rev. C **90**, 034321 (2014).

[8] A. Nieminen, P. Campbell, J. Billowes, D. H. Forest, J. A. R. Griffith, J. Huikari, A. Jokinen, I. D. Moore, R. Moore, G. Tungate, and J. Äystö, Phys. Rev. Lett. **88**, 094801 (2002).

[9] A. Voss, M. R. Pearson, J. Billowes, F. Buchinger, B. Cheal, J. E. Crawford, A. A. Kwiatkowski, C. D. P. Levy, and O. Shelbaya, Phys. Rev. Lett. **111**, 122501 (2013).

[10] K. Minamisono, P. Mantica, A. Klose, S. Vinnikova, A. Schneider, B. Johnson, and B. Barquest, Nuclear Instruments and Methods in Physics Research Section A: Accelerators, Spectrometers, Detectors and Associated Equipment **709**, 85 (2013).

[11] H. Iimura, M. Koizumi, M. Miyabe, M. Oba, T. Shibata, N. Shinohara, Y. Ishida, T. Horiguchi, and H. A. Schuessler, Phys. Rev. C **68**, 054328 (2003).

[12] K. Blaum, W. Geithner, J. Lassen, P. Lievens, K. Marinova, and R. Neugart, Nuclear Physics A **799**, 30 (2008).

[13] B. Cheal, E. Mané, J. Billowes, M. L. Bissell, K. Blaum, B. A. Brown, F. C. Charlwood, K. T. Flanagan, D. H. Forest, C. Geppert, M. Honma, A. Jokinen, M. Kowalska, A. Krieger, J. Krämer, I. D. Moore, R. Neugart, G. Neyens, W. Nörtershäuser, M. Schug, H. H. Stroke, P. Vingerhoets, D. T. Yordanov, and M. Žáková, Phys. Rev. Lett. **104**, 252502 (2010).

[14] V. N. Fedosseev, Y. Kudryavtsev, and V. I. Mishin, Phys. Scripta **85**, 058104 (2012).

[15] H. D. Witte, A. Andreyev, N. Barré, M. Bender, T. Cocolios, S. Dean, D. Fedorov, V. Fedoseyev, L. Fraile, S. Franchoo, V. Hellemans, P. Heenen, K. Heyde, G. Huber, M. Huyse, H. Jeppessen, U. Köster, P. Kunz, S. Lesher, B. Marsh, I. Mukha, B. Roussière, J. Sauvage, M. Seliverstov, I. Stefanescu, E. Tengborn, K. V. de Vel, J. V. de Walle, P. V. Duppen, and Y. Volkov, Phys. Rev. Lett. **98**, 112502 (2007).

[16] U. Köster, N. J. Stone, K. T. Flanagan, J. R. Stone, V. N. Fedosseev, K. L. Kratz, B. A. Marsh, T. Materna, L. Mathieu, P. L. Molkanov, M. D. Seliverstov, O. Serot, A. M. Sjödin, and Y. M. Volkov, Phys. Rev. C **84**, 034320 (2011).

[17] R. Ferrer, N. Bree, T. Cocolios, I. Darby, H. D. Witte, W. Dexters, J. Diriken, J. Elseviers,

S. Franchoo, M. Huyse, N. Kesteloot, Y. Kudryavtsev, D. Pauwels, D. Radulov, T. Roger, H. Savajols, P. V. Duppen, and M. Venhart, Phys. Lett. B **728**, 191 (2014).

[18] Y. Kudryavtsev, R. Ferrer, M. Huyse, P. V. den Bergh, and P. V. Duppen, Nucl.Nucl. Instrum. Meth. B **297**, 7 (2013).

[19] Y. A. Kudriavtsev and V. S. Letokhov, Appl. Phys. B **29**, 219 (1982).

[20] C. Schulz, E. Arnold, W. Borchers, W. Neu, R. Neugart, M. Neuroth, E. W. Otten, M. Scherf, K. Wendt, P. Lievens, Y. A. Kudryavtsev, V. S. Letokhov, V. I. Mishin, and V. V. Petrunin, J. Phys. B: At. Mol. Opt. Phys. **24**, 4831 (1991).

[21] K. T. Flanagan, K. M. Lynch, J. Billowes, M. L. Bissell, I. Budinčević, T. E. Cocolios, R. P. de Groote, S. D. Schepper, V. N. Fedosseev, S. Franchoo, R. F. Garcia Ruiz, H. Heylen, B. A. Marsh, G. Neyens, T. J. Procter, R. E. Rossel, S. Rothe, I. Strashnov, H. H. Stroke, and K. D. A. Wendt, Phys. Rev. Lett. **111**, 212501 (2013).

[22] S. Rothe, V. N. Fedosseev, T. Kron, B. A. Marsh, R. E. Rossel, and K. D. A. Wendt, Nucl. Instrum. Meth. B **317**, 561 (2013).

[23] V. Meyer, S. N. Bagayev, P. E. G. Baird, P. Bakule, M. G. Boshier, A. Breitrück, S. L. Cornish, S. Dychkov, G. H. Eaton, A. Grossmann, D. Hübl, V. W. Hughes, K. Jungmann, I. C. Lane, Y.-W. Liu, D. Lucas, Y. Matyugin, J. Merkel, G. zu Putlitz, I. Reinhard, P. G. H. Sandars, R. Santra, P. V. Schmidt, C. A. Scott, W. T. Toner, M. Towrie, K. Träger, L. Willmann, and V. Yakhontov, Phys. Rev. Lett. **84**, 1136 (2000).

[24] K. S. E. Eikema, W. Ubachs, W. Vassen, and W. Hogervorst, Phys. Rev. A **55**, 1866 (1997).

[25] M. Hori and A. Dax, Opt. Lett. **34**, 1273 (2009).

[26] M. Hori, A. Sótér, D. Barna, A. Dax, R. Hayano, S. Friedreich, B. Juhász, T. Pask, E. Widmann, D. Horváth, *et al.*, Nature **475**, 484 (2011).

[27] M. Reponen, I. Moore, T. Kessler, I. Pohjalainen, S. Rothe, and V. Sonnenschein, Eur. Phys. J. A **48**, 45 (2012), 10.1140/epja/i2012-12045-2.

[28] J. Sell, K. Gulyuz, and G. Sprouse, Review of Scientific Instruments **80**, 123108 (2009).

[29] N. Vitanov, B. Shore, L. Yatsenko, K. Böhmer, T. Halfmann, T. Rickes, and K. Bergmann, Opt.Commun. **199**, 117 (2001).

[30] T. Halfmann, T. Rickes, N. Vitanov, and K. Bergmann, Opt.Commun. **220**, 353 (2003).

[31] R. de Groote, G. Neyens, and K. Flanagan, *Modeling and simulation of two-step resonance ionization processes using CW and pulsed lasers*, Master's thesis, Leuven U. (2013), presented

31 Jun 2013.

[32] P. A. Butler, Reviews of Modern Physics **68**, 349 (1996).

[33] L. P. Gaffney, P. A. Butler, M. Scheck, A. B. Hayes, F. Wenander, M. Albers, B. Bastin, C. Bauer, A. Blazhev, S. Bönig, N. Bree, J. Cederkll, T. Chupp, D. Cline, T. E. Cocolios, T. Davinson, H. D. Witte, J. Diriken, T. Grahn, A. Herzan, M. Huyse, D. G. Jenkins, D. T. Joss, N. Kesteloot, J. Konki, M. Kowalczyk, T. Kröll, E. Kwan, R. Lutter, K. Moschner, P. Napiorkowski, J. Pakarinen, M. Pfeiffer, D. Radeck, P. Reiter, K. Reynders, S. V. Rigby, L. M. Robledo, M. Rudigier, S. Sambi, M. Seidlitz, B. Siebeck, T. Stora, P. Thoele, P. V. Duppen, M. J. Vermeulen, M. von Schmid, D. Voulot, N. Warr, K. Wimmer, K. Wrzosek-Lipska, C. Y. Wu, and M. Zielinska, Nature **497**, 199 (2013).

[34] D. A. Fink, T. E. Cocolios, A. N. Andreyev, S. Antalic, A. E. Barzakh, B. Bastin, D. V. Fedorov, V. N. Fedosseev, K. T. Flanagan, L. Ghys, A. Gottberg, M. Huyse, N. Imai, T. Kron, N. Lecesne, K. M. Lynch, B. A. Marsh, D. Pauwels, E. Rapisarda, S. D. Richter, R. E. Rossel, S. Rothe, M. D. Seliverstov, A. M. Sjödin, C. Van Beveren, P. Van Duppen, and K. D. A. Wendt, Phys. Rev. X **5**, 011018 (2015).

[35] R. K. Sheline, Phys. Lett. B **197**, 500 (1987).

[36] A. Coc, C. Thibault, F. Touchard, H. Duong, P. Juncar, S. Liberman, J. Pinard, J. Lermé, J. Vialle, S. Büttgenbach, A. Mueller, and A. Pesnelle, Phys. Lett. B **163**, 66 (1985).

[37] H. T. Duong, P. Juncar, S. Liberman, A. C. Mueller, R. Neugart, E. W. Otten, B. Peuse, J. Pinard, H. H. Stroke, C. Thibault, F. Touchard, J. L. Vialle, K. Wendt, and I. Collaboration, Europhys. Lett. **3**, 175 (1987).

[38] I. Budinčević, J. Billowes, M. L. Bissell, T. E. Cocolios, R. P. de Groote, S. D. Schepper, V. N. Fedosseev, K. T. Flanagan, S. Franchoo, R. F. Garcia Ruiz, H. Heylen, K. M. Lynch, B. A. Marsh, G. Neyens, T. J. Procter, R. E. Rossel, S. Rothe, I. Strashnov, H. H. Stroke, and K. D. A. Wendt, Phys. Rev. C **90**, 014317 (2014).

[39] K. M. Lynch, J. Billowes, M. L. Bissell, I. Budinčević, T. E. Cocolios, R. P. de Groote, S. De Schepper, V. N. Fedosseev, K. T. Flanagan, S. Franchoo, R. F. Garcia Ruiz, H. Heylen, B. A. Marsh, G. Neyens, T. J. Procter, R. E. Rossel, S. Rothe, I. Strashnov, H. H. Stroke, and K. D. A. Wendt, Phys. Rev. X **4**, 011055 (2014).

[40] G. Ewan, E. Hagberg, B. Jonson, S. Mattsson, and P. Tidemand-Petersson, Nuclear Physics A **380**, 423 (1982).

[41] H. Frånberg, P. Delahaye, J. Billowes, K. Blaum, R. Catherall, F. Duval, O. Gianfrancesco, T. Giles, A. Jokinen, M. Lindroos, D. Lunney, E. Mane, and I. Podadera, Nucl.Nucl. Instrum. Meth. B **266**, 4502 (2008), proceedings of the {XVth} International Conference on Electromagnetic Isotope Separators and Techniques Related to their Applications.

[42] T. Cocolios, H. A. Suradi, J. Billowes, I. Budinčević, R. P. de Groote, S. D. Schepper, V. Fedosseev, K. T. Flanagan, S. Franchoo, R. F. Garcia Ruiz, H. Heylen, F. L. Blanc, K. M. Lynch, B. A. Marsh, P. J. R. Mason, G. Neyens, J. Papuga, T. Procter, M. Rajabali, R. E. Rossel, S. Rothe, G. S. Simpson, A. J. Smith, I. Strashnov, H. H. Stroke, D. Verney, P. M. Walker, K. D. A. Wendt, and R. T. Wood, Nuclear Instruments and Methods in Physics Research Section B: Beam Interactions with Materials and Atoms **317, Part B**, 565 (2013).

[43] S. Aubin, E. Gomez, L. Orozco, and G. Sprouse, Phys. Rev. A **70**, 042504 (2004).

[44] G. Neyens, Reports on Progress in Physics **66**, 633 (2003).

[45] R. Casten, *Nuclear Structure From A Simple Perspective* (Oxford University Press Inc, 1990).

[46] I. Ragnarsson and S. G. Nilsson, *Shapes and Shells in Nuclear Structure* (Cambridge University Press, 2005).

[47] C. F. Liang, P. Paris, J. Kvasil, and R. K. Sheline, Phys. Rev. C **44**, 676 (1991).

Chapter 4

Ionization schemes for high-resolution CRIS on copper

For this PhD work, measurements of the magnetic dipole moment, electric quadrupole moment, spin and changes in mean square charge radius are all essential. This immediately excludes all laser ionization schemes that are limited to $J_1 = 1/2 \rightarrow J_2 = 1/2$ transitions, since only for $I, J > 1/2$ can a hyperfine B parameter, and therefore a quadrupole moment, be measured. The ionization potential of ionic copper (20.29239 eV for CuII [58]) prevents it from being laser-ionized to a 2^+ ion. Any CRIS measurements on copper therefore require neutralizing the ion beam so the atomic system can be probed.

The atomic levels and transitions of neutral copper that are of interest to this work are shown in figure 4.1. The ground-state configuration of copper is $3d^{10}4s\ ^2S_{1/2}$, which means that it is not sensitive to the nuclear quadrupole moment. Starting from this ground state level, there are a few candidates that have $J_2 > 1/2$. Limiting the transition wavelengths to wavelengths that can be conveniently produced using Titanium-sapphire lasers and dye lasers pumped by 532 nm pump lasers, two prominent candidates remain: the 324.7540 nm line to the $3d^{10}4p\ ^2P^\circ_{3/2}$ state at 30783.697 cm^{-1}, and the 249.2146 nm line to the $3d^9(^2D)4s4p\,(^3P^\circ)\ s^4P^\circ_{3/2}$ at 40114.01 cm^{-1}. Given the configuration of the ground- and excited state for both options, good sensitivity to changes in mean-squared charge radius can be expected for both transitions.

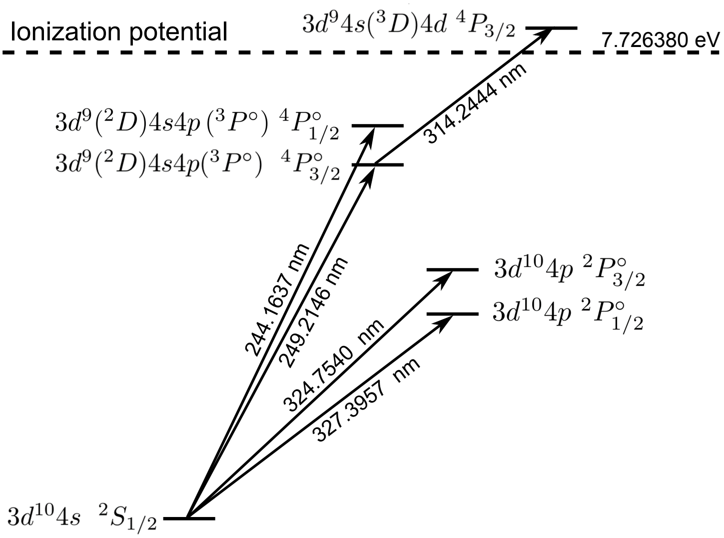

Figure 4.1: Some atomic levels and lines in neutral copper that are of interest for this work.

By far the best studied transition is the 324.7540 nm transition, which was used in previous RIB work [5, 6, 36, 56]. Hyperfine parameters are well known, and an in-depth study of the mass and field shift parameters was also performed [36]. An additional advantage is that this wavelength is also readily produced by frequency-doubling a dye laser. A first test experiment was performed in 2015, using this transition as the first step of a two-step ionization scheme. A summary of the experiment and the results are presented in section 4.1.

The characteristics of the 249.2146 nm line were investigated offline at the Johannes Gutenberg University of Mainz. The goal of these tests was to confirm the only, relatively old, measurements of the hyperfine parameters of the excited atomic state [59]. As will be shown in section 4.2, the literature assignments were correct, which means that the excited state has a very large magnetic dipole splitting and a suitable quadrupole splitting.

In this chapter, the following two articles are included:

III. High-resolution laser spectroscopy with the Collinear Resonance Ionisation Spectroscopy (CRIS) experiment at CERN-ISOLDE
RP de Groote, M Verlinde, V Sonnenschein, KT Flanagan, I Moore, and G Neyens,
Physical Review A, 95 (3), 032502, 2017.

IV. Double-resonance-ionization mapping of the hyperfine structure of the stable Cu isotopes using pulsed narrowband Ti: sapphire lasers.
RP de Groote, T Kron, A Hakimi, G Neyens, K Wendt,
Physical Review A, 92(2), 022506, 2015.

4.1 Transition 1: online tests with CRIS

The first experiment on radioactive beams on copper was performed in June 2015. The goal of the experiment was to establish the efficiency and resolving power that could be reached by using the chopping method on a strong atomic transition, after it had been successfully applied to a weak transition in francium [60]. If this efficiency was sufficiently high, the goal was to go towards ^{78}Cu. Unfortunately, many experimental difficulties prevented a successful experiment. A laser failure prevented the use of the originally envisaged ionization scheme, which was based on a transition to an auto-ionizing state. Instead, a less efficient two-step scheme with a non-resonant ionization step had to be used. Finally, two failures of the cartridges used to heat the charge exchange cell (CEC) meant that vacuum had to be broken twice in order to repair the CEC. All these factors together resulted in a very low efficiency. Together with the time lost during the various interventions, insufficient beam time was left to pursue the intended measurements. This chapter summarizes the (few) results that were obtained on ^{63,65,69,71}Cu, and compares them to the available literature.

The 324 nm continuous-wave light for the first step was produced by frequency doubling the output of a Matisse DS2 dye laser, using DCM dye. This light was chopped by the Pockels cell setup into pulses of 50 ns length, using the technique described in the previous chapter. A total of 17 mW of light entered the CRIS beamline, with a beam spot of approximately 0.5 cm diameter. Excited atoms were ionized through a non-resonant ionization step using 266 nm light, produced by frequency quadrupled Neodymium-YAG Brilliant laser. This laser system produced up to 0.5 mJ of light, at a repetition rate of 20 Hz.

Neither transition in this scheme reached saturation. For the second step this was not unexpected given the low output power of the laser and the cross section for non-resonant ionization, which are typically low. Unfortunately, the first step was also far from the saturation point (see the saturation curve in figure 4.2), making the total efficiency of the experiment too low to push beyond ^{71}Cu. Some example spectra for ^{65,71}Cu are shown in figure 4.3.

In table 4.1 the hyperfine parameters extracted for ^{63,65,69,71}Cu are shown. The uncertainties are the weighted average of the uncertainties obtained for each individual scan (two scans for ^{63}Cu, three for ^{65}Cu, and one for ^{69}Cu and

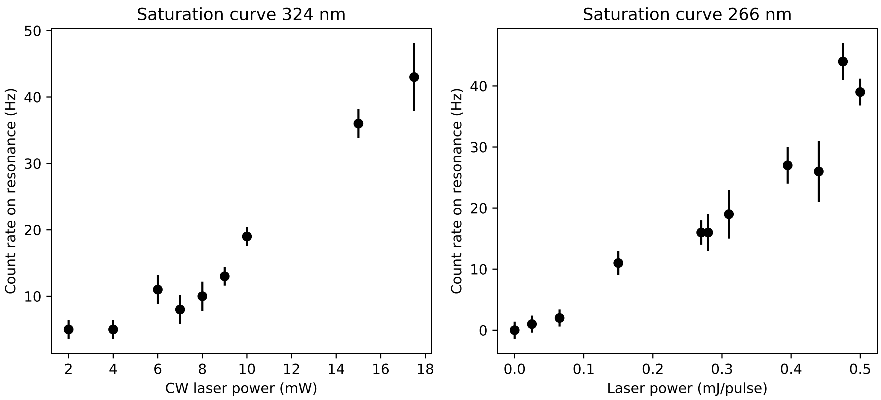

Figure 4.2: Saturation curve for both laser steps in the ionization scheme. For the 324 nm light, the laser power is the continuous-wave laser power measured with the chopping setup set to an always-on mode.

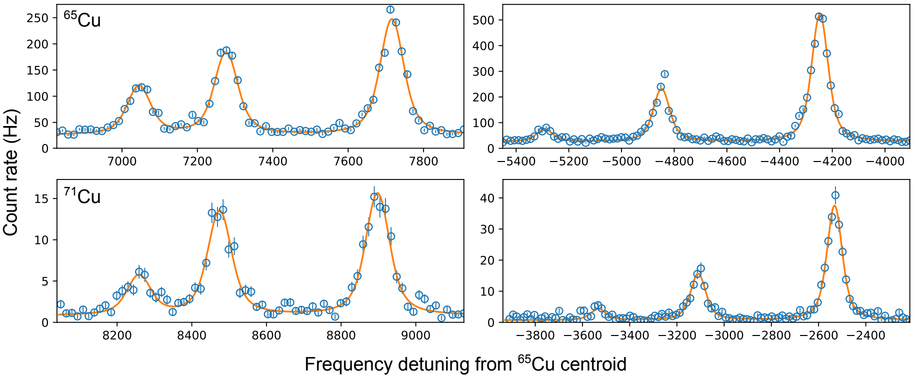

Figure 4.3: Experimental hyperfine structure spectra of ^{65,71}Cu. The centroid frequency of ^{65}Cu was subtracted from the x-values.

^{71}Cu). The hyperfine parameters are compared to those obtained with the COLLAPS experiment [5]. A similar precision is reached, though it should be noted that the small number of total scans prevents good assessment of potential systematic or scattering errors. Furthermore, the wavemeter-related issues that were uncovered in later experiments (to be discussed in section 5) may also lead to small deviations from literature. These factors, in combination with the rather poor statistics for the weakest peaks in the hyperfine structure, could explain at least in part some of the small deviations from literature.

Table 4.1: Hyperfine parameters and isotope shift extracted during the 2015 experiment, compared to literature [5]. All values are in MHz. Note that no assessment of systematic uncertainties or additional scattering effects was done, and uncertainties may therefore be underestimated.

	A_l	A_l^{lit}	A_u	A_u^{lit}
63	+5866.8(9)	+5867.2(3)	+194.7(3)	+194.5(11)
65	+6283.1(7)	+6284.29(19)	+208.4(3)	+208.4(2)
69	+7490(1)	+7490(2)	+249.5(1)	+248.7(15)
71	+6004(2)	+6001.4(14)	+200.0(7)	+199.6(8)

	B_u	B_u^{lit}	$\delta\nu$	$\delta\nu^{\text{lit}}$
63	-28(1)	-28.0(6)	-581.2(6)	-576.1(11)
65	-23.3(8)	-25.9(4)	-	-
69	-20(1)	-20(2)	+1079.4(7)	+1079(2)
71	-22(2)	-25(2)	+1526(1)	1526(9)

In conclusion, while this transition provided good sensitivity to the nuclear parameters, neither laser system could provide the power densities required for efficient resonance ionization spectroscopy. This observation provided a clear motiviation to investigate in detail how to optimize laser excitation and ionization efficiency, and furthermore how to do this without sacrificing resolution. In addition, the line distortion effects described in 3.2, while understood qualitatively, merited a quantitative investigation.

In **Article III**, some of this theoretical work is presented. More information can be found in the two Master's theses that preceded this article [61, 62].

Concerning the efficiency of the RIS process, strong transitions require the use of a pulsed laser system: only such systems can provide the photon flux required to counteract the fast decay of the excited state. Weak transitions to long-lived levels can be efficiently excited using a continuous wave laser system, since longer interaction times are possible and the excited state does not decay as rapidly. They can also be used well with pulsed laser systems, as long as they have sufficiently high output fluence. For example, in the case of francium, similarly high ionization efficiency was obtained with a pulsed Ti:sapphire laser system [54], as well as with a chopped continuous-wave Ti:sapphire laser system [60]. Another important conclusion of the article is that, through the use of weak atomic transition to long-lived excited atomic states and a delayed ionization laser, power broadening effects and lineshape distortions can be avoided completely.

Given these considerations, using the transition at 324 nm would therefore require a pulse dye laser system with a narrow bandwith (<100 MHz). The

CRIS experiment currently does not have access to such a laser system.

4.1.1 Article III: Efficient, high-resolution resonance laser ionization spectroscopy using weak transitions to long-lived excited states

Efficient, high-resolution resonance laser ionization spectroscopy using weak transitions to long-lived excited states

R. P. de Groote,[1,*] M. Verlinde,[1] V. Sonnenschein,[2]
K. T. Flanagan,[3] I. Moore,[2] and G. Neyens[1]

[1]*KU Leuven, Instituut voor Kern- en Stralingsfysica, B-3001 Leuven, Belgium*
[2]*Department of Physics, University of Jyväskylä,*
P.O. Box 35, 40014 Jyväskylä, Finland
[3]*School of Physics and Astronomy,*
The University of Manchester, Manchester M13 9PL, UK

Abstract

Laser spectroscopic studies on minute samples of exotic radioactive nuclei require very efficient experimental techniques. In addition, high resolving powers are required to allow extraction of nuclear structure information. Here we demonstrate that by using weak atomic transitions, resonance laser ionization spectroscopy is achieved with the required high efficiency (1-10%) and precision (linewidths of tens of MHz). We illustrate experimentally and through the use of simulations how the narrow experimental linewidths are achieved and how distorted resonance ionization spectroscopy lineshapes can be avoided. The role of the delay of the ionization laser pulse with respect to the excitation laser pulse is crucial: the use of a delayed ionization step permits the best resolving powers and lineshapes. A high efficiency is maintained if the intermediate level has a lifetime that is at least of the order of the excitation laser pulse width. A model that describes this process reproduces well the observed features and will help to optimize the conditions for future experiments [a].

---

[a] Simulation code available upon request to the authors.

[*] ruben.degroote@kuleuven.be

I. INTRODUCTION

The study of the fundamental ground-state properties of exotic nuclei is one of the challenges in contemporary nuclear physics research [1]. Laser spectrosopic methods contribute to this ongoing research endeavor by providing information on the nuclear electromagnetic moments, spins, and changes in mean-squared charge radii. These observables provide key input towards a theoretical description of the nucleus, as illustrated e.g. in [2]. Experimental measurements on very exotic nuclei are challenging, reflecting a combination of short half-lives and production in only minute quantities, accompanied by a large amount of unwanted contamination. Furthermore, facilities that produce these exotic nuclei only allot a limited time to a given experiment, which means that the study of the most exotic cases requires techniques that are both very selective and efficient. In addition, such measurements are often performed only once, so systematic uncertainties must be understood, removed, or at least minimized.

Many laser spectroscopic techniques have been applied in nuclear physics research, each with their strengths and weaknesses [3–5]. Resonance Ionization Spectroscopy (RIS) methods, which rely on multi-step laser ionization and subsequent ion detection, are typically very sensitive, motivating the development of numerous RIS experiments at online isotope separators [6]. To achieve efficient laser ionization, pulsed laser systems are typically used, often operating at high powers. This leads to a drawback for spectroscopy, including unwanted lineshape distortion and/or line broadening. These effects can become apparent when performing high-resolution RIS, as illustrated recently in [7]. Given the current developments towards high-resolution RIS of exotic nuclei in e.g. collinear RIS [7] and in-gas-jet laser spectroscopy [8, 9], a detailed understanding of the interaction of atoms with pulsed lasers is vital.

This article will present a model that describes the RIS process using CW or pulsed lasers for the resonant excitation and non-resonant ionization step (section II). Spontaneous decay of the intermediate level is taken into account and time delays between the two excitation steps are investigated. Through both model simulations and experimental verification, this article will address how some of the aforementioned detrimental line distortion effects can be understood and avoided by delaying the ionization laser pulse. This will be presented in section IV. Furthermore, through the same delayed-ionization approach, it is possible to remove virtually all power broadening due to both lasers in a two-step RIS scheme, which could be important for future high-precision studies on radioactive isotopes. This will be illustrated experimentally and through simulations in section III.

The delayed ionization method is greatly enhanced by using a weak transition to a long-lived excited state. Firstly, with short-lived excited states, a significant fraction of the excited state population would decay before the ionization can take place, reducing the efficiency of the method. Secondly, long-lived states result in intrinsically narrower linewidth since their natural width is smaller. The feasibility of using weak transitions for efficient resonance laser ionization spectroscopy using both continuous wave and pulsed lasers will be addressed in section V.

II. A MODEL FOR RIS

The evolution of the population of a system of two levels irradiated by a laser tuned close to resonance can be calculated by solving the Schrödinger equation with the following Hamiltonian:

$$H = \frac{\hbar}{2}\begin{pmatrix} 0 & \Omega(t) \\ \Omega(t) & 2\Delta \end{pmatrix}, \tag{1}$$

where $\Omega(t)$ is the coupling parameter of the two states, also called the Rabi frequency, and Δ is the laser-atom detuning. Define the frequency of the linearly polarized laser as ω_e, the ground state level energy as $\hbar\omega_0 = 0$, the excited state energy as $\hbar\omega_1$ and $\Delta = \omega_1 - \omega_e$. When considering two hyperfine levels with total angular momentum F_0 and F_1 and magnetic quantum number m_{F_0} and m_{F_1}respectively, $\Omega(t)$ can be calculated (up to a sign) in terms of the Einstein A coefficient of the transition as [10]:

$$\begin{aligned} \Omega(t) =& \sqrt{\frac{6\pi c^2 A P_e(t)}{\hbar(\omega_1-\omega_0)^3}}\sqrt{(2F_0+1)(2F_1+1)} \\ & \times \sqrt{2J_1+1}\begin{pmatrix} F_1 & 1 & F_0 \\ -m_{F_1} & 0 & m_{F_0} \end{pmatrix}\begin{Bmatrix} J_1 & F_1 & I \\ F_0 & J_0 & 1 \end{Bmatrix}, \end{aligned} \tag{2}$$

with () and {} respectively Wigner 3J and 6J symbols and $P_e(t)$ the power of the laser.

A second laser with laser power $P_i(t)$ can ionize excited atoms at a rate of $\Gamma = P_i(t)\sigma$, with σ the non-resonant photo-ionization cross section of the excited state at the wavelength of the ionization laser. Photo-ionization requires modeling population loss, since population has to flow out of the two-level system, into the continuum. This requires a non-Hermitian Hamiltonian, given by

$$H = \frac{\hbar}{2} \begin{pmatrix} 0 & \Omega(t) \\ \Omega(t) & 2\Delta + 2S(t) - i\Gamma(t) \end{pmatrix}, \tag{3}$$

In this Hamiltonian S is the net dynamic Stark shift induced by both the ionization laser and excitation laser, with each laser contributing a shift proportional to the laser power [11, 12]. If there are no relaxation processes, the evolution of the system can be calculated using the time-dependent Schrödinger equation

$$\dot{\rho} = \frac{1}{i\hbar} \left(H\rho - \rho H^{\dagger} \right). \tag{4}$$

The right-hand side of this equation reduces to the more familiar commutator $[H, \rho]$ for Hermitian H. The populations of the hyperfine levels are the diagonal elements of the density matrix, $\rho_{ii}(t)$. Usually the spontaneous decay of the excited state to the ground state cannot be neglected. Including incoherent relaxation processes such as spontaneous decay into equation (4) can be done as follows:

$$\dot{\rho} = \frac{1}{i\hbar} \left(H\rho - \rho H^{\dagger} \right) + L(\rho). \tag{5}$$

For the simplified two-level system, L is given by [13, 14]

$$L = \begin{pmatrix} A\rho_{11} & -\frac{1}{2}A\rho_{01} \\ -\frac{1}{2}A\rho_{10} & -A\rho_{11} \end{pmatrix}, \tag{6}$$

This additional term in the equations of motion causes decay of the excited state to the lower-lying state, and exponentially dampens the coherence terms.

These equations of motion can be generalized to systems with n_0 ground- and n_1 excited state hyperfine levels (see Fig. 1) in a relatively straightforward manner. Fully taking the degeneracy due to the magnetic sublevels of each hyperfine level into account would result in a significant increase in the computational cost. This is why, as an approximation, this degeneracy is neglegted by setting the 3j-symbol in equation (2) equal to one, which means the Hamiltonian is thus $n_0 + n_1$-dimensional. This approximation could result in incorrectly

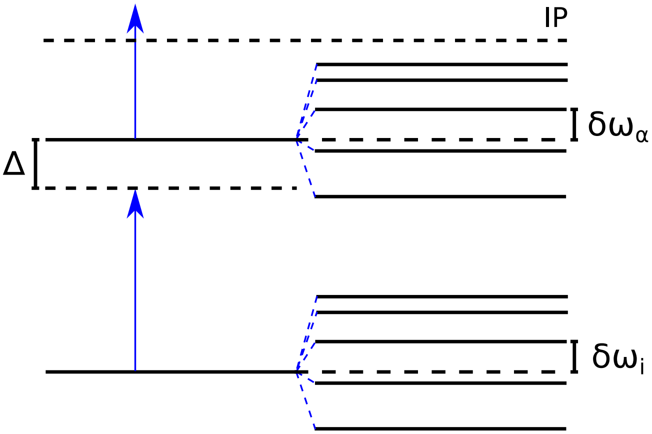

Figure 1: An atom with several hyperfine levels in the ground-state and in the excited state multiplet. Note the figure is not to scale, since the hyperfine splitting is typically 10^6 times smaller than the transition energy.

calculated relative peak intensities, but proved sufficient for this work. Using latin indices (ranging from 0 to n_0) for the ground state multiplet and Greek indices (ranging from n_0+1 to n_1) for levels in the excited state multiplet, the Hamiltonian can be written down as

$$H_{ii}(t) = \hbar\omega_i \tag{7}$$

$$H_{ij}(t) = 0 \tag{8}$$

$$H_{\alpha\alpha}(t) = \hbar(S_\alpha(t) + \Delta_\alpha - \frac{i}{2}\Gamma(t)) \tag{9}$$

$$H_{i\alpha}(t) = H_{\alpha i}(t) = \frac{\hbar}{2}\Omega_{i\alpha}(t) \tag{10}$$

$$H_{\alpha\beta}(t) = -\frac{\hbar}{2}\Gamma(t)(q+i), \tag{11}$$

with $\hbar\omega_i$ and $\hbar\omega_\alpha$ the energy of the atomic states of the ground- and excited-state hyperfine multiplet, and $\Delta_\alpha = \omega_\alpha - \omega_e$. The off-diagonal terms in (11) are due to the embedding of structure into the continuum by the high-power ionization laser, and are characterized by a Fano parameter q [15]. This q parameter plays a role in laser-induced continuum phenomena and can be calculated from first principles (see e.g. [16–19]). It induces a coupling between the excited state multiplet levels by the ionization laser via the interaction with the continuum. This coupling can influence RIS line profiles, but only for either very large values of q or for unrealistically high laser powers. For the purpose of this article the Fano parameter will be taken to be zero.

The generalized form of the matrix L can be written down using the partial decay rates defined as [20]

$$\begin{aligned}\gamma_{\alpha i} = \frac{4\alpha}{3}\frac{|\omega_\alpha - \omega_i|^3}{c^2}(2F_i+1)(2J_\alpha+1)(2J_i+1) \\ \times \,|\, \langle \alpha, L_\alpha || r || i, L_i \rangle \,|^2 \begin{Bmatrix} J_\alpha & 1 & J_i \\ F_i & I & F_\alpha \end{Bmatrix}^2 \begin{Bmatrix} L_\alpha & 1 & L_i \\ J_i & S & J_\alpha \end{Bmatrix}^2 .\end{aligned} \tag{12}$$

These rates can be calculated using the observation that the partial decay rates of an excited hyperfine level should sum up to the Einstein A coefficient. Using this definition of the partial rates, L can be written down as [13, 14]

$$L(\rho)_{ii} = \sum_\alpha \rho_{\alpha\alpha}\gamma_{\alpha i} \tag{13}$$

$$L(\rho)_{\alpha\alpha} = -\sum_i \rho_{\alpha\alpha}\gamma_{\alpha i} \tag{14}$$

$$L(\rho)_{\alpha i} = -\frac{\rho_{\alpha i}}{2}\sum_j \gamma_{\alpha j} \tag{15}$$

$$L(\rho)_{i\alpha} = -\frac{\rho_{i\alpha}}{2}\sum_j \gamma_{\alpha j} \tag{16}$$

$$L(\rho)_{\alpha\beta} = -\frac{\rho_{\alpha\beta}}{2}\sum_j \gamma_{\alpha j} + \gamma_{\beta j}. \tag{17}$$

These are the generalized equations that will be used for the simulations presented throughout this article. The computer code developed in Python used to run the simulations, is available upon request to the authors.

III. POWER BROADENING AND DELAYED IONIZATION

A. Model Predictions

In a two-step RIS scheme, both lasers can broaden the resonance line profiles. Power broadening due to the excitation laser in a closed two-level system using continuous-wave (CW) laser light is well understood in the steady-state limit. In this case, the linewidth of the optical resonance increases with the laser power [21]:

$$\mathrm{FWHM} = A\sqrt{1 + 2(\Omega/A)^2}. \tag{18}$$

In other words, population is only excited efficiently to the excited state when $|\Delta| \leq D$, with

$$D \approx A\sqrt{1 + 2(\Omega/A)^2}. \tag{19}$$

However, for pulsed laser excitation, this relationship is not always valid [22]. It can be derived that for a Gaussian shaped excitation laser pulse (in absence of ionization and spontaneous decay), the detuning range that results in excited state population after the action of the excitation pulse is given by [23]

$$D \approx \frac{\sqrt{\log\left(\Omega/\left|\Delta\right|\right)}}{T}, \tag{20}$$

with T the length of the laser pulse in time. The different power dependence of the line widths for CW and pulsed laser excitation is illustrated in Fig. 2, using $A = 10^6$/s in (19) and $T = 50\,\mathrm{ns}$ in (20). The linewidth predicted by equation (20) for pulsed laser excitation scales much more favorably with the laser power. Since this reduced linewidth is only obtained after the excitation pulse has passed, the significantly reduced power broadening presented in Fig. 2 can only be obtained by using a subsequently delayed ionization pulse. The considerable reduction of the resonance linewidth provides a strong argument in favor of using an ionization step that is delayed with respect to the pulsed excitation laser step, such that the narrower line shape is probed.

Besides power broadening due to the excitation laser, the interaction of the system with the ionization laser, if applied during the excitation laser pulse, can also further broaden the level. This can be understood in an intuitive way. Since the ionization laser couples the excited state to the continuum, the lifetime of this excited state is reduced. By virtue of the time-energy uncertainty principle, a reduction of the lifetime implies an increase in the energy uncertainty of the excited state. Indeed, the resonant excitation is probed by looking at the ions that are created by subsequent excitation of the atoms from the excited level towards the ionization continuum. The energy uncertainty induced in the intermediate level translates into a broadening of the resonance observed in the spectrum. If the ionization laser is delayed with respect to the excitation laser step, this broadening does not occur, since the perturbing ionizing laser field is not present when the resonant excitation happens.

Fig. 3 illustrates these observations by presenting numerical solutions to the equations of motion for a two-level system using the parameters presented in table I. The population of the excited state as a function of the laser detuning (x-axis) and time (y-axis) is shown. To

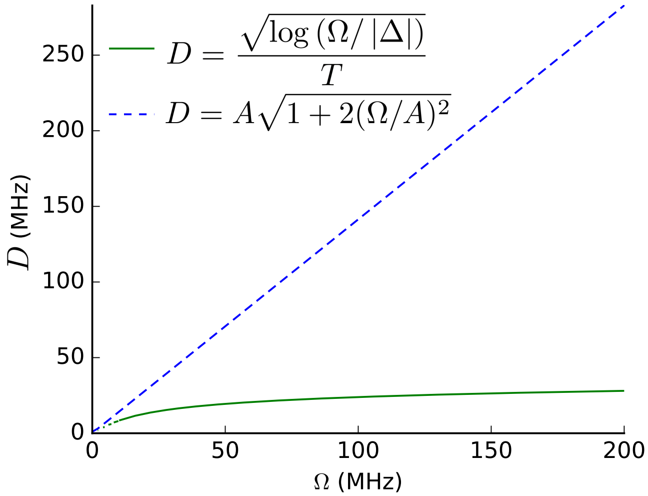

Figure 2: Comparison of equations (19) and (20), representing the line broadening D due to the excitation coupling Ω, for an Einstein A-coefficient of 10^6/s for continuous-wave lasers and T=50 ns for pulsed lasers.

the left of these plots a schematic picture of the time sequence of the excitation laser pulse and the second laser pulse is shown. The spectrum above the two-dimensional plots shows the frequency dependence of the ionization efficiency obtained at the end of the pulsed resonance ionization process. For better comparison, these ionization spectra are plotted again in Fig. 4.

In Fig. 3a it is shown that population is transfered to the excited state as the excitation laser builds up. When the ionization laser fires, the accumulated population is removed from the excited state. Upon comparing the ionization spectra shown at the top of figures 3a and 3b, it becomes apparent that delaying the ionization laser until the excitation laser has ended considerably reduces the linewidth of the final optical resonance obtained through the resonance ionization. This is due to the transient nature of the population transfer outside of the narrow region governed by equation (20): only in that region will population remain in the excited state after the action of the excitation laser. The width of the resonance ionization signal will therefore be narrower when using a delayed ionization laser. Note also in Fig. 3a how the presence of the ionization laser leads to additional broadening of

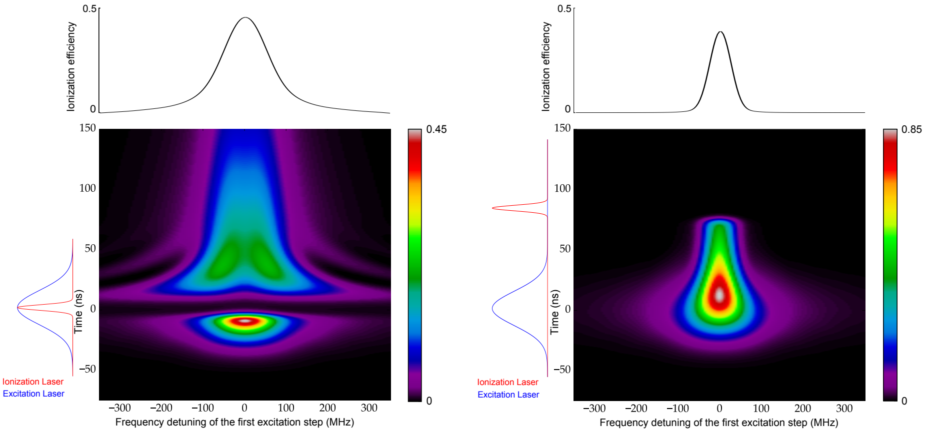

(a) Excited state population when using simultaneous laser pulses. The resonance ionization spectrum is power broadened by both laser pulses.

(b) As Fig. 3a, but with a delayed ionization pulse. Delaying the ionization step removes the power broadening from the resonance ionization spectrum.

Figure 3: Two simulations for a two-level atom, using the parameters in table I. For each of the figures, the central surface plot shows the excited state population as a function of laser detuning of the first excitation step on the x-axis and time on the y-axis. The diagram to the left of these central plot schematically displays the laser pulse sequence. On the top of each figure the resonance ionization spectrum is shown.

the excitation spectrum, an additional source of line broadening that is avoided by using a delayed ionization stage.

The goal of the experiments that are described below is to illustrate how power broadening can be mitigated by using a delayed ionization step. In this demonstration, the use of a weak transition to a long-lived excited state is crucial, since spontaneous decay from the excited state is minimal even with delayed ionization. This means that the resonance ionization process still occurs efficiently, which is critical for applications on exotic radioactive beams.

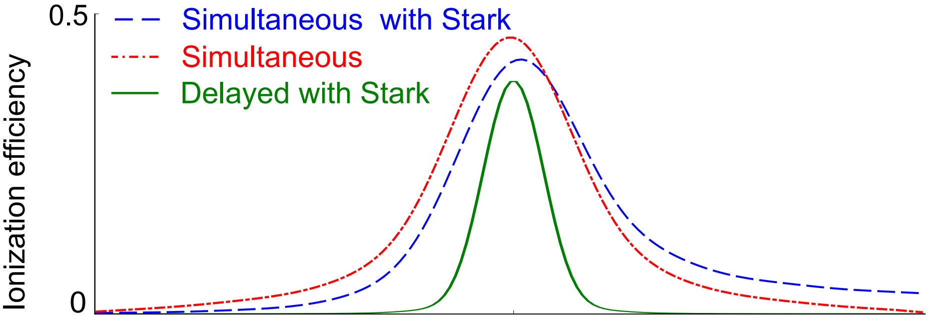

Figure 4: Comparison of the ionization spectra obtained in the top panels of figures 3a (red dot-dash line), 3b (green full line) and 9a (blue dashed line). Note how delaying the ionization step removes all power broadening and lineshape distortions.

Parameter	Value
Excitation Laser power	10 nJ
Excitation Laser pulse length	50 ns
Ionization Laser power	1 mJ
Ionization Laser pulse length	8 ns
A-parameter	10^7/s
Photo-ionization cross section σ	1 Mb
Ionization laser delay for Fig. 3a, 9a	0 ns
Ionization laser delay for Fig. 3b, 9b	80 ns
Stark effect Fig. 3	$S = 0$
Stark effect Fig. 9	$S = 0.9 \cdot \Gamma(t)$
Fano parameter q	0

Table I: Parameters used for the simulations in figures 3 and 9.

B. Experimental verification

1. Description of the experiment

Stable ^{63,65}Cu ($I = 3/2$) atoms have been laser-ionized using a two-step resonance ionization process depicted in Fig. 5. The experiment was performed at the JYFL laboratory in Jyväskylä, Finland. The resonant 244.237 nm line from the $3d^{10}4s\ ^2S_{1/2}$ ground-state to the $3d^94s4p\ ^4P^o_{1/2}$ state at 40943.78 cm^{-1} was followed by a 441.679 nm transition to the autoionizing $3d^94s\ 5s\ ^4D_{3/2}$ state at 63584.65 cm^{-1}. Given the long lifetime of the excited bound state (479(28) ns [24]), this system is well suited to study the behavior of power broadening for pulsed lasers and the role of the delay of the ionization laser on the line shape and ionization efficiency. Furthermore, the laser system used to excite the transition had a narrow bandwidth ($\approx$ 20 MHz) and could deliver an order of magnitude more laser power than the required saturation power density, resulting in clear power broadening effects.

A description of the atomic beam unit used for this work is presented in [25], but the essential features of the device are repeated here. The copper atoms were produced by resistively heating a tantalum tube containing a sample of copper. The resulting atomic beam passed through a collimation slit and then orthogonally crossed the laser beams. Electrostatic ion optics extracted the laser ionized copper atoms from the interaction region and guided them to an electron multiplier tube which served as the particle detector.

The laser system used for this work is described in detail in [26]. For the 244.237 nm line, an injection-locked Ti:sapphire laser system produced narrowband laser light (bandwidth $\approx$ 20 MHz), which was then frequency tripled. The master laser for this seeding cavity was a CW Matisse Ti:sapphire laser, which can be scanned continuously. The fundamental output of the seeded laser was 2.8 W at 10 kHz repetition rate, which after beam transport losses resulted in 300 mW/cm^2 of tripled UV light entering into the atomic beam unit. A maximum of 1.6 W/cm^2 of 411.679 nm light for the ionization step was produced using an intra-cavity frequency doubled pulsed Ti:sapphire laser. The two lasers were pumped using different Nd:YAG lasers, which introduces a jitter in the timing synchronization of both Ti:sapphire lasers of about 10 ns. This time jitter was of no consequence for the experiment. The pulse length of both lasers is typically 50 ns. The wavelength of the injection seeded Ti:sapphire was recorded using a High Finesse WS6 wavemeter and further monitored with a Toptica

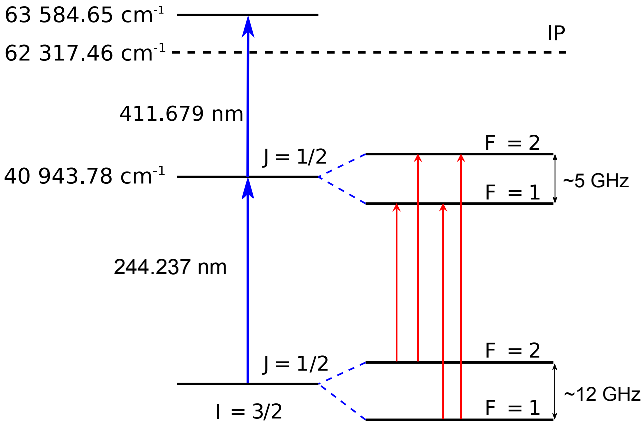

Figure 5: Ionization scheme used for ^{63}Cu and ^{65}Cu.

scanning Fabry Perot Interferometer FPI-100-0750-y with a free spectral range of 1 GHz. This interferometer was used to more precisely determine the wavelength of the laser as it was scanned. An example of a resonance ionization spectrum of ^{63,65}Cu is shown in Fig. 6,

2. Discussion of results

Ionization spectra of ^{63,65}Cu were obtained at different UV laser powers and for several time delays of the ionization step with respect to the excitation step. The linewidth of the Gaussian component of the fitted Voigt profiles was found to vary between 40 and 60 MHz for all experimental conditions. The contributions to this Gaussian component from the remaining Doppler broadening and the laser linewidth could not be separated, but are likely of a similar magnitude. The measurement performed at the lowest UV laser power (3 mW/cm^2) and using a temporally overlapped excitation and ionization laser resulted in a Lorentzian component with a width of 53.8(4) MHz. Increasing the power of the laser to 150 mW/cm^2 increased the linewidth of the Lorentzian component to 124.3(3) MHz. The two highest-frequency hyperfine transitions in the spectrum of ^{63,65}Cu measured with this larger laser power are shown in Fig. 7. The spectrum shown using red, open circles is measured with the excitation and ionization lasers firing simultaneously, while the green spectrum shown with full circles was obtained by delaying the ionization laser 40(10) ns.

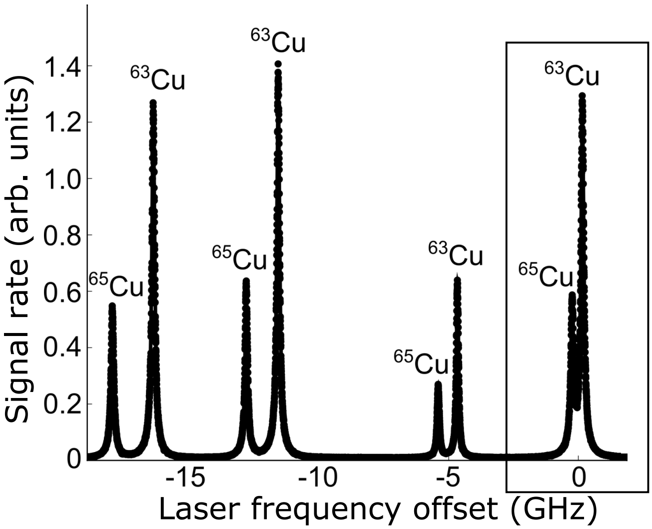

Figure 6: Ionization spectrum of ^{63,65}Cu. The black box indicates the peaks presented in the zoom-in in Fig. 7.

Symbols are the experimental data points, the full line is the fit with a Voigt line shape. As can be clearly seen by comparing the two spectra, keeping the laser power fixed and delaying the ionization laser drastically reduces the width of the resonance lines.

This sharp reduction in the experimental linewidth as the laser is delayed is further illustrated in Fig. 8. This figure shows the linewidth of the Lorentzian component as a function of the delay of the second laser. The red star and green triangle in this graph correspond to the data plotted in red and green of the spectra in Fig. 7. Also shown on Fig. 8 is a theoretical simulation, using the experimental parameters given earlier in this text. The photo-ionization cross section was set to 1 Gb to account for the enhanced ionization efficiency to the auto-ionizing state, even though the model presented in section II is only strictly applicable to ionization to a continuum. Despite this modeling inaccuracy, the general trend is well reproduced (up to the small offset between theory and experiment), indicating that the cause of the reduction in linewidth is understood; the linewidth reduction occurs when the action of the second laser is delayed, irrespective of the details of the interactions of the atomic system and the second laser. A more correct approach to modeling

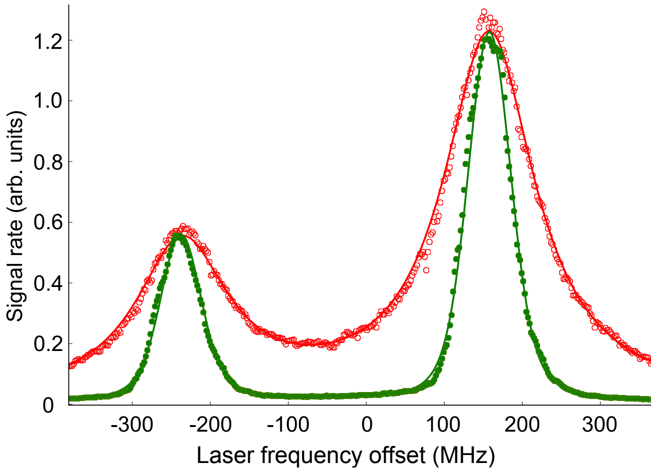

Figure 7: Two lines in the spectrum of ^{63,65}Cu (see Fig. 6 for the full spectrum). Plotted in red, open symbols is a spectrum obtained with temporally overlapping lasers (broad lines), while green full circles are used for a spectrum obtained with a delayed ionization step (40(10) ns delay). Symbols are the experimental data points, the full lines are the fit. The laser power was 150 mW / cm^2 for both measurements. A sharp reduction in the linewidth can be clearly seen, without loss in efficiency.

RIS processes with auto-ionizing states is beyond the scope of this work.

The experimental Lorentzian linewidth saturates at about 19 MHz for delay times of more than 100 ns. Note that this reduced Lorentzian linewidth is much less than the 53.8(4) MHz linewidth obtained at the lowest laser power of 3 mW/cm^2 (with temporally overlapping laser pulses). This provides direct evidence for the absence of power broadening not only from the excitation laser but also from the ionization laser.

Note finally that the efficiency loss due to spontaneous decay is negligible for delays below 50 ns due to the long lifetime of the excited state of 479(28) ns. This is the key advantage offered by using the weak transition to a long-lived state rather than a stronger transition.

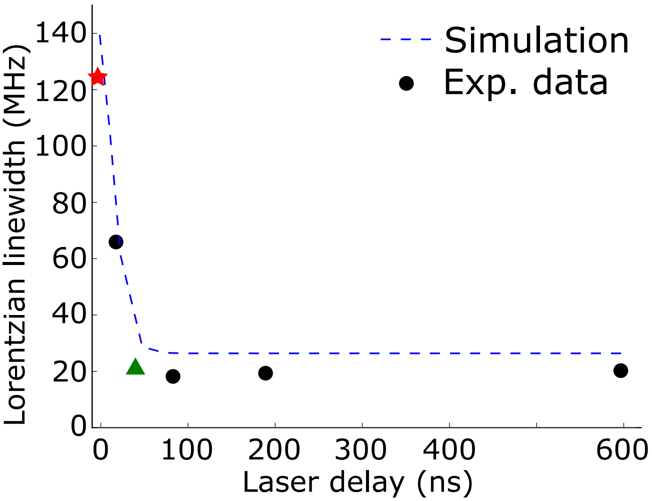

Figure 8: Linewidth of the Lorentzian component of the Voigt profile as a function of the delay time of the second laser pulse. The red star corresponds to the red spectrum in Fig. 7, the green triangle corresponds to the green spectrum in Fig. 7. Errors are smaller than the symbols. Also shown is a theoretical calculation of the linewidth as function of the laser delay, using the experimental parameters described in the text.

IV. EXPERIMENTS ON LINESHAPE DISTORTIONS AND DELAYED IONIZATION

A. Model Predictions

In addition to the power broadening effects discussed in the previous section, there is another effect to consider: the possibility of lineshape distortions induced by a high-power ionization laser. This effect is illustrated in Fig. 9. This figure repeats the simulations presented earlier in Fig. 3, but this time includes a Stark shift induced by the ionization laser (S in equation (3)). In Fig. 9a a clear asymmetry can be seen in both the population of the excited state and the final ionization spectrum. By contrast, when using a delayed ionization laser, this asymmetry is naturally absent.

The next section will discuss some experimental data which demonstrate this kind of

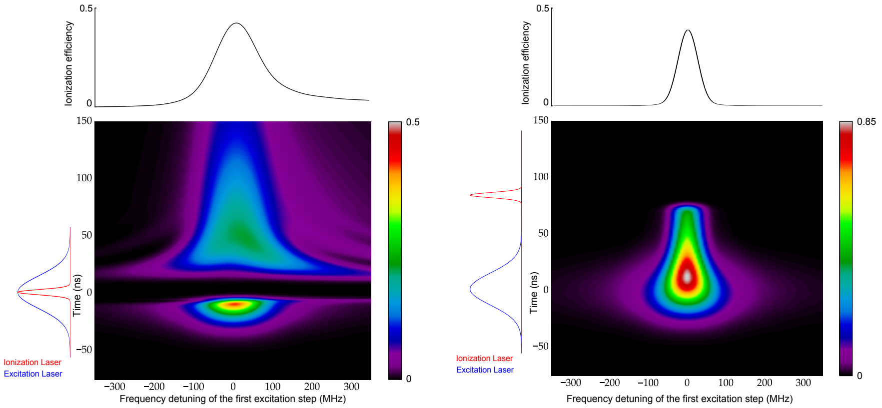

(a) Excited state population and ionization spectrum for simultaneous laser pulses. The ionization spectrum is asymmetric, which can also be seen in the population of the excited state.

(b) Excited state population and ionization spectrum for delayed laser pulses. By delaying the ionization laser, both the power broadening and asymmetry in the ionization spectrum disappear.

Figure 9: As figure 3, but including a Stark shift due to the ionization laser.

lineshape distortions. We will also show that the model for laser ionization introduced in section I can be used to qualitatively explain these distortions. Delaying the ionization laser in time with respect to the excitation laser removes the unwanted effects, since the distortion is induced after the atomic structure is already probed by the excitation laser.

B. Experimental verification

1. Description of the experiment

The possibility of ionization-related lineshape distortions, and how they can be removed by using a delayed ionization step, has been illustrated using the Collinear Resonance Ionization Spectroscopy (CRIS) experiment at ISOLDE-CERN [7, 27], using a radioactive beam of ^{221}Fr ($I = 5/2$, $t_{1/2} = 286.1\,\mathrm{s}$). The data presented in this article were obtained as part of a campaign to study the nuclear ground-state properties of several francium isotopes.

Details on the experimental set-up and measurement procedure can be found in [7], were the first application of this method allowed to study isotopes with a production rate down to 1000/s. The ionization scheme that was used is presented in Fig. 10, and consists of an excitation step from the $7s\ ^2S_{1/2}$ ground state to the $8p\ ^2P_{3/2}$ state at 23658.306 cm^{-1} (422.685 nm), and an ionization step that non-resonantly ionizes from the $8p\ ^2P_{3/2}$ state using pulsed 1064 nm light. The lifetime of the excited atomic state is 83.5(1.5) ns, sufficiently long to justify the use of a delayed ionization pulse.

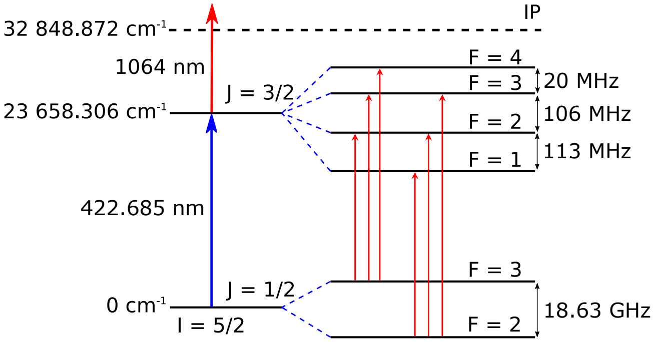

Figure 10: Ionization scheme used to excite and ionize ^{221}Fr. The size of the hyperfine splittings was calculated using the values in [28].

A ^{221}Fr ion beam was produced by the ISOLDE facility at CERN by impinging 1.4 GeV protons onto a uranium carbide target. Francium atoms diffuse out of this target and are then surface ionized in a hot capillary tube. After mass separation from the other surface-ionizing isotopes, the ^{221}Fr ion beam is then guided to a gas-filled linear Paul trap, where it is cooled and bunched. This beam is then accelerated to 30 kV and transported towards the CRIS experiment. The first stage of the CRIS experiment consists of neutralizing the ion beam through collisionless charge exchange with a hot potassium vapor [29]. This is often required, since suitable transitions are usually easier to find for neutral atoms rather than ions. The non-neutralized fraction of the beam is electrostatically deflected into a beam dump while the neutralized fraction is temporally and spatially overlapped with the laser beams in an ultra-high vacuum (UHV) interaction region. The laser frequency of the UV excitation laser is scanned across the hyperfine resonance transitions, and the resonantly ionized ^{221}Fr ions are then deflected onto a copper dynode. The secondary electrons emitted from the dynode are detected using a microchannel plate (MCP) electron detector. The UHV is required to minimize collisional ionization that would otherwise result in a constant background in the hyperfine spectra.

Because of the combination of an accelerated beam and the collinear overlap of the atom and laser beams, Doppler broadening is reduced to the point where it only contributes a few MHz to the total linewidth of the hyperfine structure spectra. The laser light for the first step was produced by frequency doubling the output of a Matisse TS cw Ti-sapphire laser with a Wavetrain external cavity frequency doubler. This continuous light was chopped into pulses of variable length through the use of a pockels cell and subsequent polarization sensitive beam optics, described in detail in [7]. This experimental configuration was used to create light pulses with a pulse length of 100 ns, at a repetition rate of 100 Hz. The 1064 nm light for non-resonant ionization was produced using a dual-cavity Litron LPY 601 50-100 PIV laser system, operated at 100 Hz and with a pulse length of 13 ns. After beam transport losses, 250 mW/cm^2 of continuous wave laser light and 32 mJ/pulse of 1064 nm laser light reached the entry of the CRIS beamline.

2. Discussion of results

Fig. 11 shows two measurements of the low-frequency component of the hyperfine structure of ^{221}Fr. The red (broad) spectrum (displayed with open symbols) is obtained with the ionization laser temporally overlapped with the 100 ns wide excitation laser pulse, as illustrated in the inset of Fig. 11. The green data points (full symbols) were obtained with an ionization pulse delayed by 100 ns from the start of the excitation pulse. Using simultaneous laser pulses distorts the high-frequency side of the peaks, which displays a clear asymmetry. This asymmetry disappears when the ionization laser is delayed, which indicates that the tailing is induced by the ionization laser.

The figure also shows simulations using the model introduced in section II. The ionization cross section σ was taken to be 1 Mb, which should at least be of the correct order of magnitude (see e.g. [30, 31] for cross sections in Rb and Cs). The Fano q parameter was taken to be zero. The effective Stark shift S was tuned to give the best match with the experimental data; a final value of $S(t) = 4\Gamma(t)$ provided good agreement. Both simulations were also rescaled with the same scaling factor to match the intensity of the highest peak in the experimental data.

Using these parameters, the asymmetric tail of the peaks is well reproduced, supporting the idea that the observed asymmetry is due to a Stark shift caused by the strong electric field of the high-power ionization laser. The intensity of the smallest resonance in the spectrum is not well reproduced by the model. The reason for this discrepancy is unclear, but may be due to the approximation used to remove the degeneracy of to the magnetic substates.

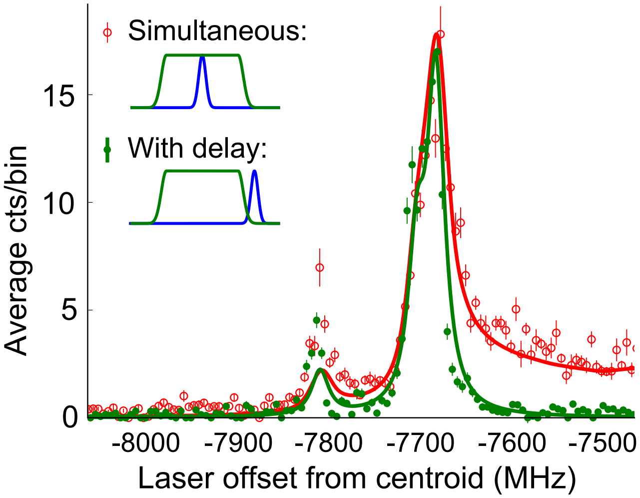

Figure 11: Resonance ionization spectra of the lowest-frequency components of the hyperfine structure of ^{221}Fr, obtained with simultaneous laser pulses (red, open symbols) and with a delayed ionization step (green, full symbols). The solid lines are fits using the model for RIS presented in section II. The asymmetry of the line disappears when the ionization laser is delayed, while the total ionization efficiency does not decrease significantly.

As with the data on the copper isotopes, delaying the ionization step does not result in significant loss in efficiency, since the excited state is long-lived. The linewidth of the resonance is 20(1) MHz. This linewidth could only be reached due to the removal of power broadening and the lineshape-distorting AC Stark shift by delaying the ionization laser. In a two-step resonance ionization scheme, this can only be done efficiently with a weak transition to a sufficiently long-lived excited state.

V. EFFICIENT LASER EXCITATION AND IONIZATION WITH WEAK TRANSITIONS

Weak transitions have shown desirable features for laser spectroscopy purposes. In addition to the inherently small linewidth, weak transitions show no sign of efficiency loss when delaying the ionization pulse. This section will further argue that weak transitions to long-lived states can be excited with very high absolute efficiencies, comparable to efficiencies obtained with stronger lines.

Applying the model of section II, one obtains the steady state population of an excited level in a two-level approximation as:

$$P_{exc}(\Delta = 0) = \frac{\Omega^2}{A^2 + 2\Omega^2} \tag{21}$$

$$\propto \frac{I/A}{1 + 2I/A}, \tag{22}$$

since $\Omega \propto \sqrt{IA}$. Since, for a fixed laser intensity, the equilibrium population is a monotonically decreasing function of A, weak transitions can achieve higher steady state population in the excited state. However, the irradiation time required to reach this steady state is longer than for strong transitions, though it also decreases with laser power. Therefore, there are two strategies to consider when maximizing the efficiency of excitations using weak transitions.

First of all, one can use high power pulsed laser systems which increase the rate at which the equilibrium population is reached, resulting in higher efficiency for short pulse lengths. This is the approach used for the first dataset in this article (see section III): a high-power pulsed laser can saturate the excitation step and therefore efficiently excite the system.

On the other hand, employing low power chopped CW laser light with long interaction times, as in the experiment of IV, also allows for high efficiency (>1-10 %). Indeed, the efficiency in the experiment described above using chopped CW laser light [7] is similar to that obtained in an earlier experiment using a pulsed high-power laser for the excitation step [27]. In both experiments, the total efficiency was 1%, where the detection efficiency was 80%, beam transport efficiency <30%, neutralization efficiency <50%, and the laser ionization efficiency therefore $> 8\%$.

The ability to reach high laser ionization efficiencies with chopped cw laser pulses is also illustrated in Fig. 12. This figure shows simulated ionization efficiencies for weak and strong transitions for a system with a ground state doublet and a single excited state, as a function of the pulse length of the excitation step, and using overlapping excitation and ionization lasers. The laser power was set to 10 mW, which is usually easily achieved with modern CW lasers. With sufficiently long interaction times, weak transitions can be excited very efficiently, with simulated ionization efficiencies better than or comparable to the efficiency obtained for short pulses and strong transitions. For time-separated laser beams, the ionization efficiency for a strong transition never reaches that of the weak transition, due to decay losses.

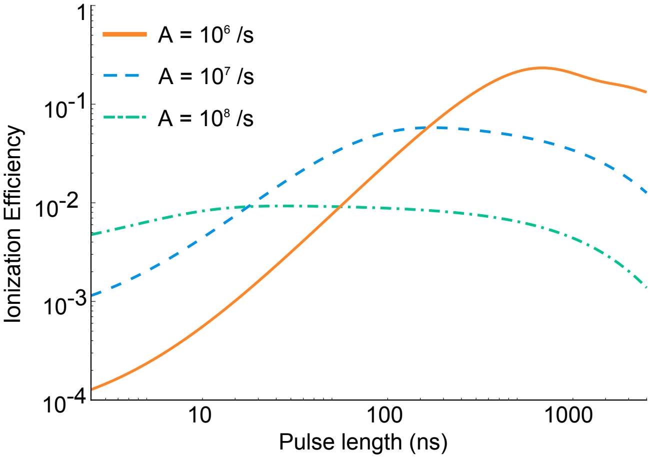

Figure 12: Ionization efficiency for a chopped cw-laser with a cw power of 10 mW, overlapped with a 1 mJ/pulse ionization laser and with a variable excitation laser pulse length. The system that was simulated here consists of a ground state doublet and a single excited state. For a weak transition ($A = 10^6$/s) the highest efficiency is reached if the pulse length is $\approx 1\,\mu s$. For extremely long laser pulses, the efficiency decreases in all cases due to optical pumping towards the other hyperfine level of the ground state.

VI. CONCLUSIONS

This article has shown that efficient resonance ionization spectroscopy with high resolving powers can be achieved with pulsed (or chopped) laser beams using weak transitions to long-lived states. This was demonstrated using simulations supported by experimental observations and illustrates the twofold advantages that weak transitions to long-lived states offer.

Firstly, it is possible to remove virtually all power broadening due to both lasers in a two-step RIS scheme by choosing a suitable delay between the excitation and the ionization laser pulses. Secondly, lineshape distortions due to the presence of a strong ionizing laser field when using non-resonant ionization can cause significant lineshape distortions, which can also be removed by delaying the ionization step. Similar arguments can be made in the case of RIS schemes that use more than two lasers, but this lies outside of the scope of the work presented here.

The long lifetime of the excited state ensures that no significant efficiency losses occur due to the delay of the ionization laser, though the requirement of needing a suitable, weak transition can potentially limit the cases that can be studied efficiently with delayed ionization method. Experimental evidence for both advantages was presented and compared to simulations with a theoretical model for resonance ionization spectroscopy. The experimental data obtained on radioactive beams of francium produced in small quantities compared to stable beams illustrate that high efficiencies can be obtained using weak transitions.

ACKNOWLEDGMENTS

We acknowledge the support of the ISOLDE collaboration and technical teams. We are grateful to the COLLAPS collaboration for the use of their CW Ti:sapphire laser system and wavetrain doubling unit. We thank Wouter Gins for fruitful discussions and for comparisons to simulations with rate equation codes. This work was supported by the BriX Research Program No. P7/12 and FWO-Vlaanderen (Belgium) and GOA 15/010 from KU Leuven, ERC Consolidator Grant no. 648381, the Science and Technology Facilities Council consolidated grant ST/F012071/1 and continuation grant ST/J000159/1, and the EU Seventh Framework through ENSAR(506065). K. T. F. was supported by STFC Advanced Fellowship Scheme Grant No. ST/G006415/1. This work was also supported by the Academy of Finland under the Center of Excellence Programme 20122017 (Nuclear and Accelerator

Based Physics Research at JYFL).

---

[1] A. Bracco, P. Chomaz, J. Gaardhøje, M. Makarow, P.-H. Heenen, G. Rosner, R. Kaiser, D. MacGregor, E. Widmann, and G. Korner, (2010).

[2] R. F. Garcia Ruiz, M. L. Bissell, K. Blaum, A. Ekström, N. Frömmgen, G. Hagen, M. Hammen, K. Hebeler, J. D. Holt, G. R. Jansen, *et al.*, Nature Physics **12**, 594 (2016).

[3] B. Cheal and K. T. Flanagan, Journal of Physics G: Nuclear and Particle Physics **37**, 113101 (2010).

[4] K. Blaum, J. Dilling, and W. Nörtershäuser, Physica Scripta **T152**, 014017 (2013).

[5] P. Campbell, I. Moore, and M. Pearson, Progress in Particle and Nuclear Physics **86**, 127 (2016).

[6] V. N. Fedosseev, Y. Kudryavtsev, and V. I. Mishin, Physica Scripta **85**, 058104 (2012).

[7] R. P. de Groote, I. Budinčević, J. Billowes, M. L. Bissell, T. E. Cocolios, G. J. Farooq-Smith, V. N. Fedosseev, K. T. Flanagan, S. Franchoo, R. F. Garcia Ruiz, *et al.*, Phys. Rev. Lett. **115**, 132501 (2015).

[8] Y. Kudryavtsev, R. Ferrer, M. Huyse, P. Van den Bergh, and P. Van Duppen, Nuclear Instruments and Methods in Physics Research Section B: Beam Interactions with Materials and Atoms **297**, 7 (2013).

[9] S. Raeder, B. Bastin, M. Block, P. Creemers, P. Delahaye, R. Ferrer, X. Flchard, S. Franchoo, L. Ghys, L. Gaffney, C. Granados, R. Heinke, L. Hijazi, M. Huyse, T. Kron, Y. Kudryavtsev, M. Laatiaoui, N. Lecesne, F. Luton, I. Moore, Y. Martinez, E. Mogilevskiy, P. Naubereit, J. Piot, S. Rothe, H. Savajols, S. Sels, V. Sonnenschein, E. Traykov, C. V. Beveren, P. V. den Bergh, P. V. Duppen, K. Wendt, and A. Zadvornaya, Nuclear Instruments and Methods in Physics Research Section B: Beam Interactions with Materials and Atoms **376**, 382 (2016), proceedings of the {XVIIth} International Conference on Electromagnetic Isotope Separators and Related Topics (EMIS2015), Grand Rapids, MI, U.S.A., 11-15 May 2015.

[10] B. King, arXiv preprint arXiv:0804.4528 (2008).

[11] N. B. Delone and V. P. Krainov, Physics-Uspekhi **42**, 669 (1999).

[12] S. Kumekov and V. Perel, Zh. Eksp. Teor. Fiz **81**, 1693 (1981).

[13] Y. B. Band, *Light and Matter: Electromagnetism, Optics, Spectroscopy and Lasers*, Vol. 1

(John Wiley & Sons, 2006).

[14] D. A. Steck, Oregon Center for Optics and Department of Physics, University of Oregon , 47 (2007).

[15] P. L. Knight and M. A. Lauder, Physics Reports **190**, 1 (1990).

[16] B. N. Dai and P. Lambropoulos, Phys. Rev. A **36**, 5205 (1987).

[17] T. Nakajima, M. Elk, J. Zhang, and P. Lambropoulos, Phys. Rev. A **50**, R913 (1994).

[18] L. P. Yatsenko, R. G. Unanyan, K. Bergmann, T. Halfmann, and B. W. Shore, Optics Communications **135**, 406 (1997).

[19] L. P. Yatsenko, T. Halfmann, B. W. Shore, and K. Bergmann, Phys. Rev. A **59**, 2926 (1999).

[20] P. R. Berman and V. S. Malinovsky, *Principles of laser spectroscopy and quantum optics* (Princeton University Press, 2010).

[21] M. L. Citron, H. R. Gray, C. W. Gabel, and C. R. Stroud, Phys. Rev. A **16**, 1507 (1977).

[22] N. Vitanov, Optics Communications **199**, 117 (2001).

[23] I. I. Boradjiev and N. V. Vitanov, Optics Communications **288**, 91 (2013).

[24] A. Kono and S. Hattori, Journal of Quantitative Spectroscopy and Radiative Transfer **28**, 383 (1982).

[25] T. Kessler, I. Moore, Y. Kudryavtsev, K. Perjrvi, A. Popov, P. Ronkanen, T. Sonoda, B. Tordoff, K. Wendt, and J. yst, Nuclear Instruments and Methods in Physics Research Section B: Beam Interactions with Materials and Atoms **266**, 681 (2008).

[26] V. Sonnenschein, *Laser Developments and High Resolution Resonance Ionization Spectroscopy of Actinide Elements*, Ph.D. thesis (2015).

[27] K. T. Flanagan, K. M. Lynch, J. Billowes, M. L. Bissell, I. Budinčević, T. E. Cocolios, R. P. de Groote, S. De Schepper, V. N. Fedosseev, S. Franchoo, R. F. Garcia Ruiz, H. Heylen, B. A. Marsh, G. Neyens, T. J. Procter, R. E. Rossel, S. Rothe, I. Strashnov, H. H. Stroke, and K. D. A. Wendt, Phys. Rev. Lett. **111**, 212501 (2013).

[28] H. T. Duong, P. Juncar, S. Liberman, A. C. Mueller, R. Neugart, E. W. Otten, B. Peuse, J. Pinard, H. H. Stroke, C. Thibault, F. Touchard, J. L. Vialle, K. Wendt, and I. Collaboration, EPL (Europhysics Letters) **3**, 175 (1987).

[29] T. J. Procter, H. Aghaei-Khozani, J. Billowes, M. L. Bissell, F. L. Blanc, B. Cheal, T. E. Cocolios, K. T. Flanagan, H. Hori, T. Kobayashi, D. Lunney, K. M. Lynch, B. a. Marsh, G. Neyens, J. Papuga, M. M. Rajabali, S. Rothe, G. Simpson, A. J. Smith, H. H. Stroke,

W. Vanderheijden, and K. Wendt, Journal of Physics: Conference Series **381**, 012070 (2012).

[30] R. V. Ambartzumian, N. P. Furzikov, V. S. Letokhov, and A. A. Puretsky, Applied physics **9**, 335 (1976).

[31] S. L. Gilbert, M. C. Noecker, and C. E. Wieman, Phys. Rev. A **29**, 3150 (1984).

4.2 Transition 2: offline tests at JGU Mainz

The 249.2146 nm line has also been studied reasonably well: hyperfine parameters have been previously measured. With an Einstein coefficient of $2.79 \cdot 10^{6}\,\mathrm{s}^{-1}$, this transition is quite a bit weaker than the 324.7540 nm line (with a strength of $1.395 \cdot 10^{8}\,\mathrm{s}^{-1}$). Since 249.2146 nm can only be produced by frequency tripling laser light, and reliable frequency tripling is currently only feasible with pulsed laser systems, the use of double-etalon Z-cavity pulsed Titanium Sapphire lasers (bandwidth $\approx$ 1 GHz) for precise spectroscopy was investigated in detail. The size of the dipole splitting is such that spectroscopy using broadband ($\approx$1 GHz bandwith) lasers appeared a possibility. At the same time, the performance of a newly developed narrowband, unseeded single mode Ti:Sapphire laser system could be compared to the Z-cavity lasers.

Off-line tests were performed at the Johannes Gutenberg University of Mainz. **Article IV** reprinted below presents some results obtained during these tests. They illustrated that reasonable precision on magnetic dipole moments can be obatined with the 1 GHz laser systems, but confirmed that the laser linewidth prevents sensitivity to the quadrupole moment. Comparison of these results with data obtained with a more narrowband (unseeded) ring cavity design (bandwidth $\approx$ 45 MHz) succeeded in extracting the hyperfine B parameter. This showed that a laser bandwidth of this order of magnitude is sufficient for online measurements on radioactive copper isotopes. Finally, no conclusions could be drawn on the isotope shift of ^{63,65}Cu for this transition during these tests.

As a spin-off of these tests, two-dimensional laser scans of the hyperfine structure of the ground and first two excited states in a three-step laser ionization scheme were also performed. Using these double-resonance maps, better resolving power can be achieved, which was shown to improve the precision on the extracted hyperfine parameters considerably. While this method could hold some promise to e.g. resolve some very collapsed hyperfine structures or to separate isomeric peaks from the nuclear ground-state hyperfine structure, the increase in scanning times probably prevent it from being used on radioactive beams. Results from these measurements are also discussed in **Article IV**.

4.2.1 Article IV: Double-resonance ionization mapping of the hyperfine structure of the stable Cu isotopes using pulsed, narrowband Ti:sapphire lasers

Double-resonance ionization mapping of the hyperfine structure of the stable Cu isotopes using pulsed, narrowband Ti:sapphire lasers

R. P. de Groote,[1,*] T. Kron,[2] A. Hakimi,[2] G. Neyens,[1] and K. Wendt[2]

[1]*Instituut voor Kern- en Stralingsfysica,*
KU Leuven, 3001 Leuven, Belgium
[2]*Institute of Physics, Johannes Gutenberg University Mainz, 55128 Mainz, Germany*

Abstract

We present two approaches to enhance the resolving power for measuring hyperfine structure constants using resonance ionization spectroscopy. The first method employs a 2D-resonance ionization spectroscopy scanning technique with pulsed, narrowband Ti:sapphire lasers (1 GHz linewidth), allowing to resolve hyperfine components that cannot be separated using the standard 1D-scanning method across only one optical transition. In a second refinement, the resolving power is further enhanced through the use of a ring design of the laser cavity. This layout leads to a reduction of the laser linewidth from 1 GHz to below 50 MHz, resulting in experimental linewidths of about 150 MHz. Motivated by the current nuclear physics interest in radioactive Cu isotopes, the hyperfine structure of the $3d^{10}4s\ ^2S_{1/2}$ ground state and the $3d^94s4p\ ^4P^o_{3/2}$ and $3d^{10}6s\ ^2S_{1/2}$ excited states in stable Cu isotopes were studied using both approaches. The hyperfine A parameter of the $3d^{10}6s\ ^2S_{1/2}$ state was measured for the first time with values of 296(18) MHz for ^{63}Cu and 307(18) MHz for ^{65}Cu.

---

[*] ruben.degroote@fys.kuleuven.be

I. INTRODUCTION

High-resolution laser spectroscopy is a powerful tool for the investigation of nuclear moments, charge radii and spins of exotic nuclei [1], i.e. short-lived radionuclides far off stability, which are produced at on-line radioactive ion beam facilities. High-resolution collinear laser spectroscopy techniques routinely demonstrate a resolution down to 50 MHz [2, 3]. In the last decade, the use of bunched ion beams produced in a linear Paul-trap ion beam cooler-buncher has allowed enhancement of the sensitivity by nearly three orders of magnitude [4]. Now, radioactive species with production rates around 1000 particles per second can routinely be studied. The study of even more exotic nuclei with yields down to 0.1 particles per second has been demonstrated by in-source resonance ionization laser spectroscopy (RIS) techniques [5–8]. However, several broadening mechanisms inherent to the in-source RIS technique limit the resolution to typically a few GHz, preventing high resolution studies suitable for extraction of nuclear parameters. The complementarity of the collinear and in-source laser spectroscopy is well illustrated by the recent studies of the nuclear structure of exotic Cu isotopes: neutron-rich Cu isotopes up to A=75 were investigated using collinear fluorescence laser spectroscopy[9–11], while still heavier Cu isotopes with lower yields were studied using in-source techniques [12–14].

Due to the low resolution in the latter experiments, only information on the magnetic moment and no information on the nuclear quadrupole moment could be obtained for the most exotic isotopes. In order to unambiguously determine the nuclear spins as well as the quadrupole moments, a combination of the sensitivity of in-source laser spectroscopy and the high resolution of collinear laser spectroscopy is required. This development has been the goal of the recently installed collinear resonance ionization spectroscopy (CRIS) experiment at ISOLDE-CERN [15–17]. The current limit to the resolution of the CRIS experiment is set by the linewidth of the pulsed narrowband Ti:sapphire laser in use [18, 19], which is typically around 1 GHz.

In this paper we present two ways to address this current limitation to the resolution and overall performance of CRIS. Firstly, this article will show how simultaneously scanning of the laser frequency of the two resonant excitation steps in a three-step resonance ionization scheme allows for the disentanglement of overlapping components of a hyperfine spectrum, in this way enhancing the resolving power of the experiment. Secondly, we present an advanced cavity design of a narrowband Ti:sapphire laser developed at Mainz University, whose previous design is discussed in [20, 21]. We illustrate that this new ring cavity geometry allows a reduction of the laser linewidth from about 1 GHz down to below 50 MHz.

The advantages and disadvantages of both spectroscopic approaches will be illustrated through hyperfine spectra measured for the two stable isotopes of Cu, ^{63}Cu and ^{65}Cu. Several transitions have already been used previously to study Cu isotopes. The $3d^{10}4s\ ^2S_{1/2} \rightarrow 3d^94s4p\ ^4P^0_{1/2}$ transition at 244.237 nm is particularly interesting because of the large hyperfine splitting of the excited state [12]. Unfortunately, this transition is not sensitive to the electric quadrupole moment. The $3d^{10}4s\ ^2S_{1/2} \rightarrow 3d^94s4p\ ^4P^0_{3/2}$ transition at 249.289 nm possesses a similarly large hyperfine splitting (see table I for these literature values), whereas it is influenced by the electric quadrupole moment of the upper level, making it an interesting candidate for further studies on nuclear moments. For both transitions however, the combination of the splitting of the ground and excited states leads to the fact that the hyperfine spectra may overlap partially or fully (see Cocolios et al. [12, 13] for the 244.237 nm transition), hindering HFS analysis. Therefore we investigate here the use of a double-resonance 2D scanning method to resolve all hyperfine levels.

The structure of this article is as follows: we start with an introduction to resonance laser ionization spectroscopy and the 2D double-resonance scanning technique in section II. Subsequently, the experimental apparatus and the new ring laser cavity design are discussed in detail in section III. The analysis of the 2D-resonance data and the high-resolution spectra obtained with the single mode ring laser are presented in section IV, and the conclusions drawn from these datasets are summarized in section V.

II. THEORETICAL CONCEPTS

RIS relies on a multi-step photon absorption process to excite and ionize an atom. In its most simple realization, the ionization proceeds in two steps. A resonant transition from the ground state to an excited state is followed by a resonant or non-resonant transition from this higher-lying state into the continuum. By scanning the wavelength of the laser in the first excitation step, the hyperfine substructures of this transition are probed. Three-step ionization schemes are commonly used for those cases, where e.g. the laser radiation frequency needed for a two-step scheme may not be generated easily or with sufficient output power. Its use in many cases enhances the overall ionization efficiency and isotope selectivity of the process. For a three-step scheme, two bound-bound resonant transitions are followed by an ionization step. Since there are two resonant steps involved, it is also referred to as double-resonance ionization spectroscopy. Typically only the laser wavelength of one excitation step is scanned with sufficient resolution to determine the relative positions of the hyperfine resonances, while the other lasers are kept fixed. Two-dimensional (2D)-scanning of both resonant laser steps with high resolution has previously been applied, primarily for resonance ionization mass spectrometry for trace analysis purposes [22, 23]. These experiments specifically implied a multiple-excitation scanning approach to enhance the selectivity of the RIS process.

Hyperfine structure is the result of the interaction of the atomic nucleus with its electron cloud; more specifically, it is the result of the interaction of the nuclear magnetic dipole moment and electric quadrupole moment with the corresponding fields of the electrons and their distributions throughout the electronic shell. These are parameterized by the angular momenta of the electrons. Correspondingly, from the study of the hyperfine structure, information on the nuclear g factor, the nuclear spin and the deformation of the nucleus can be derived. For a nucleus with a non-zero nuclear spin $\boldsymbol{I}$, the hyperfine interaction suspends the degeneracy of the electronic levels (with angular momentum $\boldsymbol{J}$), resulting in a set of substates labeled by the new quantum number $\boldsymbol{F} = \boldsymbol{I} + \boldsymbol{J}$:

$$F \in \{|I - J|, |I - J + 1|, \ldots, I + J - 1, I + J\}. \tag{1}$$

Each of these hyperfine substates is shifted in energy from the position of the original degenerate level by

$$\Delta E = \frac{A}{2} \cdot K + \frac{B}{2} \cdot \frac{3K(K+1) - 4IJ(I+1)(J+1)}{4IJ(2I-1)(2J-1)}, \tag{2}$$

where $K = F(F+1) - I(I+1) - J(J+1)$. A and B are the magnetic dipole and electric quadrupole hyperfine parameters, which are related to the magnetic dipole moment μ and electric quadrupole moment Q_s of the nucleus. Optical transitions between the hyperfine sublevels F of a lower and F' of a higher lying atomic level must obey the additional selection rule $\Delta F = 0, \pm 1$ and have a relative intensity of

$$S(F \to F') = \frac{(2F+1)(2F'+1)}{2I+1} \begin{Bmatrix} J' & F' & I \\ F & J & 1 \end{Bmatrix}^2 . \tag{3}$$

It should be noted that the experimentally observed intensity of the transitions often differs from this relation, due to e.g. optical pumping or power-related effects.

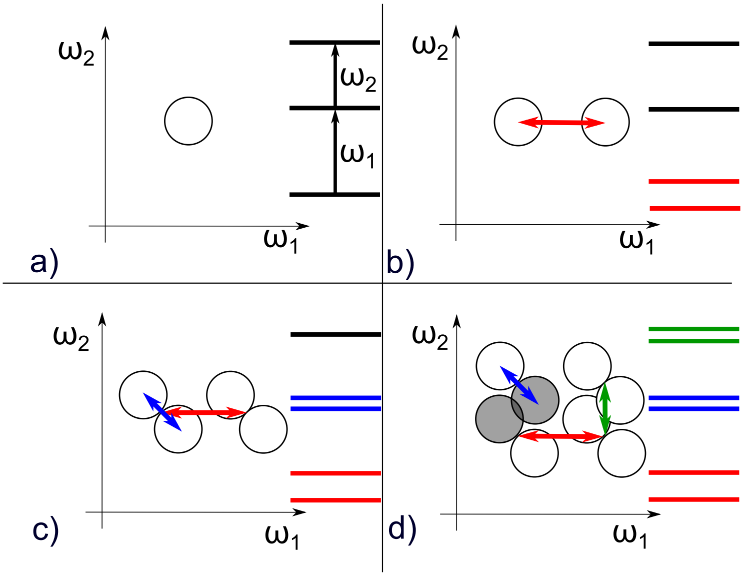

FIG. 1: (Color online) Positions of the peaks of the HFS (abstracted to circles) for the case where each bound state splits into two hyperfine states. **a)** All HFS parameters zero. **b)** Non-zero ground state splitting. **c)** Non-zero splitting of the first excited state. Note how the position of the peaks shifts along the diagonal of slope -1. **d)** Non-zero splitting of the upper state. The peaks shaded in gray can be reasonably resolved in the 2D map, but would overlap almost completely when projected on the ω_2-axis.

Fig. 1 gives a sketch to illustrate schematically how a second frequency dimension, as it is offered by a 2D scanning approach of a double resonance RIS experiment, will lead to an enhanced resolution of hyperfine patterns. The data is plotted with the spectrum of the first transition of the two-step scheme along the horizontal axis and the one of the second transition vertically. In each panel, the circles indicate the positions of the hyperfine peaks in a 2D frequency space, for a simple case in which all levels split symmetrically in two sublevels. In panel a) all the HFS parameters are zero. Panel b) only considers a pure ground state splitting, which causes the peaks in the spectrum to shift along the axis of the corresponding first step, for a well-defined value of the second step frequency. In panel c) the splitting of the first excited state is considered as well; now 4 peaks appear in the 2D spectrum. Since this additional splitting influences the resonance condition for both resonant transitions, the peaks in the 2D map shift along the diagonal instead of the vertical or horizontal axis. Note that the peak-to-peak distance along this diagonal is larger than the projected distances along the vertical or horizontal axis, where the peaks would overlap significantly. Correspondingly, the resolving power of the 2D scanning procedure and the corresponding 2D mapping of the data is better than a usual 1D spectrum obtained with a similar laser system. In panel d) the highest lying excited state is finally also taken into account, causing the peaks to split up once more, this time vertically, along the ω_2-axis. Note how all individual peaks are resolved in 2D, while in all cases peak overlap is observed for projection on either x or y axis.

III. EXPERIMENTAL SETUP

The electronic level schemes and the transitions used in this work are shown in Fig. 2. The nuclear spin for both investigated isotopes ^{63,65}Cu is $\boldsymbol{I} = \frac{3}{2}$. In the first two-step scheme labeled I, a 249.29 nm laser excites electrons from the $3d^{10}4s\ ^2S_{1/2}$ ground state of the Cu atom to the $3d^94s4p\ ^4P^o_{3/2}$ level at 40114.01 cm^{-1}. A second laser at 397.676 nm then further excites the atom to the $3d^94s5s\ ^2D_{3/2}$ auto-ionizing level at 65259.93 cm^{-1}, well above the ionization potential of 62317.46 cm^{-1}, from which the atom promptly ionizes. For the tests on 2D double-resonance mapping, bound atomic states were used, applying the three-step resonance excitation scheme labeled II. A laser at 785.252 nm induces excitations from the identical first excited $^4P^o_{3/2}$ level to the $3d^{10}6s\ ^2S_{1/2}$ at 52848.751 cm^{-1}, from which additional laser photons cause non-resonant ionization.

A. Atomic Beam Unit

The experiments were performed in the Mainz Atomic Beam Unit (MABU) which provides a well collimated beam of atoms, evaporated from a hot cavity into a high vacuum environment. While anti-collinear irradiation of the total oven volume ensures maximum ionization efficiency, it would on the other hand lead to a large Doppler broadening due

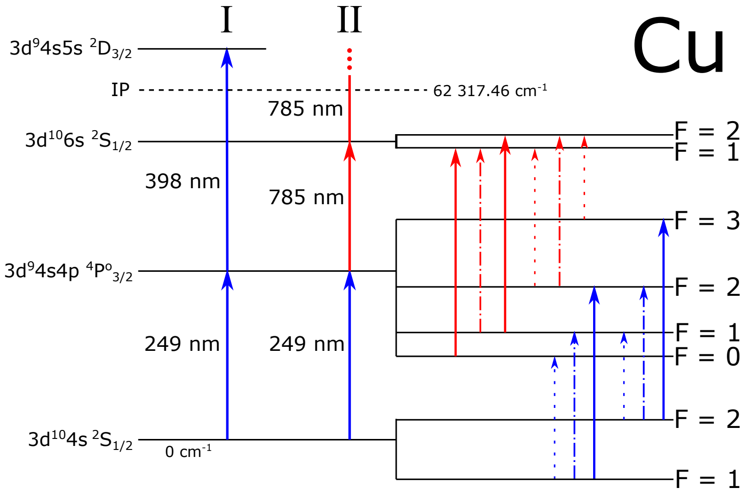

FIG. 2: (Color online) Diagram of the electronic levels (labeled by their total angular momentum F) and transitions used in this work. Dashed lines indicate weak transitions ($\Delta J = -1$), dash-dot lines indicate stronger lines ($\Delta J = 0$) and full lines represent the strongest excitation paths ($\Delta J = +1$). The two-step RIS scheme I was used for the single-resonance measurements, the three-step scheme II for the double resonance 2D mapping.

to the thermal velocity distribution of the atomic ensemble. Therefore the laser beams are directed perpendicular to the oven emission axis, as schematically shown in Fig. 3, and irradiate the atoms immediately after they passed a first electrode. This is kept on positive potential to suppress all ions, which are created inside the oven by unselective ionization processes. After resonance ionization, ion optical elements shape an ionic beam and guide it towards a 90 ° quadrupole deflector, deflecting the ions while allowing neutral species to pass to further reduce unspecific background. After deflection a quadrupole mass filter selects the mass of interest. A channeltron electron multiplier, operating in single ion counting mode, detects the ions and passes the signals to the data acquisition system. A more detailed description of the MABU can be found in several publications e.g. [24].

For precise probing of the hyperfine structure and isotope shift of the atoms narrowband laser radiation is preferred to ensure optimum spectral resolution. In this case, the observable spectral linewidth in the perpendicular crossed beam geometry is governed by the Doppler

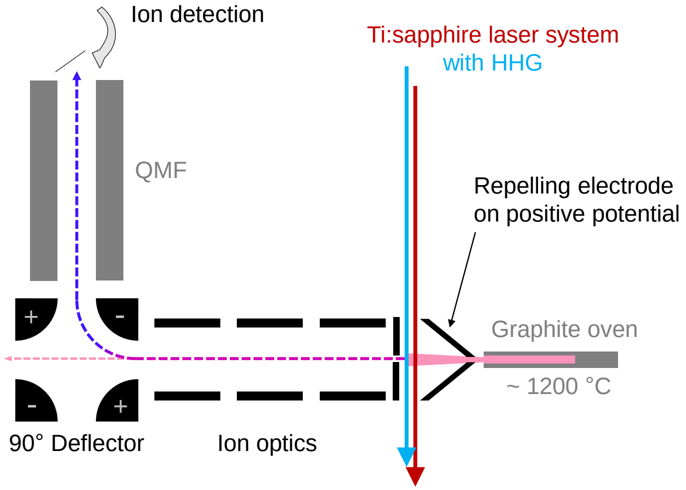

FIG. 3: (Color online) Schematic drawing of the Mainz Atomic Beam Unit. After passing a positive electrode which suppresses surface ions from the resistively heated atomic beam oven, the neutral species reach the interaction region where the Cu atoms are resonantly ionized. The isotopic selection in front of the ion detection is achieved by a commercial quadrupole mass filter.

broadening of the residual thermal velocity distribution in the laser beam direction, caused by the opening angle of the neutral atom beam effusing from the oven into the interaction region. This was estimated to be $\approx 15\,^\circ$, limited by the angular acceptance of the subsequent ion optics and the quadrupole mass filter.

B. Laser System

For production of the powerful and broadly tunable laser radiation required for RIS, we used the well established high repetition rate Ti:sapphire laser system in combination with single pass higher harmonic generation, both developed at the University of Mainz. Installation of an additional thick solid etalon in the standing wave z-shaped laser cavity enhances the spectral mode selection and reduces the spectral linewidths, i.e. the full width at half maximum (FWHM), from the standard value of typically 5 GHz down to about 1 GHz [20, 21]. Due to the overall cavity length, this corresponds to a total number of about 6 oscillating longitudinal cavity modes. All 2D maps for both isotopes ^{63,65}Cu were scanned by using two of these narrowband Ti:sapphire lasers for first and second step.

As the hyperfine splitting in atomic transitions is most often smaller than 1 GHz, further reduction of the spectral laser linewidth is desirable. Correspondingly, it is essential to lower the number of oscillating cavity modes down to an optimum of only one single mode. Unfortunately, any standing wave cavity suffers from spatial hole burning in the gain medium, which enforces the build-up of multiple longitudinal cavity modes through mode competition or beating [25–27]. In contrary, a ring cavity lets the light wave travel along the longitudinal direction and deplete the inversion over the entire path inside the gain medium. This concept prevents spatial hole burning and is implemented in single longitudinal mode lasers also including injection locked lasers, which pulse amplify the narrowband light of an external continuous wave single mode laser source. Injection-locked systems on the basis of such a ring cavity Ti:sapphire laser have demonstrated linewidths of pulsed high repetition rate radiation of 20 MHz and below [28, 29], which is close to the Fourier limit, i.e. the natural linewidth limit for laser light pulses of finite duration.

The most recent laser development at Mainz University makes use of the benefits of a single mode Ti:sapphire laser cavity while avoiding the substantial costs, complexity and restrictions which are associated with a dedicated master laser and an injection locking setup. As an alternative, Fig. 4 shows the layout of a bow tie shaped single mode Ti:sapphire laser prototype which was set up recently and is here in use for the first time for high resolution RIS. The mirror set, a Lyot filter and a thin etalon provide the initial frequency selection. Final, precise mode selection is achieved by a tunable air-spaced etalon and by accordingly tuning the cavity length through an actively controlled piezo-driven mirror. To suppress the unwanted of the two possible propagation directions inside the ring cavity, a surface reflection from a wedged glass plate in one of the exiting beam paths is reflected back into the cavity. This 0.8 % feedback increases the power in the desired propagation direction by nearly a factor of two to 2.5 W, while reducing the power of the other direction down to about 60 mW. Possible disturbing etalon effects due to this method were not experienced. The usual approach to use a conventional optical diode based on a Faraday rotator was as well successfully tested in this cavity, but led to significantly reduced output power.

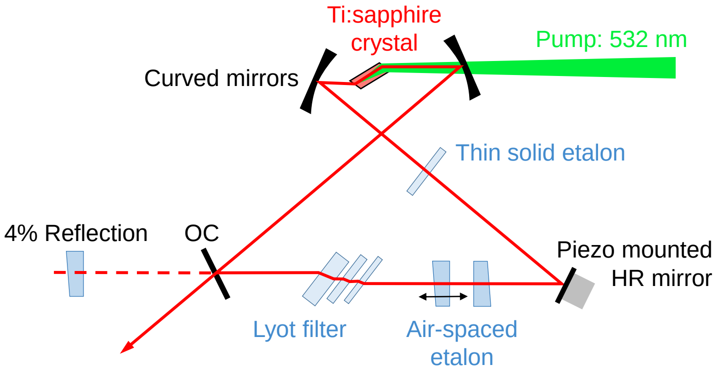

FIG. 4: (Color online) Ring cavity layout: The frequency selective elements in blue (lightest gray) consist of a 3-stage Lyot filter, a solid etalon and a tunable air-spaced etalon to achieve selection of a single cavity mode, which can be tuned by the piezo mounted high reflective (HR) mirror. Suppression of one light propagation direction is achieved by a retroreflecting surface behind the output coupler (OC).

The finally achieved spectral linewidth was analyzed using a commercial scanning Fabry-Pérot interferometer (FPI) with a free spectral range (FSR) of 4 GHz. The observed fringes in Fig. 5 show a linewidth (FWHM) of 45 MHz, whereas the intrinsic laser linewidth is even smaller, as a significant part of the fringe width is induced by the finite finesse of the FPI itself, which could not be measured precisely.

The laser is pumped by a conventional 10 kHz frequency doubled Nd:YAG with a typical pump power of 15 W, whereby it fits perfectly into the existing Ti:sapphire system. Output powers of up to 1 W in single mode operation were obtained. The spatial beam profile is slightly superior compared to that of a standard z-shaped cavity, which allows better beam transport and focusing into the interaction region of the MABU. The resulting high spectral power density is too large for most optical excitation steps of interest and has to be lowered to prevent power broadening.

There are a number of advantages associated with this laser design, which makes it especially well suitable for high resolution RIS. As for the standard laser design, the typical Ti:sapphire lasing range from 690 nm to 950 nm is covered. Almost all mechanical and optical parts as well as the water cooling are interchangeable and fully compatible to the existing laser system. Lacking the need of a master laser system, the laser's footprint of 50x30 cm^2 is quite compact and allows direct exchange to a standard Ti:sapphire laser, easy transport, as well as multiple single mode cavities installed on one standard optical table.

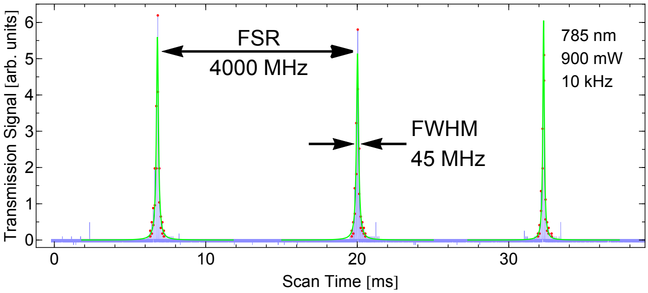

FIG. 5: (Color online) Spectral linewidth of the single mode Ti:sapphire laser observed with a scanning FPI. One scan cycle is shown, with Lorentzian profiles in green full lines fitted to the maxima of each laser pulse, shown as red dots. The fringes show a FWHM of just 45 MHz, which is an upper limit for the real laser linewidth.

During the measurements, wavelength readout was done using a High Finesse WS6 wavemeter. The scanning FPI provided relative frequency information and visible inspection of the spectral mode pattern of the laser radiation, easily revealing occasionally arising side modes. Due to the fact that the necessary automated stabilization and scanning system was not yet operational, wavelength scans and readjustments were carried out manually by continuous optimization of the length of laser cavity and air-spaced etalon by the built-in piezo actuators. As microscopic mechanical vibrations of the cavity are unavoidable and the only spectral feedback is obtained from the FPI fringes on an oscilloscope screen, this manual stabilization sometimes failed for up to a second. This produced occasional appearance of neighboring cavity modes with a frequency distance of exactly one FSR of 440 MHz. Ongoing developments aim to prevent these incidents through installation of a dedicated electronic stabilization and tuning system, which is based on power feedback and stabilization routines adapted from continuous wave laser systems.

IV. RESULTS

A. Single-resonance scans

A typical example of a single-resonance scan along the two-step excitation scheme I of Fig. 2, as obtained in this work, is shown in Fig. 6. In total, 36 of these scans were recorded for ^{63}Cu, and 8 for ^{65}Cu. A typical scan takes about one minute to complete. In all cases, a frequency tripled double etalon z-cavity laser was used for the first step and a standard broadband laser was used for the second step, leading to ionization. In the first step, an experimental linewidth of about 3 GHz was obtained. The blue circles are the experimental data, while the solid red line is the best fit, described below. The dashed lines show the underlying hyperfine structure components (green indicates transitions from the $F = 1$, black the transitions from the $F = 2$ ground state component, respectively).

The analysis was performed by fitting the experimental data with a sum of pseudo-Voigt profiles centered at the resonance positions according to equation 2. These pseudo-Voigt profiles represent an excellent approximation to the full Voigt profile, but with reduced computational cost [30]. The pseudo-Voigt profile with a HWHM of w is defined by

$$V(x) = \eta \cdot L(x) + (1-\eta) \cdot G(x) \qquad (0 < \eta < 1), \tag{4}$$

$$G(x) = \sqrt{\frac{\ln(2)}{\pi}} \frac{1}{w} \exp\left[-\ln(2) \cdot \left(\frac{x - x_0}{w} \right)^2 \right] \tag{5}$$

$$L(x) = \frac{1}{\pi w} \frac{1}{1 + (\frac{x-x_0}{w})^2}, \tag{6}$$

The hyperfine A parameters for both the ground state and the first excited state and the B parameter for the excited state are free fitting parameters. Other free parameters are the FWHM of the pseudo-Voigt profiles and the intensities of the distinguishable peaks. To reduce the correlation of the fit parameters and to avoid convergence to unphysical intensity ratios (e.g. the scenario in which the intensity of one of the peaks converges to zero), the relative intensities of the three overlapping peaks were fixed to theoretical expectation. Despite our observation that the intensity ratios of the three distinguishable peaks do not exactly match those predicted by equation 3, it is still a decent approximation, although it

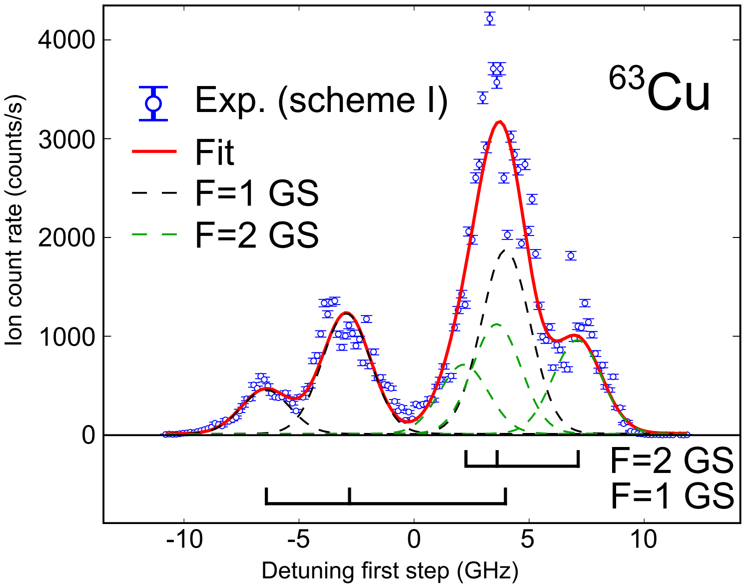

FIG. 6: (Color online) Frequency scan using RIS scheme I. The blue dots are the experimental data, the full red line is the best fitting model (as described in the main body of the text). The dashed lines show the individual hyperfine components obtained by the fit, in green (light gray) for transitions starting from the $F = 1$ ground state component, in black for $F = 2$. They are also indicated below the figure.

can introduce systematic problems in the analysis. This will be discussed in section IV D, along with the analysis results.

B. Double-resonance scanning maps

An example of a 2D double-resonance map for ^{63}Cu is shown in the top figure of Fig. 7. In the central part it shows the logarithm of the count rate as a function of the frequency of both lasers during their scans across the first and second excitation step of the three step RIS scheme II of Fig. 2. The first step was excited with a frequency tripled output of a double etalon z-cavity laser, while the second step was addressed by the fundamental output of a second double etalon z-cavity laser. Experimental linewidths of 3 GHz in the first and

1.5 GHz in the second step were obtained. White areas indicate that either no ions were detected for these laser frequencies, or that this frequency region was not scanned to keep the measuring time reasonable. In detail the map was obtained by scanning the first step laser along a given frequency interval, increasing the wavelength of the second laser by a step of 300 MHz, and then repeating the procedure until the required ranges were covered (typically about 50 times). A full map therefore typically takes 45 minutes to complete (one minute per step). This whole cycle was repeated six times for ^{63}Cu and five times for ^{65}Cu, resulting in eleven full maps in total. In contrast to the single-resonance scans, the splitting of the ground state and first excited state are clearly resolved. The six transitions from the ground state doublet to the first excited multiplet are well separated horizontally, while the hyperfine splitting of the second excited state is still too small to produce a suitable splitting up of the peaks along the vertical axis.

The exact 2D lineshapes in coherent double-resonance ionization spectroscopy can be calculated using the density matrix formalism (as described in e.g. [22] and references therein). A detailed description and simulation of the lineshapes was not attempted here, as for our experimental conditions, the lineshapes are well approximated by bivariate Gaussian distributions. These two-dimensional profiles have two width parameters, both of which are free fit parameters. Once again, the intensity ratios of the unresolved peaks (due to the small A of the $3d^{10}6s\ ^2S_{1/2}$ state) had to be fixed to the theoretical predictions (equation 3).

The bottom plot in Fig. 7 shows horizontal slices of the full 2D map of Fig. 7 along the frequency tuning of the first step, made during analysis. The vertical positions represent the corresponding detuning of the second step laser. This representation highlights that individual hyperfine components of the first step may be properly selected or, equivalently, peaks may be suppressed from the scan via proper frequency selection of the second step. Symbols represent the experimental data, the solid lines are obtained by similarly slicing the best fitting 2D hyperfine surface. The ability to suppress or specifically select components of the HFS strongly enhances the significance of the analysis of hyperfine spectra, since ambiguities introduced by fitting of overlapping peaks completely disappear. The results from the fits are presented and discussed in section IV.

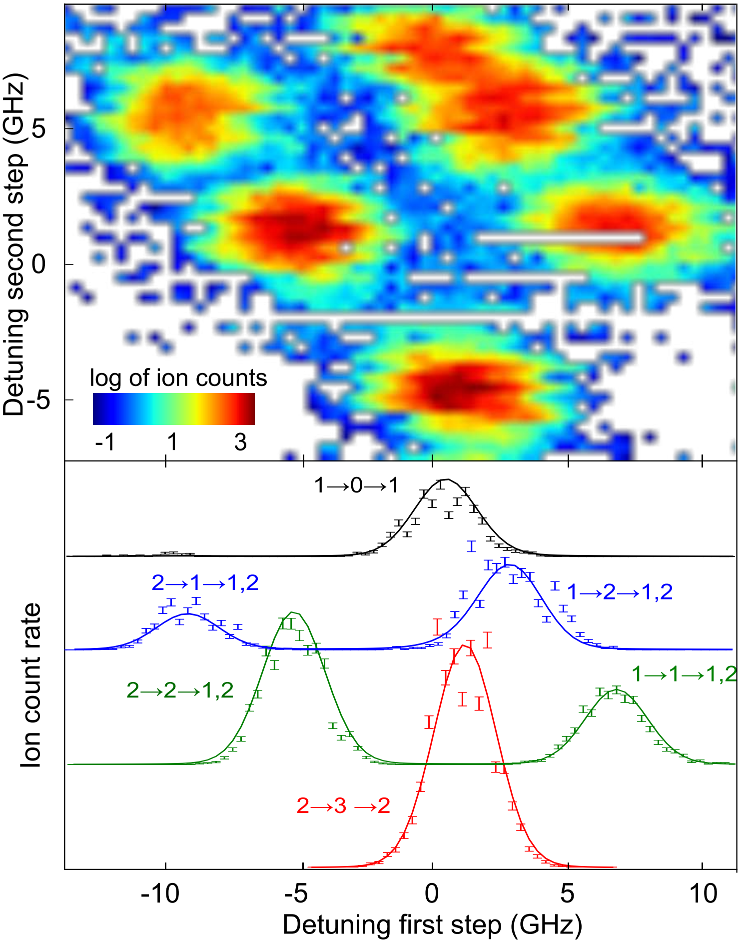

FIG. 7: (Color online) Top: 2D map obtained with two double etalon z-cavity lasers using RIS scheme II. The logarithm of the ion rate is plotted as function of the detuning of the first step (horizontal) and the second step (vertical). Bottom: Horizontal slices of the 2D-map. Symbols are the experimental points, the solid lines are the best fitting curves.

C. High-resolution single mode laser scans

In Fig. 6 and Fig. 7, three alternative ways of studying the atomic hyperfine structure are given, either using single-resonance scanning, full 2D mapping, or by scanning only selected slices of the 2D map. Hereby, a (possibly coarser) 2D map is used just to determine which frequency ranges should be scanned thoroughly in one dimension, significantly reducing the time needed to obtain conclusive information on the HFS. This aspect is particular of relevance for studying exotic isotopes far off stability. Fig. 8 takes this idea one step further by scanning narrow regions in the 2D map with a higher resolution laser system. The time required to collect six slices through the 2D map is of the order of an hour for the present working conditions. This scanning time is expected to decrease to a few minutes for an automated stabilization routine.

The high-resolution scans of the second excitation step in Fig. 8 were performed with the single mode ring cavity laser, while a double etalon z-cavity laser was used for the first transition. Each scan represents a slice through one of the structures in the 2D map. Once again, symbols indicate experimental data, while solid lines are the best fitting curves. It is obvious that the linewidth in the spectrum has decreased significantly due to the much smaller spectral linewidth of the single mode laser, to the point where the splitting of the $3d^{10}6s^2S_{1/2}$ can now be resolved; all six expected peaks can clearly be seen (see also Fig. 2). As pointed out earlier, due to the manual frequency scanning and stabilization of the ring laser, occasionally mode competition occurred. While the frequency of the dominating mode is read out by the wavemeter, a neighboring mode with a frequency distance of ± one free spectral range of the single mode cavity may also oscillate at small intensity, which is already enough to generate significant ionization at the corresponding resonant spectral position. As a consequence, some weak side-mode peaks of varying intensities were observed in the spectra, as visible e.g. , in the blue graph in Fig. 8. To ensure that these artificial structures do not influence the extraction of the correct resonance positions, this aspect was considered in the fitting routine.

The experimentally observed total linewidth (defined as the FWHM of the best fitting Gaussian profile) achieved with the single mode ring laser is 150(3) MHz. The increase with respect to the fundamental laser linewidth is caused by the residual Doppler broadening due to the opening angle of the atomic beam leaving the hot oven (See section III A). For stable

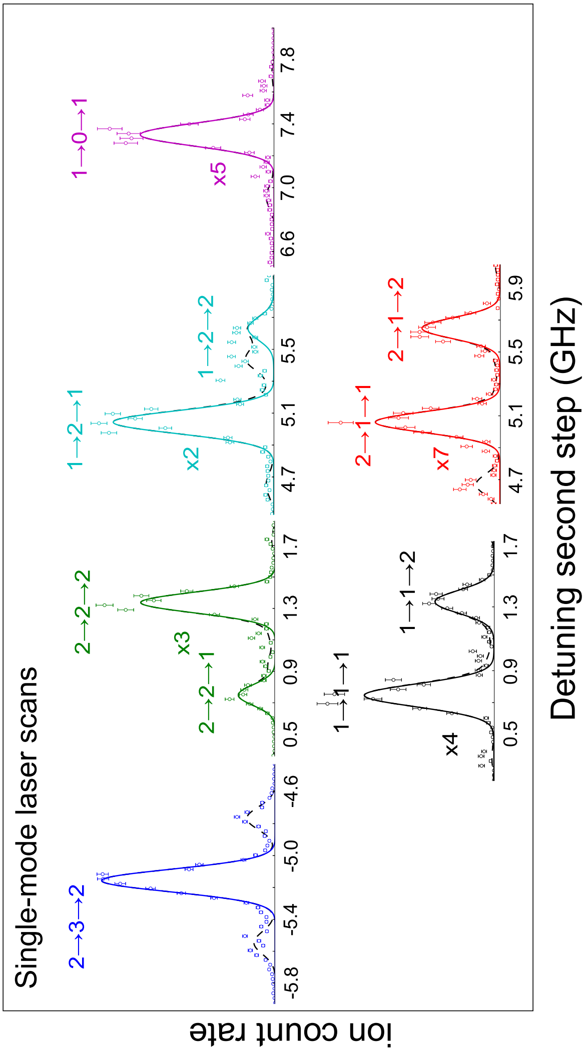

FIG. 8: (Color online) Vertical slices through map Fig. 7, obtained with the single-mode laser, one scan for each of the structures in the 2D map. Dashed lines indicate the fitted function including possible side modes. The labels near the peaks display the angular momenta F of the states involved in the RIS process for each pathway.

Cu with a Boltzmann velocity distribution corresponding to 1200 °C and a laser linewidth of

45 MHz (Fig. 5) the total linewidth can be estimated by the convolution of both distributions to be around

$$\sqrt{w_{\mathrm{Doppler}}^2 + w_{\mathrm{Laser}}^2} = 150\,\mathrm{MHz} \tag{7}$$

which fits consistently to the experimental data.

D. Analysis

For investigating and visualizing the statistics and the achievable precision in different measurements, Fig. 9 presents the distribution of the hyperfine parameters A obtained from the best fit in two correlation charts. Red data points correspond to ^{63}Cu, blue to ^{65}Cu.

Fig. 9a displays the distribution of the fitted hyperfine A parameter of the ground and first excited state for both stable Cu isotopes for the 44 measurements for ^{63}Cu and ^{65}Cu in single-resonance ionization. Note, aside of the large scattering of data, the significant positive correlation of these two fitting parameters. The scatter can be attributed to the inability of properly assigning and fitting the unresolved peak structure. The positive correlation and the resulting over-estimation of the hyperfine parameter specifically occurs for ^{63}Cu, where it may be related to multimode operation of the laser at the edges of the scan range.

Fig. 9b shows the same plot with identical scaling for the 11 double-resonance maps which were taken for the two stable copper isotopes. Scattering of the data as well as the size of the error bars is reduced. In addition, the positive correlation between the A-factors as well as the trend to incorrect large values as compared literature has completely vanished. Maximum deviations of up to 200 MHz were observed in individual scans for the value of A_{GS}, which correspond to less than 10 % of the experimental linewidths and may be caused easily by the occurrence of non symmetrical line shapes due to instabilities of the measuring process. The splitting of the second excited, highest lying bound state of RIS scheme II could also be extracted from the analysis of the 2D maps.

The graphs also include the weighted average of all N independent hyperfine scans, defined as

$$\mu = \frac{\sum_{i=1}^{N} x_i/\sigma_i^2}{\sum_{i=1}^{N} 1/\sigma_i^2}, \tag{8}$$

which are colored in black and are given quantitatively in Table I. In the absence of systematic errors the data points should be statistically distributed with a spreading corresponding to their individual variances σ_i^2. In this case the variance on the weighted mean can be calculated as

$$\sigma^2 = \frac{1}{\sum_i^N \sigma_i^{-2}}. \tag{9}$$

Fig. 9a shows that the individual x_i scatter significantly more than the variances σ_i^2, which leads to underestimated variances of the corresponding weighted averages. Given this large scatter, a better estimate for the variance of the weighted mean can be obtained by scaling σ^2 with the reduced χ^2 to obtain the corrected variance on the weighted mean σ^2_{corr}:

$$\sigma^2_{\text{corr}} = \frac{1}{\sum_i^N \sigma_i^{-2}} \frac{1}{N-1} \sum_i^N \frac{(x_i - \mu)^2}{\sigma_i^2}, \tag{10}$$

This corrected variance is quoted in Table I as the final uncertainty on the extracted hyperfine parameters.

The origin of the large observed scatter can be attributed to the presence of three unresolved peaks underneath a large central peak, as explained in section IV A. During the fitting procedure, there are 11 free parameters (6 free intensities, 3 hyperfine parameters, a shared linewidth and the centroid), many of which will strongly correlate; because three of the six peaks are not resolved, the fit is underdefined. For example, changes in the excited state $A_{P,3/2}$-parameter can be compensated for by changes in e.g the $B_{P,3/2}$ parameter, or any of the other fit parameters. Fixing the relative intensities to the theoretical predictions (3) reduces the number of fit parameters. However, this can introduce possible systematic deviations in the extracted hyperfine parameters, since the actual intensity ratios depend on the laser powers (which vary between measurements). These difficulties in the analysis motivated the alternative approaches and developments presented in this article. This higher precision and less scatter is due to the fact that each of the collected maps contains on average ten times more counts than a single 1D scan, but more importantly that all HFS peaks are resolved and so the fit parameters are not correlated. Correspondingly, it results also in much smaller σ^2_{corr}. Finally, the analysis of the high-resolution ring laser scans obviously yields most precise values for the hyperfine parameters.

Finally, Fig. 10 shows a corresponding scatter plot of the hyperfine parameters $A_{S,1/2}$ versus $A_{P,3/2}$ (red for ^{63}Cu, blue for ^{63}Cu) of the second excitation step. The green circles in Fig. 10 show the values obtained for both isotopes with the single-mode ring laser. As technical difficulties limited the number of measurements with the single mode laser prototype,

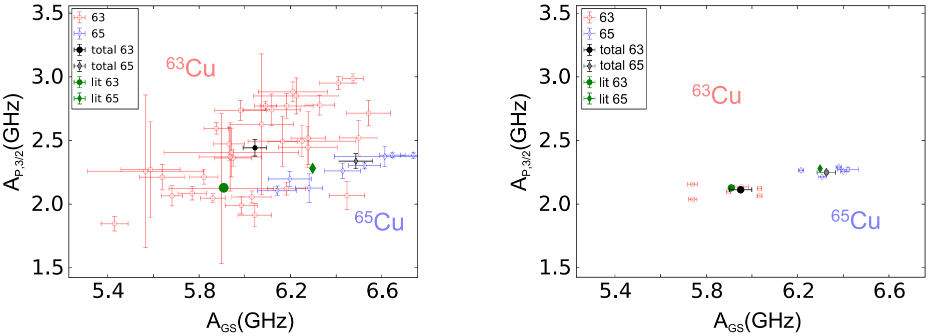

(a) (Color online) Results of A_{GS} and $A_{P,3/2}$ for the single-resonance measurements.

(b) (Color online) Results of A_{GS} and $A_{P,3/2}$ for the double-resonance measurement.

FIG. 9: Distribution of the hyperfine parameters A of the atomic ground state and first excited state obtained by applying the fitting procedure outlined in the main text. Red circles are the results for ^{63}Cu, blue diamonds are for ^{65}Cu. The black circles and gray diamonds represent the weighted average and uncertainty for ^{63}Cu and ^{65}Cu respectively. The green circles and diamonds represent the literature values for ^{63}Cu and ^{65}Cu respectively.

only one complete measurement for each isotope was made, which prevents calculation of statistical quantities like σ_{corr}. As the scatter in Fig. 9 and Fig. 10 clearly shows, σ typically underestimates the correct measurement uncertainty. The slice scans with the single mode laser might be similarly affected by the imperfections discussed above, but as the peaks are much better resolved than in the double-resonance method, this method should lead to even smaller σ_{corr} when compared to the initial σ. To determine a conservative final uncertainty value for the single single-mode measurements, σ was multiplied with the mean of the ratios $\sigma_{\mathrm{corr}}/\sigma$ obtained for the double-resonance method. A more detailed understanding of the single-mode laser measurement and its uncertainties will require further systematic measurements, which will be performed in future work.

The hyperfine parameters extracted from the single mode laser scans are also listed in Table I. All individual A and B parameters, as extracted from the up to three different measurement approaches, generally are in good agreement to each other in the size of their

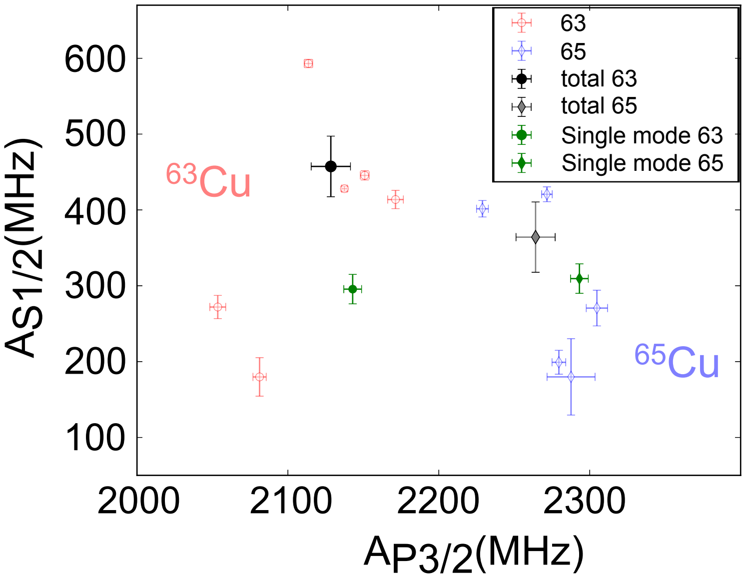

FIG. 10: (Color online) Results of $A_{P,3/2}$ and $A_{S,1/2}$ for the double-resonance ionization measurement. Red circles are the results for ^{63}Cu, blue diamonds are for ^{65}Cu. The black circles and grey diamonds represent the weighted average and uncertainty for ^{63}Cu and ^{65}Cu respectively. Green circles and diamonds represent the results from the single mode laser scans for ^{63}Cu and ^{65}Cu respectively.

individual error bars. The comparison to the literature values, which at least for the ground state are extremely precise, does not yield any direct disagreement either, except for the values for $A_{S,1/2}$ of the second excited level: 296(18) MHz and 307(18) MHz were obtained for respectively ^{63}Cu and ^{65}Cu. These values are in disagreement with the literature values from [31]. The experiment described in that article, which was initially not dedicated to spectroscopy, does not include a mass separation stage, which in combination with the obtained experimental linewidths (which lie between 1.8 and 3.6 GHz), may have hindered correct analysis of the hyperfine structure.

The uncertainties on all hyperfine parameters are of a similar order of magnitude for both isotopes, despite the larger natural abundance of ^{63}Cu. This illustrates that, while increased statistics do increase the precision on the extracted values, they do not reduce scattering

^{63}Cu	Method	A_{GS}	$A_{P,3/2}$	$B_{P,3/2}$	$A_{S,1/2}$
	Single-Resonance	6000(51)	2452(65)	30(61)	—
	Double-Resonance	5906(46)	2128(12)	-100(18)	458(35)
	Single-Mode	—	2143(6)	-33(18)	296(18)
	Literature [31–33]	5866.908706(20)	2140.0(23)	-37.9(2)	1348(100)

^{65}Cu	Method	A_{GS}	$A_{P,3/2}$	$B_{P,3/2}$	$A_{S,1/2}$
	Single-Resonance	6343(73)	2348(59)	-70(62)	—
	Double-Resonance	6275(39)	2264(12)	-60(33)	364(43)
	Single-Mode	—	2293(6)	-55(18)	307(18)
	Literature [32, 33]	6284.389972(60)	2292.3(25)	-35.0(2)	—

TABLE I: Fitted hyperfine parametes with final uncertainty estimates for both isotopes and each method in comparison to literature values (All values in MHz). Only the first excited level is sensitive to electic quadrupole splitting.

of the extracted values around their mean, and therefore do not result in significantly reduced weighted uncertainties. The uncertainties on the hyperfine $B_{P,3/2}$ parameters for both isotopes are rather large due to the reduced sensitivity to the B parameter: according to equation 2, the HFS splitting is up to a factor 11 less sensitive to $B_{P,3/2}$ than to $A_{P,3/2}$ (depending on the specific transition).

V. CONCLUSIONS AND OUTLOOK

High-resolution double resonance ionization mapping was performed on stable Cu isotopes using the Mainz atomic beam unit and the laser light produced by high-resolution pulsed Ti:sapphire lasers. These measurements also included the first application of a newly developed ring cavity prototype, demonstrating a total linewidth below 50 MHz, which is well suited for high resolution studies.

The hyperfine parameters of the $3d^{10}4s\ ^2S_{1/2}$ ground state and the $3d^94s4p\ ^4P^o_{3/2}$ levels were extracted and are consistent with literature. The hyperfine parameters of $3d^{10}6s\ ^2S_{1/2}$ were extracted with better precision and higher reliability than in literature. The 2D double-resonance mapping technique proved particularly useful for resolving the individual components of complex and possibly overlapping hyperfine structures and resulted in reduced correlations in the fitting process, which allowed precise extraction of hyperfine parameters with smallest errors. Furthermore, the information provided by the double-resonance maps allowed selection of narrow ring laser scan regions, making these scans very time-efficient. These high-resolution scans could fully resolve the splitting of the second excited state.

Still remaining scattering of data is attributed to the currently used manual frequency stabilization and control system of the ring laser. These aspects are the central part of ongoing development by adapting state-of-the art control techniques to this cavity design.

We conclude that the 2D double-resonance mapping method is ideally suited for cases in which the components of the hyperfine spectrum are poorly or not at all resolved, in particular when high precision is required. The ability to disentangle complex hyperfine structures in a second dimension predestines the method for use in laser spectroscopy on exotic nuclei, where it could help to identify which peaks belong to isomeric states and which belong to the nuclear ground state. While for such applications, data taking for a full 2D map could be too time-consuming, measurement time can however be significantly reduced by only scanning well selected slices of the hyperfine map, as we have illustrated here.

VI. ACKNOWLEDGMENTS

Fruitful discussions with K.T. Flanagan are gratefully acknowledged. This work was supported by the BriX IAP Research Program No. P7/12 and FWO-Vlaanderen (Belgium), GOA 15/010 from KU Leuven and Bundesministerium für Bildung und Forschung.

[1] B. Cheal and K. T. Flanagan, Journal of Physics G: Nuclear and Particle Physics **37**, 113101 (2010).

[2] K.-R. Anton, S. L. Kaufman, W. Klempt, G. Moruzzi, R. Neugart, E. W. Otten, and B. Schinzler, Physical Review Letters **40**, 642 (1978).

[3] B. Schinzler, W. Klempt, S. L. Kaufman, H. Lochmann, G. Moruzzi, R. Neugart, E.-W. Otten, J. Bonn, L. Von Reisky, K. P. C. Spath, J. Steinacher, and D. Weskott, Physics Letters **79B**, 209 (1978).

[4] A. Nieminen, P. Campbell, J. Billowes, D. H. Forest, J. A. R. Griffith, J. Huikari, A. Jokinen, I. D. Moore, R. Moore, G. Tungate, and J. Äystö, Physical Review Letters **88**, 094801 (2002).

[5] V. N. Fedosseev, Y. Kudryavtsev, and V. I. Mishin, Physica Scripta **85**, 058104 (2012).

[6] B. A. Marsh, B. Andel, A. Andreyev, S. Antalic, D. Atanasov, A. Barzakh, B. Bastin, C. Borgmann, L. Capponi, T. E. Cocolios, T. Day Goodacre, M. Dehairs, X. Derkx, H. De Witte, D. Fedorov, V. N. Fedosseev, G. Focker, D. Fink, K. T. Flanagan, S. Franchoo, L. Ghys, M. Huyse, N. Imai, Z. Kalaninova, U. Köster, S. Kreim, N. Kesteloot, Y. Kudryavtsev, J. Lane, N. Lecesne, V. Liberati, D. Lunney, K. M. Lynch, V. Manea, P. L. Molkanov, T. Nicol, D. Pauwels, L. Popescu, D. Radulov, E. Rapisarda, M. Rosenbusch, R. E. Rossel, S. Rothe, L. Schweikhard, M. D. Seliverstov, S. Sels, A. Sjödin, V. Truesdale, C. Van Beveren, P. Van Duppen, K. Wendt, F. Wienholtz, R. Wolf, and S. Zemlyanoy, Nuclear Instruments and Methods in Physics Research Section B: Beam Interactions with Materials and Atoms **317**, 550 (2013).

[7] T. Gottwald, C. Geppert, F. Schwellnus, K. Wies, K. Wendt, Y. Liu, C. Baktash, J. R. Beene, C. Havener, H. Krause, D. Schultz, D. Stracener, C. Vane, T. Kessler, and B. Tordoff, Nuclear Instruments and Methods in Physics Research Section B: Beam Interactions with Materials and Atoms **266**, 4398 (2008).

[8] A. Teigelhöfer, P. Bricault, O. Chachkova, M. Gillner, J. Lassen, J. P. Lavoie, R. Li, J. Meiß ner, W. Neu, and K. D. A. Wendt, Hyperfine Interactions **196**, 161 (2010).

[9] K. T. Flanagan, P. Vingerhoets, M. Avgoulea, J. Billowes, M. L. Bissell, K. Blaum, B. Cheal, M. DeRydt, V. N. Fedosseev, D. H. Forest, C. Geppert, U. Koster, M. Kowalska, J. Kramer, K. L. Kratz, A. Krieger, E. Mane, B. A. Marsh, T. Materna, L. Mathieu, P. L. Molkanov, R. Neugart, G. Neyens, W. Nortershauser, M. D. Seliverstov, O. Serot, M. Schug, M. A. Sjoedin, J. R. Stone, N. J. Stone, H. H. Stroke, G. Tungate, D. T. Yordanov, and Y. M. Volkov, Physical Review Letters **103**, 142501 (2009).

[10] K. T. Flanagan, P. Vingerhoets, M. L. Bissell, K. Blaum, B. A. Brown, B. Cheal, M. De Rydt, D. H. Forest, C. Geppert, M. Honma, M. Kowalska, J. Krämer, A. Krieger, E. Mané, R. Neugart, G. Neyens, W. Nörtershäuser, M. Schug, H. H. Stroke, and D. T. Yordanov, Physical Review C **82**, 041302 (2010).

[11] P. Vingerhoets, K. T. Flanagan, M. Avgoulea, J. Billowes, M. L. Bissell, K. Blaum, B. A. Brown, B. Cheal, M. De Rydt, D. H. Forest, C. Geppert, M. Honma, M. Kowalska, J. Krämer,

A. Krieger, E. Mané, R. Neugart, G. Neyens, W. Nörtershäuser, T. Otsuka, M. Schug, H. H. Stroke, G. Tungate, and D. T. Yordanov, Physical Review C **82**, 064311 (2010).

[12] T. Cocolios, A. Andreyev, B. Bastin, N. Bree, J. Büscher, J. Elseviers, J. Gentens, M. Huyse, Y. Kudryavtsev, D. Pauwels, T. Sonoda, P. Van den Bergh, and P. Van Duppen, Physical Review Letters **103**, 102501 (2009).

[13] T. E. Cocolios, A. N. Andreyev, B. Bastin, N. Bree, J. Büscher, J. Elseviers, J. Gentens, M. Huyse, Y. Kudryavtsev, D. Pauwels, T. Sonoda, P. V. D. Bergh, and P. Van Duppen, Physical Review C **81**, 014314 (2010).

[14] U. Köster, N. J. Stone, K. T. Flanagan, J. R. Stone, V. N. Fedosseev, K. L. Kratz, B. A. Marsh, T. Materna, L. Mathieu, P. L. Molkanov, M. D. Seliverstov, O. Serot, A. M. Sjödin, and Y. M. Volkov, Physical Review C **84**, 034320 (2011).

[15] T. J. Procter, H. Aghaei-Khozani, J. Billowes, M. L. Bissell, F. L. Blanc, B. Cheal, T. E. Cocolios, K. T. Flanagan, H. Hori, T. Kobayashi, D. Lunney, K. M. Lynch, B. a. Marsh, G. Neyens, J. Papuga, M. M. Rajabali, S. Rothe, G. Simpson, a. J. Smith, H. H. Stroke, W. Vanderheijden, and K. Wendt, in *Journal of Physics: Conference Series*, Vol. 381 (2012) p. 012070.

[16] K. M. Lynch, J. Billowes, M. L. Bissell, I. Budincevic, T. E. Cocolios, R. P. de Groote, S. De Schepper, V. N. Fedosseev, K. T. Flanagan, S. Franchoo, R. F. Garcia Ruiz, H. Heylen, B. A. Marsh, P. J. R. Mason, G. Neyens, T. J. Procter, R. E. Rossel, S. Rothe, G. S. Simpson, A. J. Smith, I. Strashnov, H. H. Stroke, P. M. Walker, K. D. A. Wendt, and R. T. Wood, EPJ Web of Conferences **01007**, 2 (2013).

[17] T. E. Cocolios, H. H. Al Suradi, J. Billowes, I. Budinčević, R. de Groote, S. De Schepper, V. N. Fedosseev, K. T. Flanagan, S. Franchoo, R. Garcia Ruiz, H. Heylen, F. Le Blanc, K. M. Lynch, B. A. Marsh, P. J. R. Mason, G. Neyens, J. Papuga, T. Procter, M. M. Rajabali, R. E. Rossel, S. Rothe, G. Simpson, A. Smith, I. Strashnov, H. H. Stroke, D. Verney, P. M. Walker, K. Wendt, and R. Wood, Nuclear Instruments and Methods in Physics Research Section B: Beam Interactions with Materials and Atoms **317**, 565 (2013).

[18] I. Budinčević, J. Billowes, M. L. Bissell, T. E. Cocolios, R. P. de Groote, S. De Schepper, V. N. Fedosseev, K. T. Flanagan, S. Franchoo, R. F. Garcia Ruiz, H. Heylen, K. M. Lynch, B. A. Marsh, G. Neyens, T. J. Procter, R. E. Rossel, S. Rothe, I. Strashnov, H. H. Stroke, and K. D. A. Wendt, Physical Review C **90**, 014317 (2014).

[19] K. T. Flanagan, K. M. Lynch, J. Billowes, M. L. Bissell, I. Budinčević, T. E. Cocolios, R. P. de Groote, S. De Schepper, V. N. Fedosseev, S. Franchoo, R. F. Garcia Ruiz, H. Heylen, B. A. Marsh, G. Neyens, T. J. Procter, R. E. Rossel, S. Rothe, I. Strashnov, H. H. Stroke, and K. D. A. Wendt, Physical Review Letters **111**, 212501 (2013).

[20] V. N. Rothe, Sand Fedosseev, T. Kron, B. A. Marsh, R. E. Rossel, and K. Wendt, Nuclear Instruments and Methods in Physics Research Section B: Beam Interactions with Materials and Atoms **317, Part B**, 561 (2013).

[21] V. Sonnenschein, I. D. Moore, H. Khan, I. Pohjalainen, and M. Reponen, Hyperfine Interactions , 1 (2014).

[22] B. A. Bushaw, W. Nortershauser, and K. Wendt, Spectrochimica Acta Part B **54**, 321 (1999).

[23] A. Hakimi, *PhD Thesis* (Univ., Mainz, 2013).

[24] J. Roßnagel, S. Raeder, A. Hakimi, R. Ferrer, N. Trautmann, and K. Wendt, Phys. Rev. A **85**, 012525 (2012).

[25] C. L. Tang, H. Statz, and G. deMars, Journal of Applied Physics **34**, 2289 (1963).

[26] T. Kimura, K. Otsuka, and M. Saruwatari, Quantum Electronics, IEEE Journal of **7**, 225 (1971).

[27] J. J. Zayhowski, Opt. Lett. **15**, 431 (1990).

[28] T. Kessler, H. Tomita, C. Mattolat, S. Raeder, and K. Wendt, Laser Physics **18**, 842 (2008).

[29] S. Hannemann, E.-J. van Duijn, and W. Ubachs, Review of Scientific Instruments **78**, 103102 (2007).

[30] T. Ida, M. Ando, and H. Toraya, Journal of Applied Crystallography **33**, 1311 (2000).

[31] B. Ankush and M. Deo, Journal of Quantitative Spectroscopy and Radiative Transfer **134**, 21 (2014).

[32] H. Figger, D. Schmitt, and S. Penselin, Colloq. Int. C. N. R. S. **164** (1967).

[33] H. Bucka, J. K. Ney, and P. Wirtnik, Zeitschrift für Physik **202**, 22 (1967).

4.3 Final choice of ionization scheme

Based on the findings presented in this chapter so far, the ionization scheme that would be used for the main results on this thesis had to be chosen. Figure 4.4 shows an optimized version of the scheme used in section 4.1 and the suggested scheme for the 249.2146 nm line. Note that a three step scheme is required for the scheme with the $3d^{10}4p\ {}^2P^\circ_{3/2}$ line, since otherwise the UV second laser step could lead to non-resonant ionization of potential low-ionization ion beam contaminants.

Advantages and disadvantages of exciting to the $3d^9({}^2D)4s4p\,({}^3P^\circ)\ {}^4P^\circ_{3/2}$ state are:

+ larger hyperfine splitting parameters
+ longer lifetime, facilitating delayed ionization
+ Easily produced second step to an auto-ionizing resonance
- Requires frequency tripled light
- Unknown mass and field shift parameter

Advantages and disadvantages of exciting to the $3d^{10}4p\ {}^2P^\circ_{3/2}$ state are:

+ Well studied, with previous work on the mass and field shift parameter
+ Only requires frequency doubled light
- CRIS has no access to a narrowband pulsed dye laser
- smaller hyperfine splitting parameters
- shorter lifetime
- Three step scheme required

Given these advantages and disadvantages, the 249.2146 nm line was chosen for the next online CRIS experiment. The results of this experiment are discussed in the next chapters. The requirement of narrowband frequency tripled light was met by using an injection-locked titanium-sapphire laser, borrowed from the University of Jyväskylä. A detailed description of this laser system can be found in [63]. It was succesfully used to saturate a high-resolution scheme using the similar 244.1637 nm line to the $3d^9({}^2D)4s4p\,({}^3P^\circ)\ s^4P^\circ_{1/2}$, providing an incidation that it is appropriate for online studies at CRIS. The unknown mass and field shift parameters will be determined through a King plot of the new data and the literature data.

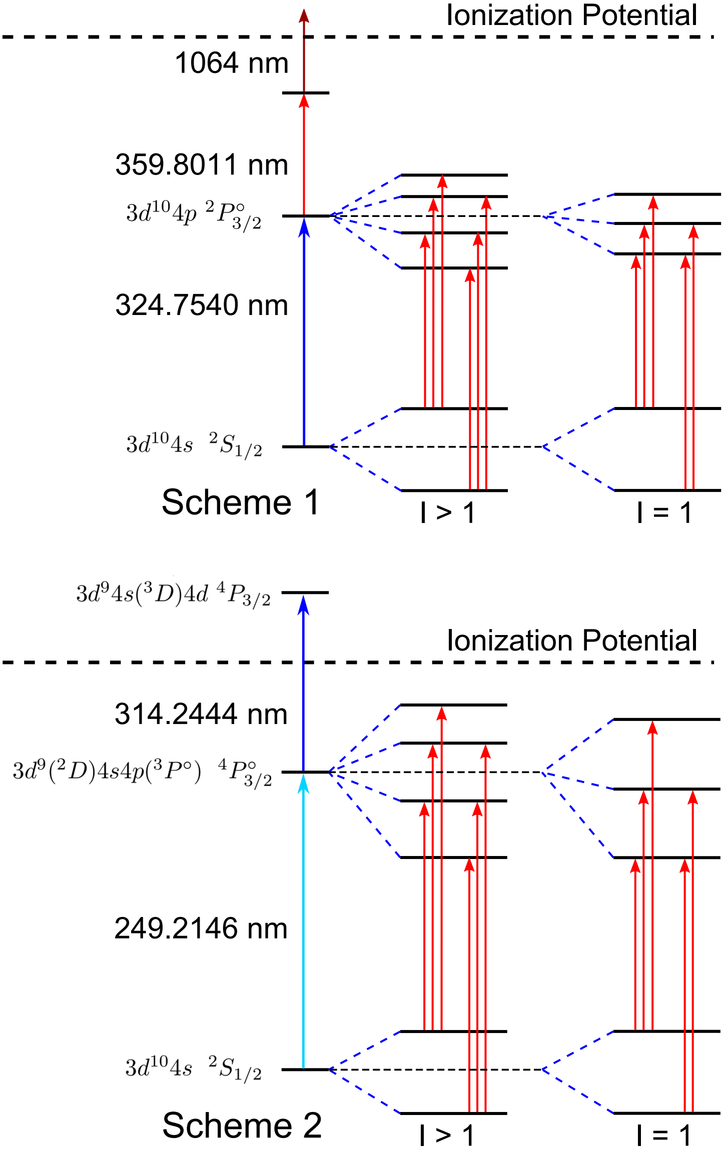

Figure 4.4: Ionization schemes used for online CRIS measurements. Scheme 1 was tested in 2015, scheme 2 was chosen for the second experiment in 2016.

Chapter 5

Analysis

Given a set of data $\mathcal{D}$ (for instance, laser wavelengths and corresponding ion counts), we wish to extract the values of a set of parameters θ (for instance, the hyperfine parameters). Furthermore, an estimate of the degree of certainty for those parameter values is desired as well. This process requires the use of statistics. In the first part of this chapter, the fundamentals of Bayesian inference will be outlined, based on the information in references [38, 64, 65], and in particular [66]. After that, a detailed description of the analysis models and corresponding assumptions will be presented. The developments presented in this chapter resulted in a publication [67], which describes in detail a software package developed to do analysis of hyperfine structure spectra.

5.1 Elements of Bayesian Inference

Bayesian statistics provides a means to estimate

$$P(\theta|\mathcal{D}), \tag{5.1}$$

that is, the probability distribution on the inference parameters, given the data $\mathcal{D}$. This distribution, called the *posterior probability distribution*, can then be used to compute the most likely values of θ. *Credibility intervals* can be computed from the posterior density $P(\theta|\mathcal{D})$. A (Bayesian) 68% credibility interval is interpreted as: given the data $\mathcal{D}$, and under the model assumptions, there is an 68% certainty that the parameter θ lies in the credible range[1]. This

---

[1] This can be contrasted with the interpretation of a (frequentist) confidence interval: if an experiment were to be repeated many many times, and for each experiment the 68%

credible interval therefore provides exactly the information we wish to infer from a particular experiment.

Obtaining $P(\theta|\mathcal{D})$ is done through application of Bayes theorem:

$$P(\theta|\mathcal{D}) = \frac{P(\mathcal{D},\theta)}{P(\mathcal{D})} = \frac{P(\mathcal{D}|\theta)P(\theta)}{P(\mathcal{D})}. \tag{5.2}$$

The joint probability density function $P(\mathcal{D},\theta)$ is also called the *model*. It is the product of the *prior* $P(\theta)$ and the *likelihood function* $P(\mathcal{D}|\theta)$. The prior $P(\theta)$ encapsulates the prior knowledge on the parameters. Priors will be discussed further in subection 5.1.1. The likelihood function $P(\mathcal{D}|\theta)$ is the probability of observing the data $\mathcal{D}$ given particular values of θ. Finally, $P(\mathcal{D})$ is the total probability of observing the data,

$$P(\mathcal{D}) = \int_\theta P(\mathcal{D}|\theta)P(\theta)\,\mathrm{d}\theta, \tag{5.3}$$

also called the normalization term. For more complex models, the normalization term is difficult to compute, which is why often the unnormalized posterior density is used instead [2]:

$$P(\theta|\mathcal{D}) \propto P(\mathcal{D}|\theta)P(\theta). \tag{5.4}$$

Some models will contain *nuisance parameters*. These are parameters that are essential for accurate modeling of the dataset, but whose values are not of direct interest to the analysis. A model with nuisance parameters will be used to infer the field and mass shift parameters from the isotope shift data in section 5.5. Bayesian inference provides a natural way to deal with these nuisance parameters through *marginalization*. If ϕ is a set of nuisance parameters, one recovers the posterior probability distribution of the parameters of interest θ by integrating over all possible values of ϕ, weighed by their posterior probability[3]:

$$P(\theta|\mathcal{D}) = \int P(\theta,\phi|\mathcal{D})\,\mathrm{d}\phi \propto \int P(\mathcal{D}|\theta,\phi)P(\theta,\phi)\,\mathrm{d}\phi \tag{5.5}$$

---

confidence interval is computed, the true value of a parameter will lie within 68% of the experimental confidence intervals. Note furthermore that, in some cases, credibility and confidence intervals do *not* coincide, see e.g. [65], which is why it is important to be aware of the precise interpretation of the two types of interval.

[2] The normalization does not affect what is the most likely value of $P(\mathcal{D})$, nor does it affect the credibility intervals, making this a harmless simplification for the purposes of parameter estimation. The normalization is required when, rather than relying on the relative likelihood of parameter values, actual probabilities are to be computed, for instance when doing model comparisons.

[3] Note that marginalization is in principle only possible within a Bayesian framework, since the integral will only yield sensible results if informative priors are specified on the nuisance parameters. More information can be found in e.g. [38].

Analytically, this is an impossible task for all but the simplest models. However, this marginalization basically comes for free when the methods described in section 5.1.3 are used.

In a Bayesian inference problem, the following three steps should be followed:

1. Define the model $P(\mathcal{D}, \theta)$. This means specifying both the priors $P(\theta)$ and the likelihood function $P(\mathcal{D}|\theta)$. Explicitly defining $P(\mathcal{D}, \theta)$ makes the inference reproducible and forces clear specification of prior bias and assumptions.
2. Using this model, the posterior probability density $P(\theta|\mathcal{D})$ can be computed (usually numerically). Parameter estimates and uncertainties can be inferred by summarizing the information of $P(\theta|\mathcal{D})$.
3. The final step is model verification. This means examining critically how well the model fits the data, but also if the choice of prior was justified (and whether or not it biases the final results).

5.1.1 Choosing the priors

Priors express any information on θ that is available before data is collected. In the case of laser spectroscopy on exotic nuclei, there is often no prior information, so a uniform distribution on e.g. the hyperfine parameters is most appropriate. Still, priors can be made more informative (and therefore also more subjective) in many cases. An example is a prior on the background rate in a counting experiment; a subjective prior that nevertheless everyone will agree on is

$$P(\mathrm{bkg}) = \begin{cases} 0 & \text{if} \quad \mathrm{bkg} < 0 \\ 1 & \text{otherwise} \end{cases} \tag{5.6}$$

Another example (that may lead to more discussion) could be to place an upper limit on e.g. the hyperfine A parameter, because an even larger A value would make the magnetic moment many times larger than the Schmidt value.

With objectivity in mind, priors should be chosen to be either non-informative (i.e. a flat prior that assigns the same likelihood to all values), or only weakly informative (like constraining a background parameter to be positive). On the other hand, the requirement that priors *must* be stated explicitly before any inference can be done, can help make analysis more reproducible, and allows to integrate out the nuisance parameters.

5.1.2 Defining the likelihood function

For a dataset $\mathcal{D}$ with N elements, $P(\mathcal{D}|\theta)$ can be factorized as

$$P(\mathcal{D}|\theta) = \prod_{i}^{N} P(\mathcal{D}_i|\theta). \tag{5.7}$$

For instance, if the goal is to infer the mean μ of a set of measurements $\mathcal{D} = \{y_i, \sigma_i\}$, a possible choice of likelihood function is:

$$P(\{y_i, \sigma_i\}|\mu) \propto \exp\left(-\frac{(\mu - y_i)^2}{2\sigma_i^2}\right), \tag{5.8}$$

$$P(\mathcal{D}|\mu) \propto \prod_{i}^{N} \exp\left(-\frac{(\mu - y_i)^2}{2\sigma_i^2}\right). \tag{5.9}$$

where normalization terms have been left out, since these can be absorbed into the normalization term $P(\mathcal{D})$ in Bayes theorem (5.2). This choice makes the assumption that the distribution of these observations y_i is normal, and that the experimental uncertainties σ_i are correctly estimated. These assumptions may not always be valid, but since they are explicitly stated, they can be evaluated later. Note that simply maximizing this likelihood function is equivalent to the default frequentist approach of chi-square minimization. An extension of this simple likelihood function that allows for the evaluation of scatter beyond the estimated uncertainties is presented in section 5.4.

Later in this chapter, several other likelihood functions will be defined and motivated (see sections 5.2.1 and 5.5).

5.1.3 Fitting the model to data

Once the model (likelihood and prior) is specified, the posterior probability density can (in principle) be computed, and parameters can be inferred from it. For simple problems, this can be done analytically. As the model gets less trivial, numerical methods are required. For models with large parameter sets, Monte Carlo Markov Chain (MCMC) methods are typically used to sample the posterior distribution parameter space and to construct an approximate posterior probability density.

Monte Carlo Markov Chain posterior distribution sampling

The goal of an MCMC algorithm is to draw randomized samples from the posterior distribution. The distribution of these random samples is then a good approximation of the real posterior distribution. There are many different possible implementations; an in-depth discussion can be found in [66]. Depending on the complexity of the model and the correlation of the model parameters, some algorithms converge faster, or sample the posterior distribution more efficiently. The reason these MCMC approaches work is that, while it is usually impossible to analytically calculate the form of the posterior distribution, it is always possible to calculate the probability of a random choice of parameters θ, which is all the information an MCMC sampler needs. Since an MCMC method returns samples from the posterior distribution, marginalization is trivially achieved: the collection of sampled values of only the parameters of interest are in fact sampled from the marginal distribution [38, 68].

In this thesis, an Affine Invarient Ensemble MCMC [69] sampler is used for analysis of hyperfine spectra and the King plot, implemented in the python Python package emcee [68]. More information on the implementation of the EMCEE sampling in the context hyperfine structure spectra analysis can be found in [67]. The approach used to combine the results of several scans into a single parameter estimate, presented in 5.4, is done using the No-U-Turn Sampler (NUTS) [70], using the PyMC package [71].

Extracting parameter and uncertainty estimates

A useful property of the posterior distribution that can be reported is the *maximum a posteriori probability estimate*, or MAP estimate. This value is the mode of Markov samples, and therefore a good approximation of the mode of the posterior distribution. The MAP values can be loosely interpreted as the parameters of best fit. While the MAP values give useful information about the posterior distribution function, they of course do not convey any information about possible multi-modality or about the width of the distribution. In this thesis, the MAP value will be used to plot the best fitting curve on top of the experimental data.

Credibility intervals can be extracted from the posterior distribution in several ways. For this thesis, since the posterior distribution of the hyperfine parameters and centroids are approximately symmetric and unimodal, the 16th and 84th percentile of the marginalized probability distribution can be used as the boundaries of the 68 % credibility interval, and the 50th percentile as the center value of the interval. Since the upper- and lower boundary are approximately the same, and since in the field of laser spectroscopy on radioactive beams usually only a single uncertainty estimate is reported for both the lower- and upper boundaries, the largest of the two boundaries is used as the 68% uncertainty estimate.

These boundaries are not scaled using the reduced chi-squared value, as is often done in χ^2 fitting procedures. This scaling procedure is problematic for several reasons [72]:

- It assumes that the uncertainty distribution is Gaussian, which is not a priori justified,
- It relies on the model being linear in all the fit parameters,
- It is equivalent to stating that, without doubt, the model is fully correct and describes the data perfectly, which is hard to verify and justify,
- And finally, the value of χ^2_{red} itself is distributed according to a χ^2_{red}-distribution, which implies that even if the three assumptions listed above are valid, χ^2_{red} can be different from one, and the uncertainties would then be increased or decreased without justification.

For these reasons (and because χ^2_{red} is also not the quantity that is optimized in the analysis presented in this chapter), no scaling of the credibility intervals is performed. The final uncertainty estimates are rather obtained from a global analysis of the full dataset, discussed in 5.4.

5.1.4 Checking the model

Besides checking whether the fitting procedure converged (e.g. by inspecting the distribution of the Markov chains or looking at the autocorrelation function), a crucial step in any inference is to check the quality of the model and of the fit. This is discussed in detail in [66]. In this thesis, a combination of the strategies listed below was used.

A first way consists of comparing the extracted parameters to literature values where available, or (for e.g. fitted linewidths, background parameters, etc.) to common sense. This first step is certainly biased towards literature, and very subjective, but serves as a first step nonetheless. As an example, the ratio of the lower-state and upper-state hyperfine A parameter should be (approximately) constant for all isotopes in an isotopic chain. Until the fitting model was adjusted to reflect the asymmetries in the lineshapes, discussed in detail in section 5.2.1, this ratio was not constant throughout the entire dataset (see section 5.2.3).

A single-value estimate for goodness-of-fit is the chi-squared value (or the reduced chi-squared). If the assumptions that underly the derivation of the chi-squared regression method are met (which is rarely the case, see [38]), the reduced chi-squared provides some information on how well the model matches experimental data. Care must be taken with interpreting the value of the reduced chi-squared however, with some references even recommending not to use it at all for anything but linear models [73]. The large values of the reduced chi-squared value obtained for reference measurements on ^{63,65}Cu in the initial stages of analysis provided a clear indication that one of the original model choices was inappropriate, and a better agreement was only achieved through implementation of the modifications presented in section 5.2.2.

Plotting the residuals (i.e., plotting the difference of the data points and the fitted model) and checking their distribution is a more robust, graphical way of estimating goodness of fit. A more advanced graphical method that takes advantage of the fact that a whole Markov chain of parameter estimates is constructed during the fitting, is to draw parameter estimates from the Markov Chain, and to graphically check if data simulated assuming these model parameters compares well to the actual observed data. This can be quantified by computing various test quantities based on these random samples (see [66] for further details).

In the end, there is not a single test that will guarantee that the model was correctly chosen and that the fit has converged to the true, global maximum. The best one can do is to perform many tests and to try different models (and priors), and see if they provide a consistent picture[4].

Finally, an important part in model validation is critical discussion with, and validation by, other scientists and peers.

5.2 Defining the model for hyperfine structure analysis

Data from all the measurement devices was combined by time-synchronizing the data streams of each device. For each data point the measured voltage V of

---

[4] This is true for Bayesian analysis as well as any other school of thought; one can *never* be sure that no mistakes were made along the way. The advantage of Bayesian methods is that they are usually very specific about assumptions and bias, making the process more transparent.

the cooler-buncher is used to do the point-per-point doppler shift to the rest frame using the following equation:

$$f_{\text{rest}} = f_{\text{lab}} \cdot \frac{1-\beta}{\sqrt{1-\beta^2}}, \quad \beta = \sqrt{1 - \frac{m^2c^4}{(eV+mc^2)^2}}, \tag{5.10}$$

where m is the atomic mass of the isotope found in [74]. Hyperfine structure spectra are constructed by binning the MCP count rate with respect to the measured laser frequency. The time-synchronization and binning algorithm is presented in appendix A.

The number of observed counts y_i in a particular time interval is usually well modeled using a Poisson distribution,

$$P(y_i|\lambda) = \frac{\lambda^{y_i} \exp(-\lambda)}{y_i!}. \tag{5.11}$$

The expectation value and the variance of samples drawn from a Poisson distribution are both equal to λ. Using a Poisson distribution represents a model choice that should be evaluated, since there may be e.g. additional processes that increases the variance of the true distribution, such that it is larger than λ. In that case, a different distribution (with more than one parameter) is required, e.g. the negative binomial distribution.

The expected number of counts λ depends on experimental conditions, for example the wavelength x_i of the probe laser. This means that the likelihood of interest is the conditional likelihood $P(y_i|\lambda, t_i, x_i)$, where the values of y_i are conditional on the model parameters, the time t_i, and the laser wavelength x_i:

$$P(y_i|\theta, x_i, v_i) = \frac{\lambda_i^{y_i} \exp(-\lambda_i)}{y_i!}, \quad \lambda_i = f(t_i, x_i, \theta) \tag{5.12}$$

A formal justification of Bayesian conditional modeling for regression problems can be found in [66]. What remains then is to write down the function $f(t_i, x_i, \theta)$. This function is what is informally referred to as the *fit function* - a function that relates the laser frequency and e.g. the hyperfine parameters to an expected number of counts. The relationship between the peak positions and the hyperfine parameters is given by equation (2.37). The function $f(t_i, x_i, \theta)$ is therefore defined as a sum of lineshape profiles, to be discussed in section 5.2.1), located at resonance frequencies determined by (2.37). The width parameter(s) and heights of these peaks, and a constant background parameter complete the set of fit parameters.

The estimates for the hyperfine parameters and the centroid should ideally not be biased in any way, which is why flat priors are chosen. For the peak intensities, linewidths, and backgrounds, the prior density (5.6) is chosen. All these priors are either objective or only weakly informative.

5.2.1 Lineshape choice

In optical spectroscopy a Voigt lineshape is often used to describe the resonance shape. This function is the convolution of a Gaussian and a Lorentzian function:

$$S_V(f, \sigma_{1,2}) = \int_{-\infty}^{\infty} S_G(f', \sigma_1) L(f - f', \sigma_2)\, \mathrm{d}f' \tag{5.13}$$

It can also be calculated using the Faddeeva function F, which is computationally faster (and therefore used in this thesis):

$$S_V(f, \sigma_{1,2}) = \frac{1}{\sqrt{2\pi}\sigma_1} \cdot \mathrm{Re}\left[F\left(\frac{f + i\sigma_2}{\sqrt{2}\sigma_1}\right)\right] \tag{5.14}$$

A Voigt lineshape is well suited to describe at the same time effects that result in Gaussian and Lorentzian broadening effects (e.g. Doppler broadening, which leads to a Gaussian shape, or power broadening, which results in a Lorentzian shape). Furthermore, lineshapes can also display asymmetry due to the charge exchange process. In addition to the charge exchange asymmetry, there are other mechanisms that can lead to lineshape distortions, e.g. those discussed in section 4.1.1. These laser-related line distortions are quite pronounced for part of the dataset. Simultaneous interaction of the atomic system with both laser pulses resulted in the appearance of a broader and smaller peak in addition to the normal Voigt resonance at the usual resonance frequencies. This is illustrated in figure 5.1, which displays three peaks of the hyperfine structure spectrum of ^{71}Cu.

The blue data points were obtained with temporally overlapped laser pulses, which lead to the appearance of additional, broader components. The red data points were obtained with an ionization laser that was delayed by 75 ns with respect to maximum of the first laser step. Measurements obtained in this way do not show this asymmetry. Note how the total efficiency is not affected by this small delay due to the long lifetime of the atomic excited state. Furthermore, the position of the narrow hyperfine structure peaks is the same in both cases. These observations motivate the definition of the fit function as a simple sum of a Voigt and a shifted Lorentzian lineshape:

$$S(f, \sigma_{1,2}, f_0, f_s, R, \sigma_3) = S_V(f - f_0, \sigma_{1,2}) + R \cdot S_L(f - f_0 - f_s, \sigma_3), \tag{5.15}$$

where f_0 is the resonance frequency, f_s and R are the frequency shift and relative amplitude of the Lorentzian distribution, and σ_3 is the width of broader Lorentzian distribution. Note that the additional component S_L should account for the charge exchange asymmetry as well. Information on the hyperfine structure spectrum of the different isotopes is then only extracted from the positions of the Voigt profiles.

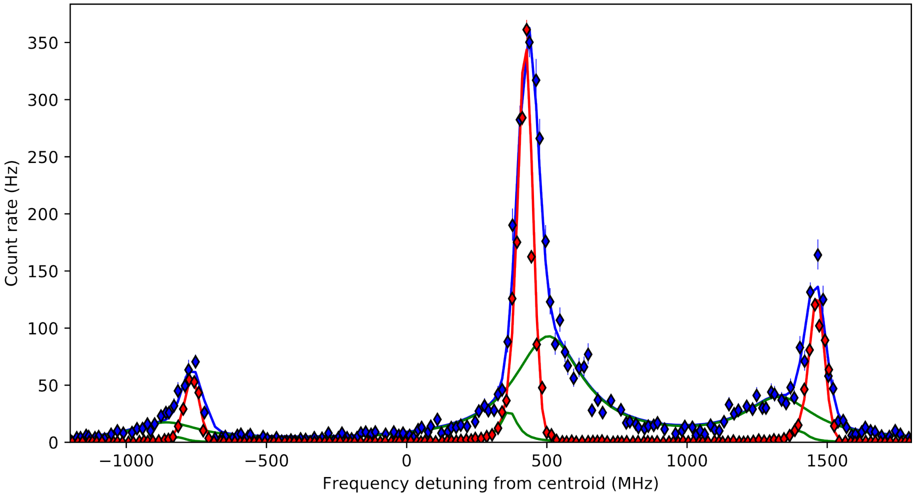

Figure 5.1: Three peaks of the hyperfine structure spectrum of ^{71}Cu, obtained with temporally overlapped laser pulses (blue). The green curve indicates the additional Lorentzian component used to model the lineshape distortions. The red points show the hyperfine structure spectrum with delayed lasers. Note that the shape asymmetry disappears, without a noticable change in total efficiency or peak positions.

The chosen prior on the linewidth parameters is the prior given in (5.6). The parameter R is further constrained to be less than 0.5. For f_s a uniform prior between -300 MHz and 300 MHz is chosen, based on visual inspection of several scans throughout the experiment. All of these priors are only weakly informative and appear well justified.

The posterior distribution of the offset parameter f_s is centered around different values for each peak within one HFS, but is consistent between all isotopes: the size and sign of the shift is the same for corresponding $F_1 \rightarrow F_2$ transitions. The precise origin of the Lorentzian components, why they are broader, and why the frequency shift is different for each set of F_1, F_2 is presently not fully understood. The full lines in figure 5.1 show the fit function using the MAP values using this lineshape.

Figures 5.2 and 5.3 show summaries of the marginal posterior distribution of A_l and the scaling and width of the asymmetric component of the lineshape for the two fits shown in figure 5.1. From the distributions and the spectra, a few things become apparent. The value of the hyperfine parameters is not affected by the asymmetry when it is modeled using (5.15). The scaling of the asymmetric component S_L is about 0.3 for the asymmetric spectrum, with the asymmetry of the middle peak opposite to that of the other two peaks. For the spectrum with a delayed ionization laser, this asymmetry is considerably reduced, and the additional component S_L is used to fit the slight low-frequency asymmetry caused by the charge exchange process. The width parameter converges to 35 MHz for the spectrum obtained with a delayed ionization pulse, rather than 150 MHz, confirming the different nature of the line asymmetries.

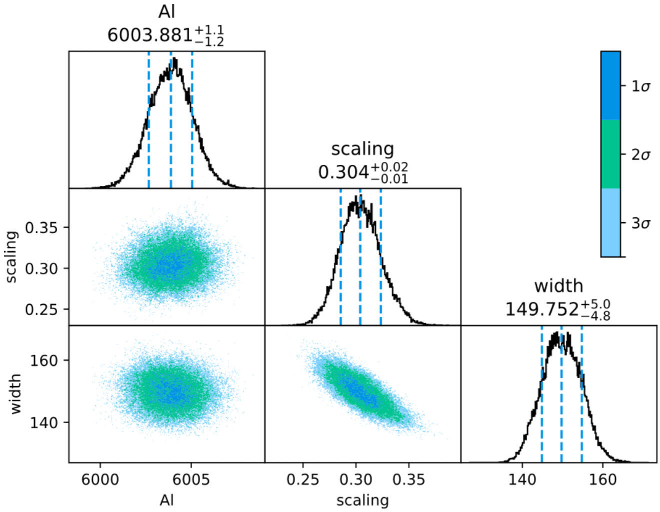

Figure 5.2: Two-dimensional marginal distributions for A_l, and the scaling and width of the asymmetric component S_L for a scan of ^{71}Cu with clear peak asymmetry.

5.2.2 Signal oscillations

Periodic oscillations in the signal intensity were observed during the reference measurements on ^{63,65}Cu. The spectrum displayed in the top plot of figure 5.4 shows an example of these oscillations. They are not present in any of the measurements of the other isotopes that were studied. The precise origin of the oscillation is not fully understood but can be traced back to the use of a fast-switching deflector plate (called the beam gate), used to reduce the beam intensity injected into ISCOOL. This was only done for ^{63,65}Cu and was needed to avoid unwanted space-charge effects in the trap. To remove all possible influence of these effects on the extracted results, the oscillations were modeled and incorporated into the fitting lineshape.

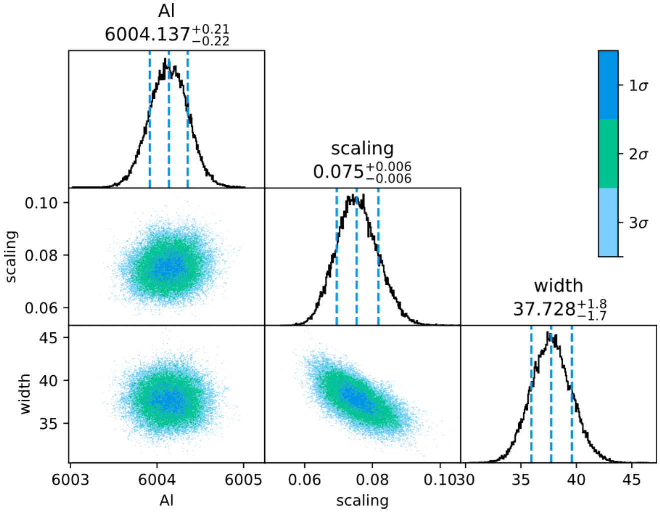

Figure 5.3: Two-dimensional marginal distributions for A_l, and the scaling and width of the asymmetric component S_L for a scan of ^{71}Cu with more symmetric lineshapes.

Fourier transformation (bottom plot in figure 5.4) of the data revealed that the oscillatory modulation has three frequency components: one with period of about 7.1 s, the other two with respectively twice and three times this value. The following modification of the lineshape was therefore introduced:

$$\begin{aligned} S_{osc} &= S_{osc}(f, t, \theta, T, a_0, a_1, a_2, \phi) \\ &= S(f, \theta) \cdot \sum_{i \in [0,1,2]} \frac{a_i}{2} \left(1 + \cos\left(\frac{2\pi(t-\phi)}{T/2^i}\right)\right) \text{(if A = 63, 65)} \end{aligned} \tag{5.16}$$

with θ a shorthand notation for the parameters already introduced in (5.15). The new parameters T, a_0, a_1, a_2, ϕ are to be inferred from the model fit. Note that the additional terms added in (5.16) are only a function of time, and not of the laser frequency. This considerably improves convergence properties of the fitting routine. An example of a this fit function using the MAP values for the parameters is shown in Fig. 5.4. The posterior distribution of A_l, T, ϕ and a_i are shown in figure 5.6. Note the correlation of e.g. T and ϕ, but also how the parameters used to model the oscillations are not correlated to the hyperfine A-parameter. Finally, note that the values of hyperfine parameters that are obtained when these oscillations are properly accounted for are not significantly different, but that the uncertainty estimates are more reliable since all features of the data are modeled correctly.

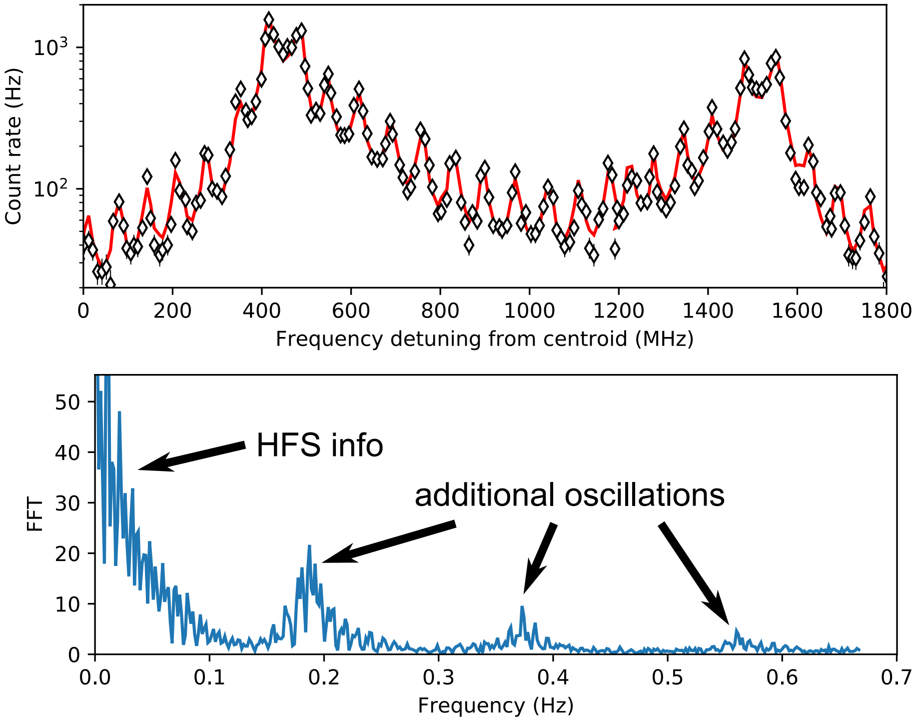

Figure 5.4: Top: two of the six resonance lines in the spectrum of ^{65}Cu. The oscillations in time are clearly visible and are well fitted by the function discussed in the text. Note the logarithmic y-axis.
Bottom: fourier transform of the timeseries data. Three broad features appear in the fourier spectrum.

5.2.3 Validation of lineshape choice: ratio of A-parameters

The more complex, asymmetric and oscillatory lineshape is required not only because any analysis should try to model the data as accurately as possible, but also because otherwise clearly incorrect results are obtained. This is illustrated in figures 5.5. This figure shows the ratio of upper and lower state A-parameter of ^{65}Cu during the course of the experiment, extracted using either simple Voigt profile or the full lineshape of equation (5.15). The shaded area indicates the final value obtained for the full dataset on all masses, which is in reasonable agreement with literature (see 6.3.1). The asymmetrization of the lineshapes is crucial in obtaining the correct ratio of A-parameters.

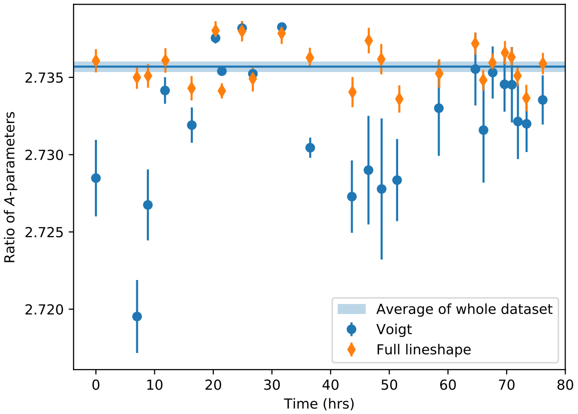

Figure 5.5: Ratio of upper- and lower-state A parameter of ^{65}Cu during the experiment, extracted using using symmetric voigt profiles. The band indicates the final value and uncertainty on this ratio, obtained using the formalism in 5.4. This value in reasonable agreement with literature, as will be discussed in 6.3.1.

Despite the clear improvement in the ratio, the scatter of the data points is still large with respect to the estimated uncertainties. The origins of this additional scatter are not clear, but could be related to a wavemeter readout drift during the experiment, which will be discussed next. The calibration procedure that will be outlined in that section was already applied to obtain the points in figure 6.14, suggesting that the precision of the wavemeter drift compensation could be insufficient. Section 5.4 will describe a method that propagates this large scatter into the final estimate of the ratio of A-parameters for all the isotopes that were studied.

5.3 Wavelength drift compensation and isotope shift extraction

Extraction of the isotope shift requires comparison of the fitted hyperfine structure centroid with that of a reference isotope. During the course of the experiment, a significant drift in the fitted centroid of the reference scans of ^{65}Cu was observed. The black circles in figure 5.7 show the evolution of these centroids as a function of time. The drift of these centroids should not

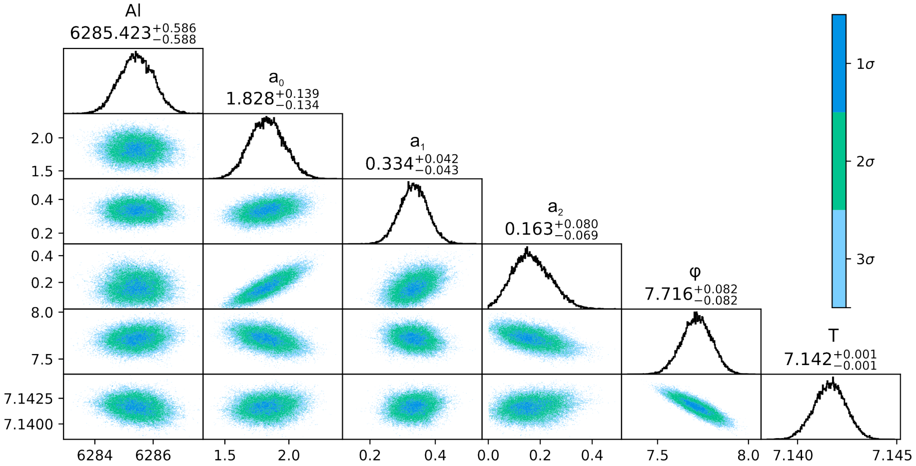

Figure 5.6: Two-dimensional marginal distributions for A_l, T, ϕ and a_i in equation (5.16).

be due entirely to drifts in the acceleration voltage since the readout of the ISCOOL cooler voltage should be sufficiently precise to measure changes of this magnitude.

The origin of the drift in the ^{65}Cu centroid wavelengths rather appears to be due to a drift in the wavemeter readout, as can be observed by comparing to the readout of the temperature-stabilized helium-Neon (HeNe) laser wavelength from the same wavemeter (green curve in figure 5.7). In order to extract reliable isotope shifts and given the long measurement times for e.g. ^{78}Cu, it is necessary to construct a calibration curve that can be used to correct the wavelength measurements in time.

A calibration function $c(t)$ needs to be constructed in such a way that analyzing the count rates with respect to $f'(t_i) = f(t_i) - c(t_i)$ (rather than $f(t_i)$) results in centroids that are (approximately) constant as a function of time. In the next section a construction of a possible $c(t)$ that uses only measurements of the HeNe wavelength and the reference measurements of ^{65}Cu is outlined.

5.3.1 Wavemeter drift compensation

Given the similarity of the time drift of the average HeNe readout $\langle H(t_i)\rangle_j$ during scan j, and the ^{65}Cu centroid C_j, a possible candidate for the calibration

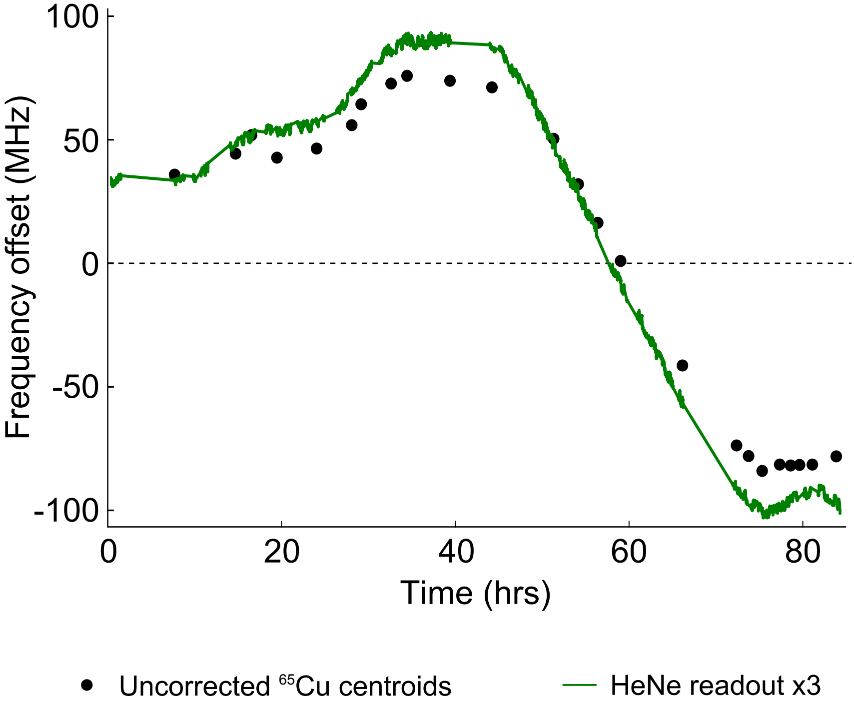

Figure 5.7: ^{65}Cu centroid frequencies, offset by their mean, as a function of time. The green curve is the readout of the stabilized HeNe laser, offset by its mean, multiplied by three.

function can be defined as

$$c(t_i) = 3 \cdot H(t_i) + g(t_i), \tag{5.17}$$

where $H(t_i)$ is the measured HeNe wavelength at time t_i and $g(t_i)$ is an function optimized to best fit $C_j - 3 \cdot \langle H(t_i) \rangle_j$. In other words, the fitted function $g(t_i)$ describes the drift due to effects other than the wavemeter calibration (e.g. drift of the HeNe laser wavelength, drift in voltmeter calibration, ...). By construction, $\langle c(t_i) \rangle_j \approx C_j$, so that $c(t_i)$ is in effect an estimator for what the centroid of a ^{65}Cu scan would have been had it been performed at time t_i. Centroids extracted from scans using $f_i - c(t_i)$ rather than just f_i will therefore be good estimators for the isotope shift for that particular scan. The fitted centroids for ^{65}Cu should be close to zero, per construction.

Looking at the measurements of the HeNe frequency H_i in detail, fast jitter

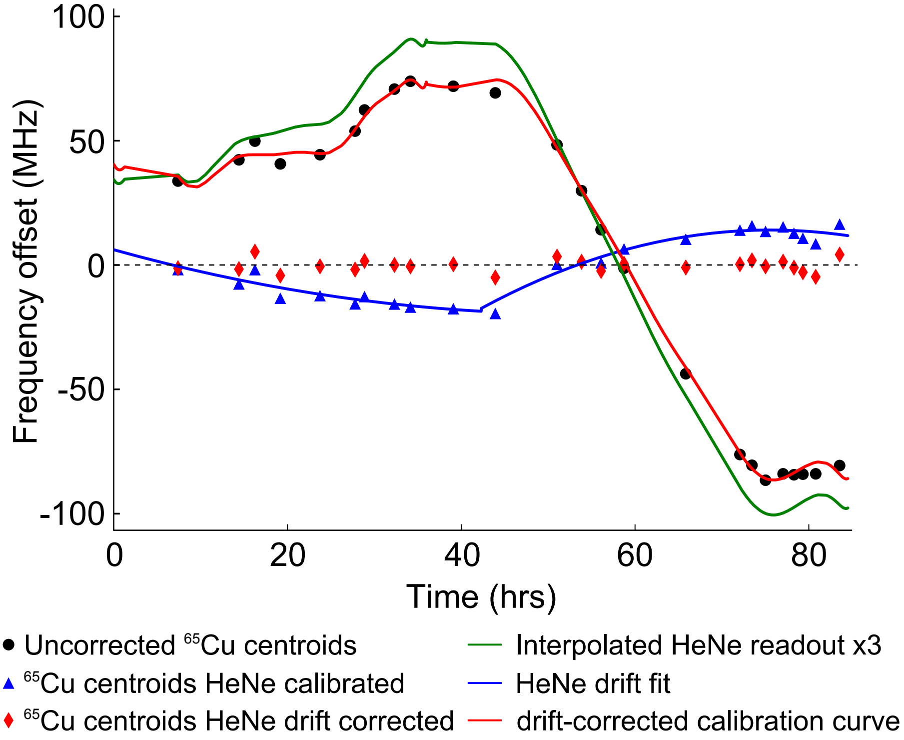

Figure 5.8: Similar to figure 5.7, but this time with the interpolated HeNe wavelength. For more information on the other curves and data points, see text.

in the order of 100 kHz occurs on a timescale of a few seconds, and slower fluctuations in the order of 1 MHz occur on a timescale of 10 minutes. These are due to a combination of measurement error of the wavemeter and instabilities of the HeNe laser itself. To avoid propagating these effects into the wavemeter calibration function $c(t_i)$, the HeNe wavelength readout is smoothed using a Gaussian filter with a kernel of 30 min, resulting in the curve shown in green in figure 5.8. The calibration function is then defined using this smoothed HeNe data rather than the raw data. The blue triangles in figure 5.8 show values of $C_j - 3 \cdot \langle H(t_i) \rangle_j$. They drift within a band of 30 MHz. Given the rather gentle evolution in time, defining $g(t)$ as a concatenation of a linear and a quadratic curve (blue curve in figure 5.8) is sufficiently precise to model the large-scale features. The deviations of the experimental ^{65}Cu centroids C_j from $c(t_j)$ scatter with a 2 MHz standard deviation, shown as red diamonds in figure 5.8). This implies a lower limit on the final precision on the isotope shifts of 2 MHz.

To determine isotope shifts for all $A \neq 65$, the response values of this drift correction model are used as reference frequencies, allowing accurate isotope shift calculations even in the absence of reference measurements. Furthermore, this approach also allows for a point-per-point drift correction to be performed. In particular, between $t = 40\,\mathrm{h}$ and $t = 70\,\mathrm{h}$, this correction can prevent possible systematic deviations in the hyperfine parameters and the isotope shifts due to wavemeter callibration drift. This is of particular importance for the measurements on ^{78}Cu, which required a slow scanning speed over many hours.

5.4 Combining information from multiple measurements

The methods outlined above provide estimates for parameter values and credibility intervals for every individual scan (labeled by index i_k) obtained for a particular isotope (labeled by index k). These estimates should then be combined into a single, best estimate $\bar{\theta}_k$ of a parameter θ_k, with an estimated uncertainty σ_k. This will only yield reliable uncertainty estimates if the individual σ_{i_k} are correctly estimated. If this is not the case, a dispersion-corrected weighted mean is more appropriate. In this case, σ_k is scaled with the reduced chi-squared:

$$\bar{\theta}_k = \frac{1}{\sum_{i_k}^{n_k} 1/\sigma_{i_k}^2} \sum_{i_k}^{n_k} \frac{\theta_{i_k}}{\sigma_{i_k}^2}, \quad \sigma_k^2 = \frac{1}{\sum_{i_k}^{n_k} 1/\sigma_{i_k}^2} \cdot \frac{1}{n-1} \sum_{i_k}^{n_k} \frac{(\theta_{i_k} - \bar{\theta}_k)}{\sigma_{i_k}^2}. \tag{5.18}$$

These formulae are very useful when several measurements were made for every isotope, since then the standard deviation can be well estimated. When there are only one or two measurements available, however, applying the equations listed above may result in unreliable uncertainty estimates. This can happen for instance if there is an additional scatter (with variance Σ^2) in the inferred parameter estimates, due to effects that do not become apparent during a single scan, but only over longer periods of time.

One way to include the effect of an additional scatter in the estimation of the final parameter values and uncertainties is to assess the value Σ^2 using the other data obtained in the same experiment. Making the assumption that the size of this scatter is the same for all isotopes (which is not necessarily true!), the following likelihood function can be defined:

$$P(\mathcal{D}|\theta_k, \Sigma) \propto \prod_k \prod_{i_k}^{n_k} \frac{1}{\sqrt{\sigma_{i_k}^2 + \Sigma^2}} \exp\left(-\frac{(\theta_{i_k} - \theta_k)^2}{2(\sigma_{i_k}^2 + \Sigma^2)}\right) \tag{5.19}$$

Placing a uniform prior on the unknown θ_k and the positive flat prior (5.6) on Σ, one can then estimate the posterior probability density distribution, and make estimates of θ_k by marginalizing out the parameter Σ. If there are many measurements for a given isotope k, the additional uncertainty Σ will not influence the final result much. If on the other hand there are only a handful of scans, the scatter uncertainty inferred from all the other scans will dominate the width of the posterior distribution of θ_k, and the final uncertainty estimate will therefore reflect the presence of additional experimental scatter. If the uncertainty estimates $\sigma^2_{i_k}$ are representative for the true scatter of the data, Σ will converge to zero.

By defining the model (5.19), a reproducible and objective way of estimating the final uncertainties on parameter estimates from the whole dataset is achieved. This approach will therefore be used in this thesis.

5.5 King plot

In order to go from isotope shifts to charge radii, values of the the mass- and field shift parameters M_k and F_k are required. They can be extracted using the modified King plot method introduced in chapter 2. In principle, all of the modified isotope shift pairs should fall on a straight line. However, as will be shown later in chapter 6, this will not be the case: the modified isotope shift pairs for ^{64,66,68m}Cu appear to deviate somewhat from the linear trend. In order to correctly treat these outliers during the linear fit, a robust linear regression method is implemented, based on the recommendations in [38]. This approach defines a log-likelihood function which takes two-dimensional uncertainties into account, and furthermore takes care of outlier pruning.

5.5.1 Linear regression with outlier pruning

For each pair (x_i, y_i) of modified isotope shifts and corresponding uncertainties $(\sigma_{xi}, \sigma_{yi})$ the column vector

$$Z_i = \begin{pmatrix} x_i \\ y_i \end{pmatrix} \tag{5.20}$$

and uncertainty tensor (if there is no correlation between x_i and y_i, which is the case here)

$$S_i = \begin{pmatrix} \sigma^2_{xi} & 0 \\ 0 & \sigma^2_{yi} \end{pmatrix} \tag{5.21}$$

can be defined. In addition, for a given slope of the straight-line fit, the unit vector $\hat{v}$ can be defined using the angle $\alpha = \tan^{-1} m$, where m is the slope:

$$\hat{v} = \begin{pmatrix} -\sin\alpha \\ \cos\alpha \end{pmatrix} \tag{5.22}$$

With these definitions the loglikelihood function for a straight-line fit with two-dimensional uncertainties can be written as:

$$\mathcal{L} \propto \sum_i -\frac{1}{2}\log\Sigma_i^2 - \frac{\Delta_i^2}{2\Sigma_i^2}, \tag{5.23}$$

where

$$\Delta_i = \hat{v}^T Z_i - b\cos\alpha, \tag{5.24}$$

$$\Sigma_i^2 = \hat{v}^T S_i \hat{v}. \tag{5.25}$$

A flat prior on the parameters[5] α and $b' = b\cos(\alpha)$ is chosen. Note that this definition of the likelihood function assumes that the uncertainties on both isotope shifts are Gaussian distributed.

One way of dealing with potentially underestimated uncertainties or outliers in a Bayesian way can be done by expanding the linear fitting model into an mixture of the original linear model and a linear model with increased uncertainty estimates:

$$\mathcal{L} \propto \sum_i \log(1-g_i) - \frac{1}{2}\log\Sigma_i^2 - \frac{\Delta_i^2}{2\Sigma_i^2} +$$

$$\log(g_i) - \frac{1}{2}\log\Sigma_i^2 - \frac{\Delta_i^2}{2(\beta\Sigma_i)^2}. \tag{5.26}$$

That is, for every data point a parameter g_i $(0 \leq g_i \leq 1)$ is introduced, as well as a single scaling parameter β. The parameters g_i encode the probability that data point i would be better described by a model with orthogonal uncertainty $\beta\Sigma$ rather than Σ. The additional parameters g_i and β are free parameters in the optimization and are finally marginalized out to obtain the final uncertainties on the angle α and intercept b' of the straight line fit. The mass- and field shift factors are then obtained from a MCMC sampling posterior distribution of the slope and intercept. Again, the confidence intervals are constructed using the 16th, 50th and 84th percentile of the marginalized distributions.

---

[5] The flat prior on the slope of the straight line is actually biased towards steeper lines: slopes $|m| < 1$ map to angles less than 45°, the much larger set of the remaining slopes map to angles larger than 45°.

5.5.2 Another way: bootstrapping

Bootstrapping is a method to estimate properties of statistical estimators (like the mean or the variance) through sampling of an approximating distribution,. For instance, in the case of the linear fit, a bootstrapping algorithm looks as follows:

1. Label the experimental data points from 0 to N.
2. Generate N random numbers between 0 and N.
3. Select the data points whose label corresponds to the generated random numbers. Note that this means the same data point can be selected several times.
4. Perform a linear fit of the randomly sampled data points, and store the fitted slope and intercept.
5. Repeat steps 2-4 as often as is reasonable.
6. The mean and variance of the fitting parameters can now be estimated from the mean and standard deviations of the stored values of the slope and intercept of all the samples.

The justification for such a procedure is as follows. Ideally, to estimate the value of a certain parameter, one would repeat experimental measurements many times, and see what this parameter is for every case. In this way a thorough sampling of the distribution of that fit parameter is performed, and a confidence interval can be estimated. In the case where no repeat experiments are available or possible, a reasonable thing to do is to approximate the underlying distribution of the data points with the empirically observed distribution. In fact, this empirical distribution represents the only information on the true distribution that is free from assumptions. Naturally, if the experimental results are in some way skewed, or not representative of the true distribution, this approach will yield similarly skewed results (but then, so would any other method).

What this bootstrapping approach is particularly good at, is dealing with one or two outlier points that would normally skew the linear fit. Since these few outlier points get sampled only infrequently, most of the bootstrap samples will not contain them, and the parameter estimate will therefore not be skewed. Parameter estimation using the distribution of the boostrapped samples is therefore more robust than standard parameter estimation. Furthermore, e.g. the standard deviation of the parameter distribution serves as a robust estimater of the parameter variance.

Note that in this procedure, the way the linear regression is performed is not specified. For instance, one could do bootstrapping estimation in combination with a normal, weighted linear least-squares fit, or with a more advanced maximum-likelihood optimization. For the King plot analysis, a simple Orthogonal-Distance Regression is chosen, since this regression method takes into account uncertainties on both x and y, and is computationally fast (which allows for many bootstrap samples to be analysed).

5.6 Summary of the analysis procedure and uncertainty assessment

In summary, extraction of hyperfine parameters and isotopes shifts for all scans is done using the following procedure:

a. Data is extracted using steps 1-3 given below.

b. Processed data for the reference measurements on ^{65}Cu is first fit by maximizing the likelihood function (5.12), to obtain a starting guess for the MCMC of the posterior distribution.

c. For every scan, many points in parameter space are sampled. Visual inspection of the resulting chains was performed to ensure the chains have begun exploring the parameter space. Typically, this requires cutting away the first 20% of the total chain length.

d. The centroid wavelengths of the reference measurements on ^{65}Cu are used to perform a wavemeter drift compensation procedure, as outlined in section 5.3.1.

e. Steps a through c are performed for all isotopes, this time with an adjusted version of step 2 of the data extraction algorithm:

    2. bis Every wavelength is doppler transformed according to equations (5.10) using the measured ISCOOL voltages. The wavelengths are calibrated point-by-point using the calibration function obtained during the wavemeter drift compensation procedure.

f. After this second likelihood maximization and random sampling of posterior parameter space, parameter values and uncertainties are established from the posterior distribution constructed from the last 80% of the Markov chain.

g. Final values and uncertainties $(\bar{\theta}, \sigma)$ on these parameters for every isotope are then computed using the inference strategy described in 5.4.

Data extraction and processing is done as follows:

1. MCP counting data, ISCOOL voltage measurements, the wavelength readout of the scanning laser and the HeNe laser are extracted from the scan files. These independently timestamped datafiles are merged and synchronized. Every measurement of the MCP counts is associated with the most recent ISCOOL voltage or frequency measurement.
2. Every wavelength is doppler transformed according to equations (5.10) using the measured ISCOOL voltages.
3. The MCP counting data is binned with respect to the doppler-shifted wavelengths using the binning algorithm presented in appendix A. This binning procedure yields the average number of MCP counts observed per DAQ trigger in every bin. This is the data that is fitted. Plots that display the average rate in Hz are obtained by dividing the bin contents by the average triggering period, in this case, this is 10 ms. In effect, this means the conversion of average counts per trigger to average rate constitutes a multiplication with a factor of 100.

Chapter 6

Results

6.1 Experimental considerations

Measurements were performed on neutron-rich copper isotopes from 21/04/2016 to 24/04/2016. These isotopes were produced by impinging up to 2 μA of 1.4 GeV protons from the Proton Synchrotron Booster onto the neutron converter [75] of a UC_x target. The (radioactive) atoms diffused out of the target into a thin tube. Both target and tube were heated to approximately 2000 °C to improve transport time and therefore minimize decay losses. The atoms in the thin tube were then ionized using the RILIS laser system. For copper, in-source laser ionization efficiencies are typically a few percent, with efficiencies of 6.6(2)% reported in literature [76, 77]. The radioactive ions were then mass-separated with the high-resolution separator. The mass-separated ions were then cooled and bunched using the gas-filled radio-frequency linear Paul trap ISCOOL [78, 79], and sent towards the CRIS beamline. Transmission through the cooler, when operated in bunched mode, was observed to be about 50% for the stable copper isotopes. Total ion transport efficiencies from the cooler to the CRIS beamline were as high as 90%.

In total, data was collected during a timespan of about 80 hours, during which 15 isotopes and 3 isomeric states were studied. In table 6.1, an overview is given of how the scans were grouped into independent full measurements of the hyperfine structure. The table also lists the total time spent collecting statistics. This time only includes data recording; it excludes e.g. mass changes, deciding on and setting up of scan ranges, background checks, saturation measurements, etc. Note how a quarter of the time was spent on ^{65}Cu reference measurements.

Finally, less time was devoted to collecting statistics on ^{77}Cu compared to ^{76}Cu despite their relative production rates: due to degrading production yields, measurements on ^{77}Cu had to be prematurely stopped.

Table 6.1: Grouping of the scans into independent, full hyperfine structure measurements for all measured masses.

A	grouping	time (h:min)
63	14, 15, 22, 111-114, 115-118, 249-252	2:16
64	216, 217	0:21
65	18, 31, 34, 39, 46, 59, 61, 66, 68, 70, 81, 92-96, 101-104, 106-109, 123-126, 142-145, 155-158, 166-169, 175-178, 193-196, 204-207, 211-214, 218-221, 245-248	10:36
66	208, 209	0:28
68	179-191, 197-203	1:43
69	23-24, 60	1:08
70	230-244	1:13
71	29-30, 62	1:09
72	170-174	0:35
73	32, 33, 65	1:51
74	159, 160-163	0:36
75	37-38, 67, 97-100	3:12
76	40-45, 69	6:39
77	48&54-58, 82-87	3:25
78	89-91&105&139-141	8:01

6.1.1 Background suppression

Measurements on exotic isotopes with low production yields are greatly facilitated by the reduced background. This is illustrated in figure 6.1, which compares (partial) spectra obtained using the COLLAPS beamline without the cooler buncher, using the COLLAPS beamline with the cooler-buncher, and using CRIS. The improvement in quality of the spectra is largely due to the improvement in signal-to-background. In the case of CRIS, this is due to a high experimental efficiency (to be discussed in section 6.1.3), but also due to the ability to suppress background events.

For collinear laser spectroscopy with photon detection, the background is due to any light that scatters into the detectors. This can be for instance laser light which scatters off of the entry window, but also light from de-excitation of collisionally excited ions and atoms in the beam or radioactive decays. It

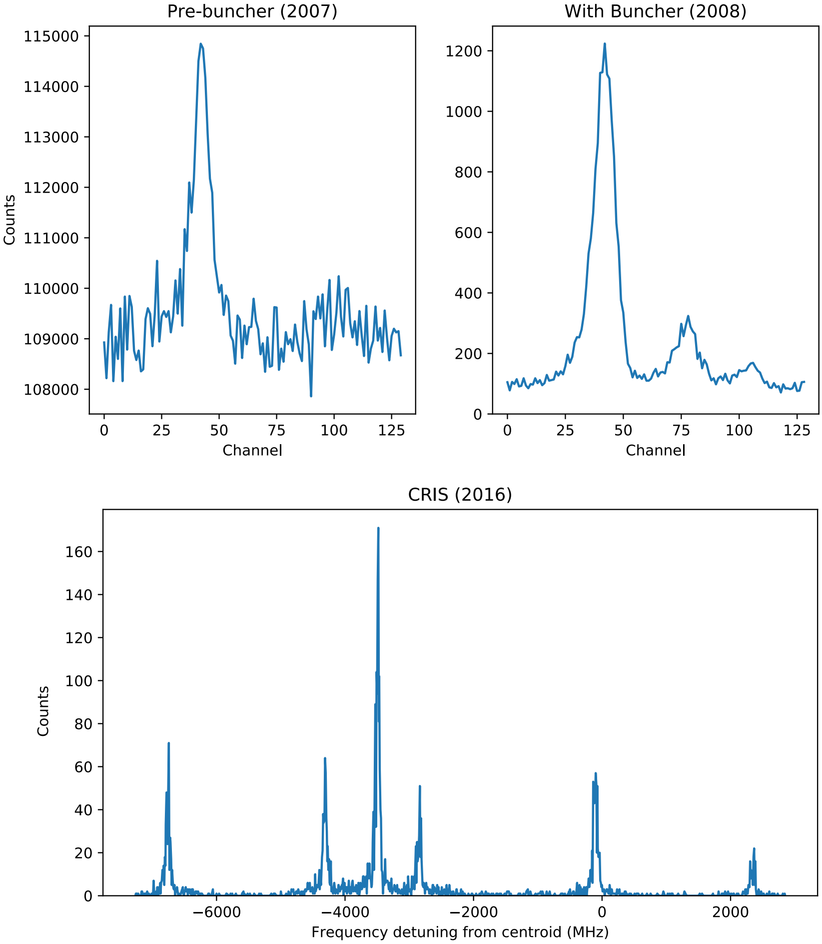

Figure 6.1: Comparison of the (partial) spectra of ^{72}Cu obtained with the COLLAPS experiment before the use of the cooler-buncher (top left), with the cooler-buncher (top-right) and using CRIS (bottom). Note the improvement in signal-to-background with each new technical development: from ≈ 0.05 without cooler-buncher, to ≈ 10 with, and to finally ≈ 150 with CRIS.

is this background that ultimately limits the cases that can be studied. For CRIS, the background is due to atoms that are ionized through processes other than the selective resonance laser ionization process. For instance, atoms can sometimes be non-resonantly ionized by one of the lasers. The most common source of background however is due to collisional ionization of the atom beam.

If there are no contaminants in the beam, this is not an issue, since the signal-to-background ratio is then the same for all isotopes. However, the presence of a large isobaric contaminant fraction can result in large background rates, and therefore prevent the measurement of hyperfine structure spectra.

Table 6.2 shows measured background rates for the most neutron-rich copper isotopes under investigation in this thesis. For these masses, most of the contamination is expected to be due to gallium and, epecially for $A > 78$, also rubidium. This is confirmed by the multi-reflection time-of-flight (MR-TOF) spectrum shown in figure 6.3, showing clear peaks for ^{79}Rb and ^{79}Ga. These MR-TOF measurements were performed in 2015 [80], but a similar beam composition can be expected for the target used during the 2016 CRIS experiment. Using the rates tabulated in table 6.2, and a conservative estimate of 10^5 contaminant ions per second for $A = 79$, a collisional re-ionization rate of $1 : 10^7$ is obtained, consistent with more recent CRIS measurements on indium and potassium. Note that these re-ionization rates were obtained with a pressure of 2×10^{-8} mbar in the interaction region of the CRIS beamline.

Protons on neutron converter

A	time (s)	events	rate (Hz)
77	400	0	$0.000^{+0.002}_{-0}$
78	400	0	$0.000^{+0.002}_{-0}$
79	400	4	$0.012^{+0.006}_{-0.004}$

Protons on target

A	time (s)	events	rate (Hz)
77	416	42	$0.10^{+0.016}_{-0.014}$
78	1910	1801	$0.94^{+0.02}_{-0.02}$

Table 6.2: Observed background rates for $^{77-79}$Cu. Uncertainties were estimated from a Poisson regression.

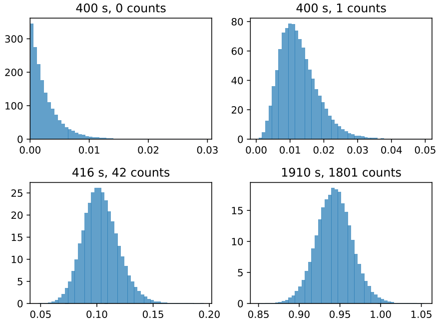

Figure 6.2: Posterior distributions of the Poisson regression for the observed events listed in table 6.2.

6.1.2 Saturation curves

Saturation curve measurements were performed for both laser steps. This was done by assessing the rate on resonance of the largest peak ($F = 2 \rightarrow F = 3$) of the hyperfine structure spectrum of ^{65}Cu. The saturation curve for the first step was obtained at the very end of the run, while the curve for the second step

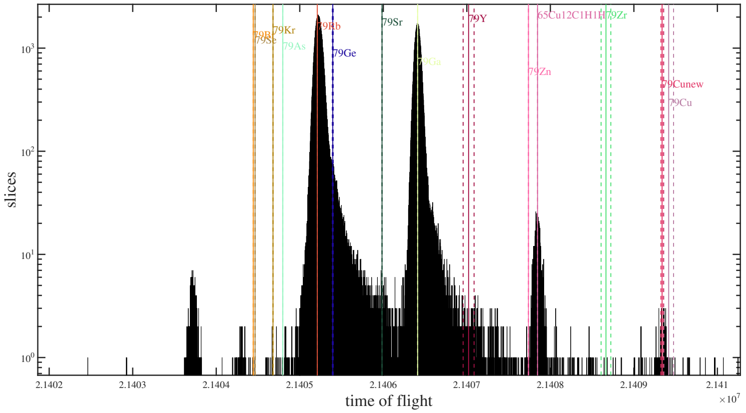

Figure 6.3: MR-TOF spectrum at mass 79, courtesy of F. Wienholtz and the ISOLTRAP collaboration [80].

was obtained in the middle of the experiment. Laser powers were measured at the entrance window of the CRIS beamline, which means that e.g. absorbance by the window is not taken into account. Both saturation curves are shown in figure 6.4.

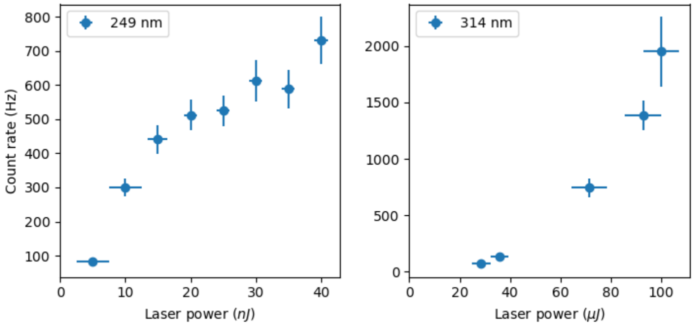

Figure 6.4: Saturation curves for the first and second laser step. The first step is quite well saturated, while the second step is far from saturation.

The output power of the 747 nm injection-locked Ti:sapphire was 250 μJ per pulse, from which 40 nJ of frequency tripled light was delivered into the CRIS beamline. This light was shaped into a circular beam spot with diameter of

3 mm, estimated by eye. Despite the inherent losses of the frequency tripling process, the 249 nm first step is well saturated.

For the 314 nm laser light, only 500 μJ out of the total 3 mJ of 628 nm light could be used for frequency doubling, since higher powers resulted in damage to the frequency-doubling crystal. A doubling efficiency of about 20 % was achieved. This light was sent through a telescope to produce an elliptical beam of about 7 mm×5 mm (again estimated by eye).

From these curves it can be concluded that the first step in this two-step scheme is well saturated, but that more laser power is required in the second step to maximize the ionization efficiency. Future measurements could therefore optimize this second step, either by finding ways to prevent doubling crystal damage, or by using a more easily saturated transition.

6.1.3 Efficiency estimates

The efficiency of the CRIS method, defined as the ratio of the number of ions injected into the CRIS beamline and the number of laser-ionized ions observed on the MCP detector, was obtained from the reference measurements on ^{65}Cu. This efficiency was evaluated at various times during the experiment, and was found to be constant throughout the run. Since the total beam of ^{65}Cu is too intense to send into ISCOOL as well as the CRIS beamline, it was reduced in intensity by pulsing the voltage on the beam gate, before the ISCOOL. By using a 10 μs beam gate length, operated at 100 Hz, the total beam intensity is reduced by a factor of 1000. A total beam current of 20 pA (which is what was typically observed), which corresponds to 1.2×10^8 particles per second, is then reduced to 1.2×10^5 particles per second. With such a beam intensity, typically 600 counts are observed per second on the MCP (when the signal, which oscillates as discussed in 5.2.2, is at its highest). This then translates into an efficiency of about 0.8%.

Using this efficiency estimate, yields for all measured isotopes can be obtained. These are presented in figure 6.5 and table 6.3. The horizontal lines indicate respectively the limit of collinear laser spectroscopy with photon detection and without the use of a cooler-buncher, the current limit of photon-detection with a cooler-buncher, and the current limit demonstrated by CRIS. Figure 6.5 also shows the yields used for the earlier collinear laser spectroscopy experiments [81], which used protons on target rather than on the neutron converter. These yields (and earlier reported yields [82]) are at least one to two orders of magnitude higher than the yields observed in 2016. This is due to the use of the neutron converter, as well as previous irradiation of the target in 2016. Furthermore,

Table 6.3: Estimated yields during the 2016 CRIS experiment, estimated based on the CRIS efficiency and as provided by the target team. Yields given as particles per μC.

A	CRIS	Target group
64	4.0×10^4	-
66	6.0×10^4	-
68	6.0×10^4	-
69	1.4×10^5	1×10^5
70	4.0×10^4	-
71	7.0×10^4	-
72	1.2×10^4	3×10^4
73	1.6×10^4	-
74	6.0×10^3	-
75	3.0×10^3	2×10^3
76	4.0×10^2	-
77	8.0×10^1	-
78	1.6×10^1	-

note from table 6.3 that the CRIS yield estimates are in good agreement with those obtained from the ISOLDE target group during the experiment.

6.1.4 The road towards ^{79}Cu

Performing laser spectrosopy on ^{79}Cu is challenging, due to the low production yields expected at ISOLDE. Based on an extrapolation of the yields presented in section 6.1.3, an average production of no more than a few ^{79}Cu atoms per second is expected. While this is in principle enough for a CRIS measurement, the high production of isobaric contaminants like ^{79}Rb and ^{79}Ga further complicate measurements. Indeed, with a production yield of 1/s and a total efficiency of 0.8%, an event rate of only 0.008 Hz is expected, while the background rate (given in table 6.2) is estimated to be $0.012^{+0.006}_{-0.004}$. These estimates imply that with the current efficiency and background suppression, a measurement of ^{79}Cu is impossible.

With production rates this low, even small changes in the event rate or background suppression can significantly improve the outcome. For instance, if the signal rate and the background can be improved by a factor of five, the spectrum in figure 6.6 could be obtained within a total measurement time of 21 hours. The precision on the extracted hyperfine parameters of such a

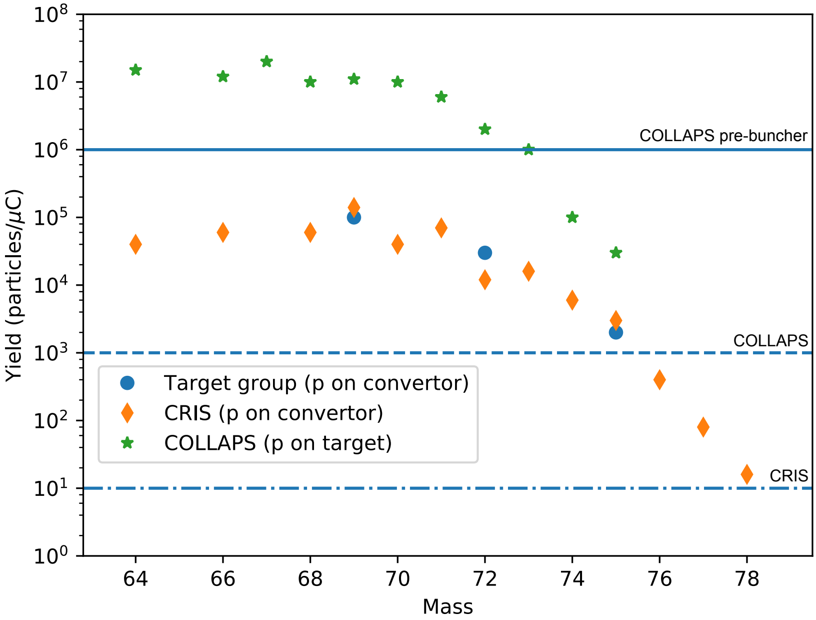

Figure 6.5: Yields (after ISCOOL) extracted by the target group (circles) and from the CRIS data, by assuming an efficiency of 0.8% (diamonds). Stars indicate the yields estimated during the previous COLLAPS measurements [5, 81], where protons were impinged onto the target rather than the neutron converter.

measurement would be sufficient for reasonably precise radii and quadrupole moments, comparable to the results on ^{77}Cu obtained in this thesis.

An increase in the signal rate could be obtained through improvements of the laser power density of the second laser step (or by looking for a more efficient auto-ionizing transition altogether), or by using a new target rather than a previously irradiated one. The enhanced background suppression can be achieved through improvements to the pressure in the interaction region of the CRIS beamline. These improvements are underway at the time of writing.

6.2 Analysis results

Figure 6.7 shows two sets of example MCMC marginalized parameter samples drawn from the posterior distribution, for the lower-state A-parameter, upper-

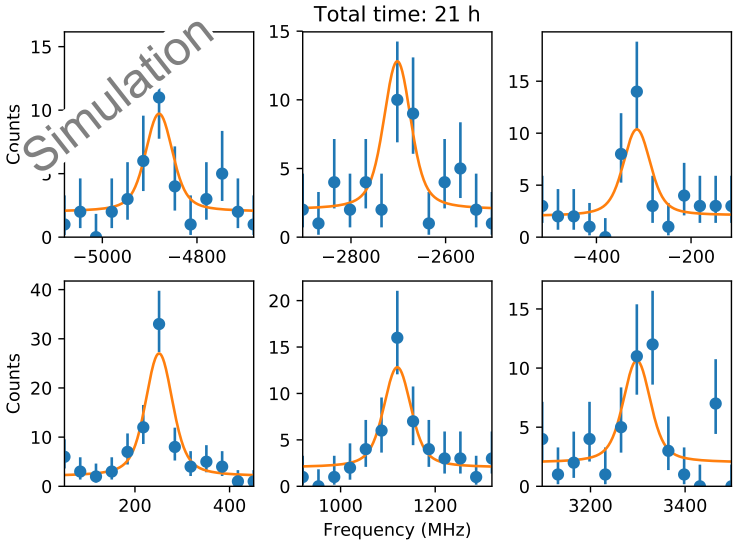

Figure 6.6: Simulated hyperfine spectrum peaks of ^{79}Cu, assuming a five-fold improvement in both the background suppression and in the signal rate.

state B-parameter and the Lorentzian component of the full-width-at-half-maximum (FWHM). Only samples taken after the red line are used for parameter estimation, since before that point the MCMC has not yet started sampling the parameter space properly. One of the spectra was taken with temporally overlapping laser pulses, which results in a broadening of the lines, as can be seen on the blue trace. When delaying the second step laser, this power broadening is removed (due to the mechanisms described in section 4.1.1), as can be seen in the orange trace.

The correlation of the fit parameters can be visualized by plotting two-dimensional marginal distributions. These marginal posterior distributions for a scan of ^{65}Cu are shown in 6.8. During this scan, the two laser pulses were overlapped in time. There is a positive correlation between the lower- and upper-state A-parameter, though the upper-state B-parameter appears uncorrelated. This is the case for all scans for all isotopes. The parameters that model the lineshape (linewidths, scaling and width of the Lorentzian pedestal) are quite strongly correlated, but are not correlated to the hyperfine parameters. The posterior distribution of the background parameter in figure 6.8 is clearly not Gaussian, but looks more exponential[1]. Similar plots for the hyperfine

---

[1] This illustrates how doing a chi-squared regression, or a scaling of the uncertainties with the reduced chi-squared is in principle not justified.

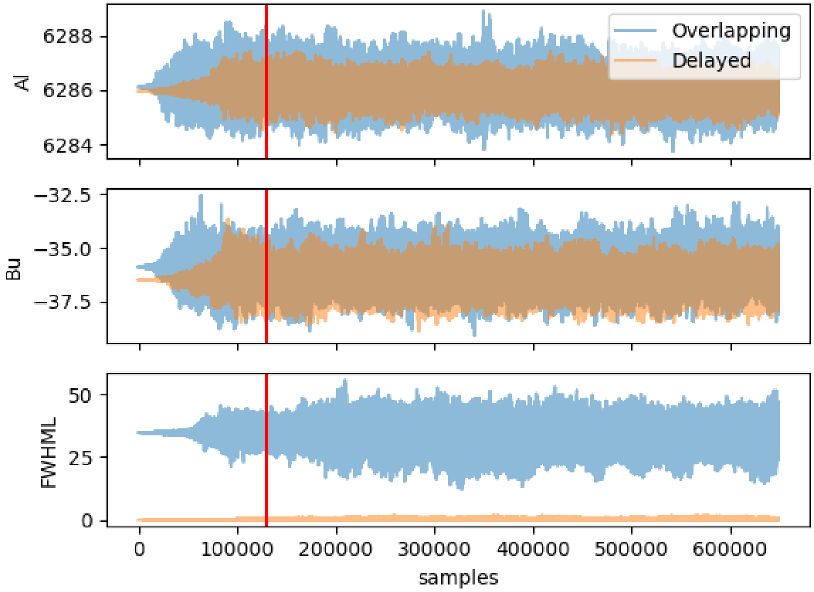

Figure 6.7: Samples from the marginal posterior distribution, drawn using a MCMC. Samples before the red line are discarded. Delaying the second laser step reduces the linewidth of the resonances considerably.

parameters for scans of ^{76,77,78}Cu are shown in figure 6.9. In figure 6.10, the same posterior samples are shown, but with similar dispersions for the x- and y-axes. This illustrates how the size of the uncertainty and the coverage in parameter space of the MCMC samples are related.

In table 6.4, the final values of the hyperfine parameters are given, obtained using the procedure outlined in chapter 5. The numbers in round brackets represent the one standard deviation estimates of the uncertainty. For ^{78}Cu, a model-independent spin assignment could not be made, which is why all the observables for several spin options are listed. Table 6.5 in turn lists the extracted moments and changes in mean-squared charge radius, and compares them to the literature values. The moments were computed using the following reference values for ^{65}Cu: $A_l = 6284.389972(6)\,\mathrm{MHz}$ [83], $B_u = -25.0(2)\,\mathrm{MHz}$ [59], $\mu = 2.38167(25)\,\mu_N$ [84] and $Q = 19.5(4)\,\mathrm{efm}^2$ [85, 86]. The calculation of the charge radii from the isotope shifts is discussed next.

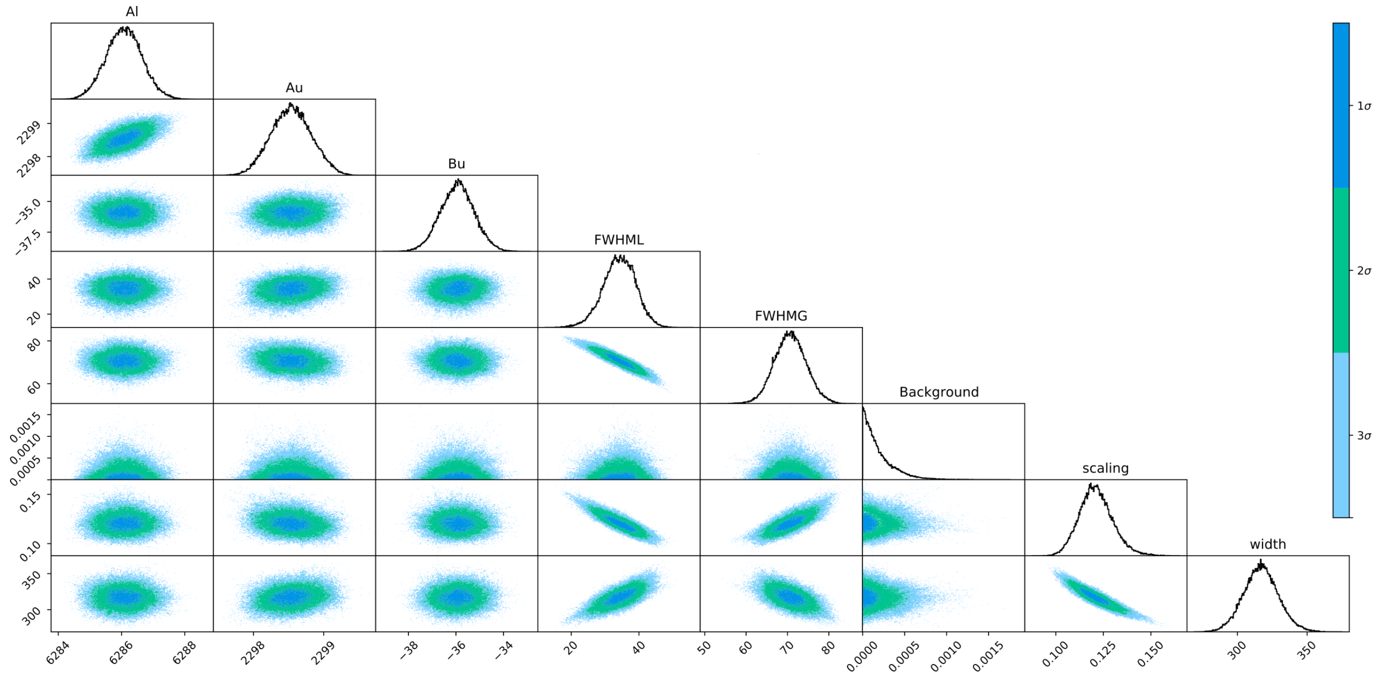

Figure 6.8: Two-dimensional marginal distributions for some of the fit parameters for a spectrum of ^{65}Cu. This hyperfine spectrum was recorded using temporally overlapping laser pulses.

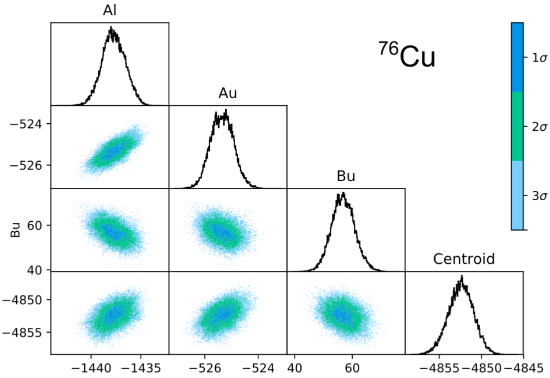

(a) Marginal posterior samples for ^{76}Cu.

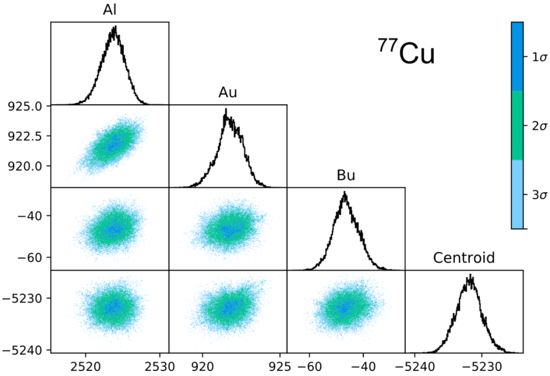

(b) Marginal posterior samples for ^{77}Cu.

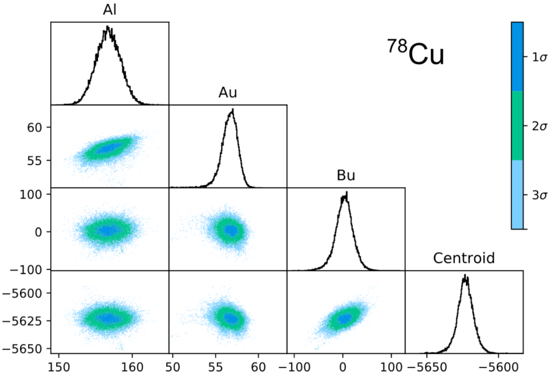

(c) Marginal posterior samples for ^{78}Cu.

Figure 6.9: MCMC samples from the marginal posterior distribution of the hyperfine parameters for typical scans of ^{76,77,78}Cu.

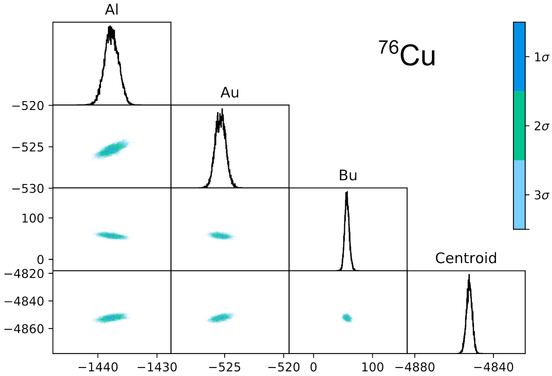

(a) Marginal posterior samples for ^{76}Cu.

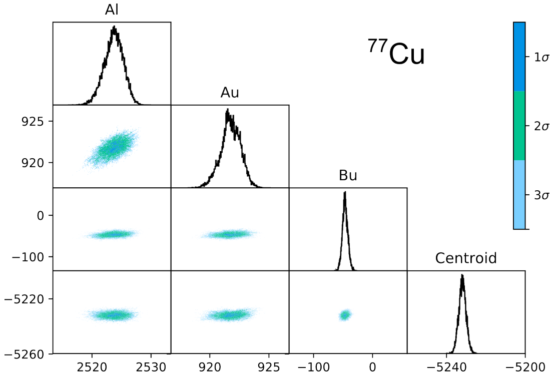

(b) Marginal posterior samples for ^{77}Cu.

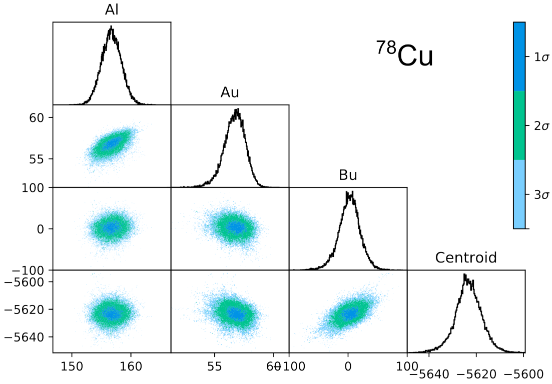

(c) Marginal posterior samples for ^{78}Cu.

Figure 6.10: MCMC samples from the marginal posterior distribution of the hyperfine parameters for typical scans of ^{76,77,78}Cu, this time with similar x- and y-axis dispersions.

Table 6.4: Hyperfine parameters, ratio of A-parameters, and isotope shifts obtained in this work, compared to the available literature [5, 59, 83].

A	I	A_l (MHz)	A_l^{lit} (MHz)	A_u (MHz)	A_l/A_u	$A_l^{\mathrm{lit}}/A_u^{\mathrm{lit}}$	B_u (MHz)	B_u^{lit} (MHz)	IS (MHz)
63	3/2	+5866.3(11)	+5866.90871(2)	+2145.3(06)	+2.734(1)	+2.741(3)	-39.2(18)	-37.9(2)	+1055.4(2.6)
65	3/2	+6284.1(5)	+6284.38997(6)	+2296.76(28)	+2.7361(5)	+2.742(3)	-36.4(10)	-35.0(2)	-
69	3/2	+7492.0(20)	+7490(2)	+2738.5(10)	+2.736(2)	-	-27.9(32)	-	-1937(5)
71	3/2	+6003.9(20)	+6001.4(14)	+2194.5(10)	+2.736(2)	-	-32.2(34)	-	-2787(4)
73	3/2	+4597.9(23)	+4597.8(12)	+1679.7(11)	+2.737(2)	-	-41(4)	-	-3634(5)
75	5/2	+1592.4(16)	+1591.5(17)	+582.5(0)	+2.734(2)	-	-49.4(31)	-	-4455(4)
77	5/2	+2524.4(26)	-	+921.9(13)	+2.738(3)	-	-47(5)	-	-5234(5)
64	1	-856.0(21)	-856.6(15)	-307.5(12)	+2.786(6)	-	+11.3(34)	-	+508(5)
66	1	+1115.0(20)	+1118(3)	+399.5(11)	+2.789(3)	-	+11.7(34)	-	-529(5)
68	1	+9471.4(20)	+9475.8(16)	+3460.6(10)	+2.737(2)	-	-13.0(32)	-	-1498(5)
68	6	+761.1(18)	+761.6(3)	+278.5(10)	+2.733(2)	-	-85.0(33)	-	-1479(4)
70	6	+7032.7(35)	+7035(5)	+2573.0(18)	+2.733(3)	-	-24(5)	-	-2375(7)
70	3	-4436.6(27)	-4437.1(12)	-1621.8(14)	+2.736(3)	-	-33(5)	-	-2390(7)
70	1	+901.0(27)	+901.4(3)	+329.4(14)	+2.735(3)	-	-50(5)	-	-2397(6)
72	2	-2663.2(29)	-2664.3(8)	-972.9(15)	+2.737(3)	-	+18(5)	-	-3240(7)
74	2	-2109.2(24)	-2109(2)	-772.2(12)	+2.733(3)	-	+46(5)	-	-4057(5)
76	3	-1437.4(20)	-	-524.8(10)	+2.739(2)	-	+62(4)	-	-4848(5)
78	1	+676(9)	-	+181(4)	+3.74(6)	-	-43(7)	-	
78	2	+406(5)	-	+132(10)	+3.1(1)	-	-68(14)	-	
78	3	+291(4)	-	+102(3)	+2.84(6)	-	-50(15)	-	
78	4	+226(4)	-	+81(2)	+2.79(4)	-	-29(16)	-	
78	5	+185.1(34)	-	+67(2)	+2.77(4)	-	-11(22)	-	
78	6	+156.7(32)	+0(400)	+57(3)	+2.76(4)	-	+3(20)	-	-5623(10)
78	7	+135.8(33)	-	+49(2)	+2.76(4)	-	+13(21)	-	

Table 6.5: Moments and radii obtained in this work. For the radii, The values in round brackets indicate the uncertainty due to the statistical uncertainty on the isotope shifts, whereas square brackets also take the uncertainty on the M and F into account. Literature values from [5, 6, 8, 36, 84–86]

A	I	$\mu(\mu_N)$	$\mu_{\text{lit}}(\mu_N)$	Q (eb)	Q_{lit} (eb)	$\delta\langle r^2\rangle^{A,65}$	$\delta\langle r^2\rangle^{A,65}_{\text{lit}}$
63	3/2	+2.2232(5)	+2.22329(18)	-21.8(11)	-21.1(4)	-0.140(7)[20]	-0.148(1)[17]
65	3/2	+2.3816(4)	+2.38167(25)	-20.3(7)	-19.5(4)	0(0)[0]	0(0)[0]
69	3/2	+2.8394(8)	+2.8383(10)	-15.6(18)	-14.7(16)	+0.24(1)[4]	+0.237(3)[34]
71	3/2	+2.2754(8)	+2.2747(8)	-17.9(20)	-19.0(16)	+0.44(2)[7]	+0.407(11)[44]
73	3/2	+1.7425(9)	+1.7426(8)	-22.9(21)	-20.0(10)	+0.52(2)[8]	+0.523(15)[58]
75	5/2	+1.0058(10)	+1.0062(13)	-27.5(18)	-26.9(16)	+0.56(1)[9]	+0.546(21)[80]
77	5/2	+1.5945(16)	+1.61(5)	-26.0(31)	-	+0.59(2)[11]	-
64	1	-0.2163(5)	-0.2164(4)	+6.3(19)	+7.2(9)	-0.09(1)[2]	-0.118(3)[13]
66	1	+0.2817(5)	+0.2823(8)	+6.5(19)	+5.6(13)	+0.01(1)[2]	+0.033(5)[12]
68	1	+2.3930(6)	+2.3933(6)	-7.3(18)	-8.2(13)	+0.13(1)[3]	+0.132(5)[31]
68	6	+1.1537(28)	+1.1548(6)	-47.4(21)	-44.0(19)	+0.17(1)[3]	+0.191(4)[31]
70	6	+1.7769(9)	+1.3666(5)	-13.3(27)	-28.5(14)	+0.32(2)[5]	+0.270(3)[44]
70	3	-3.3628(21)	-3.3641(15)	-18.4(31)	-13(4)	+0.29(2)[5]	+0.287(11)[44]
70	1	+1.366(4)	+1.7779(15)	-27.7(28)	-12(3)	+0.27(2)[5]	+0.323(11)[44]
72	2	-1.3458(15)	-1.3472(10)	+10.1(26)	+8(2)	+0.43(2)[7]	+0.429(5)[55]
74	2	-1.0658(12)	-1.068(3)	+25.5(26)	+26(3)	+0.53(1)[9]	+0.505(18)[72]
76	3	-1.0895(16)	-	+34.3(23)	-	+0.58(2)[10]	-
78	1	+0.171(2)	-	-24(4)	-		-
78	2	+0.204(2)	-	-38(8)	-		-
78	3	+0.222(3)	-	-28(9)	-		-
78	4	+0.229(4)	-	-16(9)	-		-
78	5	+0.234(4)	-	-6(12)	-		-
78	6	+0.238(5)	0.0(4)	+2(10)	-	+0.58(3)[11]	-
78	7	+0.240(6)	-	+7(12)	-		-

6.2.1 Extracting radii from the isotope shifts

Figure 6.11 shows a King plot that combines the isotope shifts for the 324 nm line found in [36] and those obtained in this work. The figure furthermore shows the line of best fit, obtained using the method outlined in 5.5.1, and a the 68% confidence band on this fit are plotted. From the slope and intercept of this best fit, and using $M_{324} = 1413(27)\,\mathrm{GHz\,fm^{-2}}$ and $F_{324} = -779(78)\,\mathrm{GHz\,u}$ [36], the mass and field shift factors for the 249 nm line can be calculated. The systematic uncertainty on the isotope shifts due to the unknown true beam energy is not included in the uncertainties; they are merely the result of the propagation of uncertainty on M_{324} and F_{324} through the fit. Figure 6.12 shows samples drawn from the (marginal) posterior distributions of the fitted M_{249} and F_{249}-parameters, as well as the uncertainty scaling parameter β in equation (5.26). Note the strong positive correlation of M_{249} and F_{249}, and how, as expected, an increase in the scaling factor β also results in wider posterior distributions for M_{249} and F_{249}.

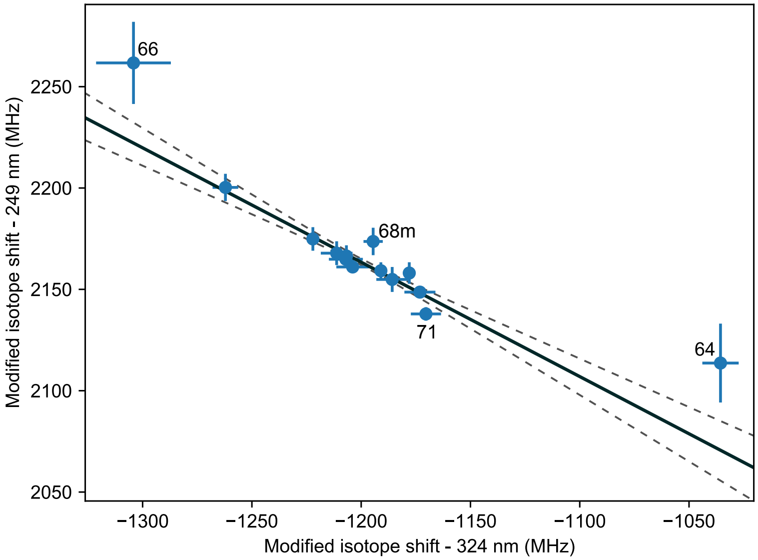

Figure 6.11: King plot of the 324 nm and 249 nm line data. The points for ^{64,66,68m}Cu (labeled on the plot) were flagged as points with potentially underestimated uncertainties by the fitting met hod. The line is the line of best fit, the band indicates the 1-σ uncertainty band.

Figure 6.13 shows the marginal distributions of the outlier classification parameters g_i for all isotopes (and isomers). The distributions are centered closer to 1 for ^{64,66,68m,71}Cu, providing indication that these points deviate somewhat from the trend of the other isotopes. The distributions of all g_i are all rather broad though, implying that none of the isotope shifts deviate too dramatically. The discrepancies are not due to a systematically under- or overestimation of the isotope shifts compared to literature, since the modified isotope shifts are obtained by multiplication of the experimental isotope shifts with the reduced mass, which is different for each isotope and even has a different sign for ^{64}Cu. The origins of the deviations of those few measurements from the trend of the other isotopes is at this moment not clear. Note that effects like a possible second-order hyperfine perturbation have not been included. Such hyperfine mixing could contribute to inconsistencies in the data. Furthermore, the hyperfine parameters of ^{64,66}Cu are quite small, and that these spectra were obtained using temporally overlapped laser pulses. It could therefore be that the approach used to asymmetrize the lineshapes, well motivated for clearly resolved peaks, is no longer valid for overlapping or partially resolved structures. Future measurements are needed to better understand these observations and to establish the cause of the deviations.

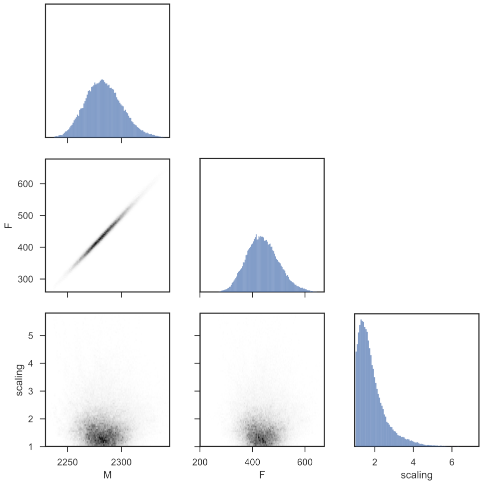

Figure 6.12: Summary of the samples drawn from the posterior disitribution of the M_{249}- and F_{249}-parameters obtained from the Bayesian analysis of the King plot, as well as the estimated scaling factor of the uncertainties of the points that were flagged as potential outliers.

Table 6.6 shows these mass and field shift factors, and compares them to those obtained using a standard chi-squared fit, and the bootstrapping approach

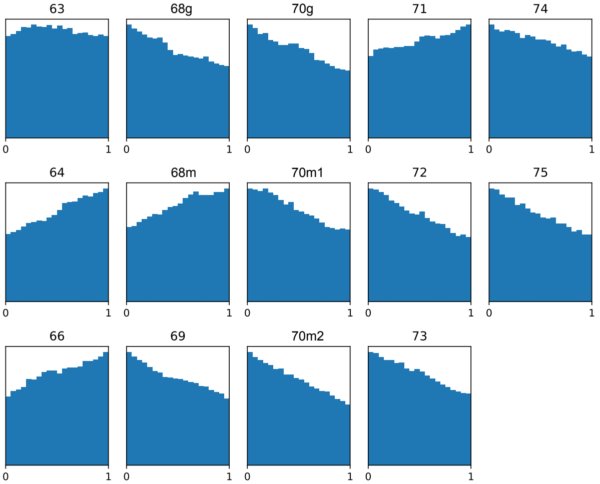

Figure 6.13: Samples of the outlier classification parameters g_i for each isotope. No clear outliers are found, but for ^{64,66,68m}Cu and perhaps ^{71}Cu, the distribution is skewed in favour of the outlier model component of model (5.26).

outlined in section 5.5.2. All results mutually compatible, though the chi-squared fit appears to result slightly smaller uncertainties. For the final numbers, the average of the values is taken, and the uncertainty is chosen as the largest of the uncertainties (which are anyhow very similar). The final values are therefore $M_{249} = 2284(24)\,\mathrm{GHz\,fm^{-2}}$ and $F_{249} = 439(80)\,\mathrm{GHz\,u}$. The charge radii obtained in this work are given in table 6.5. The King plot already illustrated good agreement of the isotope shifts with literature, which naturally also translates into good agreement of the radii with literature radii.

Table 6.6: Comparison of the different king plot fits.

Method	M_{249} (GHz fm^{-2})	F_{249} (GHz u)
χ^2-fit ($\chi^2_{\mathrm{red}} = 1.4$)	2284(21)	438(70)
Bayesian fit (see 5.5.1)	2284(24)	439(80)
Bootstrapping (see 5.5.2)	2285(24)	441(80)
Final	2284(24)	439(80)

6.3 Interpretation

6.3.1 Nuclear spins

As discussed in section 2.3.1, the ratio of the hyperfine A-parameters of the ground and excited state should be constant, which provides a nuclear-model independent way of extracting the nuclear spin of a particular state. In figure 6.14 this ratio is plotted for all isotopes (with the values also listed in table 6.4), except ^{64,66,78}Cu. The ratio for ^{64,66}Cu deviates significantly from the average of the other isotopes, for reasons that are unclear. Further measurements on ^{64,66}Cu and also ^{62}Cu (which has a similar structure) under carefully controlled conditions would help to better understand this observation. For ^{78}Cu, the uncertainty on the ratio is much larger than the scale of figure 6.14, which is why it is also not shown.

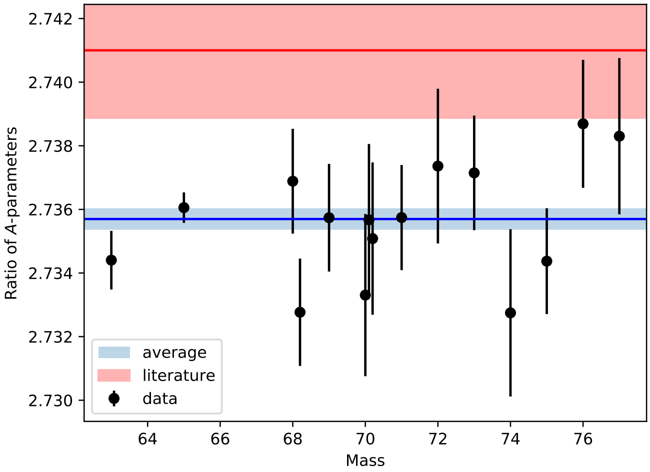

Figure 6.14: Ratio of hyperfine A-parameters for $^{63,65,69-77}$Cu. The blue band indicates the average the ratios of all the isotopes, the red band is obtained using literature values.

The blue band in figure 6.14 represents the weighted average of the ratio for all isotopes. The data is consistent with the ratio being constant; i.e. no strong evidence for the presence of a hyperfine anomaly can be observed. For ^{76,77}Cu, the ratio for $I = 3$ and $5/2$ is used. These spin assignments will be discussed further in this section.

The ratio of A-parameters obtained using literature values of A_l [83] and A_u [59] are shown using the red band. Our new value agrees with the literature value within two standard deviations. While this deviation could be simply a statistical effect, it is worth noting that this experiment is the only one that simultaneously measured both A-parameters, and that our measured values of A_l agree with all available literature values. Furthermore, the level-crossing measurement of A_u found in [59] does not directly measure the A_u, but required an independent measurement of the electron Landé factor g_J.

Tentative spin assignments have been made for $^{76-78}$Cu, mostly based on β-decay studies. For ^{76}Cu, tentative assignments of I=$(3^-, 4^-)$ have been made [87]. For ^{77}Cu, an assignment of I=5/2 was made based on the intensity ratio of partially resolved hyperfine structures obtained with in-source laser spectroscopy [8], in agreement with earlier β-decay studies [88, 89]. Finally, For ^{78}Cu, spin $(4^-,5^-,6^-)$ were suggested in literature. Spins $(4^-,5^-)$, proposed in [87] are based on absence of β feeding to (2^+) and (6^+) levels in ^{78}Zn, and from shell-model predictions. A spin (6^-) suggestion was additionally added based on β feeding to high-spin 6^+, 8^+ states in ^{78}Zn [90].

The ratio of hyperfine A-parameters can be used to perform spin assignments in a shell-model independent way. From this figure, it is clear that the ground-state spins of ^{76,77}Cu are 3 and 5/2, respectively.

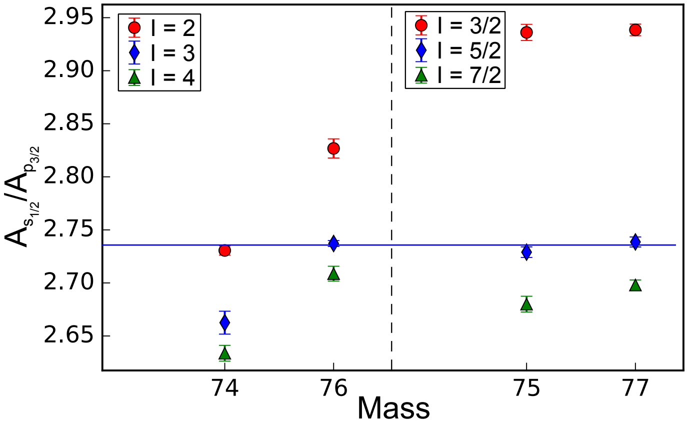

Figure 6.15: Ratio of hyperfine A-parameters for different assumptions of I for ^{74,75,76,77}Cu. Literature assignments are confirmed for ^{74,75}Cu, and new and unambiguous spin assignments of $I = 3$ and $I = 5/2$ for ^{76,77}Cu are possible.

For ^{78}Cu, the ratio test is only sufficiently sensitive to rule out spins 1,2 and perhaps 3, as is shown in figure 6.16.

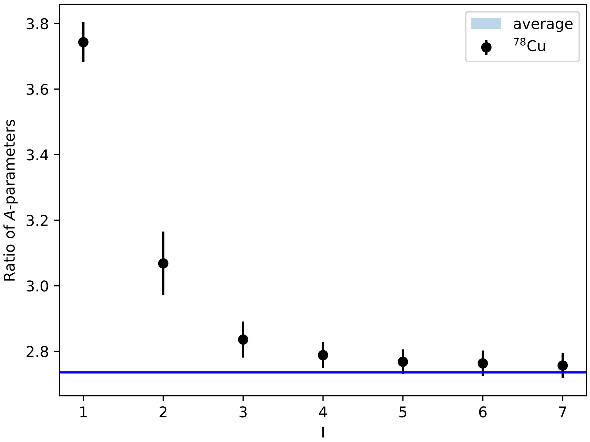

Figure 6.16: Ratio of hyperfine A-parameters for different assumptions of I for ^{78}Cu. The blue line indicates the averate ratio obtained using all the other isotopes.

6.3.2 Article V: Dipole and quadrupole moments of $^{73-78}$Cu as a test of the robustness of the $Z = 28$ shell closure near ^{78}Ni

A detailed discussion of the magnetic dipole moments and the electric quadrupole moments of $^{76-78}$Cu, and what they can tell us about the robustness of the $Z = 28$ shell closure is presented in **Article V**, printed below. Some supplementary information will be presented afterwards.

Dipole and quadrupole moments of $^{73-78}$Cu as a test of the robustness of the $Z = 28$ shell closure near ^{78}Ni

R. P. de Groote,[1,*] J. Billowes,[2] C. L. Binnersley,[2] M. L. Bissell,[2] T. E. Cocolios,[1]
T. Day Goodacre,[3] G. J. Farooq-Smith,[1] D. V. Fedorov,[4] K. T. Flanagan,[2]
S. Franchoo,[5] R. F. Garcia Ruiz,[2] Á. Koszorús,[1] K. M. Lynch,[6] G. Neyens,[1,6]
F. Nowacki,[7] T. Otsuka,[1,8,9,10] S. Rothe,[2,3] H. H. Stroke,[11] Y. Tsunoda,[10]
A. R. Vernon,[2] K. D. A. Wendt,[12] S. G. Wilkins,[2] Z. Y. Xu,[1] and X. F. Yang[1]

[1]*KU Leuven, Instituut voor Kern- en Stralingsfysica, B-3001 Leuven, Belgium*

[2]*School of Physics and Astronomy,*
The University of Manchester, Manchester M13 9PL, UK

[3]*Engineering Department, CERN, CH-1211 Geneva 23, Switzerland*

[4]*Petersburg Nuclear Physics Institute, 188350 Gatchina, Russia*

[5]*Institut de Physique Nucléaire d'Orsay, F-91406 Orsay, France*

[6]*Physics Department, CERN, CH-1211 Geneva 23, Switzerland*

[7]*Institute Pluridisciplinaire Hubert Curien,*
23 rue du Loess, F-67037 Strasbourg Cedex 2, France

[8]*Department of Physics, University of Tokyo,*
Hongo, Bunkyo-ku, Tokyo 113-0033, Japan

[9]*RIKEN Nishina Center, 2-1 Hirosawa, Wako, Saitama 351-0198, Japan*

[10]*Center for Nuclear Study, University of Tokyo,*
Hirosawa, Wako, Saitama 351-0198, Japan

[11]*Department of Physics, New York University, New York, New York 10003, USA*

[12]*Institut für Physik, Johannes Gutenberg-Universität, D-55128 Mainz, Germany*

Abstract

Nuclear spins and precise values of the magnetic dipole and electric quadrupole moments of the ground-states of neutron-rich $^{76-78}$Cu isotopes were measured using the Collinear Resonance Ionization Spectroscopy (CRIS) experiment at ISOLDE, CERN. The nuclear moments of the less exotic ^{73,75}Cu isotopes were re-measured with similar precision, yielding values that are consistent with earlier measurements. The moments of the odd-odd isotopes, and $^{78}_{29}$Cu ($N = 49$) in particular, are used to investigate excitations of the assumed doubly-magic ^{78}Ni core through comparisons with large-scale shell-model calculations. Despite the narrowing of the $Z = 28$ shell gap between $N \sim 45$ and $N = 50$, the magicity of $Z = 28$ and $N = 50$ is restored towards ^{78}Ni. This is due to weakened dynamical correlations, as clearly probed by the present moment measurements.

The atomic nucleus is a complex system consisting of many interacting particles that nevertheless exhibits shell structure. Theoretical understanding of the shell gaps and, in particular, the magic nucleon numbers of 28 and 50, required the introduction of a strong spin-orbit force [1, 2]. In recent years, evidence interpreted as an evolution of the magic numbers when going away from the valley of stability has steadily grown, making the study of shell evolution one of the challenges in nuclear physics [3, 4]. The very exotic ^{78}Ni ($Z = 28, N = 50$) nucleus is a cornerstone in this investigation, and a large volume of theoretical and experimental work has already been devoted to testing these magic numbers [4–16]. However, low production rates of isotopes in the vicinity of ^{78}Ni (and, in particular, low production rates of the nickel isotopes themselves) have slowed experimental progress.

Information on the size of the shell gaps as well as the correlations in the ^{78}Ni system are required in order to confirm or refute its magicity. Nuclear dipole and quadrupole moments provide some of the most sensitive and direct tests for calculated nuclear wavefunctions [17], and are therefore crucial observables to help settle the ongoing debate. Previously measured magnetic moments of copper ($Z = 29$) isotopes [18–22] revealed the presence of proton excitations across $Z = 28$, and therefore provided evidence for a breaking of this shell closure around $N = 45$ [23]. Recent shell-model calculations predicted the size of the shell gap at $N = 50$ to be smaller than at $N = 45$ [24, 25]. The reduction in the size of the shell gap could lead to a destabilization of ^{78}Ni. However, any discussion of the magicity of ^{78}Ni is incomplete without experimental information on proton-neutron excitations of the ^{78}Ni core. As far as the copper isotopes are concerned, only the magnetic dipole moment of ^{77}Cu has been measured beyond $N = 46$ [26]. Much-needed studies closer to $N = 50$ were initiated through laser spectroscopy of gallium ($Z = 31$) [27, 28] and zinc ($Z = 30$) [29, 30]. These results confirm the rapid evolution of proton and neutron shell gaps due to the strong $\pi f_{5/2} - \nu g_{9/2}$ interaction [7]. Unfortunately, the presence of additional valence protons prevent these studies from pinning down the role of the nickel core excitations. Therefore, the need for experimental data on isotopes in close proximity of ^{78}Ni remains, especially in light of the rapid shell evolution in this region of the nuclear chart.

In this Letter we present precision measurements of the nuclear magnetic dipole and electric quadrupole moments of $^{76-78}$Cu ($Z = 29$). Through comparisons of the experimental moments to state-of-the-art shell-model calculations, the evolution of the robustness of the $Z = 28$ closure towards $N = 50$ is directly investigated. The odd-odd isotopes, and in

Table I. Hyperfine parameters, magnetic dipole moments μ and electric quadrupole moments Q obtained in this work, compared to literature [20, 21, 26] and results from shell-model calculations using A3DA-m and PFSDG-U.

Mass	I	A_l (MHz)	μ (μ_N)			
		This work	This work	Literature	A3DA-m	PFSDG-U
73	$3/2^-$	+4598(2)	+1.7425(9)	+1.7426(8)	+1.75	-
74	2^-	-2109(2)	-1.0658(12)	+1.068(3)	-1.12	-1.04
75	$5/2^-$	+1592.4(16)	+1.0058(10)	+1.0062(13)	+1.01	+0.90
76	3^-	-1437(2)	-1.0895(15)	-	-1.09	-1.04
77	$5/2^-$	+2524(3)	+1.5945(17)	+1.61(5)	+1.62	+1.55
78	(6^-)	+157(2)	+0.238(3)	0.0(4)	-0.04	+0.35
79	$(5/2^-)$	-	-	-	+1.96	+1.96
Mass	I	B_u (MHz)	Q (e fm^2)			
		This work	This work	Literature	A3DA-m	PFSDG-U
73	$3/2^-$	-41(4)	-23(2)	-20.0(8)	-18.15	-
74	2^-	+45(3)	+25(3)	+26(3)	+21.84	+23.03
75	$5/2^-$	-49(4)	-27.5(17)	-26.9(16)	-27.66	-29.20
76	3^-	+62(4)	+34(2)	-	+33.73	+35.86
77	$5/2^-$	-47(4)	-26(3)	-	-26.44	-28.10
78	(6^-)	+3(20)	+2(10)	-	+13.40	+10.57
79	$(5/2^-)$	-	-	-	-22.71	-22.50

particular ^{78}Cu, are advantageous probes for the structure of the ^{78}Ni core. This advantage lies in the proximity of these isotopes to ^{78}Ni, and in the sensitivity of their nuclear moments to simultaneously proton- and neutron excitations. This Letter therefore also highlights the importance of studying the static moments of odd-odd systems near doubly-closed shells for stringent testing of theoretical models.

The copper isotopes of interest were produced at the ISOLDE facility at CERN by impinging 1.4 GeV protons onto the neutron converter [31] of a UC$_x$ target. After diffusing out of the target, the copper isotopes were laser ionized using the RILIS laser ion source [26, 32, 33], extracted at 30 keV and mass separated by the high-resolution separator. The ions were then injected into the gas-filled radio-frequency linear Paul trap ISCOOL [34, 35]. After 10 ms of accumulation in ISCOOL, the bunches of copper ions were extracted at 30 keV. The electromagnetic moments of the copper isotopes were then measured using the Collinear Resonance Ionization Spectroscopy (CRIS) technique [36, 37], which combines high sensitivity with high resolution, thus allowing experiments on exotic beams with intensities as low as 20 ions/s (such as ^{78}Cu). Upon entering the CRIS beamline, the ion bunches produced by ISCOOL were neutralized by passing through a potassium-vapour charge-exchange cell [38]. The remaining ionic fraction was electrostatically deflected, so only neutral atoms entered the laser-atom interaction region. These neutral atoms were collinearly overlapped with two pulsed laser beams to induce two-step resonant laser ionization. The ions of interest were deflected from the background neutral atoms, onto a micro-channel plate detector. This provides nearly background free detection: in this experiment, the suppression of collisional background counts was estimated at 1:10^7 at mass 78, representing an improvement by two orders of magnitude compared to our previous work [36]. By recording the number of resonant ions as a function of the laser frequency, the hyperfine structure of the copper atoms was measured. The resonant ion detection rate for the most exotic isotope ^{78}Cu was at most approximately 0.05/s. Only due to the high background suppression and efficiency could the hyperfine spectrum shown in Fig. 1 be measured in just 8 hours.

Atoms were resonantly excited from the $3d^{10}4s\ ^2S_{1/2}$ ground state to the $3d^9(^2D)4s4p(^3P^\circ)\ ^4P^\circ_{3/2}$ level at 40114.01 cm^{-1}. This was achieved using an injection-locked titanium-sapphire laser system developed by the Johannes Gutenberg-Universität Mainz and the University of Jyväskylä [39, 40]. Through pulsed amplification of 749 nm continuous-wave seed light produced by a M-squared SolsTis titanium-sapphire laser, narrowband pulsed laser light was produced at a repetition rate of 1 kHz. This laser light was then frequency tripled using two nonlinear crystals to produce the required narrowband (≈40 MHz) 249 nm light for the resonant excitation step. Resonant ionization of these excited atoms was achieved using a 314.2444 nm transition to the $3d^94s(^3D)4d\ ^4P_{3/2}$ auto-ionizing state at 71927.28 cm^{-1}, using light produced by a frequency-doubled Spectron Spectrolase 4000 pulsed-dye laser pumped by a Litron LPY 601 50-100 PIV Nd:YAG laser, at a repetition rate of 100 Hz. The 344(20) ns lifetime [41] of the excited state allowed the 314 nm laser pulse to be delayed by 50 ns with respect to the first laser pulse, removing lineshape distortions and power broadening effects [37, 42] in the observed hyperfine spectra, without measurable losses in

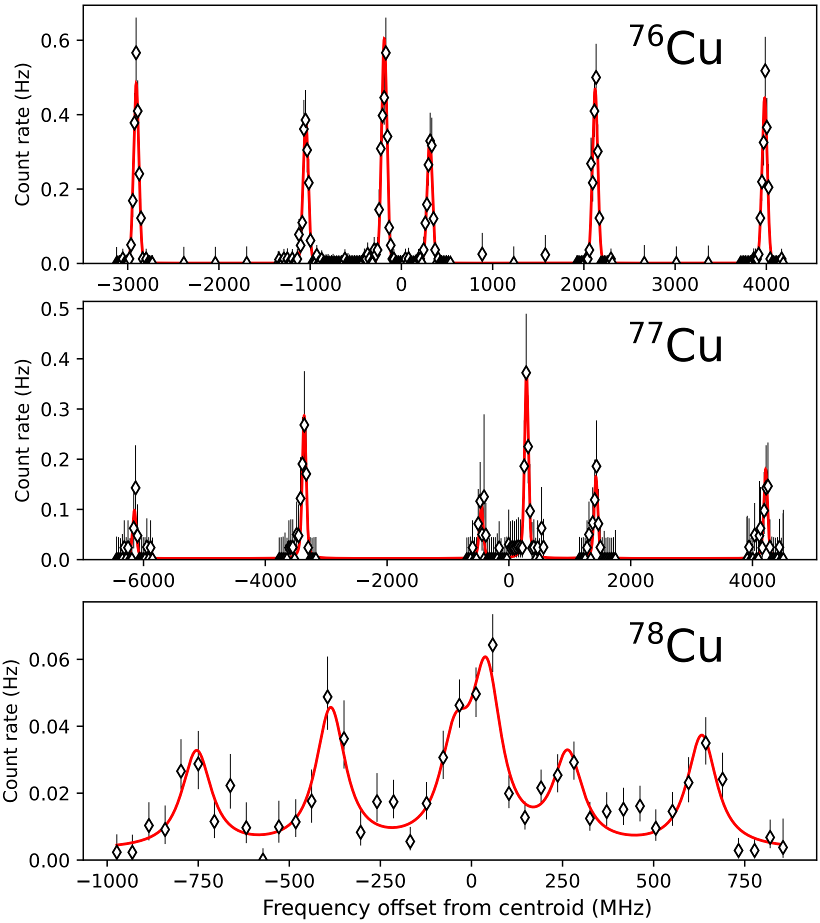

Figure 1. Example spectra of $^{76-78}$Cu plotted relative to their individual fitted centroid frequencies. A FWHM of 75 MHz was achieved, due in part to the laser linewidth of ≈40 MHz.

efficiency.

Table I shows the extracted hyperfine A and B parameters, defined as $A = \frac{\mu B_0}{IJ}$ $B = eQV_{zz}$, with B_0 and V_{zz} respectively the magnetic field and the electric field gradient generated by the electrons at the nucleus. By combining these equations with literature values, the dipole and quadrupole moments of $^{73-78}$Cu were obtained, listed in Table I. For every scan, the hyperfine parameters and uncertainty estimates were extracted using a maximum-likelihood optimization, performed using the SATLAS code [43]. A Voigt lineshape was used, with additional modifications to model small lineshape asymmetries (to be detailed in a later publication). Final values for each isotope were then computed as a dispersion-corrected weighted mean, using the inverse square of the statistical fit uncertainties as weights. All reported uncertainties represent the 68 % credible intervals. The moments were calculated with ^{65}Cu as the reference, using $\mu = 2.3817(3)\mu_\mathrm{N}$ [44], $Q = -19.5(4)\,\mathrm{e\,fm}^2$ [45, 46], $A = 6284.389972(60)\,\mathrm{MHz}$ [47] and $B = -35.0(2)\,\mathrm{MHz}$ [48]. The results are compared to literature values where available, showing excellent agreement and similar precision, demonstrating the performance of this CRIS set-up.

The ratio of the hyperfine A parameters of the atomic ground and excited state is a constant for all isotopes of an element (aside from the negligibly small hyperfine anomaly [48, 49]). This was verified with the data obtained on $^{63-75}$Cu, as will be discussed in a later publication. If this ratio can be determined with sufficient precision, it provides a model-independent way to determine the nuclear spin. Based on this ratio, firm spin assignments of $I = 3$ for ^{76}Cu and $I = 5/2$ for ^{77}Cu can be made, consistent with earlier tentative values of 3 or 4 for ^{76}Cu [50] and 5/2 for ^{77}Cu [26, 51, 52]. The larger uncertainties and the reduced sensitivity of the A-ratio for higher values of I prevents a firm spin assignment for ^{78}Cu using this test. However, shell-model calculations (which will be introduced later) were found to be in best agreement for spin 6. This value provides further evidence for the earlier tentative assignment presented in [53]. For the remainder of this Letter, a spin 6 will therefore be assumed for ^{78}Cu. Note that, while the agreement is best for $I = 6$, the other spin options $I = 4, 5, 7$ also result in fair agreement. More details on these spin assignments will be reported in a later publication.

An overview of the model spaces used in the shell-model calculations presented in this Letter is shown in Fig. 2. Calculations starting from a ^{56}Ni core, with protons and neutrons restricted to the $f_{5/2}, p_{3/2}, p_{1/2}, g_{9/2}$ shell between $N, Z = 28$ and $N, Z = 50$ are performed using the JUN45 interaction [54]. Calculations in a more extended space which includes the $f_{7/2}$ orbits below 28 and the $d_{5/2}$ orbits above 50 were performed using the A3DA-m [11, 55] interaction. The results for the most neutron-rich isotopes, from $N = 45$ onwards, are also compared to calculations including the full negative parity pf shell for protons and full positive parity sdg shell for neutrons using the recently developed PFSDG-U interaction [16]. For all magnetic moment calculations, a spin-quenching factor of 0.75 was used, based

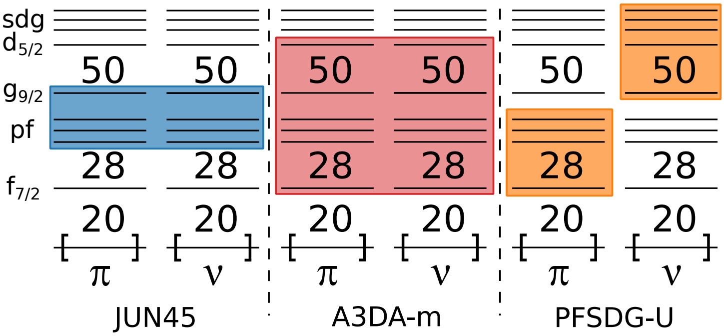

Figure 2. Model spaces used in this Letter for the JUN45, A3DA-m and PFSDG-U calculations.

on the value of 0.75±0.02 suggested in [56] for pf-shell nuclei. Effective orbital g-factors were taken to be 1.1 and −0.1 for protons and neutrons respectively. For the quadrupole moment calculations, effective charges of $e_p = 1.5, e_n = 1.1$ were assumed for JUN45 [54]. For A3DA-m and PFSDG-U calculations the microscopically derived effective charges of $e_p = 1.31, e_n = 0.46$ [57] were chosen. Table I summarizes the results of these calculations.

In panels a and c of Fig. 3, the experimental and theoretical moments of the odd-A copper isotopes between $N = 44$ and $N = 50$ are presented. Where possible, the weighted mean of this work and literature values are plotted. Earlier calculations for the odd-even isotopes, which were performed in a model space that included the full pf-shell for protons and limited the neutrons to orbits up to $N = 50$, illustrated the need for excitations of protons across $Z = 28$ [23]. Excitations of neutrons across $N = 50$, absent due to the model space that was used, seemed unneeded, and quadrupole moments were furthermore not compared to. The importance of these cross-shell proton excitations is confirmed in panel a: the A3DA-m and PFSDG-U magnetic moments are in excellent agreement with the data for all odd-A copper isotopes, while the JUN45 values deviate, in particular for ^{73}Cu. From the comparison of the quadrupole moments of the odd-A copper isotopes to the different calculations, shown in panel c, no firm conclusions can be made considering the importance of neutron excitations. This is due to the larger uncertainties on $Q(^{77}\mathrm{Cu})$.

However, the odd-odd moments are much more sensitive probes to test the validity of the different wave functions. The magnetic moment of the high-spin ^{78}Cu in particular provides a clean probe for purity of the nuclear wavefunction. As can be seen in panels b

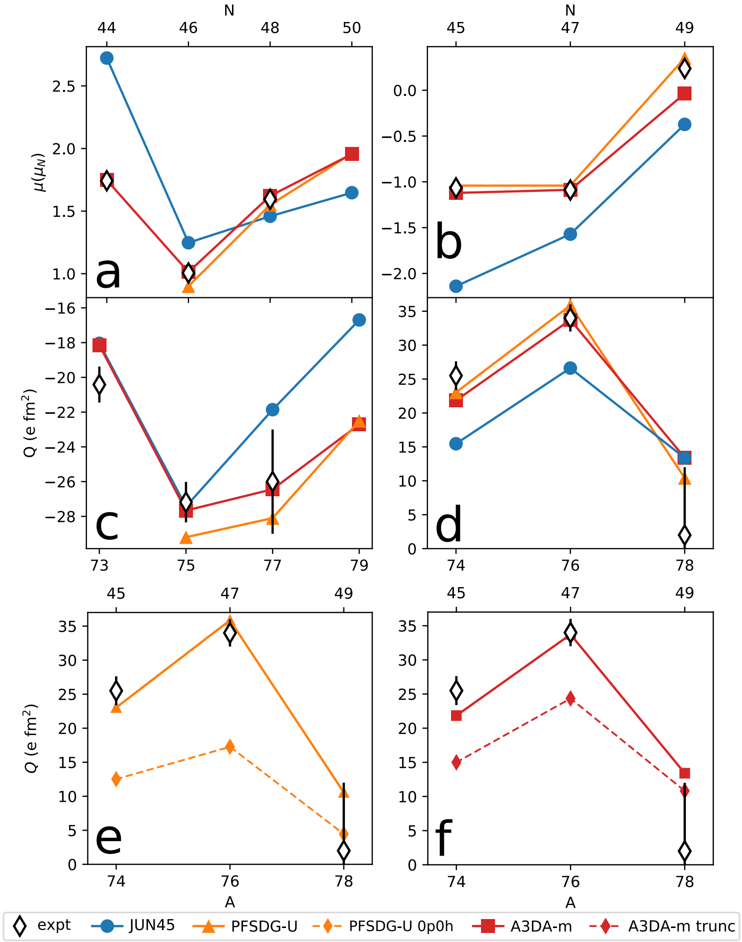

Figure 3. Panel a (b): Dipole moments of the odd-even (odd-odd) copper isotopes. Panel c (d): Quadrupole moments of the odd-even (odd-odd) copper isotopes. Panels e and f: Quadrupole moments of the odd-odd copper isotopes compared to PFSDG-U calculations without cross-shell excitations (labeled '0p0h') and A3DA-m calculations where the $d_{5/2}$ orbit is removed from the model space (labeled 'trunc').

and d in Fig. 3, the JUN45 calculations do not agree with the values of both μ and Q for the odd-odd isotopes. The A3DA-m and the PFSDG-U predictions do agree very well with experimental values of μ and Q, despite the increased complexity of shell-model calculations for such systems. This improved agreement can be attributed to the presence of excitations of protons as well as neutrons across the $Z = 28$ and $N = 50$ gaps respectively, which are absent in the JUN45 calculations.

The need for these core excitations is further illustrated in panel e of Fig 3, which compares to odd-odd Q moments from PFSDG-U calculations where all cross-shell proton and neutron excitations are blocked, and panel f where A3DA-m calculations with neutrons restricted to the $f_{7/2}, f_{5/2}, p_{3/2}, p_{1/2}$ and $g_{9/2}$ orbits are shown. In these truncated A3DA-m calculations, excitations across the $N = 50$ gap are therefore absent. Both restricted calculations yield moments that deviate from the experimental values, highlighting the sensitivity of the moments of these odd-odd copper isotopes to excitations of the underlying nickel core, and furthermore illustrate the importance of neutron excitations. For ^{78}Cu, the truncated calculations deviate less from the full-space calculations, which illustrates the reduction of correlations towards for ^{78}Cu. The moments of the odd-odd isotopes are therefore the key to uncovering the evolution of both proton and neutron correlations.

The persistence of proton- and neutron excitations across $Z = 28$ and $N = 50$ beyond $N = 45$ can be investigated in more detail by looking at the occupations of the proton and neutron orbits above the $Z = 28$ and the $N = 50$ gaps, shown in Fig. 4. These occupancies remain rather constant from ^{73}Cu to ^{77}Cu for both A3DA-m and PFSDG-U. However, proton and neutron cross-shell excitations decrease suddenly from ^{78}Cu onwards. These weakened core excitations indicate a restoration of the $Z = 28$ and $N = 50$ shell closures when $N = 50$ is approached, despite the reduction in the size of the single-particle $Z = 28$ shell gap. This reduction is due to the central and tensor forces [5, 7], and was recently calculated to be 2 MeV between $N = 40$ and $N = 50$ [11, 24, 25]. Together with the recently measured ^{77}Cu level scheme [24] and the recent mass-measurements of copper isotopes up to ^{79}Cu [25], clear evidence in favor of a doubly-magic ^{78}Ni has therefore been obtained. This conclusion relies crucially on the experimental verification of the weakening correlations, which the current measurements of the moments of the odd-odd isotopes finally provide.

In conclusion, this Letter reports on the first high-resolution laser spectroscopy measurements of $^{76-78}$Cu. Since ^{78}Cu was only produced at a rate of 20 particles per second, an improvement of the background suppression by two orders of magnitude as compared to previous experiments was required. The excellent agreement of the moments of the odd-odd

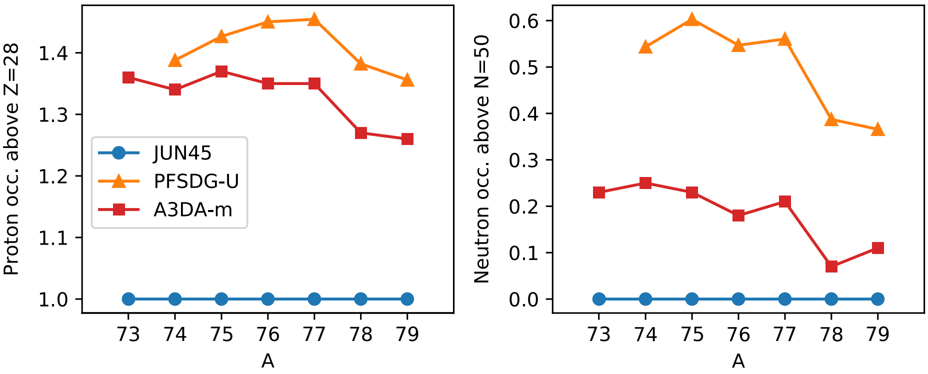

Figure 4. Comparison of the occupations above $Z = 28$ and $N = 50$ for the JUN45, A3DA-m and PFSDG-U calculations.

copper isotopes with state-of-the-art shell-model calculations in extended model spaces provides a clear indication for the weakening of correlations towards $N = 50$: both the proton and neutron excitations across $Z = 28$ and $N = 50$ decrease for ^{78,79}Cu. Strong evidence in favour of a restoration of the magicity of $N = 50$ and $Z = 28$ is therefore obtained, despite the reduction in the size of the shell gaps. This investigation into the doubly magic character of ^{78}Ni relies crucially on measurements of the moments of odd-odd nuclei. While their increased complexity can make calculation and interpretation more difficult, the unique information contained in their nuclear moments helps to clarify the subtle interplay of the single-particle properties and collective correlations in exotic nuclei, where experimental data are otherwise scarce. Finally, the nuclear spins of ^{76,77}Cu were measured to be 3 and 5/2 respectively.

We acknowledge the support of the ISOLDE collaboration and technical teams, and the University of Jyväskylä for the use of the injection-locked cavity. The Monte Carlo Shell-Model calculations were performed on K computer at RIKEN AICS (hp160211, hp170230). This work was supported in part by FNPMLS ERC Consolidator Grant no. 648381, MEXT as “Priority Issue on Post-K computer” (Elucidation of the Fundamental Laws and Evolution of the Universe) and JICFuS, the BriX Research Program No. P7/12, FWO-Vlaanderen (Belgium), GOA 15/010 from KU Leuven, the Science and Technology Facilities Council consolidated grant ST/F012071/1 and continuation grant ST/J000159/1, the EU Horizon2020 research and innovation programme through ENSAR2 (no. 654002), and Ernest Rutherford Grant No. ST/L002868/1. We acknowledge the financial aid of the Ed Schneiderman Fund at New York University.

---

* ruben.degroote@kuleuven.be

[1] M. G. Mayer, Phys. Rev. **75**, 1969 (1949).

[2] O. Haxel, J. H. D. Jensen, and H. E. Suess, Phys. Rev. **75**, 1766 (1949).

[3] T. Otsuka, R. Fujimoto, Y. Utsuno, B. A. Brown, M. Honma, and T. Mizusaki, Phys. Rev. Lett. **87**, 082502 (2001).

[4] O. Sorlin and M.-G. Porquet, Progress in Particle and Nuclear Physics **61**, 602 (2008).

[5] T. Otsuka, T. Suzuki, R. Fujimoto, H. Grawe, and Y. Akaishi, Phys. Rev. Lett. **95**, 232502 (2005).

[6] J. Hakala, S. Rahaman, V.-V. Elomaa, T. Eronen, U. Hager, A. Jokinen, A. Kankainen, I. Moore, H. Penttilä, S. Rinta-Antila, *et al.*, Phys. Rev. Lett. **101**, 052502 (2008).

[7] T. Otsuka, T. Suzuki, M. Honma, Y. Utsuno, N. Tsunoda, K. Tsukiyama, and M. Hjorth-Jensen, Phys. Rev. Lett. **104**, 012501 (2010).

[8] A. Korgul, K. P. Rykaczewski, J. A. Winger, S. V. Ilyushkin, C. J. Gross, J. C. Batchelder, C. R. Bingham, I. N. Borzov, C. Goodin, R. Grzywacz, J. H. Hamilton, W. Królas, S. N. Liddick, C. Mazzocchi, C. Nelson, F. Nowacki, S. Padgett, A. Piechaczek, M. M. Rajabali, D. Shapira, K. Sieja, and E. F. Zganjar, Phys. Rev. C **86**, 024307 (2012).

[9] Marchi, T., de Angelis, G., Baugher, T., Bazin, D., Berryman, J., Bonaccorso, A., Clark, R., Coraggio, L., Covello, A., Crawford, H., Doncel, M., Farnea, E., Gade, A., Gadea, A., Gargano, A., Glasmacher, T., Gottardo, A., Gramegna, F., Itaco, N., Kumar, R., Lenzi, S. M., McDaniel, S., Michelagnoli, C., Napoli, D.R., Quintana, B., Ratkiewicz, A., Recchia, F., Sahin, E., Stroberg, R., Valiente-Dobn, J.J., Weisshaar, D., Wimmer, K., and Winkler, R., EPJ Web of Conferences **66**, 02066 (2014).

[10] Z. Xu, S. Nishimura, G. Lorusso, F. Browne, P. Doornenbal, G. Gey, H.-S. Jung, Z. Li, M. Niikura, P.-A. Söderström, *et al.*, Phys. Rev. Lett. **113**, 032505 (2014).

[11] Y. Tsunoda, T. Otsuka, N. Shimizu, M. Honma, and Y. Utsuno, Phys. Rev. C **89**, 031301 (2014).

[12] L. Coraggio, A. Covello, A. Gargano, and N. Itaco, Phys. Rev. C **89**, 024319 (2014).

[13] K. Sieja and F. Nowacki, Phys. Rev. C **85**, 051301 (2012).

[14] M.-G. Porquet and O. Sorlin, Phys. Rev. C **85**, 014307 (2012).

[15] G. Hagen, G. R. Jansen, and T. Papenbrock, Phys. Rev. Lett. **117**, 172501 (2016).

[16] F. Nowacki, A. Poves, E. Caurier, and B. Bounthong, Phys. Rev. Lett. **117**, 272501 (2016).

[17] G. Neyens, Reports on Progress in Physics **66**, 633 (2003).

[18] T. Cocolios, a. Andreyev, B. Bastin, N. Bree, J. Büscher, J. Elseviers, J. Gentens, M. Huyse, Y. Kudryavtsev, D. Pauwels, T. Sonoda, P. Van den Bergh, and P. Van Duppen, Phys. Rev. Lett. **103**, 102501 (2009).

[19] T. E. Cocolios, a. N. Andreyev, B. Bastin, N. Bree, J. Büscher, J. Elseviers, J. Gentens, M. Huyse, Y. Kudryavtsev, D. Pauwels, T. Sonoda, P. V. D. Bergh, and P. Van Duppen, Phys. Rev. C **81**, 014314 (2010).

[20] K. T. Flanagan, P. Vingerhoets, M. Avgoulea, J. Billowes, M. L. Bissell, K. Blaum, B. Cheal, M. De Rydt, V. N. Fedosseev, D. H. Forest, C. Geppert, U. Köster, M. Kowalska, J. Krämer, K. L. Kratz, A. Krieger, E. Mané, B. A. Marsh, T. Materna, L. Mathieu, P. L. Molkanov, R. Neugart, G. Neyens, W. Nörtershäuser, M. D. Seliverstov, O. Serot, M. Schug, M. A. Sjoedin, J. R. Stone, N. J. Stone, H. H. Stroke, G. Tungate, D. T. Yordanov, and Y. M. Volkov, Phys. Rev. Lett. **103**, 142501 (2009).

[21] P. Vingerhoets, K. T. Flanagan, M. Avgoulea, J. Billowes, M. L. Bissell, K. Blaum, B. A. Brown, B. Cheal, M. De Rydt, D. H. Forest, C. Geppert, M. Honma, M. Kowalska, J. Krämer, A. Krieger, E. Mané, R. Neugart, G. Neyens, W. Nörtershäuser, T. Otsuka, M. Schug, H. H. Stroke, G. Tungate, and D. T. Yordanov, Phys. Rev. C **82**, 064311 (2010).

[22] P. Vingerhoets, K. Flanagan, J. Billowes, M. Bissell, K. Blaum, B. Cheal, M. De Rydt, D. Forest, C. Geppert, M. Honma, M. Kowalska, J. Krämer, K. Kreim, A. Krieger, R. Neugart, G. Neyens, W. Nörtershäuser, J. Papuga, T. Procter, M. Rajabali, R. Sánchez, H. Stroke, and D. Yordanov, Physics Letters B **703**, 34 (2011).

[23] K. Sieja and F. Nowacki, Phys. Rev. C **81**, 061303 (2010).

[24] E. Sahin, F. L. Bello Garrote, Y. Tsunoda, T. Otsuka, G. de Angelis, A. Görgen, M. Niikura, S. Nishimura, Z. Y. Xu, H. Baba, F. Browne, M.-C. Delattre, P. Doornenbal, S. Franchoo, G. Gey, K. Hadyńska-Klęk, T. Isobe, P. R. John, H. S. Jung, I. Kojouharov, T. Kubo, N. Kurz, Z. Li, G. Lorusso, I. Matea, K. Matsui, D. Mengoni, P. Morfouace, D. R. Napoli, F. Naqvi,

H. Nishibata, A. Odahara, H. Sakurai, H. Schaffner, P.-A. Söderström, D. Sohler, I. G. Stefan, T. Sumikama, D. Suzuki, R. Taniuchi, J. Taprogge, Z. Vajta, H. Watanabe, V. Werner, J. Wu, A. Yagi, M. Yalcinkaya, and K. Yoshinaga, Phys. Rev. Lett. **118**, 242502 (2017).

[25] A. Welker and et al, To be submitted to Phys. Rev. Lett..

[26] U. Köster, N. J. Stone, K. T. Flanagan, J. R. Stone, V. N. Fedosseev, K. L. Kratz, B. A. Marsh, T. Materna, L. Mathieu, P. L. Molkanov, M. D. Seliverstov, O. Serot, A. M. Sjödin, and Y. M. Volkov, Phys. Rev. C **84**, 034320 (2011).

[27] B. Cheal, J. Billowes, M. L. Bissell, K. Blaum, F. C. Charlwood, K. T. Flanagan, D. H. Forest, C. Geppert, M. Kowalska, K. Kreim, A. Krieger, J. Krmer, K. M. Lynch, E. Man, I. D. Moore, R. Neugart, G. Neyens, W. Nrtershuser, J. Papuga, T. J. Procter, M. M. Rajabali, H. H. Stroke, P. Vingerhoets, D. T. Yordanov, and M. kov, Journal of Physics: Conference Series **381**, 012071 (2012).

[28] T. J. Procter, J. Billowes, M. L. Bissell, K. Blaum, F. C. Charlwood, B. Cheal, K. T. Flanagan, D. H. Forest, S. Fritzsche, C. Geppert, H. Heylen, M. Kowalska, K. Kreim, A. Krieger, J. Krämer, K. M. Lynch, E. Mané, I. D. Moore, R. Neugart, G. Neyens, W. Nörtershäuser, J. Papuga, M. M. Rajabali, H. H. Stroke, P. Vingerhoets, D. T. Yordanov, and M. Žáková, Phys. Rev. C **86**, 034329 (2012).

[29] X. F. Yang, C. Wraith, L. Xie, C. Babcock, J. Billowes, M. L. Bissell, K. Blaum, B. Cheal, K. T. Flanagan, R. F. Garcia Ruiz, W. Gins, C. Gorges, L. K. Grob, H. Heylen, S. Kaufmann, M. Kowalska, J. Kraemer, S. Malbrunot-Ettenauer, R. Neugart, G. Neyens, W. Nörtershäuser, J. Papuga, R. Sánchez, and D. T. Yordanov, Phys. Rev. Lett. **116**, 182502 (2016).

[30] C. Wraith, X. Yang, L. Xie, C. Babcock, J. Biero, J. Billowes, M. Bissell, K. Blaum, B. Cheal, L. Filippin, R. G. Ruiz, W. Gins, L. Grob, G. Gaigalas, M. Godefroid, C. Gorges, H. Heylen, M. Honma, P. Jnsson, S. Kaufmann, M. Kowalska, J. Krmer, S. Malbrunot-Ettenauer, R. Neugart, G. Neyens, W. Nrtershuser, F. Nowacki, T. Otsuka, J. Papuga, R. Snchez, Y. Tsunoda, and D. Yordanov, Physics Letters B **771**, 385 (2017).

[31] U. Köster, The European Physical Journal A - Hadrons and Nuclei **15**, 255 (2002).

[32] L. Weissman, U. Köster, R. Catherall, S. Franchoo, U. Georg, O. Jonsson, V. N. Fedoseyev, V. I. Mishin, M. D. Seliverstov, J. Van Roosbroeck, S. Gheysen, M. Huyse, K. Kruglov, G. Neyens, and P. Van Duppen (IS365 Collaboration and ISOLDE Collaboration), Phys. Rev. C **65**, 024315 (2002).

[33] S. Rothe, T. D. Goodacre, D. Fedorov, V. Fedosseev, B. Marsh, P. Molkanov, R. Rossel, M. Seliverstov, M. Veinhard, and K. Wendt, Nuclear Instruments and Methods in Physics Research Section B: Beam Interactions with Materials and Atoms **376**, 91 (2016), proceedings of the {XVIIth} International Conference on Electromagnetic Isotope Separators and Related Topics.

[34] E. Mané, J. Billowes, K. Blaum, P. Campbell, B. Cheal, P. Delahaye, K. T. Flanagan, D. H. Forest, H. Franberg, C. Geppert, T. Giles, A. Jokinen, M. Kowalska, R. Neugart, G. Neyens, W. Nörtershäuser, I. Podadera, G. Tungate, P. Vingerhoets, and D. T. Yordanov, The European Physical Journal A **42**, 503 (2009).

[35] H. Frnberg, P. Delahaye, J. Billowes, K. Blaum, R. Catherall, F. Duval, O. Gianfrancesco, T. Giles, A. Jokinen, M. Lindroos, D. Lunney, E. Mane, and I. Podadera, Nuclear Instruments and Methods in Physics Research Section B: Beam Interactions with Materials and Atoms **266**, 4502 (2008), proceedings of the {XVth} International Conference on Electromagnetic Isotope Separators and Techniques Related to their Applications.

[36] K. T. Flanagan, K. M. Lynch, J. Billowes, M. L. Bissell, I. Budinčević, T. E. Cocolios, R. P. de Groote, S. De Schepper, V. N. Fedosseev, S. Franchoo, R. F. Garcia Ruiz, H. Heylen, B. A. Marsh, G. Neyens, T. J. Procter, R. E. Rossel, S. Rothe, I. Strashnov, H. H. Stroke, and K. D. A. Wendt, Phys. Rev. Lett. **111**, 212501 (2013).

[37] R. P. de Groote, I. Budinčević, J. Billowes, M. L. Bissell, T. E. Cocolios, G. J. Farooq-Smith, V. N. Fedosseev, K. T. Flanagan, S. Franchoo, R. F. Garcia Ruiz, H. Heylen, R. Li, K. M. Lynch, B. A. Marsh, G. Neyens, R. E. Rossel, S. Rothe, H. H. Stroke, K. D. A. Wendt, S. G. Wilkins, and X. Yang, Phys. Rev. Lett. **115**, 132501 (2015).

[38] T. J. Procter, H. Aghaei-Khozani, J. Billowes, M. L. Bissell, F. L. Blanc, B. Cheal, T. E. Cocolios, K. T. Flanagan, H. Hori, T. Kobayashi, D. Lunney, K. M. Lynch, B. A. Marsh, G. Neyens, J. Papuga, M. M. Rajabali, S. Rothe, G. Simpson, A. J. Smith, H. H. Stroke, W. Vanderheijden, and K. Wendt, Journal of Physics: Conference Series **381**, 012070 (2012).

[39] T. Kessler, H. Tomita, C. Mattolat, S. Raeder, and K. Wendt, Laser Physics **18**, 842 (2008).

[40] V. Sonnenschein, I. D. Moore, S. Raeder, M. Reponen, H. Tomita, and K. Wendt, Laser Physics **27**, 085701 (2017).

[41] A. Kono and S. Hattori, Journal of Quantitative Spectroscopy and Radiative Transfer **28**, 383 (1982).

[42] R. P. de Groote, M. Verlinde, V. Sonnenschein, K. T. Flanagan, I. Moore, and G. Neyens, Phys. Rev. A **95**, 032502 (2017).

[43] W. Gins and R. de Groote, Submitted for publication in Computer Physics Communications (2017).

[44] O. Lutz, H. Oehler, and P. Kroneck, Zeitschrift für Physik A Atoms and Nuclei **288**, 17 (1978).

[45] R. M. Sternheimer, Phys. Rev. A **6**, 1702 (1972).

[46] N. J. Stone, Atomic Data and Nuclear Data Tables **90**, 75 (2005).

[47] H. Figger, D. Schmitt, and P. S, Colloq. Int. C. N. R. S. **164** (1967).

[48] H. Bucka, J. K. Ney, and P. Wirtnik, Zeitschrift für Physik **202**, 22 (1967).

[49] P. Locher, Phys. Rev. B **10**, 801 (1974).

[50] J. Van Roosbroeck, H. De Witte, M. Gorska, M. Huyse, K. Kruglov, D. Pauwels, J.-C. Thomas, K. Van de Vel, P. Van Duppen, S. Franchoo, J. Cederkall, V. N. Fedoseyev, H. Fynbo, U. Georg, O. Jonsson, U. Köster, L. Weissman, W. F. Mueller, V. I. Mishin, D. Fedorov, A. De Maesschalck, N. A. Smirnova, and K. Heyde, Phys. Rev. C **71**, 054307 (2005).

[51] N. Patronis, H. De Witte, M. Gorska, M. Huyse, K. Kruglov, D. Pauwels, K. Van de Vel, P. Van Duppen, J. Van Roosbroeck, J. C. Thomas, S. Franchoo, J. Cederkall, V. N. Fedoseyev, H. Fynbo, U. Georg, O. Jonsson, U. Köster, T. Materna, L. Mathieu, O. Serot, L. Weissman, W. F. Mueller, V. I. Mishin, and D. Fedorov, Phys. Rev. C **80**, 034307 (2009).

[52] S. V. Ilyushkin, J. A. Winger, C. J. Gross, K. P. Rykaczewski, J. C. Batchelder, L. Cartegni, I. G. Darby, C. Goodin, R. Grzywacz, J. H. Hamilton, A. Korgul, W. Królas, S. N. Liddick, C. Mazzocchi, S. Padgett, A. Piechaczek, M. M. Rajabali, D. Shapira, and E. F. Zganjar, Phys. Rev. C **80**, 054304 (2009).

[53] C. Gross, J. Winger, S. Ilyushkin, K. Rykaczewski, S. Liddick, I. Darby, R. Grzywacz, C. Bingham, D. Shapira, C. Mazzocchi, *et al.*, Acta Physica Polonica B **40**, 447 (2009).

[54] M. Honma, T. Otsuka, T. Mizusaki, and M. Hjorth-Jensen, Phys. Rev. C **80**, 064323 (2009).

[55] N. Shimizu, T. Abe, Y. Tsunoda, Y. Utsuno, T. Yoshida, T. Mizusaki, M. Honma, and T. Otsuka, Progress of Theoretical and Experimental Physics **2012**, 01A205 (2012).

[56] E. Caurier, G. Martínez-Pinedo, F. Nowacki, A. Poves, and A. P. Zuker, Rev. Mod. Phys. **77**, 427 (2005).

[57] M. Dufour and A. P. Zuker, Phys. Rev. C **54**, 1641 (1996).

6.3.3 Additional information on the dipole and quadrupole moments

Dipole and quadrupole moments prior to this work

Figure 6.17 plots all magnetic and quadrupole moments for the odd-A copper isotopes measured prior to this work [5, 6, 8, 56, 91, 92]. These moments are compared to effective single particle moments as well as calculations with the JUN45 interaction using a spin-quenching factor of 0.7 and effective orbital g-factors of 1 and 0 for protons and neutrons, and effective charges of $e_p = 1.5, e_n = 1.1$. Due to the model space, the JUN45 calculations predict the effective single particle moments for ^{57,79}Cu. For all but ^{69}Cu, clear deviations from the effective moments as well as from the JUN45 moments are observed. These deviations can be attributed to the contribution of excitations across $Z = 28$, and in particular to $M1$ transitions from the $\pi f_{7/2}$ orbital to the $\pi f_{5/2}$ orbital [5], as was verified for the neutron-deficient isotopes using the GXPF1 interaction [56, 91] as well as for the neutron-rich isotopes [9]. The deviations seem especially large for ^{71,73}Cu. For ^{75,77}Cu, the dominant contribution to the ground-state proton wave function is due to the $\pi f_{5/2}$ orbital [6, 8], and these isotopes have a ground-state spin of 5/2. This results in a sudden change in trend for both magnetic and quadrupole moments.

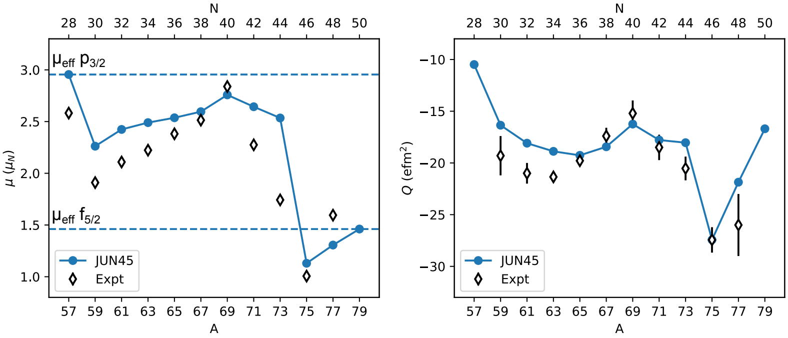

Figure 6.17: Literature values for the dipole and quadrupole moments of the odd-A copper isotopes. Calculations using JUN45 are also shown.

The JUN45 reproduces the experimental quadrupole moments reasonably well. For neutron-deficient isotopes, a systematic under-estimation is apparent. This could be due to the absence of excitations across $N, Z = 28$ [5, 56]. The experimental quadrupole moments below $N = 40$ show a clear increase when going to $N = 28$, with the trend looking parabolic. A similar trend exists for the neutron-rich isotopes. This is better visualized on figure 6.18, which plots

$$Q' = Q \cdot \frac{2j+2}{2j-1}, \tag{6.1}$$

removing some of the orbital dependence that can be seen in e.g. (2.24). Parabolic fits of the experimental data have been plotted as well to guide the eye. A clear dip is visible at $N = 40$, with minima suggested at $N = 28, 50$ as well.

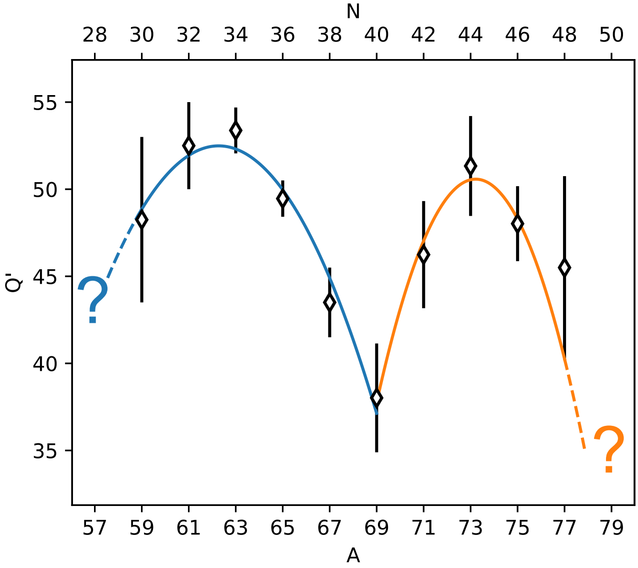

Figure 6.18: Plot of Q' as function of A. Clear parabolic trends become apparent.

Moments of odd-odd isotopes are often harder to interpret. Shell-model calculations were shown to agree with experiments relatively well [5, 7, 56]. These shell model calculations calculate large contributions the $\pi f_{5/2}$ orbit to the wavefunction, a signature of the lowering of the $\pi f_{5/2}$ orbit. The calculated wave function of ^{73}Cu is still dominated by $\pi p_{3/2}$ by both JUN45, as well as the more recent PFSDG-U and A3DA-m calculations (to be discussed later). So, the inversion of the $\pi p_{3/2}, f_{5/2}$ orbits becomes apparent earlier in the odd-odd isotopes than for odd-even isotopes. This illustrates that the moments of odd-odd isotopes are complimentary to those of the odd-even isotopes, a message that is confirmed in **Article V**.

Empirical moments of odd-odd copper isotopes

While the structure of odd-odd isotopes in general can be more difficult to interpret correctly, the magnetic moments of the odd-odd copper isotopes can be described quite well by approximating these odd-odd isotopes by a system consisting of the coupling of a single proton and a neutron (hole). The net g-factor of such a system can be calculated using equation (2.17). By applying this formula for the odd-odd isotopes $^{72-78}$Cu, figure 6.19 is obtained. When the g-factors of ^{79m}Zn and ^{69}Cu are used for the neutron-and proton g-factors, poor agreement is obtained. This is because the wavefunction of ^{72,74}Cu is dominated by a proton in the $f_{5/2}$ orbital rather than the $p_{3/2}$ orbital [5, 7]. Indeed, calculations that use the magnetic moment of ^{75}Cu are in much better agreement with the data, since the proton wavefunction is also mostly of $f_{5/2}$ character. Note that this picture does not change much if other odd-A copper nuclei are chosen: only if their wavefunction is dominated by a single proton in the $f_{5/2}$ orbit, is reasonable agreement obtained.

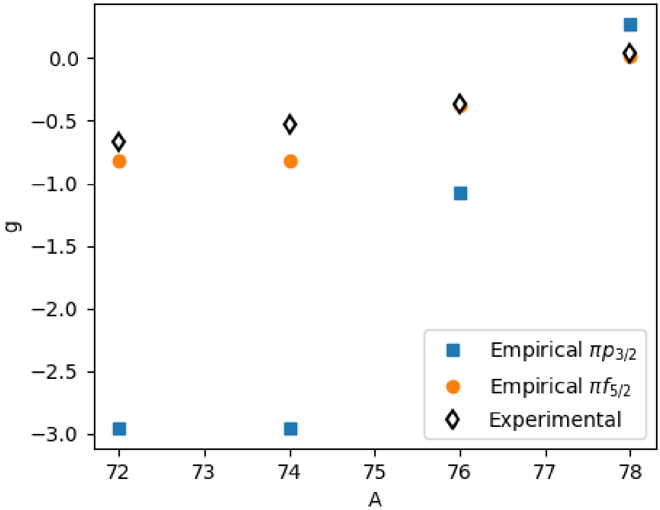

Figure 6.19: g-factors of the odd-odd isotopes $^{72-78}$Cu compared to empirical calculations using the addition theorem. Squares indicate calculations that used the experimental g-factor of ^{79m}Zn and ^{69}Cu as empirical values for the neutron-and proton g-factors, while the circles used the magnetic moment of ^{77}Cu instead.

Finally, note that for ^{78}Cu, only the g-factors for the spin 6 option were plotted in figure 6.19. While no firm spin assignment for ^{78}Cu could be made in this thesis, figure 6.20 does provide support for $I = 6$ and $I = 7$ if the proton wavefunction has a large $f_{5/2}$-component. A similar argument based on the most recent shell-model calculations is also given in **Article V**. If the single valence proton of ^{78}Cu occupies mostly $\pi p_{3/2}$ through some rather unexpected phenomena, a spin 5 should be considered the favourite.

According to large-scale shell model calculations however, states with a $\pi p_{3/2}$ character are much higher in excitation energy. Both a $\pi f_{5/2} \otimes \nu g_{9/2}$ and a $\pi p_{3/2} \otimes \nu g_{9/2}$ coupling can result in states with spins 3-6, unlike states with a spin 2 or 7, which cannot result from a $\pi p_{3/2} \otimes \nu g_{9/2}$ coupling. The levels with spin 3-6 can therefore mix, and will lower in energy. The high energy of the spin 7 states therefore make spin 6 the most likely option.

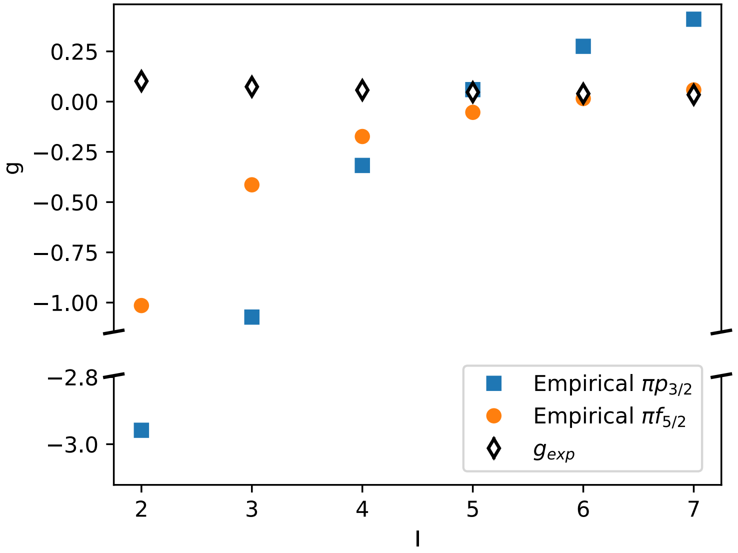

Figure 6.20: g-factor of the odd-odd isotope ^{78}Cu, for possible spins 2-7, compared to empirical calculations using the addition theorem. Squares indicate calculations that used the experimental g-factor of ^{79m}Zn and ^{69}Cu as empirical values for the neutron-and proton g-factors, while the circles used the magnetic moment of ^{77}Cu instead.

Note on the choice of effective g-factors and charges in A3DA-m and PFSDG-U

In **Article V**, the moments of $^{73-78}$Cu are compared to calculations using the JUN45, the modified A3DA and PFSDG-U interaction. To facilitate comparison of the data with these three models, all theoretical moments were calculated using a spin quenching factor of 0.75 and effective orbital g-factors of 1.1 and -0.1 for protons and neutrons. For the quadrupole moments, $e_p = 1.5, e_n = 1.1$ was chosen for JUN45, whereas for A3DA-m and PFSDG-U $e_p = 1.3, e_n = 0.46$, based on [93]. All experimental and the new theoretical results for the whole chain of odd-even isotopes are shown in figure 6.21.

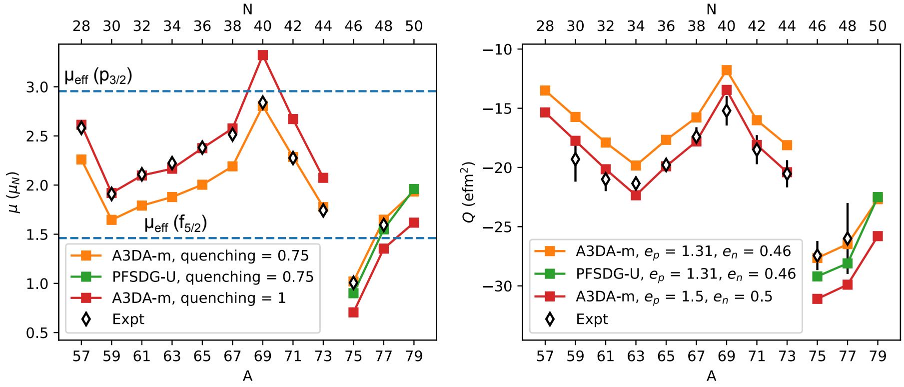

Figure 6.21: Dipole and quadrupole moments of $^{57-78}$Cu compared to A3DA-m and PFSDG-U calculations. For A3DA-m, two different choices of effective g-factors and charges were plotted (see text for details).

Interestingly, there is a clear discrepancy between the A3DA-m calculations and experiment for $A < 69$, which can be completely resolved by using free values rather than effective values. The reason for this is not clear. Furthermore, choosing $e_p = 1.5, e_n = 0.5$ for the A3DA-m calculations does seem to result in better agreement for the isotopes below $N = 46$, but seems to result in an overestimation of the quadrupole moments for ^{75,77}Cu. A consistent explanation for this observation has not been found yet.

Restricted A3DA-m calculations

In **Article V** a comparison is given of the moments with A3DA-m calculations where excitations across the $N = 50$ shell are blocked. This shows clearly that these cross-shell excitations are crucial for the reproduction of both dipole and quadrupole moments. For these restricted calculations, the effective charges were modified to $e_p = 1.5, e_n = 0.6$. There is no rigorous justification for these charges; rather, they were fitted to best reproduce the quadrupole moments of $^{71-75}$Cu. Note however that no choice of effective charges results in good reproduction of the quadrupole moments for $N > 44$ of both the odd-A and even-A isotopes, something that the full-space A3DA-m and PFSDG-U calculations do achieve. An overview of all the experimental and theoretical calculations, including these restricted A3DA-m calculations, is shown in figure 6.22.

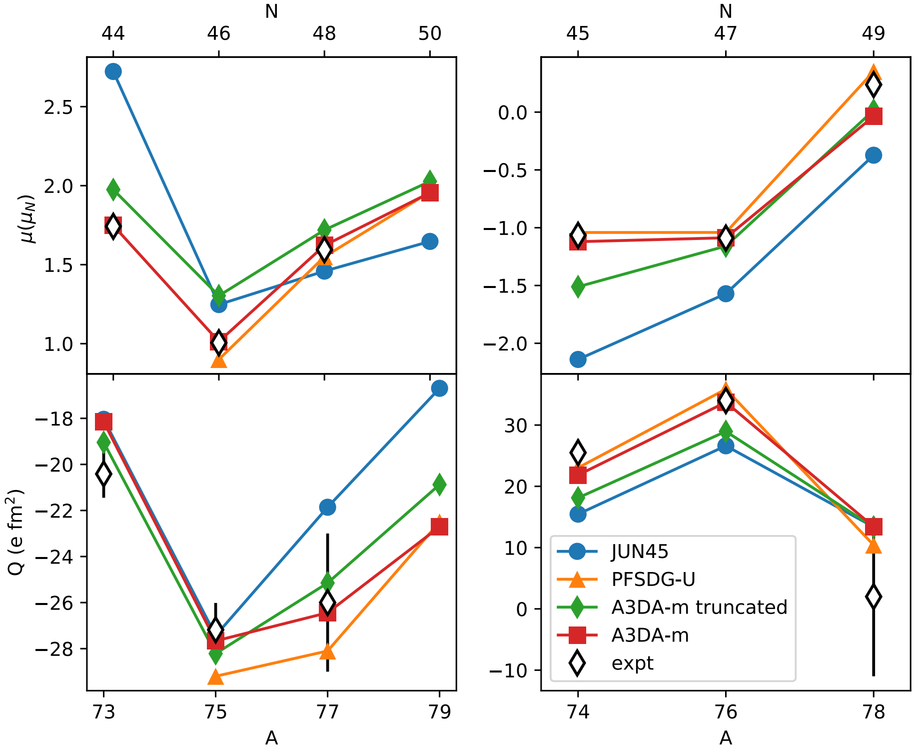

Figure 6.22: Dipole and quadrupole moments of neutron-rich copper isotopes, compared to JUN45, PFSDG-U, full-space A3DA-m, and calculations with neutrons restricted to the pfg shell.

Finally, calculations where proton excitations across $Z = 28$ are forbidden were also performed (see figure 6.23). Again, neither dipole or quadrupole moments are well reproduced. Here, the effective charges were tuned to $e_p = 1.5, e_n = 0.95$ to best match the odd-A isotopes. Combining the information of both restricted calculations illustrates that excitations across both $Z = 28$ and $N = 50$ are vital components of the nuclear wavefunctions.

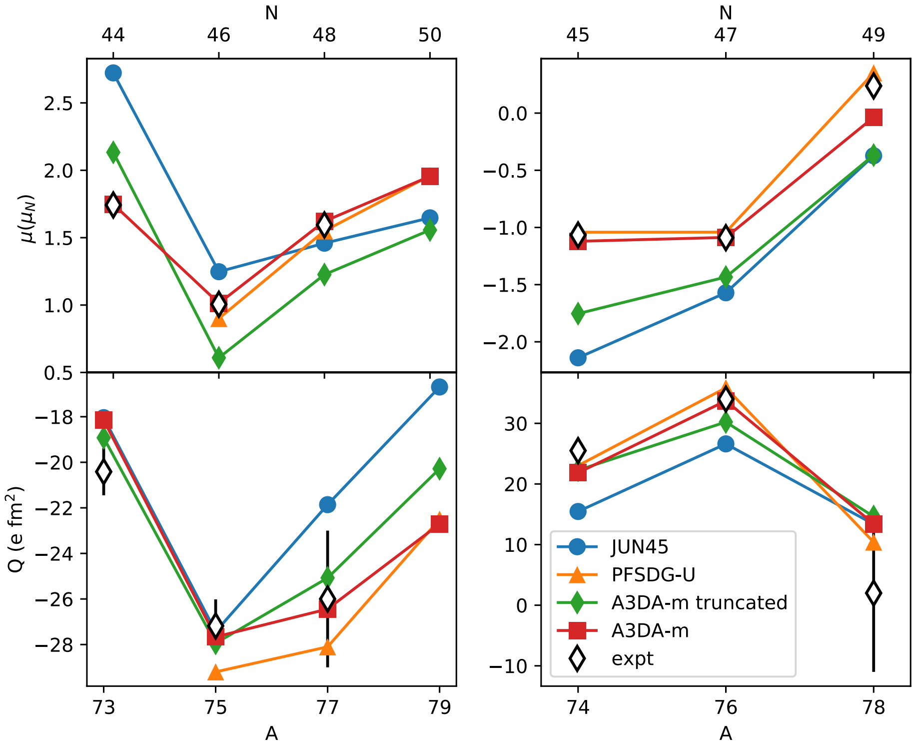

Figure 6.23: Dipole and quadrupole moments of neutron-rich copper isotopes, compared to JUN45, PFSDG-U, full-space A3DA-m, and calculations with proton excitations across $Z = 28$ blocked.

This can be studied in more detail by investigating the effect that these restrictions have on the occupations numbers. In figure 6.24, the total occupation of the orbits above $Z = 28$ and $N = 50$ are shown for the full-space A3DA-m, PFSDG-U and JUN45 calculations and also for the calculations with restricted protons or neutrons. These graphs show that the proton excitations lead to increased neutron excitations, and vice versa. This explains why the magnetic moments are not reproduced by the calculations that restrict the neutrons, even though the magnetic dipole moment is primarily sensitive to the $M1$-excitations across $Z = 28$. The absence of neutron excitations leads to a reduction in the proton excitations, which are crucial to reproduce the dipole moments.

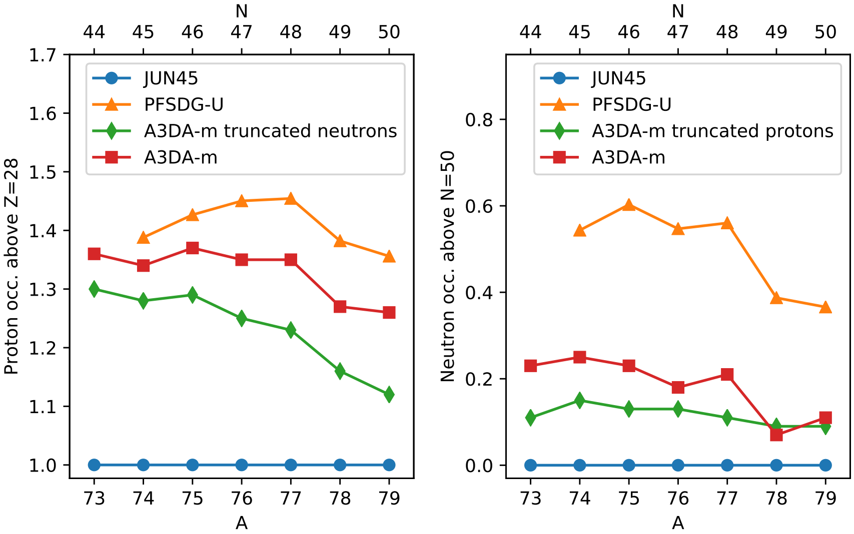

Figure 6.24: Occupation numbers of protons above $Z = 28$ and neutrons above $N = 50$ with JUN45, PFSDG-U and A3DA-m. In addition, proton occupations for calculations with neutron excitations across $N = 50$ blocked are also shown, as well as neutron occupations for the calculations wtih protons across $Z = 28$ blocked.

6.3.4 Changes in mean-squared charge radii

The charge radii measured in this work are plotted in figure 6.25. The statistical uncertainties are displayed as error bars, while the uncertainty due to the theoretical uncertainty on M_{249} and F_{249} is indicated with the dotted line. The new data for $^{76-78}$Cu reveals a slower increase of the radii past $N = 45$, though a more precise measurement on ^{78}Cu would help to interpret this trend even better. This flattening is also observed in Ga and Kr [24] (see figure 6.26), and could be interpreted as a sign for the end of collectivity as the neutron shell closure is approached. Supplementing the existing data with additional measurements on Ge, As, Se and Br would help to complete this picture.

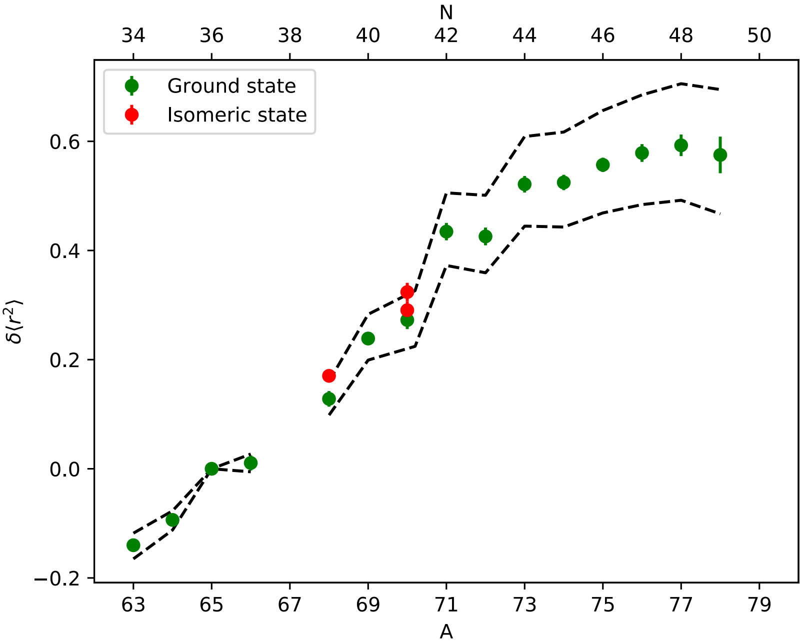

Figure 6.25: Charge radii obtained in this work. Statistical uncertainties are shown using error bars, while the dashed line indicates the uncertainty due to the uncertainty on the M_{249}- and F_{249} parameters.

Another interesting feature of the nuclear charge radii is the odd-even staggering (OES). The OES can be visualized by plotting the following three-point difference

$$\Delta_r^{(3)} = \frac{1}{2}(r_{A-1} - 2r_A + r_{A+1}), \tag{6.2}$$

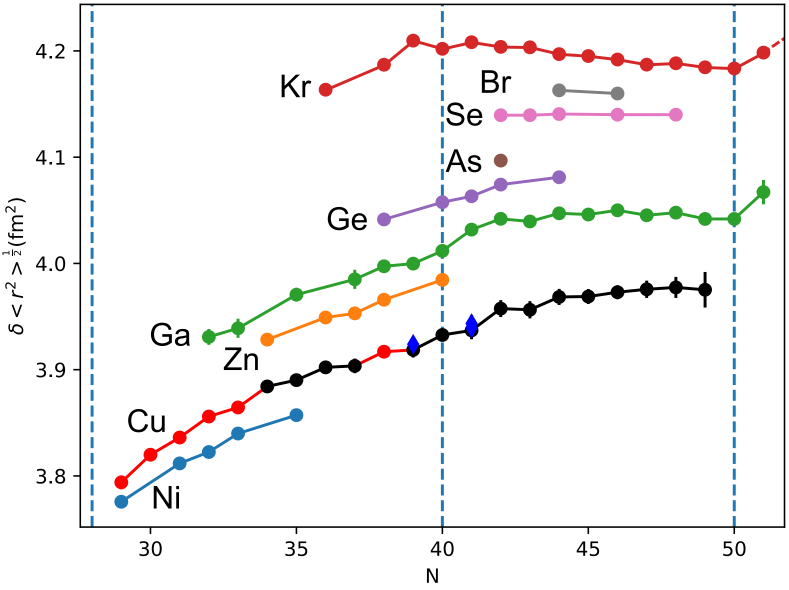

Figure 6.26: Charge radii of the region, showing the available data for Ni, Cu, Zn, Ga and Kr. No systematic errors are shown. For the copper isotopes, the data obtained in this thesis is supplemented with literature radii taken from [36] (shown in red). Other data is taken from [24].

as is done in e.g [94] for the calcium isotopes. Since the odd-even isotopes are larger than their odd-odd neighbours, $\Delta_r^{(3)} < 0$ for A even, and $\Delta_r^{(3)} > 0$ for A odd. This quantity is plotted in figure 6.27. When available, the values of $\delta \left\langle r^2 \right\rangle$ measured during this thesis are used. Otherwise, values are taken from [36]. After $A \approx 71$, the size of the OES reduces, and becomes zero (within uncertainties) for $A \geq 74$. The origins of this reduction in OES is not understood (much like how OES in itself is generally not understood).

Early work interpreted the main mechanism behind the odd-even staggering in terms of enhanced deformation of the odd-A isotopes [95–97] due to e.g. core polarization due to the valence neutrons [98], which was also suggested to lead to a reversal of the normal OES [26]. While in some cases the increased charge radius can indeed be linked to an increase in deformation, this explanation was not found satisfactory in general, since even nuclei are not found to be consistently more deformed than their odd neighbours [99].

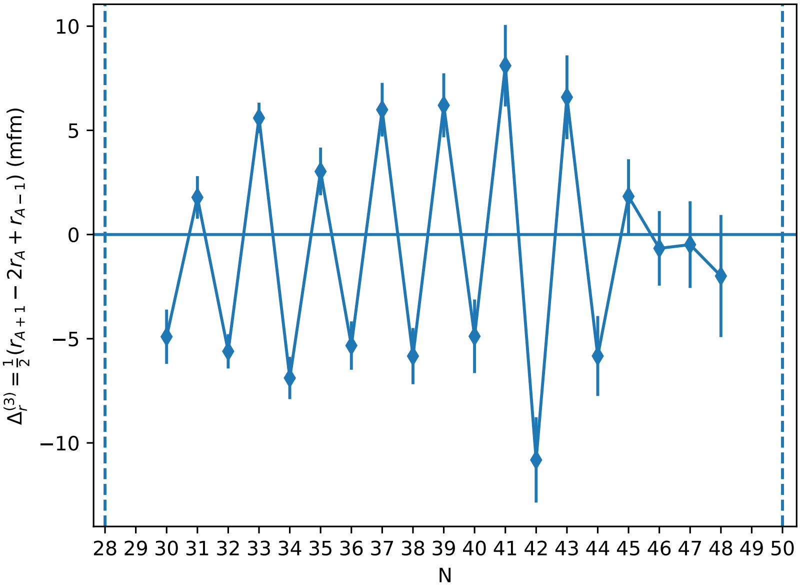

Figure 6.27: OES of the copper isotopic chain visualised using $\Delta_r^{(3)}$.

Later work pointed out that an odd neutron or proton leads to blocking of the ground-state quadrupole correlations, and that this could be responsible for the odd-even staggering in radii and masses [99]. Similarly, the addition of three- and four-body forces in a Hartree-Fock-Bogoliubov type calculations was also shown to lead to fair reproduction of odd-even staggering [100–102]. The intuitive picture is that proton pairing leads to an increase in the charge radius (since proton pairing leads to partial occupation of orbits above the Fermi level). The addition of an unpaired neutron blocks neutron pairing, and, due to the presence of four-body correlations, also influences the proton pairing. This therefore gives rise to staggering in the charge radii.

Many of the approaches described above are however plagued by a reliance on phenomenological assumptions and fit parameters. Microscopically calculated results using these physical mechanisms consistently result in effects too small to explain the observations [100]. More recent calculations of the charge radii of the calcium isotopes using a shell model approach provide a microscopic picture [103]. Through the inclusion of higher-than 2p-2h excitations across the shell gaps at nucleon numbers 20 and 28, and by relating the occupation of the fp-shell to an increase in the charge radius (as suggested in [104]), good agreement with experiment could be obtained. Density Functional Theory (DFT) have managed to explain the odd-even staggering of charge radii in terms of a density-dependent nucleonic pairing [105], which has lead to a renewed interest of the community [94].

Quantitative discussions on the OES are complicated by the absence of a solid theoretical framework, but it is nevertheless interesting to compare the OES of the copper isotopes with other systems with a single proton (hole) outside of a filled shell near a double shell closure. The quantity $\Delta_r^{(3)}$ for the indium ($Z = 49$), thallium and bismuth ($Z = 81, 83$) isotopes are shown in figure 6.28. Insufficient data is available for antimony ($Z = 51$). The indium data hints at a similar effect as is the case for copper, with the OES reducing in size, and approaching zero for $N = 76, 77$. The similarity of $\Delta_r^{(3)}$ for the indium and copper would suggest that a similar mechanism could be at play.

However, the trends look different for thallium and bismuth - a gradual decrease in $\Delta_r^{(3)}$ is also observed, but never gets close to zero. Further data on all these isotopic chains, in addition to the antimony isotopes, could help in the development of a good explanation for the observed OES.

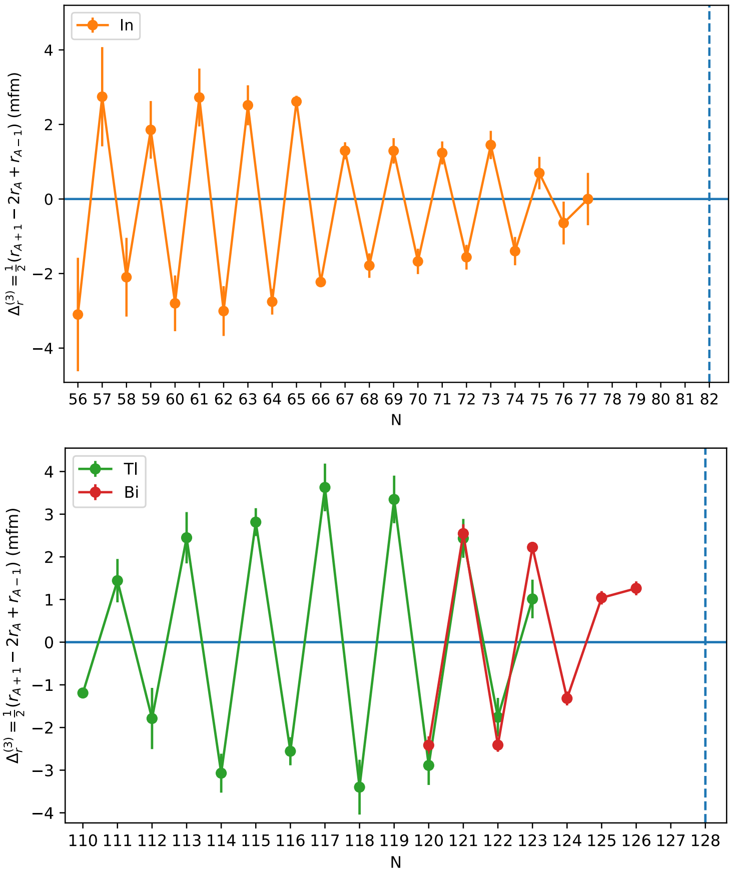

Figure 6.28: $\Delta_r^{(3)}$ of the indium ($Z = 49$) chain (top), thallium ($Z = 81$) and bismuth ($Z = 83$) isotopic chains (bottom).

Chapter 7

Conclusion

This thesis has presented laser spectroscopy measurements of the very neutron-rich copper isotopes $^{76-78}$Cu. These isotopes are situated in the vicinity of ^{78}Ni, one of the cornerstones of contemporary nuclear physics research. They are an excellent probe of the underlying nickel cores, and their moments shed light on the validity of the shell closures at $Z = 28$ and $N = 50$. Furthermore, assignments of the nuclear spin were possible in a model-independent way, for all isotopes except for ^{78}Cu. Finally, the changes in the mean-squared charge radii were also determined with good precision.

All results were obtained using the collinear resonance ionization spectroscopy method, which is an extension of the venerable technique of collinear laser spectroscopy. Previous theses have demonstrated the superior efficiency and background suppression of the technique, and the developments presented in this thesis have firmly established its high-resolution capabilities. This combination of efficiency and resolution have allowed high-resolution measurements to be pushed to ^{78}Cu, which is produced at a rate of only a few 10 particles per second.

The technical achievements required an in-depth study of laser-atom interactions in general, and laser ionization schemes of copper in particular. From these studies the negative impact of high-power lasers on the lineshapes became very apparent. One way to mitigate those effects, by using weak transitions and a long-lived excited state, was theorized and demonstrated. This thesis also provided an in-depth description of an analysis procedure that can be used to handle wavemeter calibration drifts, asymmetric linsehapes, and periodic signal modulations, within one consistent Bayesian framework.

The magnetic dipole and electric quadrupole moments of $^{73-78}$Cu were compared to large-scale shell-model calculations. This comparison provides evidence in support of the doubly-magic status of ^{78}Ni, and confirms that contemporary shell model theories provide good understanding of the nuclear structure in the region. The nuclear spins of ^{76,77,78}Cu, 3, 5/2 and (6) respectively, further confirm the dominant $f_{5/2}$ character of the proton wavefunction and establish the continuation of the inversion of the $\pi f_{5/2}$ and $\pi p_{3/2}$ as $N = 50$ is approached. Finally, from the measurements of the isotope shifts of these isotopes, the mean-squared charge radii of the copper chain could be extended. A flattening of the trend is observed, in agreement with the radii of neighbouring isotopes, as well as an uncharacteristic end to the odd-even staggering of the radii. Whereas the former effect is understood in terms of a reduction in collectivity as the $N = 50$ shell closure is approached, the latter remains puzzling.

While these measurements have pushed high-resolution laser spectroscopy closer to the edge of production at ISOL facilities, there is still further work that can be done. Staying close to the physics case that was investigated in this thesis, measurements of ^{79}Cu should be possible in the (hopefully near) future. The radius and moments of this nucleus will provide a benchmark of nuclear theory. Widening the scope somewhat, the nickel, cobalt and iron isotopes currently represent largely uncharted territory, on both the proton- and neutron-rich sides. Measurements of the properties of these isotopes will probably require the development of high-resolution and efficient methods at facilities other than the ISOLDE facility. The insight into how to best combine high-resolution measurements with resonance ionization spectroscopy methods that was gained as part of this thesis will play a vital role in this future work.

Appendix A

Data processing and binning procedure

The CRIS data acquisition collects data from devices connected to different computers, sometimes in different buildings. The data streams from these devices need to be time-synchronized and interleaved so that the MCP count data can be correlated to other information. All computers connected to the CERN network are time-synchronized with a precision of a few ms using the Network Time Protocol, much better than is required for the CRIS experiment. In this appendix the data extraction algorithm will be outlined, and functioning python code that implements it will be included as well. The data is structured in a tabular way, with columns containing the timestamp, time synchronization offset with respect to the central data server, the mass and scan number, and then device-specific information, e.g. the laser wavelength of the number of observed MCP counts.

Figure A.1 schematically illustrates data extraction algorithm. The goal is to take any two timestamped data columns, and to construct a single dataset that combines the two using a common timestamp. The first step of the algorithm is to simply concatenate the two datasets. This results in a two-column timestamped dataset, with half the values undefined for now. Then, they are sorted based on their timestamp (assumed synchronized with sufficient precision). The undefined values are then filled in. In this example, the missing values in the wavelength column are filled with the last available measurement (if there is no previous value, the value closest in time is used). Note that, to avoid double counting, the 'counts' column is *not* filled in in this way. After the filling step, the dataset is condensed by removing rows that still contain an undefined value. While this procedure is somewhat memory-inefficient, the use of standard operations that are implemented in many data analysis libraries across languages means that it is easily implemented, and results in clean and more easily debugged code. A python implementation of this algorithm, using the Pandas framework, is shown in code snippet A.1.

Once the data is extracted and properly combined, it still needs to be binned. Usually, one is interested in binning e.g. MCP counts with respect to the laser wavelength. A schematic picture of a binning algorithm for such a use case is shown in figure A.2.

The algorithm works as follows. First, using a user-defined list of bin edges, every row is assigned a bin number, based on which bin the laser frequency of that row belongs in. Then, the dataset is split into groups based on this bin number. For every bin number, an aggregated value is produced. For instance, in the case of e.g. the laser wavelength or the ISCOOL voltage, a logical aggregation is to compute the mean of the values within the bin. In the case of MCP counts, the sum is a more useful aggregation operator. Uncertainties can also be computed, for instance as the standard deviation of the values in that bin. For counting data, which is assumed to be sampled from a poisson distribution, a good aggregator is to estimate the 1 σ levels using the percent point function, i.e. the inverse cumulative density function. After this aggregation is applied, the data is recombined into a single data set. A python implementation of this algorithm is shown in code snippet A.2. A code snippet used to calculate the poissonian data uncertainties is shown in A.3.

```
import pandas as pd
import h5py

devices = ['cris','wavemeter','ISCOOL']
columns = ['counts','wavenumber_1','voltage']
scan = '42'

# open hdf5 data file
with h5py.File(path, 'r') as store:
    ## Read in separate data sets
    frames = []
    # iterate over all the device location, column name pairs
    for dev_name,col_name in zip(devices,columns):
        data_set = store[dev_name][scan]
        # get format out of hdf5 metadata
        format = list(data_sets[-1].attrs['format'])
        col = format.index(col_name)
        frame = pd.DataFrame({'time'   : data_set[:,0  ],
                              col_name : data_set[:,col] })
        frames.append(frame)
    ## Merge
    df = pd.concat(frames)
    df.set_index(['time'])
    ## Sort
    df = df.sort_index()
    ## Fill
    df[['wavenumber_1','voltage']] = \
            df[['wavenumber_1','voltage']].fillna(
                                        method='ffill')
    # bfill in case there is a missing value on the first row
    df[['wavenumber_1','voltage']] = \
            df[['wavenumber_1','voltage']].fillna(
                                        method='bfill')
    ## Condense
    df = df.dropna() # this df is the desired dataframe
```

Code A.1: Example of the data extraction algorithm. This code snippet extracts the MCP counting data, wavelength readout, and ISCOOL voltage measurements for a single scan, in this case 42. The Pandas library does most of the heavy lifting.

```python
import pandas as pd
import numpy

to_bin = < extracted data using previous code >
bins = < some array containing edges >
## Digitize
to_bin['bin_nr'] = np.digitize(to_bin['wavenumber_1'], bins)
## Grup by
groups = yo_bin.groupby('bin_nr')

df = pd.DataFrame() # Stores the final binned data

## Apply correct aggregation function
df[['x','xe']] = groups['wavenumber_1'].agg([np.mean,np.std])
df['nr_of_rows'] = groups['bin_nr'].sum()/df.index.values
df['y'] = groups['counts'].sum()
# for the case of MCP counts we construct the 1 sigma
# intervals using the poisson distribution
df['ye_b'] = (df['y']-poisson_low(df['y'])) / df['nr_of_rows']
df['ye_t'] = (poisson_high(df['y'])-df['y']) / df['nr_of_rows']
```

Code A.2: Example of the data binning algorithm. This code snippet bins the MCP counts into evenly spaced wavelength bins.

```python
from scipy.stats import chi2
import numpy as np

def poisson_high(data, alpha=0.32):
    high = chi2.ppf(1 - alpha / 2, 2 * data + 2) / 2
    return high

def poisson_low(data, alpha=0.32):
    low = chi2.ppf(alpha / 2, 2 * data) / 2
    low = np.nan_to_num(low)
    return low
```

Code A.3: Code snippet used to determine upper and lower 1σ intervals assuming the data is drawn from a poisson distribution.

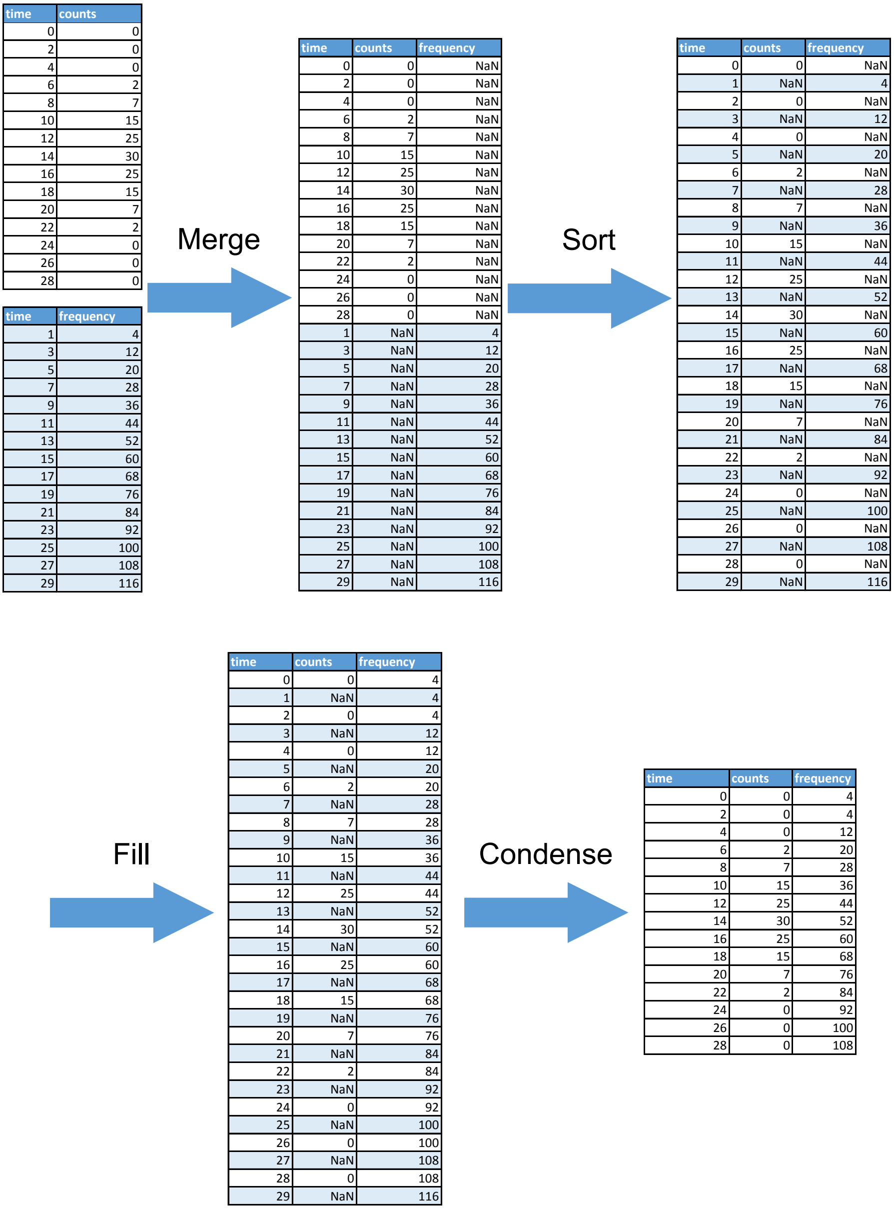

time	counts
0	0
2	0
4	0
6	2
8	7
10	15
12	25
14	30
16	25
18	15
20	7
22	2
24	0
26	0
28	0

time	frequency
1	4
3	12
5	20
7	28
9	36
11	44
13	52
15	60
17	68
19	76
21	84
23	92
25	100
27	108
29	116

time	counts	frequency
0	0	NaN
2	0	NaN
4	0	NaN
6	2	NaN
8	7	NaN
10	15	NaN
12	25	NaN
14	30	NaN
16	25	NaN
18	15	NaN
20	7	NaN
22	2	NaN
24	0	NaN
26	0	NaN
28	0	NaN
1	NaN	4
3	NaN	12
5	NaN	20
7	NaN	28
9	NaN	36
11	NaN	44
13	NaN	52
15	NaN	60
17	NaN	68
19	NaN	76
21	NaN	84
23	NaN	92
25	NaN	100
27	NaN	108
29	NaN	116

time	counts	frequency
0	0	NaN
1	NaN	4
2	0	NaN
3	NaN	12
4	0	NaN
5	NaN	20
6	2	NaN
7	NaN	28
8	7	NaN
9	NaN	36
10	15	NaN
11	NaN	44
12	25	NaN
13	NaN	52
14	30	NaN
15	NaN	60
16	25	NaN
17	NaN	68
18	15	NaN
19	NaN	76
20	7	NaN
21	NaN	84
22	2	NaN
23	NaN	92
24	0	NaN
25	NaN	100
26	0	NaN
27	NaN	108
28	0	NaN
29	NaN	116

time	counts	frequency
0	0	4
1	NaN	4
2	0	4
3	NaN	12
4	0	12
5	NaN	20
6	2	20
7	NaN	28
8	7	28
9	NaN	36
10	15	36
11	NaN	44
12	25	44
13	NaN	52
14	30	52
15	NaN	60
16	25	60
17	NaN	68
18	15	68
19	NaN	76
20	7	76
21	NaN	84
22	2	84
23	NaN	92
24	0	92
25	NaN	100
26	0	100
27	NaN	108
28	0	108
29	NaN	116

time	counts	frequency
0	0	4
2	0	4
4	0	12
6	2	20
8	7	28
10	15	36
12	25	44
14	30	52
16	25	60
18	15	68
20	7	76
22	2	84
24	0	92
26	0	100
28	0	108

Figure A.1: Schematic illustration of the data extraction procedure. In this example, MCP counting data and wavemeter data are combined into a single dataset.

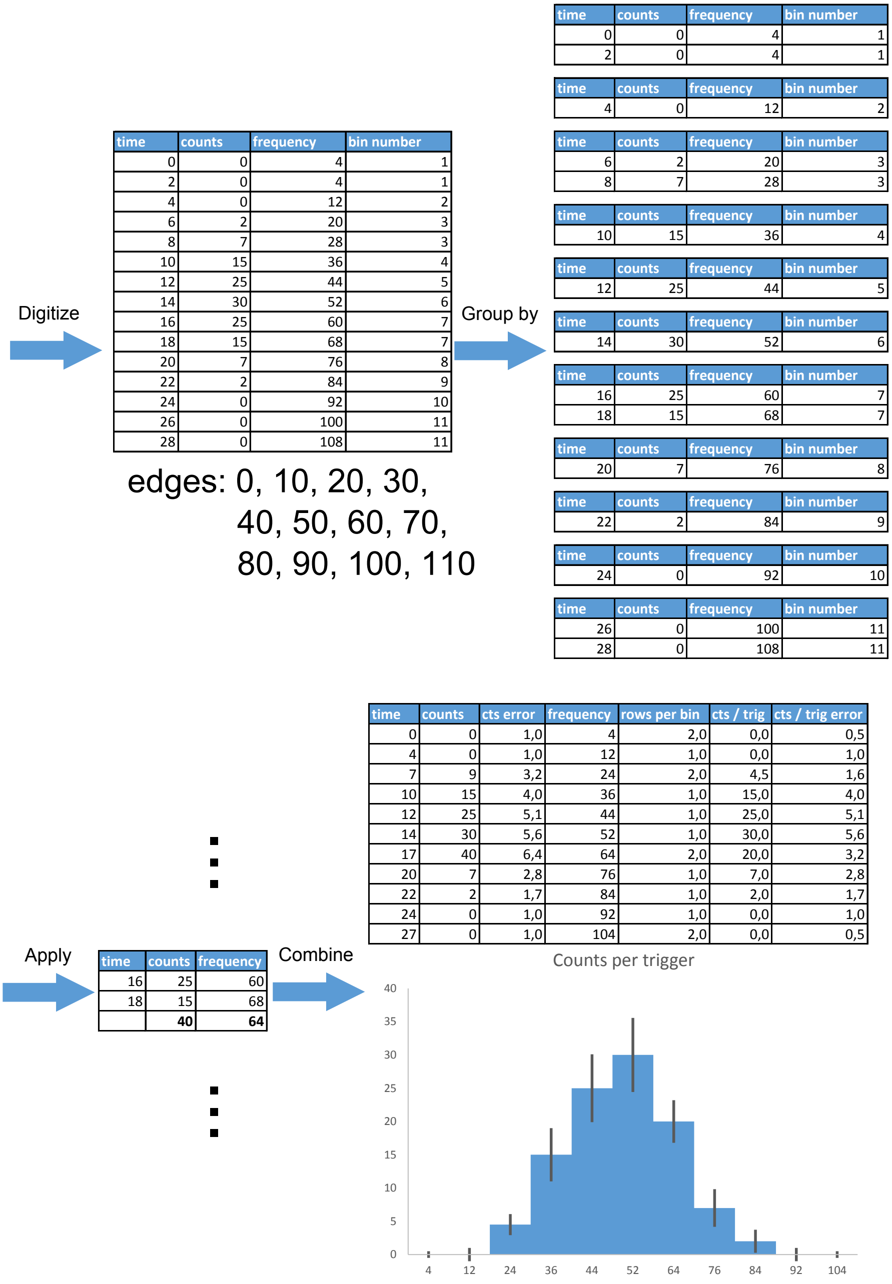

time	counts	frequency	bin number
0	0	4	1
2	0	4	1
4	0	12	2
6	2	20	3
8	7	28	3
10	15	36	4
12	25	44	5
14	30	52	6
16	25	60	7
18	15	68	7
20	7	76	8
22	2	84	9
24	0	92	10
26	0	100	11
28	0	108	11

time	counts	frequency	bin number
0	0	4	1
2	0	4	1

time	counts	frequency	bin number
4	0	12	2

time	counts	frequency	bin number
6	2	20	3
8	7	28	3

time	counts	frequency	bin number
10	15	36	4

time	counts	frequency	bin number
12	25	44	5

time	counts	frequency	bin number
14	30	52	6

time	counts	frequency	bin number
16	25	60	7
18	15	68	7

time	counts	frequency	bin number
20	7	76	8

time	counts	frequency	bin number
22	2	84	9

time	counts	frequency	bin number
24	0	92	10

time	counts	frequency	bin number
26	0	100	11
28	0	108	11

time	counts	frequency
16	25	60
18	15	68
	40	**64**

time	counts	cts error	frequency	rows per bin	cts / trig	cts / trig error
0	0	1,0	4	2,0	0,0	0,5
4	0	1,0	12	1,0	0,0	1,0
7	9	3,2	24	2,0	4,5	1,6
10	15	4,0	36	1,0	15,0	4,0
12	25	5,1	44	1,0	25,0	5,1
14	30	5,6	52	1,0	30,0	5,6
17	40	6,4	64	2,0	20,0	3,2
20	7	2,8	76	1,0	7,0	2,8
22	2	1,7	84	1,0	2,0	1,7
24	0	1,0	92	1,0	0,0	1,0
27	0	1,0	104	2,0	0,0	0,5

Figure A.2: Schematic illustration of the data binning procedure. In this example, the dataset extracted in example A.1 is binned in equal wavelength bins.

Bibliography

[1] O. Sorlin et al. *Progress in Particle and Nuclear Physics*, 61(2):602 – 673, 2008.

[2] T. Otsuka et al. *Physical Review Letters*, 95:232502, 2005.

[3] T. Otsuka et al. *Physical Review Letters*, 104:012501, 2010.

[4] S. Franchoo et al. *Physical Review Letters*, 81:3100–3103, 1998.

[5] P. Vingerhoets et al. *Physical Review C*, 82(6):064311, 2010.

[6] K. T. Flanagan et al. *Physical Review Letters*, 103(14):142501, 2009.

[7] K. T. Flanagan et al. *Physical Review C*, 82(4):041302, 2010.

[8] U. Köster et al. *Physical Review C*, 84(3):034320, 2011.

[9] K. Sieja et al. *Physical Review C*, 81:061303, 2010.

[10] F. Nowacki et al. *Physical Review Letters*, 117:272501, 2016.

[11] G. Hagen et al. *Physical Review Letters*, 117:172501, 2016.

[12] M. G. Mayer. *Physical Review*, 75:1969–1970, 1949.

[13] O. Haxel et al. *Physical Review*, 75:1766–1766, 1949.

[14] E. Caurier et al. *Rev. Mod. Phys.*, 77:427–488, 2005.

[15] V. Lapoux et al. *Physical Review Letters*, 117:052501, 2016.

[16] R Casten. *Nuclear structure from a simple perspective*, volume 23. Oxford University Press on Demand, 2000.

[17] M. Honma et al. *Physical Review C*, 80:064323, 2009.

[18] T. Otsuka et al. *Journal of Physics G: Nuclear and Particle Physics*, 43(2):024009, 2016.

[19] N. Shimizu et al. *Progress of Theoretical and Experimental Physics*, 2012(1):01A205, 2012.

[20] Y. Tsunoda et al. *Physical Review C*, 89:031301, 2014.

[21] V. Paar. *Nuclear Physics A*, 331(1):16–28, 1979.

[22] G. Fricke et al. *Atomic Data and Nuclear Data Tables*, 60(2):177 – 285, 1995.

[23] G. Fricke et al. *Nuclear charge radii.* Springer Berlin, 2004.

[24] I. Angeli et al. *Atomic Data and Nuclear Data Tables*, 99(1):69 – 95, 2013.

[25] I. Budinčević et al. *Physical Review C*, 90:014317, 2014.

[26] P. Lievens et al. *EPL (Europhysics Letters)*, 33(1):11, 1996.

[27] B. Castel et al. *Modern theories of nuclear moments.* Clarendon Press, 1990.

[28] K. L. G. Heyde. *The nuclear shell model.* Springer, 1990.

[29] Th. Schmidt. *Zeitschrift für Physik*, 106(5):358–361, 1937.

[30] B.H. Flowers. *The London, Edinburgh, and Dublin Philosophical Magazine and Journal of Science*, 43(347):1330–1334, 1952.

[31] R. J. Blin-Stoyle et al. *Proceedings of the Physical Society. Section A*, 67(10):885, 1954.

[32] A. Arima et al. *Progress of Theoretical Physics*, 12(5):623, 1954.

[33] V. Gerginov et al. *Physical Review Letters*, 91:072501, 2003.

[34] K. Kreim et al. *Physics Letters B*, 731:97 – 102, 2014.

[35] B. Cheal et al. *Physical Review A*, 86:042501, 2012.

[36] M. L. Bissell et al. *Physical Review C*, 93:064318, 2016.

[37] W. H. King. *Journal of the Optical Society of America*, 53(5):638–639, 1963.

[38] David W. Hogg et al. *arXiv preprint arXiv:1008.4686*, 2010.

[39] A. Bohr et al. *Physical Review*, 77:94–98, 1950.

[40] J. S. Grossman et al. *Physical Review Letters*, 83:935–938, 1999.

[41] J. E. Rosenthal et al. *Physical Review*, 41:459–470, 1932.

[42] M. F. Crawford et al. *Physical Review*, 76:1310–1317, 1949.

[43] J.R. Persson. *Atomic Data and Nuclear Data Tables*, 99(1):62 – 68, 2013.

[44] P. Campbell et al. *Progress in Particle and Nuclear Physics*, 86:127 – 180, 2016.

[45] Yu. A. Kudriavtsev et al. *Applied Physics B*, 29(3):219–221, 1982.

[46] C. Schulz et al. *Journal of Physics B: Atomic, Molecular and Optical Physics*, 24(22):4831, 1991.

[47] T. J. Procter et al. In *Journal of Physics: Conference Series*, volume 381, page 012070. IOP Publishing, 2012.

[48] K. M. Lynch et al. In *Journal of Physics: Conference Series*, volume 381, page 012128. IOP Publishing, 2012.

[49] K. M. Lynch et al. *Hyperfine Interactions*, 216(1-3):95–101, 2013.

[50] M. M. Rajabali et al. *Nuclear Instruments and Methods in Physics Research Section A: Accelerators, Spectrometers, Detectors and Associated Equipment*, 707:35–39, 2013.

[51] K. T. Flanagan et al. volume 227, pages 131–137. JC Baltzer, 2013.

[52] K. M. Lynch et al. volume 63, page 01007. EDP Sciences, 2013.

[53] T. E. Cocolios et al. *Nuclear Instruments and Methods in Physics Research Section B: Beam Interactions with Materials and Atoms*, 317:565–569, 2013.

[54] K. T. Flanagan et al. *Physical Review Letters*, 111:212501, 2013.

[55] K. M. Lynch et al. *Physical Review X*, 4(1):011055, 2014.

[56] P. Vingerhoets et al. *Physics Letters B*, 703(1):34–39, 2011.

[57] R. Neugart et al. *Journal of Physics G: Nuclear and Particle Physics*, 44(6):064002, 2017.

[58] J. Sugar et al. *Journal of Physical and Chemical Reference Data*, 19(3):527–616, 1990.

[59] H. Bucka et al. *Zeitschrift für Physik*, 202:22–31, 1967.

[60] R. P. de Groote et al. *Physical Review Letters*, 115:132501, 2015.

[61] R. P. de Groote. Master's thesis, Instituut voor kern-en stralingsfysica, KU Leuven, 2013.

[62] M. Verlinde. Master's thesis, Instituut voor kern-en stralingsfysica, KU Leuven, 2016.

[63] V. Sonnenschein. PhD thesis, University of Jyväskylä, 2015.

[64] R. J. Barlow. *Statistics: a guide to the use of statistical methods in the physical sciences*, volume 29. John Wiley & Sons, 1989.

[65] J. VanderPlas. *arXiv preprint arXiv:1411.5018*, 2014.

[66] A. Gelman et al. *Bayesian data analysis*, volume 2. Chapman & Hall/CRC Boca Raton, FL, USA, 2014.

[67] W. Gins et al. *Accepted for publication in computer Physics Communications*, 2017.

[68] D. Foreman-Mackey et al. *Publications of the Astronomical Society of the Pacific*, 125(925):306, 2013.

[69] J. Goodman et al. *Communications in applied mathematics and computational science*, 5(1):65–80, 2010.

[70] M. D. Hoffman et al. *Journal of Machine Learning Research*, 15(1):1593–1623, 2014.

[71] J Salvatier et al. *PeerJ Computer Science*, 2:e55, 2016.

[72] R. Andrae et al. *arXiv preprint arXiv:1009.2755*, 2010.

[73] R Andrae et al. *arXiv preprint arXiv:1012.3754*, 2010.

[74] G.and others Audi. *Chinese physics C*, 41(3):030001, 2017.

[75] U. Köster. *The European Physical Journal A - Hadrons and Nuclei*, 15(1):255–263, 2002.

[76] J Lettry et al. *Review of scientific instruments*, 69(2):761–763, 1998.

[77] U. Köster et al. *Nuclear Instruments and Methods in Physics Research Section B: Beam Interactions with Materials and Atoms*, 160(4):528 – 535, 2000.

[78] E. Mané et al. *The European Physical Journal A*, 42(3):503–507, 2009.

[79] H. Frånberg et al. *Nuclear Instruments and Methods in Physics Research Section B: Beam Interactions with Materials and Atoms*, 266(19–20):4502 – 4504, 2008.

[80] Frank Wienholtz. Private Communications, 2017.

[81] P. Vingerhoets. PhD thesis, Instituut voor kern-en stralingsfysica, KU Leuven, 2011.

[82] J. Äystö et al. *The European Physical Journal A-Hadrons and Nuclei*, 13(1):109–115, 2002.

[83] H. Figger et al. *Colloq. Int. C. N. R. S.*, 164(355), 1967.

[84] O. Lutz et al. *Zeitschrift für Physik A Atoms and Nuclei*, 288(1):17–21, 1978.

[85] R. M. Sternheimer. *Physical Review A*, 6:1702–1709, 1972.

[86] N. J. Stone. *Atomic Data and Nuclear Data Tables*, 90(1):75–176, 2005.

[87] J. Van Roosbroeck et al. *Physical Review C*, 71:054307, 2005.

[88] N. Patronis et al. *Physical Review C*, 80:034307, 2009.

[89] S. V. Ilyushkin et al. *Physical Review C*, 80:054304, 2009.

[90] C. J. Gross et al. *Acta Physica Polonica B*, 40(3):447–455, 2009.

[91] T. Cocolios et al. *Physical Review Letters*, 103(10):102501, 2009.

[92] T. E. Cocolios et al. *Physical Review C*, 81(1):014314, 2010.

[93] M. Dufour et al. *Physical Review C*, 54:1641–1660, 1996.

[94] P-G Reinhard et al. *arXiv preprint arXiv:1704.07430*, 2017.

[95] L. Wilets et al. *Physical Review*, 91(6):1488, 1953.

[96] A. R. Bodmer et al. *Proceedings of the Physical Society. Section A*, 67(7):622, 1954.

[97] W.J. Tomlinson et al. *Nuclear Physics*, 60(4):614 – 633, 1964.

[98] I. Talmi. *Nuclear Physics A*, 423(2):189 – 196, 1984.

[99] S. Balbir et al. *Nuclear Physics A*, 161(2):385 – 400, 1971.

[100] D. Zawischa. *Physics Letters B*, 155(5):309 – 312, 1985.

[101] D. Zawischa et al. *Physics Letters B*, 185(3):299 – 303, 1987.

[102] U. Regge et al. *Physical Review Letters*, 61:149–152, 1988.

[103] E. Caurier et al. *Physics Letters B*, 522(3):240 – 244, 2001.

[104] E. Caurier et al. *Physics Letters B*, 96(1):15 – 18, 1980.

[105] S.A. Fayans et al. *Nuclear Physics A*, 676(1):49 – 119, 2000.

FACULTY OF SCIENCE
DEPARTMENT OF PHYSICS AND ASTRONOMY
NUCLEAR MOMENTS
Celestijnenlaan 200D box 2418
B-3001 Leuven
ruben.degroote@kuleuven.be
https://fys.kuleuven.be/iks/nm/home